

FABRICATION AND CHARACTERIZATION OF ZINC OXIDE
AND LEAD ZIRCONATE TITANATE NANOSTRUCTURES

ALI KHORSAND ZAK

THESIS SUBMITTED IN FULFILLMENT OF
THE REQUIREMENT FOR THE DEGREE
OF DOCTOR OF PHILOSOPHY

PHYSICS DEPARTMENT
FACULTY OF SCIENCE
UNIVERSITY OF MALAYA
KUALALUMPUR
2012

**To my wife
for her support and love**

UNIVERSITY OF MALAY

ORIGINAL LITERARY WORK DECLARATION

Name of Candidate: **Ali Khorsand Zak** (Passport No: **L11713467**)

Registration/Matric No: **SHC080049**

Name of Degree: **Doctor of Philosophy**

Title of Thesis: **Fabrication and characterization of zinc oxide and lead zirconate titanate nanostructures**

Field of Study: **Nanophysics**

I do solemnly and sincerely declare that:

- (1) I am the sole author of this work;
- (2) This Work is original;
- (3) Any use of any work in which copyright exists was done by way of fair dealing and for permitted purposes and any excerpt or extract from, or reference to or reproduction of any copyright work has been disclosed expressly and sufficiently and the title of the Work and its authorship have been acknowledged in this Work;
- (4) I do not have any actual knowledge nor do I ought reasonably to know that the making of this work constitutes an infringement of any copyright work;
- (5) I hereby assign all and every rights in the copyright to this Work to the University of Malaya ("UM"), who henceforth shall be owner of the copyright in this Work and that any reproduction or use in any form or by any means whatsoever is prohibited without the written consent of UM having been first had and obtained;
- (6) I am fully aware that if in the course of making this Work I have infringed any copyright whether intentionally or otherwise, I may be subject to legal action or any other action as may be determined by UM.

Candidate's Signature

Date

Subscribed and solemnly declared before,

Witness's Signature

Date

Name:

Designation:

ABSTRACT

Since 1990, research on nanostructures and nanoparticles has attracted the interest of many researchers. Several methods have been developed to fabricate nano-sized materials. The main concern is to establish method that can be used to produce these materials at low cost, which is attractive for industry. Based on this motivation, in this thesis, I attempt to develop and investigate new and modified routes for preparing ZnO and PZT nanostructures and nanoparticles, which are the two materials that have attracted the most interest in in this decade. The aim of this work is to design and modify simple, inexpensive, fast, and safe methods for preparing the nanopowders of these two materials on a large scale and to study the characteristics of the nanostructures, such as structure, morphology, and optical properties by various characterization tools. To date, four different preparation techniques have been used to prepare ZnO nanoparticles, i.e., sol-gel synthesis, sol-combustion synthesis, solvothermal synthesis, and sonochemical synthesis. In addition, the sol-gel synthesis process has been used to prepare PZT nanoparticles. Initially, ZnO nanoparticles were prepared by the sol-gel method in two different media, i.e., gelatin and starch. These two natural materials were used as the polymerization agent. ZnO NPs were also synthesized by the sol-combustion method in which DEA was used as the polymerization agent and stabilizer, and citric and nitric acids were used as fuel. In the second preparation technique, the ZnO nanoparticles and nanostructures were prepared by the solvothermal method. The ethanolamine family, (MEA, DEA, and TEA), was investigated to determine its effect on the morphology of the ZnO nanostructures. The ZnO nanostructures (rods and flowers) were prepared successfully using the third preparation technique, i.e., the sonochemical method. NaOH and NH₃ solutions were used to control the pH of the Zn²⁺. The sonication process was applied for 5, 15, 30, and

60 min. In the fifth preparation technique, the PZT nanoparticles were prepared by the modified sol-gel method. Polyethylenglycol (PEG) and 2-methoxyethanol (EGME) were used as separate solvents to prepare the PZT nanoparticles. The structures of the ZnO and PZT nanoparticles also were investigated theoretically. Different theoretical models, such as Williamson-Hall and the Size-Strain Plot, were applied to analyze the XRD data of the ZnO and PZT nanoparticles. We also investigated the effect of calcination temperature on the mechanical properties of the nanoparticles. In addition, we investigated the optical properties of PZT nanoparticles prepared in different solvents, i.e., PEG and EGME. The dielectric properties of the PZT nanoparticles (with and without PVDF matrix) were investigated in the frequency range of 100 Hz to 40 MHz. The characterization of the materials using various techniques, such as XRD, TEM, SEM, and UV-vis, proved that good quality (narrow size distribution and uniform morphology) ZnO nanoparticles can be produced by the preparation technique that uses gelatin, while good quality (narrow size distribution and uniform morphology) PZT nanoparticles can be produced by the preparation technique that uses 2-methoxyethanol. These preparation techniques are attractive because they can be used to prepare these nanoparticles in large-scale production facilities, which is suitable for industry. In the future, these preparation methods can also be modified to prepare other metal oxide nanostructures, such as MgO and NiO, which also have various potential applications, such as in the medical field and electronics industries.

ABSTRAKT

Kajian terhadap struktur nano dan partikel nano telah mendapat perhatian sejak 1990. Beberapa kaedah telah dijalankan untuk menghasilkan bahan yang bersaiz nano. Tumpuan utama adalah untuk mewujudkan kaedah penyediaan yang boleh digunakan untuk penghasilan pada yang kos rendah, yang pastinya menarik bagi pihak industri. Berdasarkan motivasi ini, tesis ini bertujuan untuk mengembangkan dan mengkaji cara baru dan cara yang telah diubahsuai untuk menyediakan struktur nano dan partikel nano ZnO dan PZT sebagai dua bahan yang paling menarik pada dekad ini. Matlamat kajian ini adalah untuk mereka dan mengubahsuai kaedah yang ringkas, murah, pantas dan selamat untuk penyediaan serbuk nano dalam skala besar dan mengkaji sifat struktur nano tersebut dari segi struktur, morfologi, dan sifat-sifat optik melalui pelbagai peralatan pencirian. Lima teknik penyediaan yang berbeza telah dilakukan seperti sintesis sol-gel, pembakaran sol, solvotermal dan sintesis sonokimia untuk partikel nano ZnO dan sintesis sol-gel untuk partikel nano PZT. Partikel nano ZnO pada awalnya disediakan melalui kaedah sol-gel di dalam dua media yang berbeza; gelatin dan kanji. Kedua-dua bahan semulajadi ini telah digunakan sebagai agen pempolimeran. Partikel nano ZnO juga disintesis melalui kaedah pembakaran sol. Dalam kaedah ini, DEA telah digunakan sebagai agen pempolimeran dan penstabil, serta asid sitrik dan asid nitrik berperanan sebagai bahan bakar. Dalam teknik penyediaan yang kedua, partikel nano dan struktur nano ZnO dihaasilkan melalui kaedah solvotermal. Kesan kumpular/rangkaian etanolamin (MEA, DEA, TEA) terhadap morfologi struktur nano ZnO telah dikaji. Struktur nano ZnO (rod dan bunga) telah berjaya dihasilkan menggunakan kaedah penyediaan yang ketiga iaitu kaedah sonokimia. NaOH dan NH₃ digunakan untuk mengawal pH Zn²⁺. Proses sonikasi telah diaplikasikan pada jangka masa berlainan iaitu 5, 15, 30 dan 60 minit. Dalam kaedah penyediaan kelima, partikel

nano PZT telah disediakan melalui proses sol-gel yang telah diubahsuai. Polyethyleneglycol (PEG) dan 2-methoxyethanol (EGME) telah digunakan sebagai dua pelarut yang berbeza untuk menghasilkan partikel nano PZT. Struktur partikel nano ZnO dan PZT juga turut dikaji secara teori. Model teori yang berlainan seperti Williamson-Hall dan Plot Regangan Saiz telah digunakan untuk menganalisa data XRD bagi partikel nano ZnO dan PZT serta kesan suhu pemanasan terhadap sifat-sifat mekanik partikel nano juga dikaji. Sebagai tambahan, sifat-sifat optik partikel nano PZT yang disediakan menggunakan pelarut berbeza iaitu PEG dan EGME turut dikaji. Sifat dielektrik partikel nano PZT (dengan matriks PVDF dan tanpa matriks PVDF) telah dikaji pada skala frekuensi 100 Hz hingga 40 MHz. Pencirian bahan menggunakan pelbagai teknik seperti XRD, TEM, SEM dan UV-vis telah membuktikan bahawa partikel nano ZnO yang berkualiti (taburan saiz yang sempit dan morfologi seragam) boleh dihasilkan melalui kaedah penyediaan yang menggunakan gelatin manakala partikel nano PZT yang berkualiti (taburan saiz yang sempit dan morfologi seragam) boleh diperolehi melalui penyediaan yang menggunakan 2-methoxyethanol. Kaedah penyediaan ini amat menarik kerana ianya mampu menghasilkan partikel nano ZnO dan PZT dalam skala besar, yang amat sesuai untuk industri. Pada masa hadapan, kaedah-kaedah penyediaan ini juga boleh diubahsuai untuk menghasilkan logam oksida yang lain seperti MgO dan NiO, yang juga mempunyai pelbagai aplikasi dalam bidang perubatan dan industri elektronik.

ACKNOWLEDGEMENTS

This thesis arose in part out of years of research that has been done since I came to Low Dimensional Materials Research Center (LDMRC). By that time, I have worked with a great number of people whose contribution in assorted ways to the research and the making of the thesis deserved special mention. It is a pleasure to convey my gratitude to them all in my humble acknowledgment especially to Prof. Seyed Mohammad Hosseini, my master degree supervisor and he passed away three months ago, who suggested and helped me to come to this center.

In the first place, I would like to record my gratitude to Prof. Dr. Wan Haliza Abd. Majid for her supervision, advice, and guidance from the very early stage of this research as well as giving me extraordinary experiences throughout the work. Above all and the most needed, she supports me in various ways. Her truly scientist intuition has made her as a constant oasis of ideas and passions in science, which exceptionally inspire and enrich my growth as a student, a researcher and a scientist want to be. I am indebted to her more than she knows.

I gratefully acknowledge my good friends, Mr. Gan, Dr. Reza Mahmoudian, Dr. Majid Darroudi, Dr. Ramin Yousefi, Dr. Huang, and Dr. Selvi, for their advice, help, and crucial contribution, which made them a backbone of this research and so to this thesis. I am grateful in every possible way and hope to keep up our collaboration in the future.

Many thanks go in particular to Bright Sparks Unit employees and university of Malaya for their helps, financial support and scholarship that helped me too much to study with a free mind.

I gratefully thank my good friend and partner in research Rehana Razali for her contribution on this thesis and I hope to continue our contribution in future. It is a pleasure to pay tribute also to Mr. Muhamad Arouf and Mrs. Lela for their assistance and also my friends Mr. Siamak Pilban, Mr. Amir Moradi, Ms. Mahmudian, and Mrs. Banihashemi for their kind supports.

In addition, I would like to gratefully thank my parents for their love and supports. There are many people that I cannot remember but I would like to acknowledge them all and apologies if I forgot to mention their name.

Finally yet importantly, my warmest thanks and loves go to my wife, Toktam, and my daughter, Yeganeh, for all their love and continuing supports throughout this research work.

Ali Khorsand Zak

Kuala Lumpur, Malaysia

November 2011

TABLE OF CONTENTS

	Page
ABSTRACT	i
ABSTRAK	iii
ACKNOWLEDGEMENTS	vii
TABLE OF CONTENTS	ix
LIST OF TABLES	xii
LIST OF FIGURES	xiii
LIST OF SYMBOLS AND ABBREVIATIONS	xx
CHAPTER I: INTRODUCTION	1
1.1. Nanoparticles research	1
1.2. Background and scope of study	2
1.3. Aim and objective	5
1.4. Thesis structure	6
CHAPTER II: FUNDAMENTAL PROPERTIES OF NANOPARTICLES	7
2.1. Introduction	7
2.2. Fabrication of nanostructured materials	9
2.2.1. Fabrication of ZnO nanostructures	9
2.2.2. Fabrication of PZT nanostructures	14
2.3. Fundamental properties and theoretical models	17
2.3.1. Crystal structure of ZnO	17
2.3.2. Crystal structure of PZT	19
2.3.3. Optical properties	21
2.3.3.1. Optical properties of ZnO	22
2.3.3.2. Optical properties of PZT	26
2.3.4. Band-gap of semiconductors	26
2.3.5. Quantum confinement effect	30
2.4. Dielectric function of materials	31
2.4.1. Lorentz oscillator model for calculating dielectric constant	31
2.4.2. Kramers-Kronig method for calculating optical properties.....	32
2.5. Summary	35

CHAPTER III: SYNTHESIS AND CHARACTERIZATION TECHNIQUES OF ZnO AND PZT NANOPARTICLES	36
3.1. Introduction	36
3.2. Synthesis of ZnO nanoparticles and nanostructures	37
3.2.1. Gelatin stabilized sol-gel synthesis of ZnO nanoparticles	37
3.2.2. Starch stabilized sol-gel synthesis of ZnO nanoparticles	39
3.2.3. Sol-combustion synthesis of ZnO nanoparticles using DEA	40
3.2.4. Solvothermal synthesis of ZnO nanostructures in MEA, DEA, and TEA	42
3.2.5. Sonochemical synthesis of ZnO nanostructures in aqueous solution	44
3.3. Synthesis of PZT nanoparticles	45
3.3.1. Sol-gel synthesis of PZT nanoparticles using polyol solution	45
3.3.2. Sol-gel synthesis of PZT nanoparticles using 2-methoxyethanol	47
3.4. Characterization techniques and instrumental	50
3.4.1. X-ray diffraction (XRD) analysis	50
3.4.2. Fourier transforms infrared spectroscopy (FTIR)	51
3.4.3. Transmission electron microscopy (TEM)	52
3.4.4. Field emission scanning electron microscopy (FESEM)	53
3.4.5. Ultraviolet-Visible spectroscopy (UV-vis)	53
3.4.6. Thermogravimetric analysis (TGA)	54
3.5. Summary	55
CHAPTER IV: RESULTS AND DISCUSSIONS 1: CHARACTERIZATION OF ZnO AND PZT NANOSTRUCTURES	56
4.1. Introduction	56
4.2. ZnO-NPs and nanostructures	56
4.2.1. ZnO-NPs prepared using gelatin media	57
4.2.2. ZnO-NPs prepared using starch media	62
4.2.3. ZnO-NPs prepared by sol-gel combustion method	68
4.2.4. ZnO-NPs prepared by solvothermal method	74
4.2.4.1. Effects of ethanolamine family on morphology of the ZnO nanostructures	79
4.2.5. ZnO nanostructures prepared by sonochemical method	81
4.3. PZT-NPs	92
4.3.1. PZT-NPs prepared by sol-gel method using aqueous polyol solution ..	92
4.3.2. PZT-NPs prepared by sol-gel method using 2-methoxyethanol	98
4.4. Summary	102

CHAPTER V: RESULTS AND DISCUSSIONS 2: THEORETICAL STUDIES AND APPLICATION PROPERTIES OF ZnO AND PZT NANOPARTICLES	103
5.1. Introduction	103
5.2. X-ray peak broadening analysis of ZnO-NPs	103
5.2.1. Average crystallite size calculation by Scherrer method	105
5.2.2. Mechanical properties calculation of ZnO by W-H methods	106
5.2.3. Mechanical properties calculations of ZnO-NPs by SSP method	111
5.2.4. TEM analysis of the ZnO-NPs	112
5.3. X-ray peak broadening analysis of PZT-NPs by W-H method.....	116
5.4. Effect of solvent on optical properties of PZT-NPs in infrared region	118
5.4.1. X-ray diffraction and TEM results	118
5.4.2. FTIR analysis	120
5.4.3. Optical constant spectrum	122
5.4.4. Optical phonon modes	125
5.5. Experimental and theoretical studies of PZT-NPs dielectric behavior in PVDF thin film matrix	126
5.5.1. Sample preparation	126
5.5.2. Characterization results	127
5.5.3. Theoretical studies of the dielectric behavior of PZT-NPs/PVDF nanocomposite thin film	134
5.6. Summary	139
 CHAPTER VI: CONCLUSION	 140
REFERENCES	144

LIST OF TABLES

	Page
Table 2.1: Acoustic and optical modes in a crystal with wurtzite structure considering number of the unit cell atoms.	24
Table 2.2: Phonon mode frequencies of wurtzite ZnO at the center of the Brillouin zone obtained from infrared spectroscopic ellipsometry and Raman scattering.	24
Table 4.1: Lattice parameters of ZnO-NPs prepared at different calcination temperatures; 400, 500, and 600 °C. (The measurements were done at room temperatures of 25 °C).	65
Table 4.2: lattice parameters of ZnO-NPs prepared at calcination temperatures of 600, 650 and 750 °C. (The measurements were done at room temperatures of 25 °C)	70
Table 4.3: The crystal size of ZnO-NPs prepared at calcination temperatures of 600, 650 and 750 °C.	71
Table 4.4: The structure parameters of ZnO-NS prepared at different ultrasonication times of 15, 30, and 60 min.	82
Table 4.5: Lattice parameters of PZT-NPs prepared at different temperatures of (b) 550, (c) 600 and (d) 650 °C for 2 hrs.	96
Table 4.6: Average particle size of prepared PZT-NPs at different calcination temperatures for 2 h; 550 (a), 600 (b) and 650 °C (c).	97
Table 4.7: Lattice parameters of PZT-NPs prepared at different temperatures of 600, 650 and 700 °C for 1h.	100
Table 4.8: The diameter size of PZT-NPs obtained from different methods.	101
Table 5.1. The structure parameters of ZnO-NPs calcinated at 650 °C and 750 °C.	104
Table 5.2: Geometric parameters of ZnO-NPs calcined at 650 °C and 750 °C.	115
Table 5.3: the crystallite size and strain of the PZT-NPs prepared at different temperatures.	116
Table 5.3: Vibration bands and band widths for PZT-EGME and PZT-PEG calcined at 600 °C and 650 °C.	121
Table 5.4: Optical phonon for PZT-EGME and PZT-PEG calcined at 600 °C and 650 °C.	125
Table 5.5: Characteristic bands with specific vibrational modes and crystalline phases.	130

LIST OF FIGURES

	Page
Figure 1.1: Worldwide Zinc Oxide Applications.	3
Figure 1.2: Number of publications per year on ZnO nanostructures. The data were extracted on 25 Jun 2011 through the Institute of Scientific Information (ISI) database using the following keywords that appeared in topic: ZnO or zinc oxide together with nanostructure, nanoparticles, nanopowders, and nanorods.	4
Figure 1.3: Number of publications per year on PZT nanostructures. The data were extracted on 25 Jun 2011 through the Institute of Scientific Information (ISI) database using the following keywords that appeared in topic: PZT together with nanostructure, nanoparticles, and nanopowders.	4
Figure 2.1: Synthesis diagrams of the nanostructures.	10
Figure 2.2: ZnO nanowires (a) and nanobelts (b) prepared by CVD method.	11
Figure 2.3: The flower like ZnO nanostructures that have been made by hydrothermal method.	12
Figure 2.4: The ZnO nanorods prepared by microwave assisted method.	13
Figure 2.5: The low (a) and high (b) magnification micrographs of ZnO/CdS core-shell synthesized by sonochemical methods.	13
Figure 2.6: SEM micrograph of PZT nanoparticles which prepared by sol-combustion method and calcined at 650 °C for 2h.	16
Figure 2.7: PZT wires prepared by hydrothermal method with heating treatment of (a) 12 h and (b) 24 h.	16
Figure 2.8: ZnO crystal structure (a) cubic rocksalt (B1), (b) cubic zinc blende (B3), and hexagonal wurtzite (B4).	18
Figure 2.9: the hexagonal wurtzite structure of zinc oxide.	18
Figure 2.10: The perovskite structure of PZT in three forms of cubic, tetragonal, and rhombohedral.	20
Figure 2.11: The morphotropic phase boundary of the ferroelectric material serves as the boundary between different phases in terms of the electric polarization direction and crystal structure.	20
Figure 2.12: Absorption spectra of ZnO nanowires sol (a) and powder reflectance (b) spectra of zinc oxide nanowires.	23

Figure 2.13: Atomic vibrations in wurtzite ZnO. The large atom represents Zn while the smaller one is O. X = (100), Y = (010), and Z (001) represents the optical polarization directions: (a) for general wave vector and (b) for zone center phonons.	25
Figure 2.14: Schematic infrared active normal vibrations of a TiO ₆ octahedron, ν_1 , higher frequency stretching vibration, ν_2 , lower frequency bending vibration.	26
Figure 2.15: The direct and indirect electron transition in band gap of the semiconductors.	27
Figure 2.16: Band-gap measurement using Kubelka-Munk method for ZnO prepared by different concentration of poly (sodium 4-styrene-sulfonate) (PSS).	29
Figure 2.17: band gap estimate from the maximum of the derivative of absorbance spectrum.	29
Figure 2.18: The band-gap of CdS nanoparticles correspond to their size.	30
Figure 2.19: Quantum size effect on the absorbance of ZnO nanoparticles.	30
Figure 2.20: The refraction index (n) and reflectivity for solid model plotted as function of frequency.	34
Figure 2.21: Dielectric function $\epsilon(\omega)$. There is an absorption in the infrared ω_{IR} and another one is in UV reign ω_{UV} .	34
Figure 3.1: The expended materials after calcination process because of gelatin.	38
Figure 3.2: A) The prepared solution placed in an oil-bath to remove the water, B) the honey-wish formed gel, C) the gel was rubbed inside crucibles, D) the ZnO-NPs after calcination process.	38
Figure 3.3: The hydrolysis process of Starch and the binding side of zinc cation.	40
Figure 3.4: The used reflux system to get a more homogenous solution.	42
Figure 3.5: The autoclave and its Teflon vessel used for experiment.	43
Figure 3.6: (a) Ultrasound system, (b) the Zn ²⁺ solution before sonication (c) the ZnO colloid in solution after sonication.	44
Figure 3.7: Flowchart of synthesis of PZT-NPs by sol-gel method.	46
Figure 3.8: Figure 3.8: The PZT nanoparticles prepared by sol-gel method	47
Figure 3.9: By adding some water, the solution transformed to gel state.	48
Figure 3.10: The structure of the formed gel.	48
Figure 3.11: Synthesis flowchart of the PZT-NPs prepared by sol-gel method.	49

Figure 3.12: Schematic of the diffraction of an X-ray beam by parallel atomic planes in crystalline materials.	51
Figure 4.1: TGA and DTA curves of gels from 50 °C to 900 °C. The trace shows 71% loss weight in four steps to achieve ZnO-NPs.	57
Figure 4.2: FTIR spectra of the ZnO-NPs prepared at different calcination temperatures: (a) 400, (b) 500, (c) 600 and (d) 700 °C. The absorption band related to Zn-O vibration mode was clearly observed at 420 cm ⁻¹ .	58
Figure 4.3: XRD patterns of ZnO-NPs prepared at different calcination temperatures of 400, 500, 600 and 700 °C.	59
Figure 4.4: TEM images of ZnO-NPs prepared at different calcination temperatures.	61
Figure 4.5: TGA and DTA curves of gels from 50 °C to 900 °C. The trace shows 52% loss weight in four steps to achieve ZnO-NPs.	63
Figure 4.6: FTIR spectra of the (a) starch, (b) dried gel, and ZnO-NPs prepared at different calcination temperatures: (c) 400, (d) 500, and (e) 600 °C. The absorption band related to Zn-O vibration mode was clearly observed at 420 cm ⁻¹ .	64
Figure 4.7: XRD pattern of (a) dried gel and ZnO-NPs prepared at different calcination temperatures of (b) 400, (c) 500, and (d) 600 °C.	65
Figure 4.8: TEM images of ZnO-NPs prepared at different annealing temperatures: (a) 400, (b) 500, and (c) 600 °C. It is clearly observed that the particle sizes increases when the annealing temperature increases.	67
Figure 4.9: TGA and DTA curves of xerogels from 50 °C to 900 °C. The traces show two steps; (a) is related to the evaporation of water and (b) is related to the decomposition of organic materials.	68
Figure 4.10: FTIR spectra of the ZnO-NPs prepared at different annealing temperatures: (a) 600 °C, (b) 650 °C and (c) 750 °C. The absorption band related to Zn-O vibration mode was clearly observed.	69
Figure 4.11: XRD pattern of ZnO-NPs prepared at different annealing temperatures. A slight change of intensity and position was observed for the (201) peak.	70
Figure 4.12: TEM images of ZnO-NPs prepared at different annealing temperatures: (a) 600, (b) 650 and (c) 750 °C. The nearly hexagonal plate shape of the ZnO-NPs is clearly shown (in I, for example).	72
Figure 4.13: Absorption edge (inset) and band gap of the ZnO-NPs prepared at different annealing temperatures: (a) 600, (b) 650 and (c) 750 °C.	73

Figure 4.14: The FTIR patterns of the ZnO-NPs prepared by the solvothermal method at 150°C.	74
Figure 4.15: The XRD patterns of the ZnO-NPs prepared by the solvothermal method at 150°C.	75
Figure 4.16: The UV-vis absorbance spectrum of ZnO-NPs from 200 nm to 1000 nm. Inset shows the derivative of the absorbance spectrum.	76
Figure 4.17: The TEM morphology image of ZnO-NPs (a), the SEM micrograph of the ZnO-NPs (b), and the particle size distribution of the ZnO-NPs (c).	77
Figure 4.18: Schematic images of formation of the ZnO-NPs from the ZnO seed, and the role of TEA as a polymerization agent.	78
Figure 4.19: ZnO nanostructures prepared in different medias of (a) MEA, (b) DEA, (c) TEA.	80
Figure 4.20: Schematic images to show the growth mechanism of the ZnO nanostructures in different medias of MEA, DEA, and TEA.	81
Figure 4.21: XRD patterns for samples prepared after various ultrasonication time (a) 5 minutes, (b) 15 minutes, (c) 30 minutes and (d) 60 minutes.	83
Figure 4.22: FESEM and TEM micrographs for (a) Zn (OH) ₂ crystals, (b) ZnO nanorods, (c,d) ZnO flowers.	85
Figure 4.23: FESEM micrographs for ZnO nanorods (a) and nanoflowers (b) with varying magnification.	86
Figure 4.24: The Zn(OH) ₂ crystals are formed after 5 min ultrasonication. After about 7 min, ZnO nanoseeds are formed. The ZnO nanorods are formed by continuing the ultrasonication time to 15 min and by further ultrasonication times ZnO flowers are formed.	87
Figure 4.25: (a) End of a nodular structure, (b) Nanoscaled crystallites in the nodular, (c) Lattice image of the crystallites, (d) FFT pattern of (b) and (c).	88
Figure 4.26: (a) SAED rings of Figure 4.25 (b) and (c), (b) Indexed SAED pattern of (a).	88
Figure 4.27: (a) TEM image of ZnO nanorod, (b) HRTEM image of ZnO nanorod, (c) Enlarged HRTEM image of (b), (d) Modified and enlarged lattice image of (c) and its SAED in inset.	89

Figure 4.28: (a) [-2110] SAED pattern of Figure 4.27b, (b) FFT pattern of Figures 4.27b-4.27d, (c) Another SAED pattern of Figure 4.27b, (d) FFT pattern corresponding to (c).	90
Figure 4.29: UV-Visible absorption spectra for ZnO samples for 15 min, 30 min and 60 min.	91
Figure 4.30: Thermal analyses (TGA-DTA) of xerogel of PZT.	93
Figure 4.31: FTIR spectra of prepared PZT-NPs at different calcination temperatures for 2 h; 500 (a), 550 (b), 600 (c) and 650 °C (d).	94
Figure 4.32: Typical XRD patterns of prepared PZT-NPs at different calcination temperatures for 2 h; 500 (a), 550 (b), 600 (c) and 650 °C (d).	95
Figure 4.33: SEM and TEM micrographs of the prepared PZT-NPs calcinated at 650 °C (b) for 2 h.	97
Figure 4.34: Thermal gravity and derivation analysis (TGA-DTA) of dried gel of PZT.	99
Figure 4.35: FTIR spectra of prepared PZT-NPs at different calcination temperatures for 1h; 600 (a), 650 (b) and 700 (c).	99
Figure 4.36: XRD patterns of PZT nanoparticles prepared at different calsination temperatures of 600, 650, and 700 °C.	101
Figure 4.37: TEM micrograph of the prepared PZT-NPs at calcination temperatures of 650 °C for 1h.	102
Figure 5.1: The XRD pattern of ZnO-NPs calcined at 650 °C and 750 °C. The XRD pattern shows that the sample product is crystalline with a hexagonal wurtzite phase and free from pyrocholore phases.	104
Figure 5.2: Sherrer plots of ZnO-NPs calcined at 650 °C and 750 °C. Fit to the data, the crystalline size D is extracted from the slope of the fit.	107
Figure 5.3: The W-H analysis of ZnO-NPs calcined at 650 °C and 750 °C assuming UDM. Fit to the data, the strain is extracted from the slope and the crystalline size is extracted from the y-intercept of the fit.	108
Figure 5.4: The modified form of W-H analysis assuming USDM for ZnO-NPs calcinated at 650 °C and 750 °C.	109
Figure 5.5: The modified form of W-H analysis assuming UDEDM for ZnO-NPs calcined at 650 °C and 750 °C. Fit to the data, the density of energy is extracted from the slope and the crystalline size is extracted from the y-intercept of the fit.	111

Figure 5.6: The SSP plots of ZnO-NPs calcined at 650 °C and 750 °C. The particle size is achieved from the slop of the liner fitted data and the root of y-intercept gives the strain.	113
Figure 5.7: TEM micrographs of ZnO-NPs calcinated at 750 °C. This figure shows a nonuniform strain for some of the ZnO-NPs (ii as an example). The size distribution and abundance of the ZnO-NPs was shown in inset.	113
Figure 5.8: The W-H analysis of PZT-NPs; T=650 °C (a) and T=700 °C (b).	117
Figure 5.9: X-ray diffraction patterns of PZT-EGME (a) and PZT-PEG (b) calcined at 600 °C and 650 °C. Pure perovskite structure was obtained at 650 °C. Also the first XRD peak of PZT-PEG clearly shows a tetragonal phase.	119
Figure 5.10: TEM morphology of the PZT-NPs prepared in different solvent media. (a) PZT-PEG and (b) PZT-EGME.	120
Figure 5.11: FTIR pattern of PZT-EGME and PZT-PEG calcined at 600 °C and 650 °C. The two important bands those are related to perovskite structure are seen in all FTIR traces.	121
Figure 5.12: The reflectance and phase change spectrum, a , refractive index and extinction coefficient, b , real and imaginary parts of dielectric functions, c , and Electron-energy-loss function, d , of PZT-EGME and PZT-PEG calcined at 600 °C.	123
Figure 5.13 The reflectance and phase change spectrum, a , refractive index and extinction coefficient, b , real and imaginary parts of dielectric functions, c , and Electron-energy-loss function, d , of PZT-EGME and PZT-PEG calcined at 650 °C.	124
Figure 5.14: X-ray diffraction patterns for PZT-NPs calcined at different temperatures. The pure perovskite phase was achieved at 700 °C.	127
Figure 5.15: X-ray diffraction patterns for (a) pure PVDF, and (b) PVDF/PZT-NPs. The pattern of pure PVDF shows exists of α , β and γ phase in the compound.	128
Figure 5.16: FTIR traces for (a) pure PVDF and (b) PVDF/PZT-NPs. The results show exists of α , β and γ phase in the compound.	129
Figure 5.17: TEM morphology of the PZT-NPs (a), SEM micrographs of PVDF/PZT-NPs film (b), dried PVDF film (c), and PVDF film annealed at 110 °C. The inset image of figure 4b shows the coverage of the polymer surrounding the nanoparticles.	131
Figure 5.18: Crystallization starts from a nucleus of a crystal and grows in a blend melt with a tree-like architecture.	131
Figure 5.19: The experimental dielectric constant and loss of the PZT-NPs as a function of frequency at room temperature, from 100Hz to 40MHz. The inset	132

shows the resonance area.

Figure 5.20: The experimental dielectric constant of the pure PVDF and PVDF/PZT-NPs as a function of frequency at room temperature, from 100Hz to 40MHz. 133

Figure 5.21: The experimental dielectric loss of the pure PVDF and PVDF/PZT-NPs as a function of frequency at room temperature, from 100Hz to 40MHz. The inset shows that the loss value of PVDF/PZT and PVDF are almost same in frequency range of 100 Hz to 30 KHz. 134

Figure 5.22: Dielectric constant of PVDF/PZT-NPs obtained from experimental test and theoretical calculation (Furukawa, Maxwell and Rayleigh theories) at room temperature, from 100 Hz to 40 MHz. 137

Figure 5.24: Dielectric constant of PVDF/PZT-NPs obtained from experimental test and theoretical calculation (Yamada and EMT theories) at room temperature, from 100 Hz to 40 MHz. 138

LIST OF SYMBOLS AND ABBREVIATIONS

acac	Acetylacetonate
DEA	Diethanolamine
EGME	2-Methoxyethanol
FESEM	Field Emission Scanning Electron Microscopy
FTIR	Fourier Transition Infrared spectroscopy
FWHM	Full Wide Half Maximum
K-K	Kramers-Kronig
MEA	Monoethanolamine
NPs	Nanoparticles
PEG	Poly Ethylene Glycol
PVDF	Polyvinylidene Fluoride
SSP	Size Strain Plot
TEA	Triethanolamine
TEG	Thermogravometric analysis
TEM	Transmission Electron Microscopy
UDEDM	Uniform Deformation Energy Density Model
UDM	Uniform Deformation Model
USDM	Uniform Stress Deformation Model
UV-vis	Ultraviolet-Visible spectroscopy
W-H	Williamson-Hall
XRD	X-ray diffraction
Y	Young's modulus
β_{hkl}	Full Wide Half Maximum

CHAPTER 1: INTRODUCTION

1.1. NANOPARTICLES RESEARCH

Nanoparticles research, including synthesis, characterization of the structural, physical and chemical properties, assembly into 1-, 2-, and 3-dimensional and with hierarchical structure principles, and application in various fields of technology, show a fundamental side of nanoscience and nanotechnology. Nanomaterials with a wide range of compositions, well-defined and uniform crystallite sizes, unprecedented and extraordinary crystallite shape, and complex assembly properties can be achieved by many different synthesis techniques. Gas-phase process are low-cost production method to synthesis the nanopowders (Heszler, 2002, Jia et al., 2010, Kim and Zachariah, 2007, Kruis et al., 2000, Lähde et al., 2008, Moreno-Couranjou et al., 2009, Swihart, 2003, van Ommen et al., 2010, Wegner and Pratsinis, 2005), but liquid-phase synthesis methods are more flexible to control the structure and morphology of the nanomaterials. Synthesis of particles and control their size, shape and size distribution is not the main goal of nanoscience, but has been an integral part of colloid chemistry for decades. Nowadays, it is clear that the fundamental role of uniform powders in many areas of science and technology is very important. The development of highly advanced analytical tools, have made it possible to characterize small structures with atomic resolution, and the size of the targeted objects and devices decreased rapidly to below the 100 nm limit. Great demands to the synthesis methodology were made by the preparation of nanostructures on such a small size scale. Therefore it could be a great challenge to develop a “synthetic chemistry” of nanoparticles. Research on the synthesis

of inorganic nanoparticles and nanostructures has always been, and still will be, at the heart of nanoscience for the next few years.

1.2. BACKGROUND AND SCOPE OF STUDY

Metal oxides of interest include the semiconductors and dielectrics such as ZnO, PZT, BaTiO₃, NiO, SnO₂, MgO, and CdS. ZnO has a wide and direct band gap, which is nearly 3.37 eV at room temperature, and is transparent in visible light. It is also a reliable luminescence material at both ambient and high temperature as it has a large excitation binding energy that is approximately 60 meV (Shao et al., 2010). ZnO is also applicable for use in electronic and optoelectronic devices (Djurisic et al., 2010, Gong et al., 2010, Gopalakrishnan et al., 2011, Kassab et al., 2010, Lee et al., 2007, Phillips et al., 2011, Prakash et al., 2008, Wang et al., 2007), gas sensors (Ahn et al., 2009, Chang et al., 2010, Gui et al., 2008, Hongstith et al., 2010, Hsueh et al., 2007, Lokhande et al., 2009, Lupan et al., 2008, Ma et al., 2011, Xu et al., 2006b, Yi et al., 2011, Zhang and Zhang, 2008), solar cells (Chen et al., 2011, Chou et al., 2009, Zhu et al., 2011), display windows (Jin et al., 1988, Mitsui and Sato, 2004), and optical transparency in the visible range (Chen and Bi, 2008, Tsuji and Hirohashi, 2000). It is also widely used in medicine, pigment (Ekambaram, 2005, Lavat et al., 2008, Li et al., 2010, Sulcova and Trojan, 1999, Yebra et al., 2006, Yu et al., 2008b). In addition, ZnO is also used in sensors and actuators due to its piezoelectric (Blom et al., 1990, Shibata et al., 2002) (especially for high frequency) and pyroelectric properties (Hsiao et al., 2009, Wei et al., 2006). This material shows interesting properties in its low dimensional structure. In the nano size range, ZnO is expected to possess interesting physical properties, and profound coupling effect compare to the respective bulk counterpart. The average usage of zinc oxide in worldwide is in excess of 1200000 tons annually. China is the largest

supplier and user in the world followed by USA. The major use of the ZnO is in rubber product. In addition, it is widely use in ceramics market and as oil additive compounds especially within the USA, Figure 1.1.

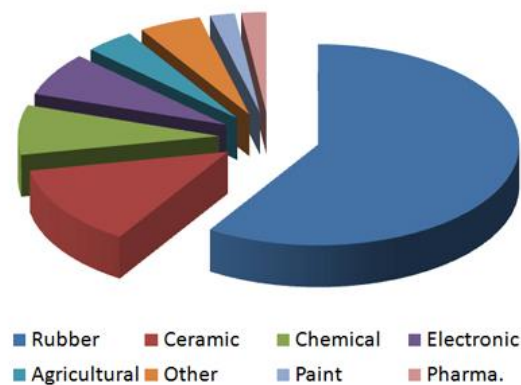


Figure 1.1: Worldwide Zinc Oxide Applications in 2010 (www.znoxide.org).

Lead zirconate titanate materials, (PZT), in their perovskite structure form, display unique ferro-, piezo-, pyro-, dielectric and electrooptic responses when subjected to an applied electric field, and have many potential applications. PZT can be used in electronic devices such as MEMS (Zinck et al., 2004) because of its ferroelectric properties (Dong and Ye, 2001), FRAM (Sik Kim et al., 1999), waveguide (Cardin et al., 2005), and hydrophone (Zeng et al., 2006). In addition, it can be used to make sensors (Gebhardt et al., 2007), welding systems (Tsujino et al., 2002) vibration devices (Yasui et al., 2002), and actuators (Chen et al., 2007). Medical diagnostics (Bove et al., 2001), pyroelectric sensor (Es-Souni and Zhang, 2004), medical imaging (Zhang et al., 2006b), and gravimetric systems (Tsai et al., 2009) are the other applications of this material.

ZnO is not a new material and PZT was reported by Yutaka Takagi, Gen Shirane and Etsuro Sawaguchi, physicists at the Tokyo Institute of Technology in 1952.

According to the information and published paper in web of science, synthesis of ZnO and PZT nanostructures were started around 1991 but it increased dramatically after 1998, Figure 1.2 and Figure 1.3. It shows the interest of using these materials in different applications.

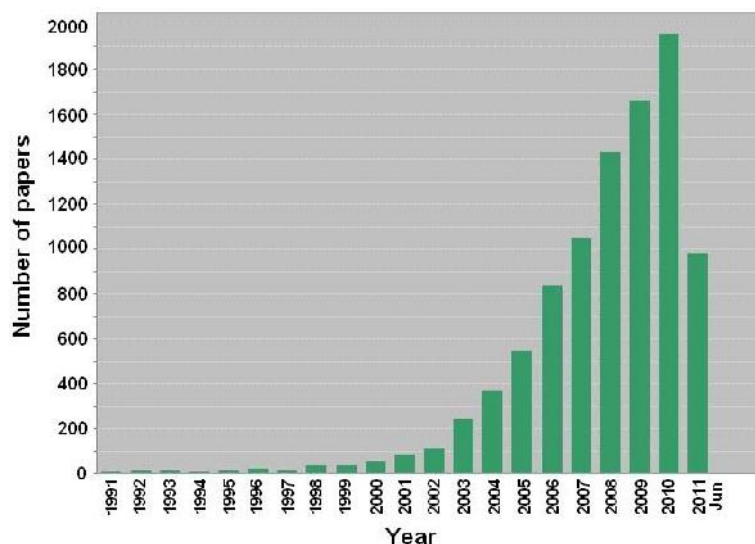


Figure 1.2: Number of publications per year on ZnO nanostructures. The data were extracted on 25 Jun 2011 through the Institute of Scientific Information (ISI) database using the following keywords that appeared in topic: ZnO or zinc oxide together with nanostructure, nanoparticles, nanopowders, and nanorods.

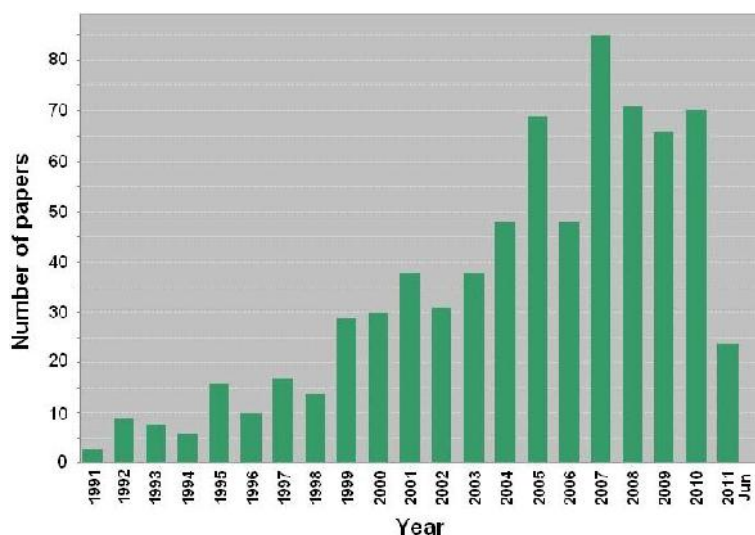


Figure 1.3: Number of publications per year on PZT nanostructures. The data were extracted on 25 Jun 2011 through the Institute of Scientific Information (ISI) database using the following keywords that appeared in topic: PZT together with nanostructure, nanoparticles, and nanopowders.

1.3. AIM AND OBJECTIVES

Developing a good method that is suitable for preparing of nanostructures is very important and one of the biggest challenges in nanomaterial researches. It is because; quality and morphology of the nanostructures affect their properties. Too many methods, physical and chemical, have been used to prepare nanostructures as well as ZnO and PZT nanostructures. Nevertheless, still researchers try to develop methods that are easier, cheaper, safer, and industrial. Based on these observations, simple, inexpensive, but effective growth chemical methods of ZnO and PZT nanostructures and their characteristics are presented in this thesis.

In particular the objectives in this thesis are:

i) To design and modify sol-gel techniques for preparing ZnO and also PZT nanoparticles that are suitable for industrial applications.

ii) To identify suitable polymerization agent to control morphology and size of the nanoparticles.

iii) To use green energies such as sound energy for preparing the nanostructures.

It is expected that a good quality (narrow size distribution and uniform morphology) ZnO and PZT nanostructures can be produced from the above-mentioned methods, which also can be used as industrial techniques to prepare these nanostructures.

1.4. THESIS STRUCTURE

The thesis was written in seven chapters. In chapter one the background, scope, and objective of the studies were presented. Chapter Two includes a literature review of ZnO and PZT nanostructures and fundamental properties of ZnO and PZT. The synthesis of the ZnO nanostructures (using: sol-gel, sol-combustion, solvothermal, and sonochemical methods) and PZT nanostructures (using: sol-gel method) were summarized in Chapter Three. In addition, the instrumental and characterization techniques were explained in this chapter. Chapter Four presents the characterization result of the prepared ZnO and PZT nanostructures. Chapter Five contains the theoretical studies of the ZnO and PZT nanoparticles. In this chapter, the effect of strain on peak broadening of the nanoparticles was investigated using Williamson-Hall (W-H) and Size Strain Plot (SSP). In addition, the optical properties of the PZT-NPs in infrared region were investigated using Kramers-Kronig (K-K) method. Chapter Six provides the conclusion of this thesis as well as several suggestions for future works.

CHAPTER 2:

FUNDAMENTAL PROPERTIES OF

NANOPARTICLES

2.1. INTRODUCTION

Nanoparticles (NPs) exhibit a new class of materials with new properties that do not exist in bulk form materials (Capobianco et al., 2002, Li et al., 2004, Rozenberg et al., 2006). NPs come in a wide range of sizes and shapes, with varied electronic, optical, and chemical properties. However, according to these properties a universal concept is applicable: the properties of NPs are depending on their nanoscale size and atomic-scale structure. Understanding these properties requires careful consideration of the nature of bonding both between the constituent atoms of NPs and between atoms and molecules in their structures which can be controlled by synthesis conditions. In these respects theoretical models have played a central role and have provided interpretations for many experimental observations. It is useful at the outset to explain some nomenclature. The terms nanoparticles, nanostructures, and clusters are often encountered in the literature and are frequently used interchangeably.

i) A particle of matter is normally referred to as a NP if its extension in all three dimensions is less than 100 nm. To better understand, this size is about one thousandth of the width of a human hair.

ii) A nanostructure is generally referred to as a particle if it grows at least in one dimension less than 100 nm, so nanoparticle is also is a nanostructure.

iii) Finally, clusters are particles containing a very small number of atoms such that it is no longer possible to clearly distinguish “bulk” atoms from those at the surface.

There is no universally understood definition but a general rule is a few hundred atoms or smaller. There is considerable variety in the types of NP systems that have been fabricated and studied. Aside from differences in their size and shape, one important variable is their composition. Almost every element in the periodic table, together with various alloys and compounds, can form NPs. They can be metallic (Choi et al., 2010, Gupta et al., 2011, Jeong, 2009, Riddin et al., 2010), semiconducting (Hamdeh et al., 2010, Kruis et al., 1996, Kumar et al., 2006, Park et al., 2011, Zhang et al., 2005), or insulating (Chao et al., 2008, Roux et al., 1995) and typically their properties are very different to those of the corresponding bulk material.

2.2. FABRICATION OF NANOSTRUCTURE MATERIALS

Preparation methods for nanoparticles can be classified into three general categories such as wet synthesis, dry synthesis, and milling process as shown in Figure 2.1. In wet and dry synthesis approaches, nanoparticles are generally produced in a bottom up way from atomic precursors, whereas in the milling method, nanoparticles are produced from the top down by mechanically breaking down larger particles (Goya, 2004, Hedayati et al., 2011, Ohara et al., 2010, Suwanboon et al., 2011, Wang and Jiang, 2007). Wet approaches include sol-gel and precipitation methods and dry approaches encompass combustion and pulse laser deposition synthesis of nanoparticles. In all cases, the narrowness of the size distribution of the nanoparticles is very important. Also, it is concerned about the degree of agglomeration. By adjusting the process parameters, the size distribution can be modified. Milling is very energy-intensive, and it may not be useful for some materials, such as pure metals because they are malleable. In precipitation methods, it is necessary to add capping ligands to solution to control the growth of the nanoparticles. These ligands bind to the surface of the particles, and they must be removed in a separate processing step. Agglomeration of nanoparticles is a big problem during high temperature heating process. It can be eliminated by simultaneously quenching and diluting but still can affect the product. It also because, if the nanoparticles suspended in the gas are more dilute, more energy is required to recover them.

2.2.1. Fabrication of ZnO nanostructures

According to recorded information in Web of Science data source, the first syntheses of ZnO nanostructures have been reported by Hingorami (Hingorani et al., 1993). They

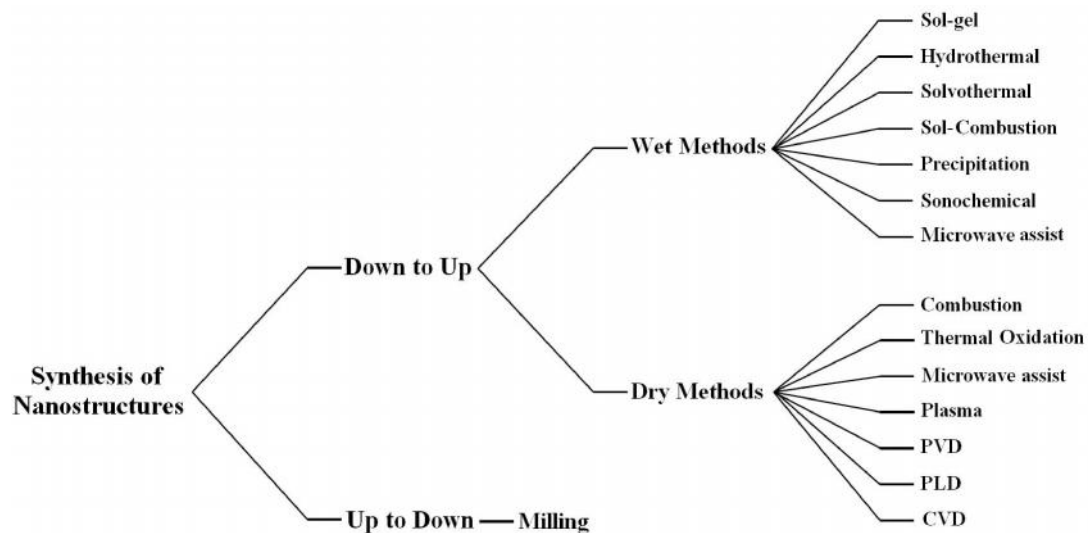


Figure 2.1: Synthesis diagrams of the nanostructures.

obtained ZnO-NPs in the size range of 5-40 nm by microemulsion-mediated method. About 2 years later, Elshall (ElShall et al., 1995) prepared ZnO-NPs using laser ablation method using Zn target. But in the beginning of 20 century, many different methods have been developed to prepare ZnO nanostructures. The synthesis methods are used regarding to the needed applications of the final product. Some of these methods that were applied to synthesis of ZnO nanostructures can be listed as sol-gel (Erol et al., 2010, Lee et al., 2009, Vafaei and Ghamsari, 2007), sol-combustion (de Sousa et al., 2000, Hwang and Wu, 2004, Lathika Devi et al., 2011, Yue et al., 1999, Zhang et al., 2005), hydrothermal and solvothermal (Chen et al., 2008, Cimitan et al., 2009, Ismail et al., 2005, Luo et al., 2011, Sahoo et al., 2011, Tonto et al., 2008, Wang et al., 2006), physical vapor deposition, PVD, (Jimenez-Cadena et al., 2010), chemical vapor deposition, CVD, (Han et al., 2010, Liu et al., 2005, Phan et al., 2010), which is suitable to prepare ZnO nanowires (Yousefi and Zak, 2011) and ZnO nanobelts (Yousefi and Kamaluddin, 2009) on a silicon substrate as shown in Figure 2.2, pulse laser deposition, PLD, (Muller et al., 2011, Song et al., 2009) thermal oxidation (Amekura et al., 2006, Labuayai et al., 2009, Liao et al., 2011, Nakamura et al., 2007), sonochemical

(Bhattacharyya and Gedanken, 2008, Kandjani et al., 2008, Yadav et al., 2008), precipitations, microwave assisted, polymerization method (Liu, 2006, Panigrahy et al., 2009), spray (Joni et al., 2009).

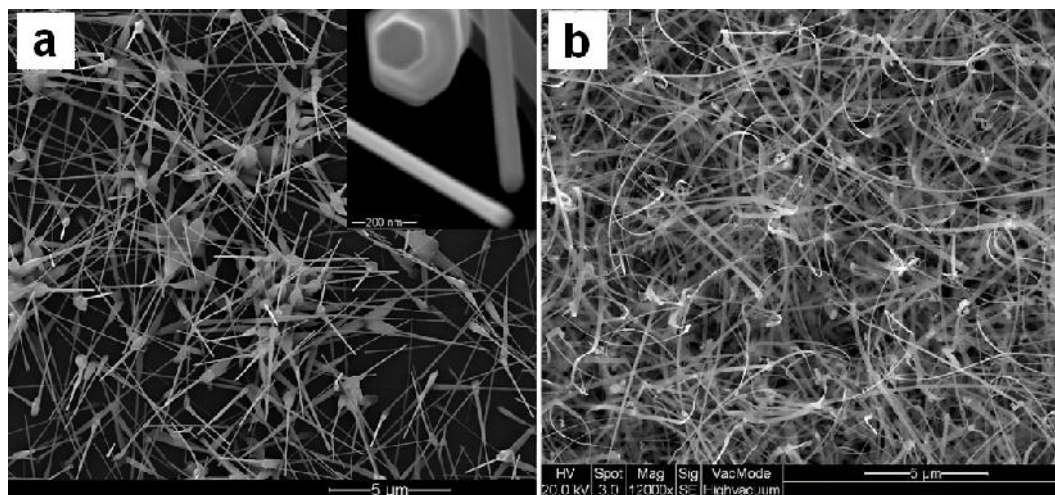


Figure 2.2: ZnO nanowires (a) and nanobelts (b) prepared by CVD method, (Porto and Krishnan, 1967, Yousefi and Kamaluddin, 2009, Yousefi and Zak, 2011).

Sol-gel and gel-combustion methods are the most famous routes that have been used to prepare ZnO nanoparticles. In this method the growth of nanoparticles can be controlled by several materials. As an example, silica matrix can control the growth of the ZnO nanoparticles (Moleski et al., 2006). In this method, zinc glycerolate nanoparticles were used as sacrificial agents. These nanoparticles can be produced within glycerol-heptane microemulsions which stabilized by bis-ethylhexyl sodium sulfosuccinate (AOT). Subsequently they are surface-modified with bistrimethoxysilyl-ethane (BTME) and copolymerized with tetramethoxysilane (TMOS) to get a composite silicate material. During the polymerization stage, the Zn-Gly nanoparticles are largely dissolved and it is providing a uniform distribution of zinc in the silica material. By calcination of the composite, uniform and well dispersed small ZnO nanoparticles will be achieved. Gel combustion method gives homogenous, high-purity, and high-quality nanopowders with the possibility of stoichiometric control (Yue et al., 1999). Sousa et

al. (de Sousa et al., 2000) used metallic nitrate plus urea and made a ZnO nanopowder with a size of about 0.4-0.5 μm for a varistor application. Hwang et al. (Hwang and Wu, 2004) worked on ZnO nanopowder made by a combustion method.

Solvothermal and hydrothermal methods are very useful to prepare different morphologies of the ZnO such as ZnO nanoparticles, ZnO nanorods, and ZnO flower. The morphology of the ZnO nanostructures can be controlled by changing the solvent (Huang and Caro, 2010) or polymer agent (Feng et al., 2011). Also, pH of the solution plays an important role to control the ZnO nanostructure morphology (Sun et al., 2010); therefore, these methods are known as powerful methods to control of the ZnO nanostructure morphologies and make it possible to grow some beautiful ZnO nanostructures as shown in Figure 2.3. The most important reactions that happened in the hydrothermal process are as below:

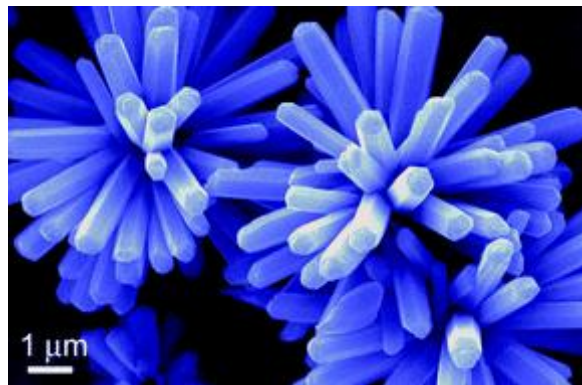


Figure 2.3: The flower like ZnO nanostructures that have been made by hydrothermal method (Sun et al., 2010).

Recently, microwave radiation has been used to prepare ZnO nanostructures in many researches (Bai et al., 2011, He, 2004, Padmanabhan et al., 2009, Thongtem et al.,

2010). The microwave induced supersaturation of Zn^{2+} and $\text{Zn}(\text{OH})^+$ species under the moderately basic pH condition, and the resultant initial growth through the oxygen terminated $(000\bar{1})$ facet, have been identified as the key steps responsible for the formation of ZnO nanostructures (Padmanabhan et al., 2009) as shown in Figure 2.4.

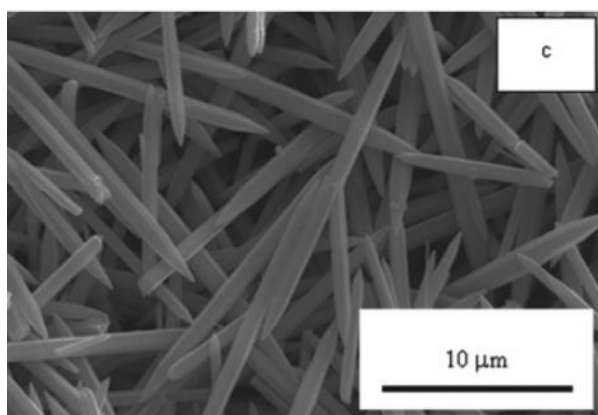


Figure 2.4: The ZnO nanorods prepared by microwave assisted method, (Padmanabhan et al., 2009).

In sonochemical method, the needed energy in formation of ZnO from the solution is obtained from the sound energy. Previously, ZnO nanoparticles were prepared by this method (Qian et al., 2003) and also this method have been useful to prepare ZnO/CdS core-shell (Geng et al., 2011) Figure 2.5.

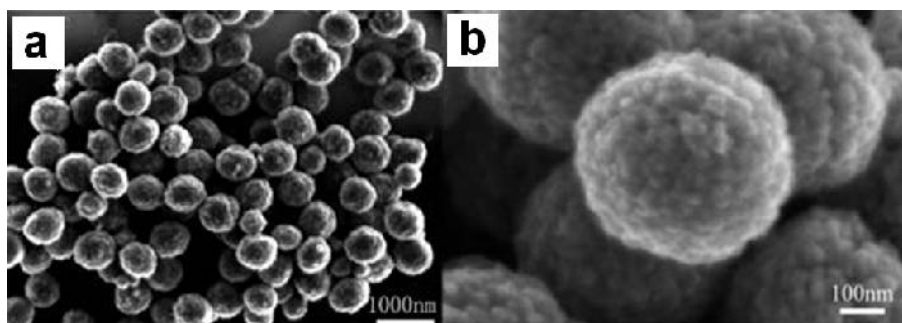


Figure 2.5: The low (a) and high (b) magnification micrographs of ZnO/CdS core-shell synthesized by sonochemical methods, (Geng et al., 2011).

2.2.2. Fabrication of PZT nanostructures

According to recorded information in Web of Science data source, the first study which published about the synthesis of PZT nanostructures has been done by Ohnishi et al., 1991 using sol-gel method. Sol-gel was a common method to prepare PZT-NPs until 2001 (Dong and Ye, 2001, Kundu and Chakravorty, 1995, Seol et al., 2002, Tanase et al., 2002, Tartaj et al., 2001, Wen et al., 1998). Nualpralaksana (Nualpralaksana et al., 2001), developed hydrothermal method to prepare PZT-NPs for the first time. After this year, In order to synthesis of PZT nanostructures, many wet-chemical routes have been developed, such as sol-gel (De-Qing et al., 2007, Linardos et al., 2006, Mu et al., 2007, Naksata et al., 2003, Wu et al., 2000, Zhang et al., 2003), hydrothermal (Cho et al., 2001, Deng et al., 2003), solvothermal (Modeshia and Walton, 2010), sol-gel combustion (Chakrabarti and Maiti, 1997, Chandratreya et al., 1981, Ghasemifard et al., 2009b, Nersisyan et al., 2005), pyrolysis (Bezzi et al., 2005, Gong et al., 2004, Law et al., 1998), co-precipitation (Choy et al., 1995, Choy et al., 1997, Xu et al., 2003, Xu et al., 2006a), electro hydrodynamic atomization (Gajbhiye et al., 2007), and ultrasonic spray combustion synthesis, USCS, (Lee and Jun, 2005). The sol-gel process is the most widely used wet-chemical route to prepare PZT powders, thin films and bulks. This technique is particularly important for the preparation of ceramic powders, since the mixing of the reagents occurs on an atomic rather than a particulate scale. This allows control over stoichiometry and is thus advantageous for the synthesis of multi-component oxides. Another advantage comes from the low processing temperatures that facilitate integration with semiconductors (Jayasinghe et al., 2005). Many different sol-gel systems are used to synthesize PZT, with lead acetate, zirconium and titanium alkoxides used as common reagents and methoxyethanol or acetic acid used as common solvents (Bruncková et al., 2004, Lee and Jun, 2005). In these systems, the hydrolysis

and condensation reactions are sensitive to the presence of water and the humidity of the air, so it is necessary to add a stabilizing agent, such as acetyl acetone, to control the reaction process. Tu (Tu et al., 1996) researched some sol-gel processes with complex polyalcohols, such as propanediol, butanediol and 1, 1, 1-trihydroxymethyl ethane, as solvents and acetylacetonate modified zirconium alkoxides and titanium alkoxides as starting reagents. They found that, in the polyalcohol system, the sensitivity of the sol-gel reaction to water and humidity was reduced, and the stable sol was easily obtained. In earlier work, Zhang De-Qing (De-Qing et al., 2007) used ethylene glycol, EG, as a solvent to prepare PZT-NPs. They could achieve particle distribution sizes of 50-100 nm. Ghasemifard (Ghasemifard et al., 2009b) could prepare PZT nanoparticles in the range size of 35-80 nm by calcination of xerogel which was prepared by sol-combustion method at 650 °C. They used citric acid as a fuel and the gel was dried by adding nitric acid. Although the sol combustion method is a dangerous method, the resulted powders are very fine as shown in Figure 2.6.

Hydrothermal is a good method to prepare PZT nanorod. Cho (Cho et al., 2001) used this method to prepare rod shape of the PZT nanostructures as shown in Figure 2.7. They used tetramethylammonium hydroxide pentahydrate as a polymerization agent to control the morphology of the PZT nanostructure. Still there were some non-perovskite phases that can be easily detected from the XRD pattern. (Haixiong and et al., 2011) bring a solution to remove the non-perovskite phases from the composite. They annealed the powder at 600 °C for 2 h and then it was observed that the non-perovskite phases were transformed to perovskite.

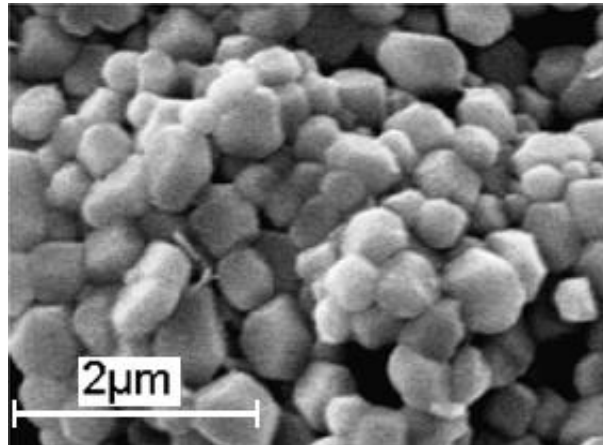


Figure 2.6: SEM micrograph of PZT nanoparticles which prepared by sol-combustion method and calcined at 650 °C for 2h, (Ghasemifard et al., 2009c).

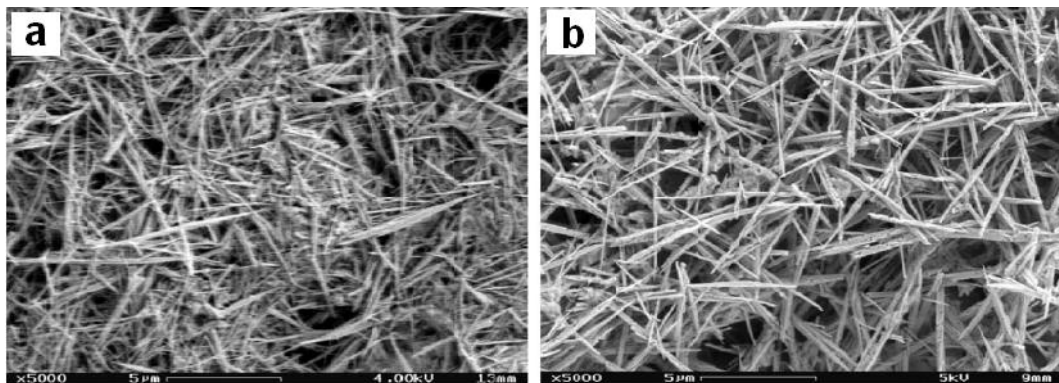


Figure 2.7: PZT wires prepared by hydrothermal method with heating treatment of (a) 12 h and (b) 24 h, (Cho et al., 2001).

2.3. FUNDAMENTAL PROPERTIES AND THEORETICAL MODELS

For better understanding of the materials behavior, it is necessary to study about their fundamental properties. The fundamental properties of the materials are characteristic that can be used to separate and categorize them. But these properties may be affected by some phenomena. For example, the band gap and electrical properties of materials will be changed when their sizes are very small in the range of nano meter. In addition, in this range of size, the structure of materials may transform to other structure which may not be similar compare to the structure in the bulk system.

2.3.1. Crystal structure of ZnO

Normally, the group II-VI binary compound semiconductors crystallize in either zinc blende, cubic or hexagonal wurtzite structure. In all of these structures, each anion (oxygen) is surrounded by four cations (Zinc) at the corners of a tetrahedron, and vice versa. This tetrahedral coordination is typical of sp^3 covalent bonding nature, but the bandgap beyond the one expected from the covalent bonding can be increased in these materials by a substantial ionic character. ZnO is a II-VI compound semiconductors that has these structures as schematically shown in Figure 2.8. At ambient conditions, wurtzite is thermodynamically stable phase but the zinc blende structure can be obtained only by growth on cubic structures. The rocksalt structure may be obtained in high pressures (Özgür et al., 2005). Figure 2.9 shows the hexagonal structure of ZnO. This structure can be described as a number of alternating planes composed of tetrahedrally coordinated Zn^{2+} and O^{2-} ions, arranged alternatively along the c-axis. The wurtzite

structure has a hexagonal unit cell with two lattice parameters (a) and (c) and the ratio of c/a is about 1.633 for an ideal lattice.

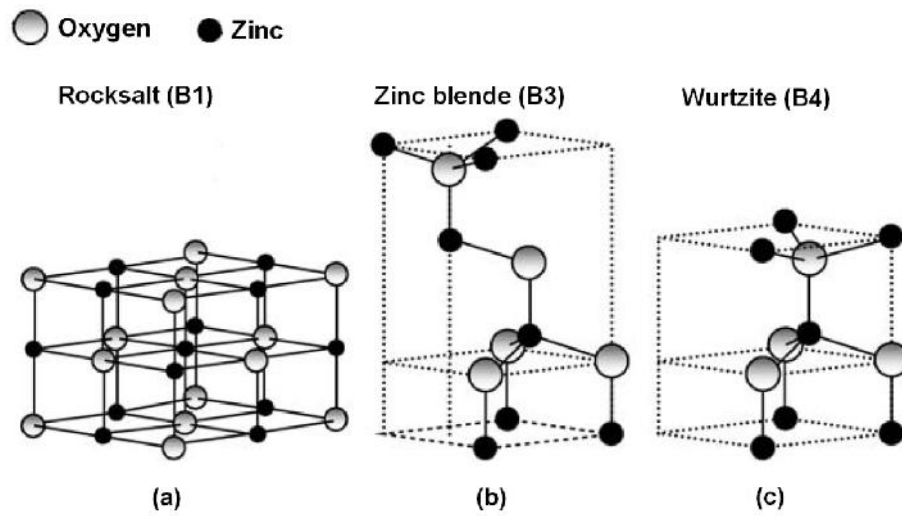


Figure 2.8: ZnO crystal structure (a) cubic rocksalt (B1), (b) cubic zinc blende (B3), and hexagonal wurtzite (B4). (Özgür et al., 2005)

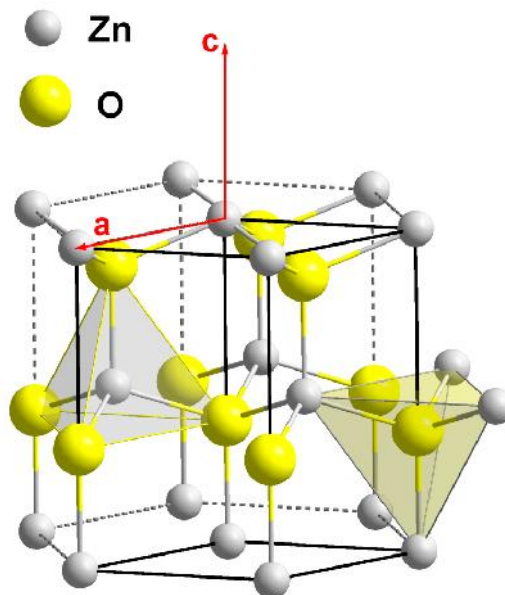


Figure 2.9: the hexagonal wurtzite structure of zinc oxide. (http://en.wikipedia.org/wiki/File:Wurtzite_polyhedra.png, 2011).

The wurtzite lattice parameters such as the values of d , the distance between adjacent planes in the Miller indices (hkl) (calculated from the Bragg equation, $\lambda=2d \sin\theta$), lattice constants a , b , and c , interplanar angle (the angle φ between the planes

$(h_1k_1l_1)$, of spacing d_1 and the plane $(h_2k_2l_2)$ of spacing d_2 , and unit cell volumes can be calculated from the *Lattice Geometry* equation as presented below (Cullity, 1956).

$$\frac{1}{d^2} = \frac{4}{3} \left(\frac{h^2 + hk + k^2}{a^2} \right) + \frac{l^2}{c^2} \quad (2 - 4)$$

$$V = \frac{\sqrt{3}a^2c}{2} = 0.866a^2c \quad (2 - 6)$$

$$\cos \varphi = \frac{h_1h_2 + k_1k_2 + \frac{1}{2}(h_1k_2 + h_2k_1) + \frac{3a^2}{4c^2}l_1l_2}{\sqrt{\left(h_1^2 + k_1^2 + h_1k_1 + \frac{3a^2}{4c^2}l_1^2\right)\left(h_2^2 + k_2^2 + h_2k_2 + \frac{3a^2}{4c^2}l_2^2\right)}} \quad (2 - 7)$$

2.3.2. Crystal structure of PZT

Pb (Zr_{1-x}, Ti_x) O₃, PZT (as like as many other piezoelectric materials) form in crystal structures belonging to the perovskite family with the general formula ABO₃ (Here A=Pb, B=Zr or Ti, and O is the oxygen). The ideal, cubic perovskite structure is shown in Figure 2.10. PZT crystallites are centro-symmetric cubic (isotropic) before poling but after poling exhibit tetragonal or rhombohedral symmetry (anisotropic structure) below the Curie temperature.

The phase diagram of PZT is shown in Figure 2.11. At room temperature, PZT exhibit ferroelectric properties for titanium concentration of more than 48% (x>48) and the structure will be tetragonal (P4mm) with a symmetry R3c and c/a ratio will be between 1.02 and 1.065. For titanium concentration of below 48% (x<48), PZT forms in rhombohedral structure with a symmetry R3m. The rhombohedral distortion is about 0.3°. There is transition between the tetragonal and the rhombohedral phase near to the morphotropic (i.e. independent of temperature). The Curie temperature point above which PZT becomes para-electric (Pm3m) starts from 230°C for PbZrO₃ to 490°C for

PbTiO₃. For a zirconium concentration of more than 94%, PZT exhibit anti-ferroelectric properties with an orthorhombic structure (Pb2a) (Neppiras, 1972).

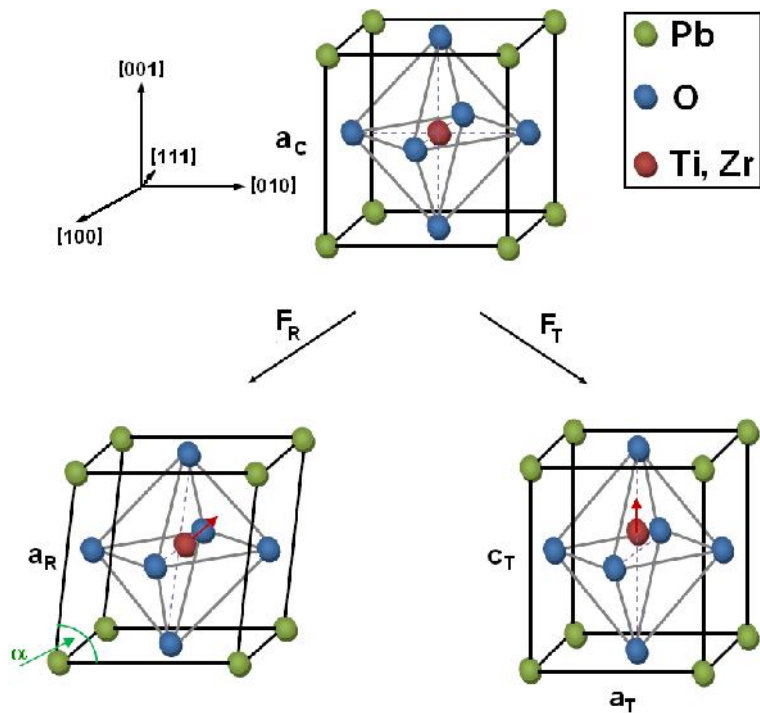


Figure 2.10: The perovskite structure of PZT in three forms of cubic, tetragonal, and rhombohedral.

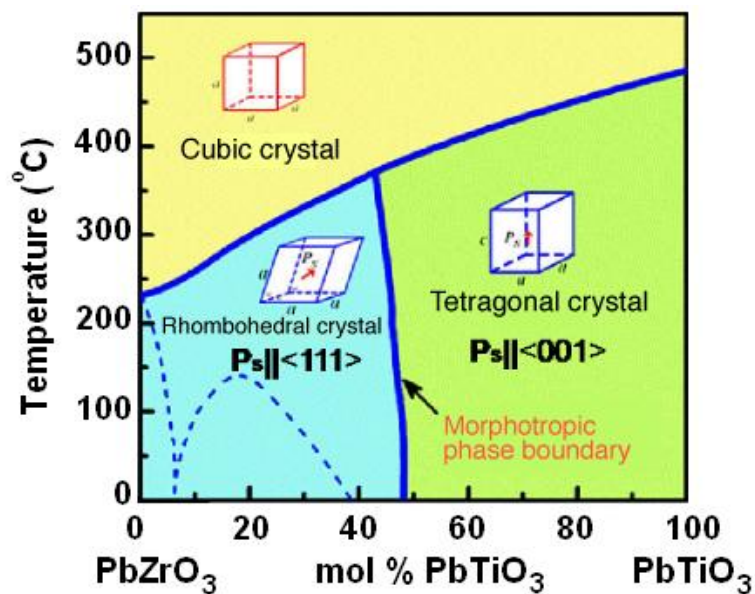


Figure 2.11: The morphotropic phase boundary of the ferroelectric material serves as the boundary between different phases in terms of the electric polarization direction and crystal structure.

The lattice constants a, b, c , interplanar angle, the angle φ between the plane $(h_1k_1l_1)$, of spacing d_1 , and the plane $(h_2k_2l_2)$, of spacing d_2 , and cell volumes are calculated from the following equation (Cullity, 1956).

Tetragonal:

$$\frac{4\text{Sin}^2\theta}{\lambda^2} = \frac{h^2 + k^2}{a^2} + \frac{l^2}{c^2} \quad (2 - 8)$$

$$V = a^2c \quad (2 - 9)$$

$$\text{Cos}\varphi = \frac{\frac{h_1h_2 + k_1k_2}{a^2} + \frac{l_1l_2}{c^2}}{\sqrt{\left(\frac{h_1^2 + k_1^2}{a^2} + \frac{l_1^2}{c^2}\right)\left(\frac{h_2^2 + k_2^2}{a^2} + \frac{l_2^2}{c^2}\right)}} \quad (2 - 10)$$

Rhombohedral:

$$\frac{a\text{Sin}^2\theta}{\lambda^2} = \frac{(h^2 + k^2 + l^2)\text{Sin}^2\alpha + 2(hk + kl + hl)(\text{Cos}^2\alpha + \text{Cos}\alpha)}{a^2(1 - 3\text{Cos}^2\alpha + 2\text{Cos}^3\alpha)} \quad (2 - 11)$$

$$V = a^3\sqrt{1 - 3\text{Cos}^2\alpha + 2\text{Cos}^3\alpha} \quad (2 - 12)$$

$$\text{Cos}\varphi = \frac{a^4d_1d_2}{V^2} (\text{Sin}^2\alpha(h_1h_2 + k_1k_2 + l_1l_2)(\text{Cos}^2\alpha - \text{Cos}\alpha)(k_1l_2 + k_2l_1 + l_1h_2 + l_2h_1 + h_1k_2 + h_2k_1)) \quad (2 - 13)$$

2.3.3. Optical properties

Both of the intrinsic and extrinsic effects affect the optical properties of a semiconductor. Intrinsic optical transitions happen between electrons in the conduction band and holes in the valance band. It includes excitonic effects due to coulomb

interactions. Excitons can be classified into two types, including free and bound excitons (Özgür et al., 2005). For a sample with low impurity concentration, the free exciton can also exhibit excited states in addition to their ground-state transitions. They usually generate discrete electronic states in the band gap and, therefore affect both optical-absorption and emission processes (Özgür et al., 2005).

A basic understanding of the optical and electrical properties in terms of low- and high-field carrier transport needs precise knowledge of the vibrational modes of the crystal, which are related to mechanical properties. Vibrational properties of ZnO studied by techniques such as Raman scattering were determined before (Arguello et al., 1969, Calleja and Cardona, 1977, Callender et al., 1973, Damen et al., 1966, Mitra et al., 1969, Porto and Krishnan, 1967, Tsuboi and Wada, 1968). In this method, phonons have been arbitrarily chosen to be discussed under the mechanical properties of the crystal rather than under its optical properties. A suitable discussion of vibrational modes, some of that are active Raman modes, some are active in IR study, and some are optically inactive (silent) modes, is provided (Cardano, 1982). Vibrational modes, which related to the main part of the mechanical properties, are very sensitive to crystallite strain, defects, and dopant in that the phonon mode frequencies and their frequency broadening can be used to get important information about the semiconductor.

2.3.3.1. Optical properties of ZnO

Optical properties of ZnO as well as its refractive index were widely studied before from far infrared to vacuum ultraviolet including phonons, plasmons, dielectric constant, and refractive indices (Özgür et al., 2005). The interest in ZnO arises because of its applications in optoelectronics due to its direct wide bandgap ($E_g \sim 3.3$ eV at 300

K), large exciton binding energy ($\sim 60\text{meV}$, (Look, 2001)), and efficient radiative recombination. The spectrum reveals a characteristic absorption peak of ZnO at wavelength between 370-380 nm, Figure 2.12, which can be assigned to the intrinsic band-gap absorption of ZnO due to the electron transitions from the valence band to the conduction band ($O_{2p} \rightarrow Zn_{3d}$) (Yu et al., 2006).

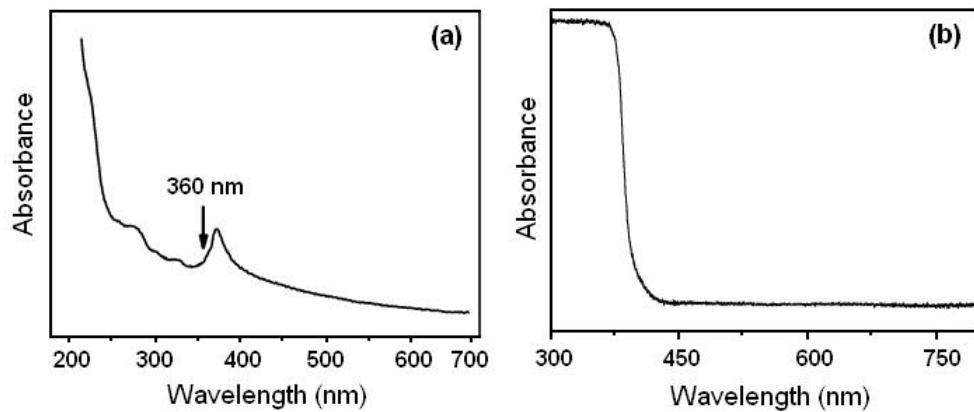


Figure 2.12: Absorption spectra of ZnO nanowires sol (a) and powder reflectance (b) spectra of zinc oxide nanowires (Cao et al., 2004).

In the case of ZnO with wurtzite structure (in IR region), the number of atoms per unit cell $s=4$, and there is a total of 12 phonon modes, namely, 2 transverse acoustic (TA), 1 longitudinal acoustic (LA), 3 longitudinal optical (LO), and 6 transverse optical (TO) branches, the details of which are listed in Table 2.1 and Table 2.2. In the zinc blende polytypes with $s=2$, only six modes are present, three of which are acoustical (one LA and two TA) and the other three are optical (one LO and two TO) branches. Infrared (IR) reflection and Raman spectroscopies have been commonly employed to derive zone center and some zone boundary phonon modes in ZnO (Stroscio and Dutta, 2001), Figure 2.13.

Table 2.1: Acoustic and optical modes in a crystal with wurtzite structure considering number of the unit cell atoms.

<i>Mode type</i>	<i>Number of modes</i>
<i>Longitudinal acoustic</i>	<i>1</i>
<i>Transverse acoustic</i>	<i>2</i>
<i>Total acoustic modes</i>	<i>3</i>
<i>Longitudinal optical</i>	<i>s-1</i>
<i>Transverse optical</i>	<i>2s-2</i>
<i>All optical modes</i>	<i>3s-3</i>
<i>All modes</i>	<i>3s</i>

S=4 for lattice with wurtzite structure and s=2 for lattice with zinc blende structure.

Table 2.2: Phonon mode frequencies of wurtzite ZnO at the center of the Brillouin zone obtained from infrared spectroscopic ellipsometry and Raman scattering.

Symmetry	Raman spectroscopy (cm⁻¹)	Infrared spectroscopy (cm⁻¹)	Theoretical calculations (cm⁻¹)
A ₁ -TO	380 (a)	380 (b)	382 (d)
E ₁ -TO	410 (a)	409 (a)	407 (e)
A ₁ -LO	574 (a)	570 (b)	548 (d)
E ₁ -LO	587 (a)	590 (c)	628 (d)

Ref: (a) (Ashkenov et al., 2003), (b) (Damen et al., 1966), (c) (Arguello et al., 1969), (d) (Bairamov et al., 1983), (e) (Koyano et al., 2002).

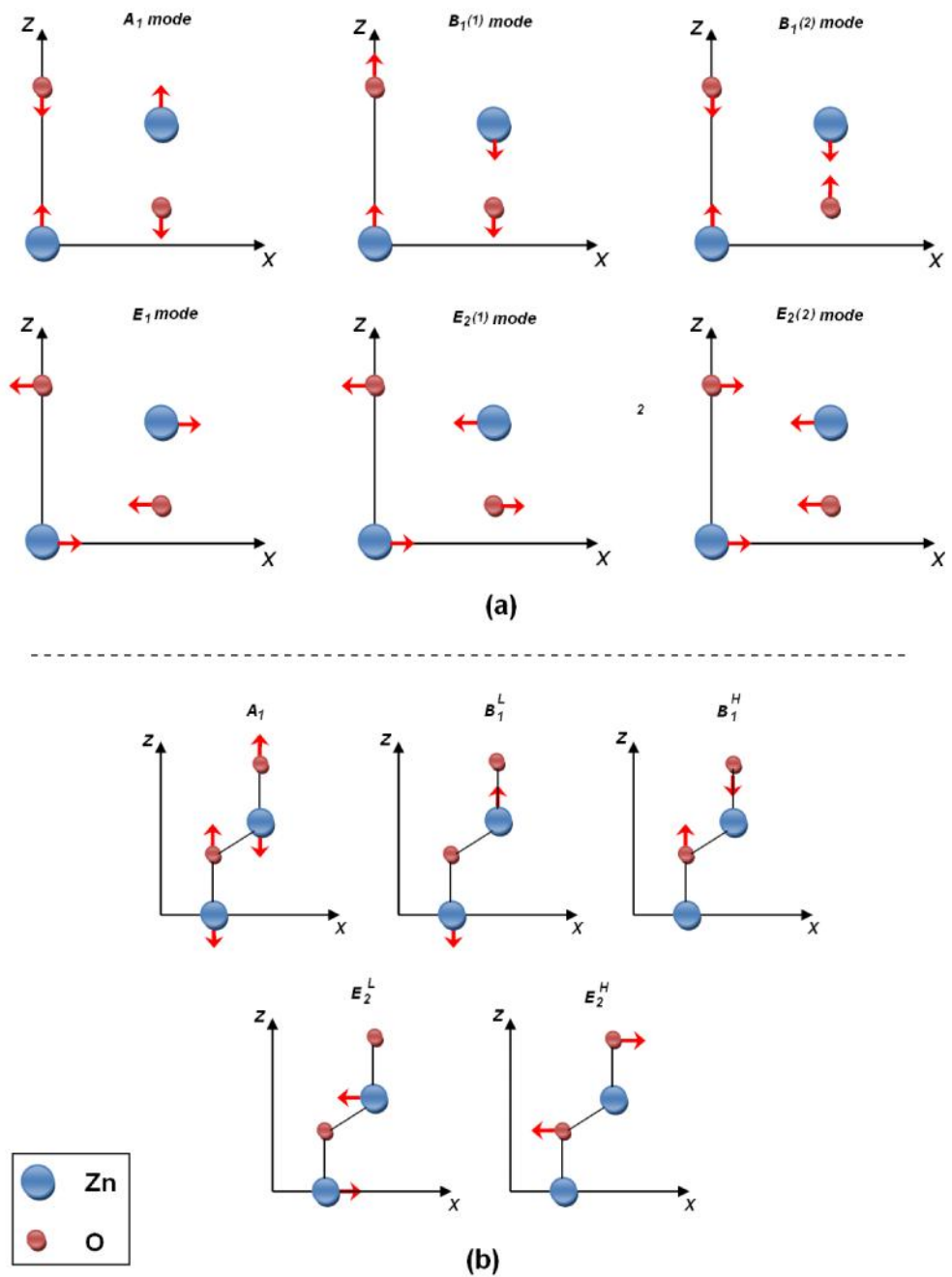


Figure 2.13: Atomic vibrations in wurtzite ZnO. The large atom represents Zn while the smaller one is O. X = (100), Y = (010), and Z (001) represents the optical polarization directions: (a) for general wave vector and (b) for zone center phonons.

2.3.3.2. Optical properties of PZT

In the perovskite PZT structure, one Ti\Zr ion was bonded to six oxygen ions. A vertical axis was considered, connecting one Ti\Zr ion to two oxygens, as shown in Figure 2.14. The stretching vibration is the motion of Ti\Zr and O that changes the length of the Ti\Zr-O₁ bond, as in Figure 2.14(a). The bending vibration occurs when there is a change in the O₁-Ti\Zr-O₂ bond angle, as shown in Figure 2.14(b). The higher frequency band, ν_1 , is assigned to the stretching normal vibration, and the lower band, ν_2 , is assigned to the bending normal vibration (Spitzer et al., 1962).

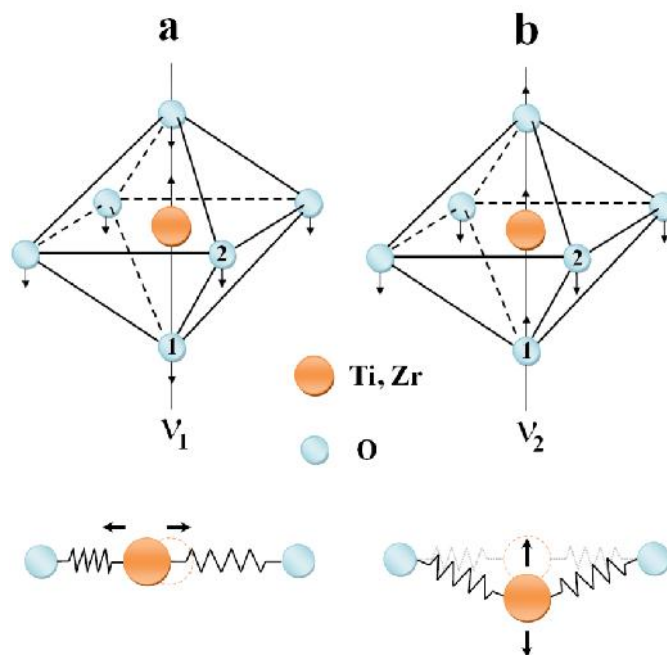


Figure 2.14: Schematic infrared active normal vibrations of a TiO₆ octahedron, ν_1 , higher frequency stretching vibration, ν_2 , lower frequency bending vibration.

2.3.4. Band gap of semiconductors

The band gap of the semiconductors can be in two forms of direct and indirect. The distinction concerns the relative positions of the valence band maximum and the

conduction band minimum. In the indirect band, the electron wave vector will be changed significantly when it jump from the valence band to the conduction band, Figure 2.15. This transition is not possible for electron just by absorption of a photon alone. The transition must involve a phonon also to change the momentum of the electron. But in direct band gap, electron can be moved to the conduction band by attracting one photon.

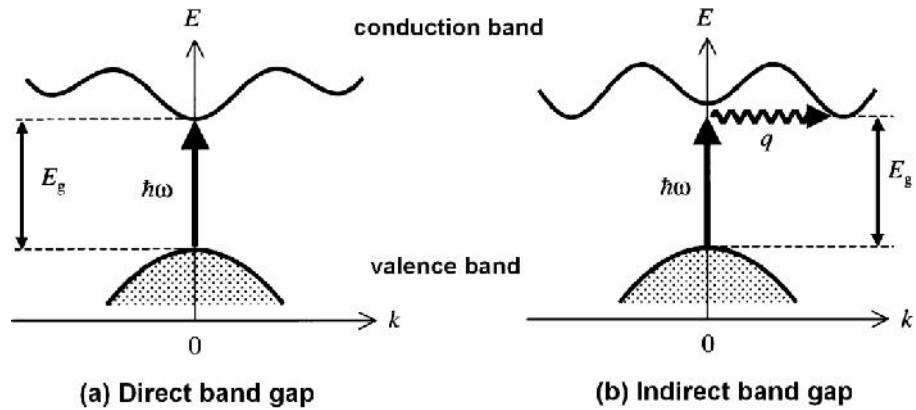


Figure 2.15: The direct and indirect electron transition in band gap of the semiconductors.

The optical absorption coefficient α is calculated by quantum mechanical transition rate $W_{i \rightarrow f}$ to excite an electron from one state Ψ_i to other state Ψ_f by absorption of a photon of angular frequency ω . According to Fermi's golden rule:

$$W_{i \rightarrow f} = \frac{2\pi}{\hbar} |M|^2 g(\hbar\omega) \quad (2 - 14)$$

where M is the matrix element and $g(\hbar\omega)$ is the density of states.

The total energy needed for transitions in direct band gap materials like ZnO is.

$$\hbar\omega = E_g + \frac{\hbar^2 k^2}{2m_e^*} + \frac{\hbar^2 k^2}{2m_h^*} \quad (2 - 15)$$

where m_h^* = hole effective mass and m_e^* = electron effective mass. Therefore the electron-hole mass μ can be rewrite as:

$$\frac{1}{\mu} = \frac{1}{m_e^*} + \frac{1}{m_h^*} \quad (2 - 16)$$

Then we can rewrite Equation (2-15) in the below form:

$$\hbar\omega = E_g + \frac{\hbar^2 k^2}{2\mu} \quad (2 - 17)$$

by substituting Fermi golden rule to Equation (2-14):

$$\begin{cases} \hbar\omega < E_g, & g(\hbar\omega) = 0 \\ \hbar\omega \geq E_g, & g(\hbar\omega) = \frac{1}{2\pi^2} \left(\frac{2\mu}{\hbar^2}\right)^{3/2} (\hbar\omega - E_g)^{1/2} \end{cases} \quad (2 - 18)$$

It is clear that the density of states factor rises as $(\hbar\omega - E_g)^{1/2}$ for photon energies greater than the band gap. According to the Fermi's golden rule, the absorption rate for a dipole allowed inter-band transition is proportional to the joint density of state. Therefore, we can write, (Mark, 2001):

$$\begin{cases} \hbar\omega < E_g, & \alpha\hbar\omega = 0 \\ \hbar\omega \geq E_g, & \alpha\hbar\omega \propto (\hbar\omega - E_g)^{1/2} \end{cases} \quad (2 - 19)$$

Kubelka and Munk, (Kubelka and Munk, 1931) developed model to estimate band gap from UV absorption results of the materials regarding to the above results. According to this model,

$$\alpha\hbar\omega \propto (\hbar\omega - E_g)^{1/2} \implies (\alpha\hbar\omega)^2 = C(\hbar\omega - E_g) \quad (2 - 20)$$

The direct band gap is estimated from a plot of $(\alpha\hbar\omega)^2$ versus the photon energy $(\hbar\omega)$ as shown in Figure 2.16, (Yu et al., 2008a).

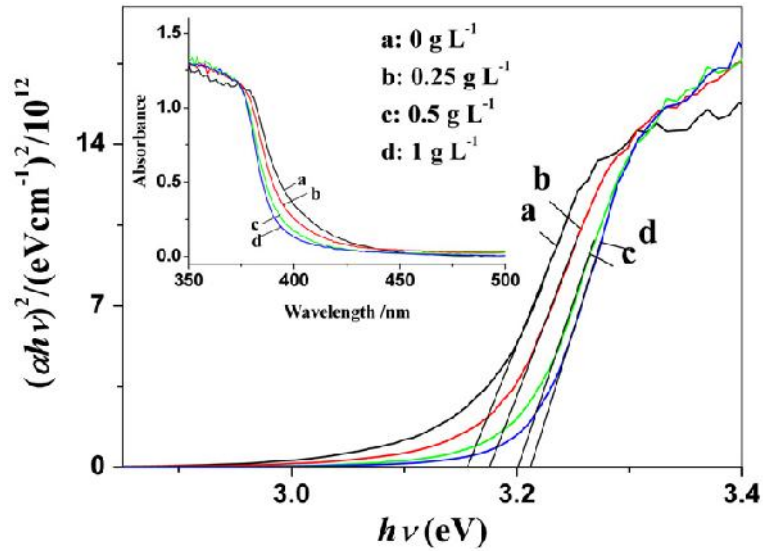


Figure 2.16: Band-gap measurement using Kubelka-Munk method for ZnO prepared by different concentration of poly (sodium 4-styrene-sulfonate) (PSS), (Yu et al., 2008a).

The band gap also can be estimated by using the UV reflection results. In this method, the band gap can be estimated from a plot of $\left(\frac{1-R}{R^2} \hbar\omega\right)^2$ versus the photon energy ($\hbar\omega$). There is another method to calculate band gap developed by (Ebrahimizadeh Abrishami et al., 2010). According this method, the band gap is obtained from the maximum of the derivative of absorbance spectrum as shown in Figure 2.17.

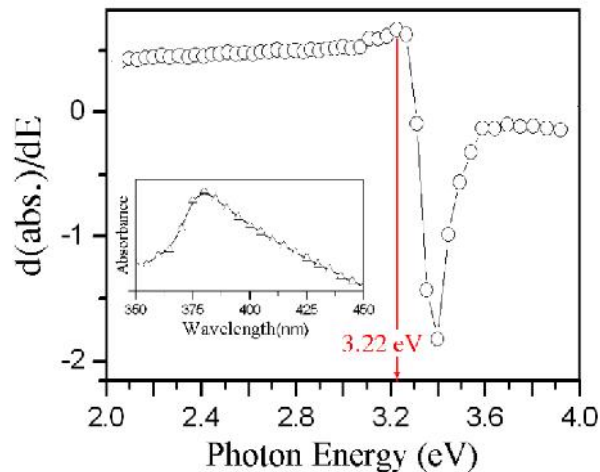


Figure 2.17: band gap estimate from the maximum of the derivative of absorbance spectrum (Ebrahimizadeh Abrishami et al., 2010).

2.3.5. Quantum confinement effect

The quantum confinement effects contribute to the exceptional electronic, mechanical, magnetic, and optical properties of materials in nanoscale size. For example, the copper nanoparticles below size of 50 nm show different behavior compare to their bulk and the conductivity is very low. This phenomenon affects the band-gap of the materials. The band-gap is increased by decreasing the particle size as shown in Figure 2.18. This change in band-gap can be clearly detected in the absorption spectra, Figure 2.19.

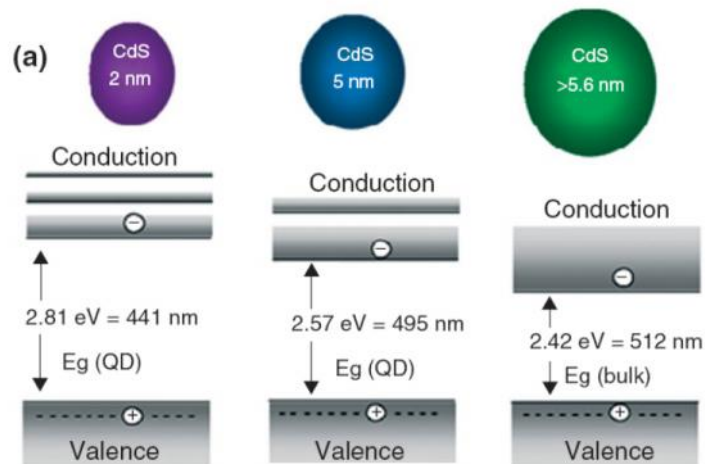


Figure 2.18: The band-gap of CdS nanoparticles correspond to their size, (Mansur, 2010). QD: Quantum Dot.

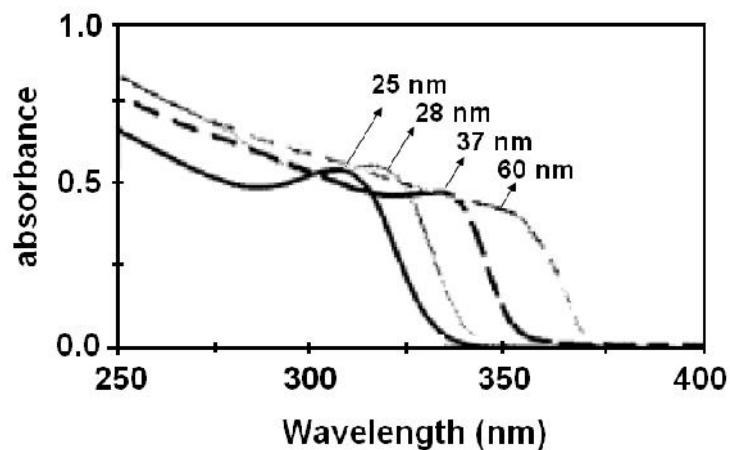


Figure 2.19: Quantum size effect on the absorbance of ZnO nanoparticles, (Shaw et al., 1997).

2.4. DIELECTRIC FUNCTION OF MATERIALS

For most optical materials the dielectric function has a form in which a transparent frequency (or wavelength) window is limited to high energy side by electron–hole excitations (dominating the UV edge) and to the low energy side by IR absorptions given by optical phonon modes (lattice vibrations). The dielectric function in general form can be written as Kramers-Heisenberg form, (Kittel, 1988).

$$\varepsilon(k, \omega) = 1 + \sum_j \frac{\alpha_{k,j}}{\omega^2 - \omega_{k,j}^2 - i\omega\eta_{k,j}} \quad (2 - 21)$$

where $\alpha_{k,j}$ is the amplitude, $\omega_{k,j}$ the frequency and $\eta_{k,j}$ the damping of the particular excitation j . In the next section, two methods are described for calculating the dielectric constant of the materials.

2.4.1. Lorentz oscillator model for calculating dielectric constant

The equation of motion can be used to explain the oscillation of the electrons and cores in the materials. According to a damped harmonic oscillator:

$$\frac{m d^2 x}{dt^2} = \frac{-m \gamma dx}{dt} - m \omega_0^2 x - e E_0 \exp(-i \omega t) \quad (2 - 22)$$

Here, m is the mass and e is the electrical charge of electron, γ is the damping constant, ω_0 is the resonance frequency, E_0 is the amplitude of the electric field of the light.

The general motion equation can be assumed as:

$$\begin{cases} x(t) = x_0 \exp(-i \omega t) \\ x_0 = -e E_0 / [m(\omega_0^2 - \omega^2 - i \gamma \omega)] \end{cases} \Rightarrow P_{resonant} = \frac{n e^2}{[m(\omega_0^2 - \omega^2 - i \gamma \omega)]} \quad (2 - 23)$$

where n is the number of the electrons per unit volume and P is the polarization vector.

Then the electric displacement can be written as:

$$\begin{aligned} D &= \varepsilon_0 E + P_{background} + P_{resonant} \\ &= \varepsilon_0 E + \varepsilon_0 \chi_{background} E + P_{resonant} \end{aligned} \quad (2 - 24)$$

Then it is resulted to the following equations:

$$\varepsilon(\omega) = \frac{1 + \chi + ne^2}{[\varepsilon_0 m(\omega_0^2 - \omega^2 - i\gamma\omega)]} \quad (2 - 25)$$

where $\varepsilon(\omega) = \varepsilon'(\omega) - i\varepsilon''(\omega)$, therefore the real and imaginary part of dielectric constant will be obtained as below:

$$\varepsilon'(\omega) = \frac{1 + \chi + ne^2(\omega_0^2 - \omega^2)}{\{\varepsilon_0 m[(\omega_0^2 - \omega^2)^2 + (\gamma\omega)^2]\}} \quad (2 - 26)$$

$$\varepsilon''(\omega) = \frac{ne^2\gamma\omega}{\{\varepsilon_0 m[(\omega_0^2 - \omega^2)^2 + (\gamma\omega)^2]\}} \quad (2 - 27)$$

2.4.2. Kramers-Kronig (K-K) method to calculate optical properties

The K-K method is a powerful method to evaluate the optical constant of optical materials using FTIR or UV-vis spectra. Absorption is characterized by a decrease in transmitted light intensity through the sample. The quantity used to discuss absorption as a function wavenumber is the transmittance (T), which is the ratio of the intensity of the light transmitted through the sample (I) to the initial light intensity (I_0). The transmittance is related to the more common percent transmittance ($T\%$) by $T\% = 100T$. The absorption (A) is defined as $\log_{10}(I/I_0)$, according to Lambert's principle (Harris and Bertolucci, 1978).

$$A(\omega) = \log_{10} \frac{I_0}{I} = \log_{10} \frac{1}{T(\omega)} = 2 - \log_{10}(T(\omega)\%) \quad (2 - 28)$$

$$R(\omega) = 100 - [T(\omega) + A(\omega)] \quad (2 - 29)$$

where $R(\omega)$ is the reflectivity in the particular frequency. The reflective index N is the most widely used physical quantity in optical design. It is generally a complex quantity:

$$\tilde{N}(\omega) = n(\omega) + ik(\omega) \quad (2 - 30)$$

where $n(\omega)$ is the real part and $k(\omega)$ is the imaginary part of a complex reflective index.

These constants can be calculated by the following equation:

$$n(\omega) = \frac{1 - R(\omega)}{1 + R(\omega) - 2\sqrt{R(\omega)} \cos \varphi(\omega)} \quad (2 - 31)$$

$$k(\omega) = \frac{2\sqrt{R(\omega)} \sin \varphi(\omega)}{1 + R(\omega) - 2\sqrt{R(\omega)} \cos \varphi(\omega)} \quad (2 - 32)$$

Where $R(\omega)$ is the reflectivity and $\varphi(\omega)$ is the phase change between the incidence and the reflected signal at a particular wave number ω . This phase change can be obtained from the K-K dispersion relation, (Lucarini et al., 2004).

$$\varphi(\omega) = \frac{-\omega}{\pi} \int_0^{\infty} \frac{\ln R(\omega') - \ln R(\omega)}{\omega'^2 - \omega^2} d\omega' \quad (2 - 33)$$

Where $R(\omega)$ is the reflectivity and $\varphi(\omega)$ is the phase change between the incidence and the reflected signal at a particular wave number ω . $\varphi(\omega)$ is obtained from Fourier transform of K-K dispersion relation (Ghasemifard et al., 2009a).

$$\varphi(\omega_j) = \frac{4\omega_j}{\pi} \times \omega \times \sum_i \frac{\ln(\sqrt{R(\omega)})}{\omega_i^2 - \omega_j^2} \quad (2 - 34)$$

where $\Delta\omega = \omega_{(i+1)} - \omega_i$ and if the data interval j is an odd number then $i=2,4,6, \dots, j-1, j+1, \dots$ while if j is an even number then $i=1, 3, 5, \dots, j-1, j+1, \dots$

The reflectivity and refractive index for the solid model is plotted as function of logarithmic frequency in Figure 2.20.

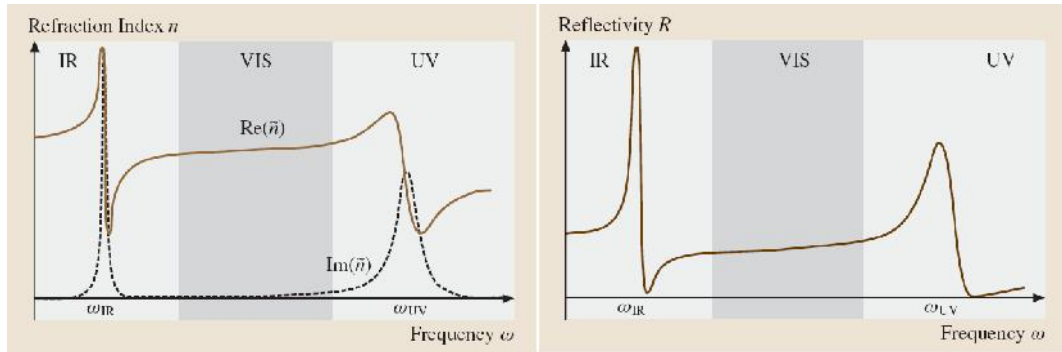


Figure 2.20: The refractive index (\tilde{n}) and reflectivity for solid model plotted as function of frequency, (Harris and Bertolucci, 1978).

The dielectric function is the square of the refractive index. Consequently, the real and imaginary parts of the complex dielectric function can be written as follows:

$$\tilde{\epsilon}(\omega) = [\tilde{N}(\omega)]^2 = [n(\omega) + ik(\omega)]^2 \quad (2 - 35)$$

$$\epsilon'(\omega) + i\epsilon''(\omega) = n^2(\omega) - k^2(\omega) + 2in(\omega)k(\omega) \quad (2 - 36)$$

$$\begin{cases} \epsilon'(\omega) = n^2(\omega) - k^2(\omega) \\ \epsilon''(\omega) = 2n(\omega)k(\omega) \end{cases} \quad (2 - 37)$$

Figure 2.21 shows a schematic view of the dielectric function

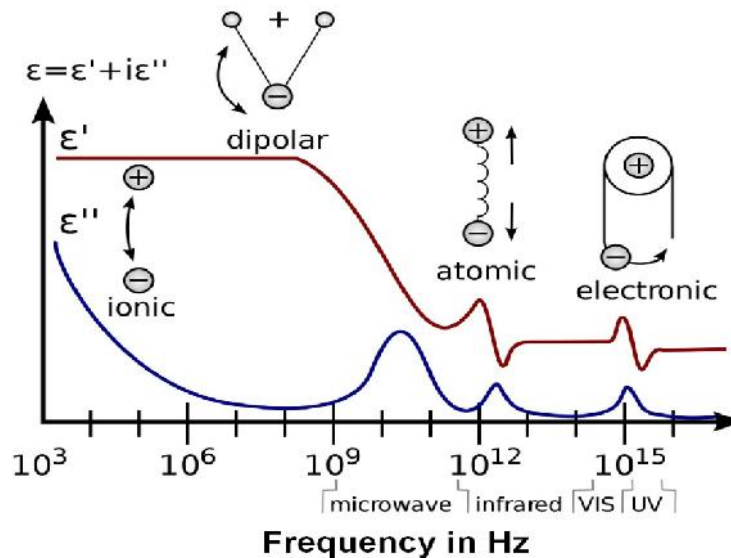


Figure 2.21: Dielectric function $\epsilon(\omega)$. There is an absorption in the infrared ω_{IR} and another one is in UV region ω_{UV} .

2.5. SUMMARY

In this chapter, the fundamental properties of ZnO and PZT were presented according to the literature. In addition, the different synthesis methods of nanoparticles especially ZnO and PZT are presented. All of the data that presented in this chapter were used in the synthesis and characterization of the ZnO and PZT nanostructures, in this thesis.

CHAPTER 3:

SYNTHESIS AND CHARACTERIZATION

TECHNIQUES OF ZNO AND PZT

NANOPARTICLES.

3.1. INTRODUCTION

This chapter contains of two main parts. The first part is about the synthesis methods of the nanostructures. In order to prepare ZnO and PZT nanostructure, choosing a suitable, easy, fast, cheap, and safe method is very important. In addition, it is very important that the synthesis method must be practical and industrial. In the second part, characterization techniques and instruments that have been used in this thesis project are described. It is very important to apply good and suitable characterization techniques on the prepared samples such that suitable preparation method can be suggested. Sol-gel, Sol-combustion, Solvothermal, and Sonochemical methods were used to prepare the nanostructures. In all of these methods, a metal salt like nitrate, chloride, or acetate is used as precursor, water, alcohols or acids are used as solvent, and organic or inorganic polymers are used as stabilizer or polymerization agent. The sol-gel method is included of three main steps. Initially, a solution is prepared by precursors materials. After that, the solution is transformed to gel. Finally, the gel is calcined to get the final product. Whereas, in sol-combustion, the gel is transformed to xerogel before calcination. In solvothermal process, the sol is poured in an autoclave and then placed in an oven for heating treatment to get the final product but in sonochemical the needed energy is applied to solution by sound waves.

3.2. SYNTHESIS OF ZNO NANOPARTICLES AND NANOSTRUCTURES

In these projects, ZnO nanoparticles and nanostructures were prepared by different methods such as sol-gel, sol-combustion, and sonochemical routes. Different stabilizers of gelatin and starch were used in sol-gel process because of their organic ligands which made them suitable for this application. Also, they are very cheap and can be found in shop. DEA is another stabilizer that is used in sol-combustion method to get fine powder of the ZnO. The sonochemical method was used to prepare the ZnO nanostructures. This method was used because the final product can be obtained by green method in a short time. All the chemicals were analytical and used as received without further purification. Zinc acetate ($\text{Zn}(\text{CH}_3\text{COO})_2 \cdot \text{H}_2\text{O}$ 99.3% Merck) and Zinc nitrate ($\text{Zn}(\text{NO}_3)_2 \cdot 6\text{H}_2\text{O}$ 98% System) are used as precursor to prepare Zn^{2+} solution. Distilled water (H_2O), Ethanol absolute ($\text{C}_2\text{H}_5\text{OH}$, HmbG chemicals), and Ammonium solution (NH_3 25% in water, Riedel-deHaen) were used as solvent. Monoethanolamine, Deethanolamine, and Triethanolamine (MEA, DEA, TEA, Sigma-Aldrich), Starch (Soluble in water, Sigma-Aldrich), and gelatin (type B, Sigma Aldrich) were used as stabilizer and polymerization agents.

3.2.1. Gelatin stabilized sol-gel synthesis of ZnO nanoparticles

In this project, a simple sol-gel route was created to prepare ZnO nanoparticles (NPs) in gelatin media. Gelatin was used as a polymerization agent, and it serves as a terminator for growing the ZnO-NPs because it expands during the calcination process and the particles cannot come together easily as shown in Figure 3.1.

To prepare 5 g of ZnO-NPs, 18.3 g of zinc nitrate was dissolved in 50 ml of distilled water and then stirred for 30 min. Meanwhile, 5 g of gelatin was dissolved in 75 ml of distilled water and stirred for 30 min at 60 °C to achieve a clear gelatin solution. After that, the zinc nitrate solution was added to the gelatin solution, and the container was moved to a water bath. The temperature of the water bath was fixed at 80 °C. Stirring was continued for 12 h to obtain a light brown gel. The final product was calcined at different temperatures (400, 500, 600 and 700 °C) in air for 2 h to obtain ZnO-NPs, Figure 3.2.



Figure 3.1: The expanded materials after calcination process because of gelatin.

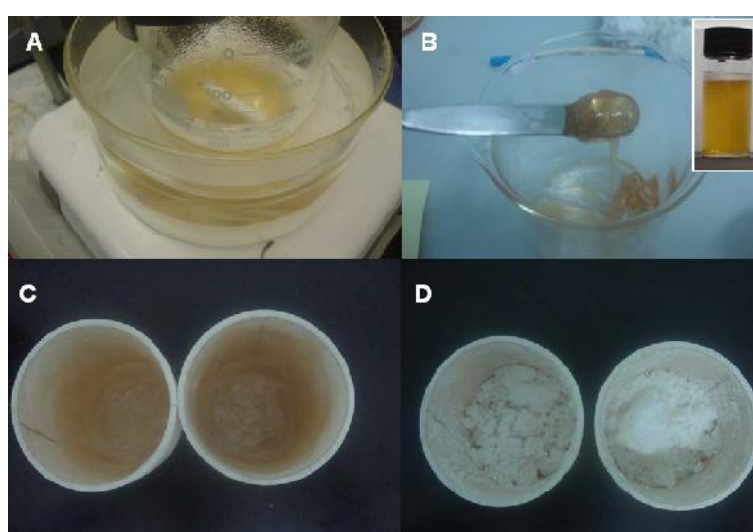


Figure 3.2: A) The prepared solution placed in an oil-bath to remove the water, B) the honey-wish formed gel, C) the gel was rubbed inside crucibles, D) the ZnO-NPs after calcination process.

3.2.2. Starch stabilized sol-gel synthesis of ZnO nanoparticles

As mentioned in previous section for gelatin, starch also was used as a polymerization agent, and it served as a terminator for growing the ZnO-NPs because of its long chain made with glucose, which terminates the mobility of the cations. Therefore, the particles cannot come together easily. Starch becomes soluble in water when the temperature of the cloudy solution reaches 75°C and the semi-crystallite structure is lost. After adding the zinc nitrate solution to starch solution, the metal cations are attracted by oxygen of the OH branches. By continuing the heating process to decrease the amount of water, the smaller amylose molecules start to form a network that holds water, and increases the mixture's viscosity. This process is called starch gelatinization. The nitrate decomposed to nitrogen dioxide and oxygen during the heating process, and will be removed from the compounds. The schematic hydrolysis process and zinc cation attachment is shown in Figure 3.3.

To prepare 5 g of ZnO-NPs, 18.3 g of zinc nitrate was dissolved in 50 ml of distilled water and then stirred for 30 min. Meanwhile, 10 g of starch was dissolved in 150 ml of distilled water and stirred for 30 min at 75°C to achieve a starch cloudy solution. Then, the zinc nitrate solution was added to the cloudy solution of starch. After the mixture achieved a gelatinized state, the container was moved to a water bath, with the temperature fixed at 80°C for 10 h to obtain a yellowish dried gel. The final product was calcined at different temperatures (400, 500, and 600°C) in air for 2 h to obtain ZnO-NPs.

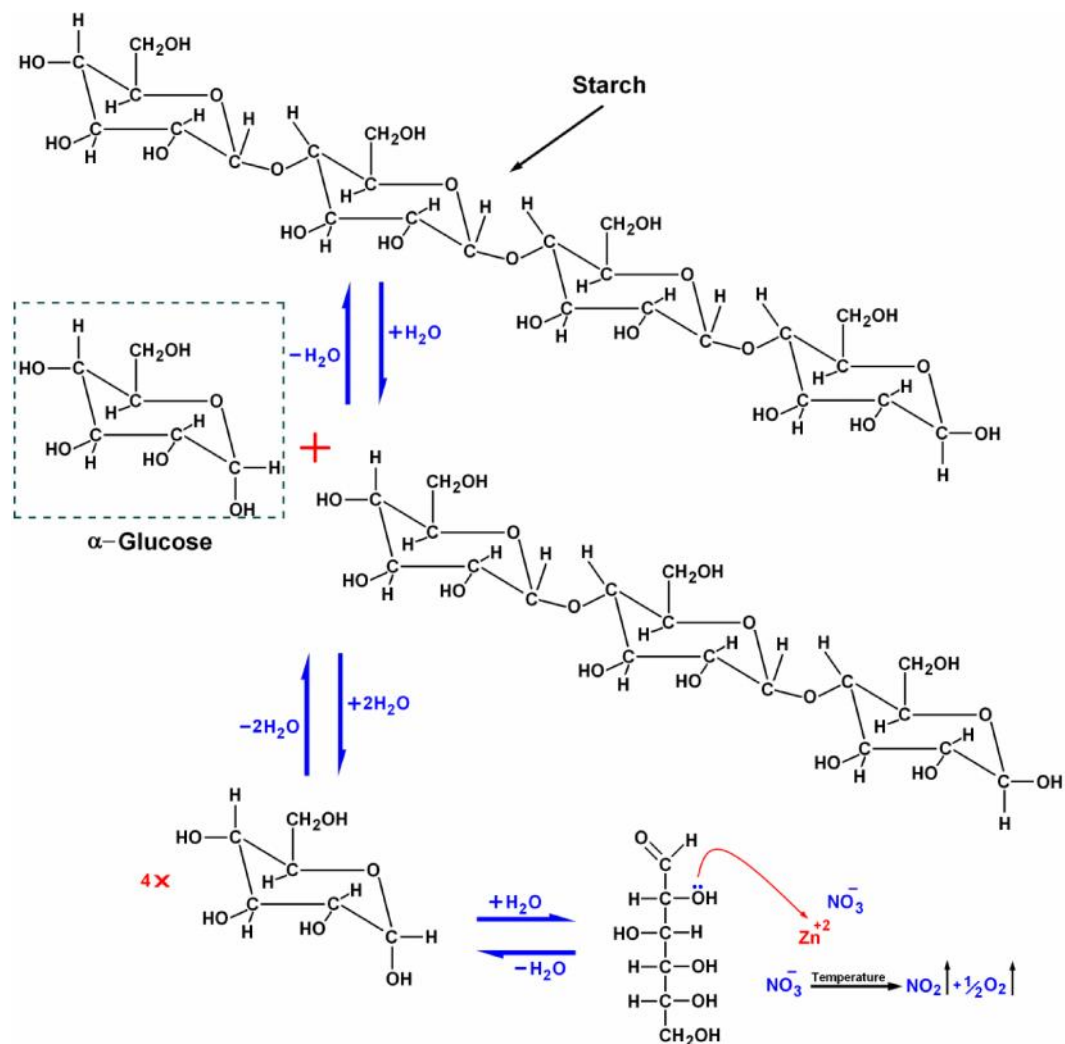


Figure 3.3: The hydrolysis process of Starch and the binding side of zinc cation.

3.2.3. Sol-combustion synthesis of ZnO nanoparticles using DEA

A modified sol-gel combustion method was used to prepare ZnO nanoparticles, using nitric acid as the fuel, diethanolamine as the complexing agent and acetic acid as the polymerization agent. In order to prepare 10 g of the ZnO-NPs, 135 mL of pure water was mixed with 65 mL of isopropanol, and the solution was stirred for 5 min at 30 °C. Water is a necessary solvent to hydrolyze the solution, but disorder reactions can occur when adding excess water to the solution. The temperature was then increased to 45 °C, and 27 g of zinc acetate was gradually added to the solution. The stirring was continued

to achieve a clear sol of Zn^{+} cations. In this process, suitable polymerization and complexing agents should be used. While citric acid and ethylene glycol are normally used for this application, in this work, acetic acid and diethanolamine were used as the polymerization and complexing agents, respectively. The high combustion temperature of citric acid, however, caused the reaction to be more difficult to control compared to the use of acetic acid. The weight ratio of these materials was chosen as follows:

$$(\text{Diethanolamine/Metal Cation}) = 1$$

$$(\text{Acetic Acid/Metal Cation}) = 2$$

The acetic acid was mixed with diethanolamine, and the mixture was stirred to achieve a clear solution. Subsequently, the solution was added to the zinc solution. The mixture then stirred for 30 min at 40 °C. One of the advantages of using these materials is that the pH of the solution reaches 7 spontaneously without requiring the addition of ammonium hydroxide to control the pH. To obtain homogenous nanoparticles and a stable sol, the solution was then refluxed for 4 h at 110 °C (the refluxing temperature must be higher than the boiling temperature of the solvents) as shown in Figure 3.4. The solution was then placed in a water bath, and the temperature was held at 80 °C for 16 h to prepare a viscous gel from the refluxed sol. Finally, a xerogel was obtained by treating the gel with acid nitric. The xerogel was calcined for 2 h at 600, 650, and 750 °C to obtain white ZnO-NP powders.

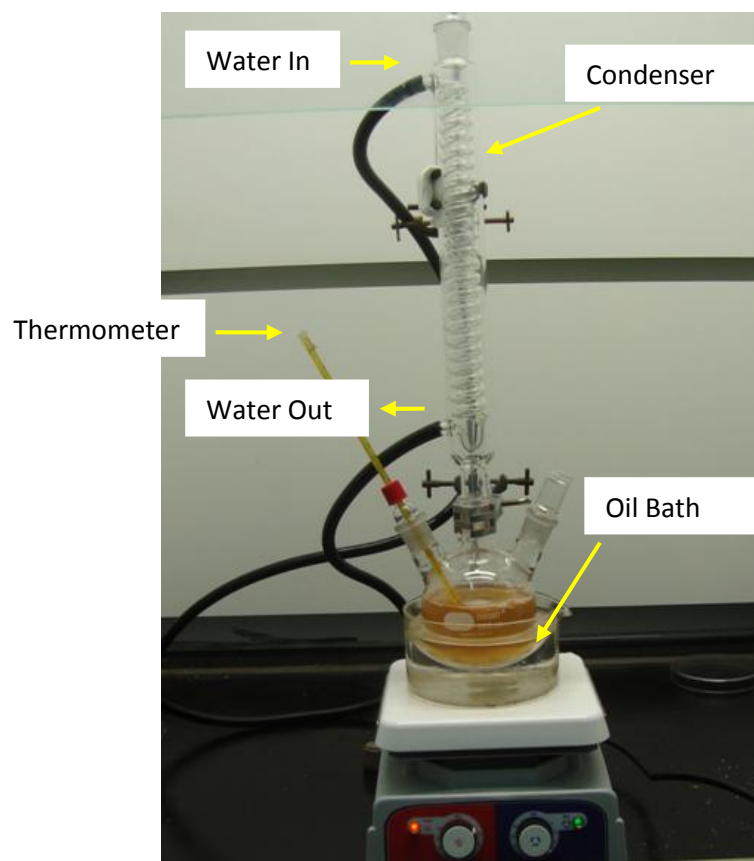


Figure 3.4: The reflux system used to get a more homogenous solution.

3.2.4. Solvothermal synthesis of ZnO nanostructures in MEA, DEA, and TEA media

In this work herein, a simple solvothermal method was used to prepare the ZnO nanostructures. The aim of this research is the preparation of ZnO-NPs and nanostructures with a narrow size distribution that is suitable for medical applications such as in sun-screen protection. Triethanolamine (TEA) was used as a polymerization agent in order to control the morphology of the ZnO-NPs because of its special structure. Zinc acetate, ethanol, and Triethanolamine (TEA) were used as starting materials. 0.5 M zinc acetate solution was prepared by dissolving 7.68 g of zinc acetate

in 35 mL of ethanol. The solution was stirred at 60°C, and then the TEA was added to the solution, all at one time. The molar ratio of TEA/ Zn^{2+} was fixed at 1:1. The solution was stirred at 60°C for 1 h. After the stirring period, a clear and homogenous solution was obtained. The Zn^{2+} solution was then aged at room temperature for another hour. The solutions were poured in a stainless steel autoclave in a 50 mL Teflon vessel as shown in Figure 3.5, and placed in the furnace for 18 h at 150°C. After the expected time, the sample was cooled down to room temperature. The same experimental procedure was repeated to prepare ZnO nanostructure in monoethanolamine, MEA, and Diethanolamine, DEA, medias by solvothermal method at 150 °C for 18 h. The formed white precipitates were dispersed in ethanol solution (30% in deionized water). The precipitates were separated by centrifugation of the mixture (4000 rpm for 4 min) at room temperature. These washing steps were repeated three times to remove the TEA polymers. Subsequently, the white precipitates were dried in an oven at 60°C overnight.



Figure 3.5: The autoclave and its Teflon vessel used for experiment.

3.2.5. Sonochemical synthesis of ZnO nanoparticles in aqueous solution

In this work, a new, fast, and simple sonochemical route was created to prepare hierarchical nanostructured ZnO (ZnO-NS). To prepare the Zn^{2+} solution, 11g Zinc acetate was dissolved in 100 mL $\text{NH}_3 \cdot \text{H}_2\text{O}$ 25 %. Then 4g NaOH was added to the solution. All these processes were made in the room temperature without any specific condition. Then, deionized water was added in until the final concentration of Zn^{2+} became one molar of Zn^{2+} solution. Four 30 mL glass bottles was taken and 25 mL of the solution was poured in each of them and then they were placed in an ultrasonication machine for 5, 15, 30, and 60 min, separately, Figure 3.6. The resulting white color product were washed with distilled water for three times and then dried in the oven at 60 °C over night.

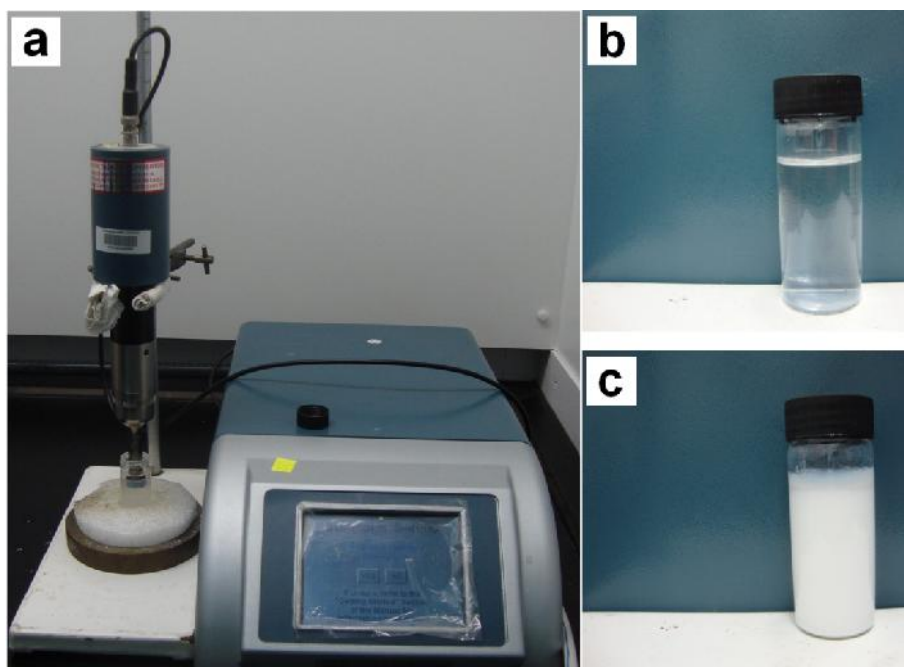


Figure 3.6: (a) Ultrasound system, (b) the Zn^{2+} solution before sonication (c) the ZnO colloid in solution after sonication.

3.3. SYNTHESIS OF PZT NANOPARTICLES

In this PhD work, PZT nanoparticles were prepared by sol-gel method. Polyethyleneglycol and 2-methoxyethanol were used as solvent and stabilizer in the sol-gel process because of their organic ligands which made them suitable for this application. All the chemicals were analytical and used as received without further purification. Lead acetate ($\text{Pb}(\text{CH}_3\text{COO})_2 \cdot 3\text{H}_2\text{O}$ 99.5% Merck), Zirconium n-propoxide ($\text{Zr}(\text{OCH}_2\text{CH}_2\text{CH}_3)_4$ 70% in propanol, Sigma-Aldrich), and Titanium isopropoxide ($\text{Ti}(\text{C}_3\text{H}_7\text{O})_4$, 98% Merck) are used as precursor to prepare the solution. Distilled water (H_2O), acetic acid ($\text{C}_2\text{H}_4\text{O}_2$ 99.5% Merck), and 2-methoxyethanol ($\text{C}_3\text{H}_8\text{O}_2$, 99.3% Merck) were used as solvent. Polyethyleneglycol (MW=600, Merck) were used as stabilizer and polymerization agent.

3.3.1. Sol-gel synthesis of PZT nanoparticles using polyol solution

In this work, PZT-NPs have been synthesized by a sol-gel method in aqueous poly ethylene glycol (PEG) solution with metal alkoxides and acetic acid as solvents. The primary sol was prepared in PEG. PEG acts as a stabilizer. PZT-NPs were prepared by sol-gel synthesis according to the scheme shown in Figure 3.7. The lead acetate solution was prepared by dissolving lead acetate in a minimum amount of acetic acid and stirred for 30 min. 5% additional lead was added, in order to compensate for the loss of Pb in the subsequent thermal treatment. The lead solution was added to an equal volume of PEG. The solution was stirred for 15 min to achieve a homogenous solution. Then, zirconium n-propanol was added to the solution and stirred at 70 °C for 30 min. The mixture was then cooled to ambient temperature and titanium isopropoxide was added

following the same procedure, and stirring continued until a milky colored solution was obtained. The sol was placed in a closed flask for 24 h and then stirred at 90 °C for 1 h. Finally, the temperature of the solution was increased up to 130 °C to achieve a clear yellow gel. As the process continued, the gel color gradually changed to dark brown. The temperature was increased up to 300 °C to produce a black xerogel. This xerogel was then milled by a ball milling machine to get a black dry gel powder. In order to prepare the PZT-NPs, the black powder was calcinated at different temperatures of 500, 550, 600 and 650 °C for 2 h, with a heating rate of 2 °C/min as shown in Figure 3.8.

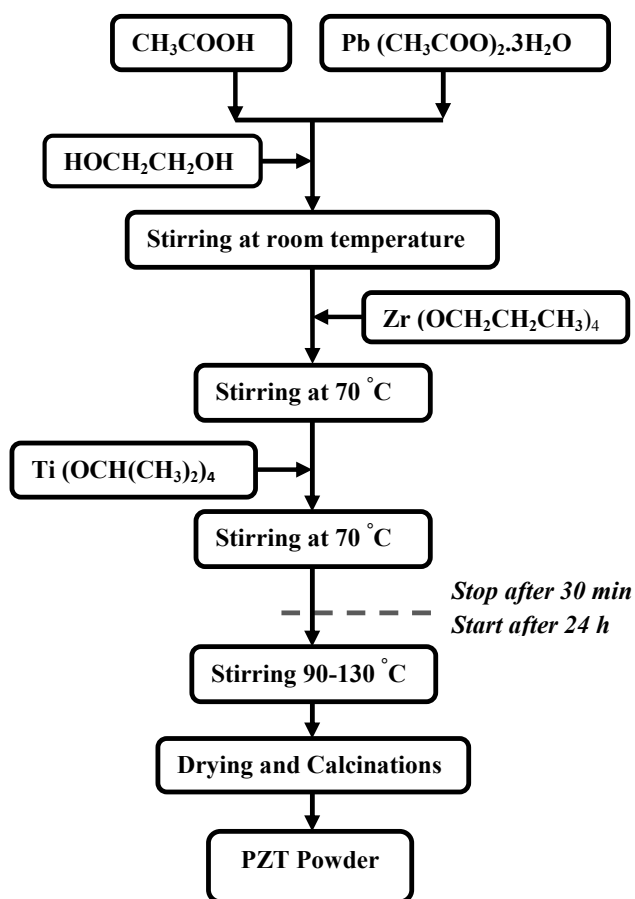


Figure 3.7: Flowchart of synthesis of PZT-NPs by sol-gel method.



Figure 3.8: The PZT nanoparticles prepared by sol-gel method

3.3.2. Sol-gel synthesis of PZT nanoparticles using 2-methoxyethanol

The rhombohedral free standing PZT-NPs were prepared by a simple modified sol-gel method in a polymeric system. This method is used to control nanostructure materials on the molecular scale because individual metal ions can be reduced by growing polymer nets. The segregation of particular metals was reduced by the immobilization of metal complexes, thus ensuring compositional homogeneity on a molecular scale.

The atomic ratio of the Pb:Zr:Ti of the solution was 1:0.52:0.48 and 10 % excess lead acetate was introduced. Initially, 11.65 grams lead acetate was dissolved in 50 ml 2-methoxyethanol and stirred for 1 h at room temperature. Simultaneously, 7.2 ml zirconium n-propoxide was dissolved in 80 ml 2-methoxyethanol and stirred for 30 min at room temperature. Subsequently, 4.4 ml titanium isopropoxide was added to this solution and a small measure of solvent was added to the solution to reach 100 ml in total. Then it was stirred for 30 min at room temperature for the second time. The high sensitivity of titanium isopropoxide and zirconium n-propoxide to oxygen requires the solutions to be prepared in a glove box with an Argon atmosphere. While stirring the Zirconium-Titanium solution, lead solution was added to the solution and stirring was

continuously carried out for 30 min at 60 °C temperature. The PH of the solution was adjusted to 5 by adding a small amount of pure water. After about 3 min, the color of the solution changed from clear to milky and the state of the solution changed from liquid to gelatinous as shown in Figure 3.9 and Figure 3.10.

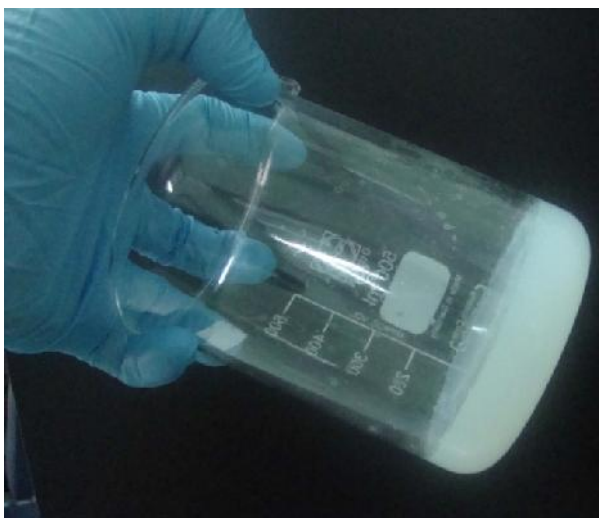


Figure 3.9: By adding some water, the solution transformed to gel state.

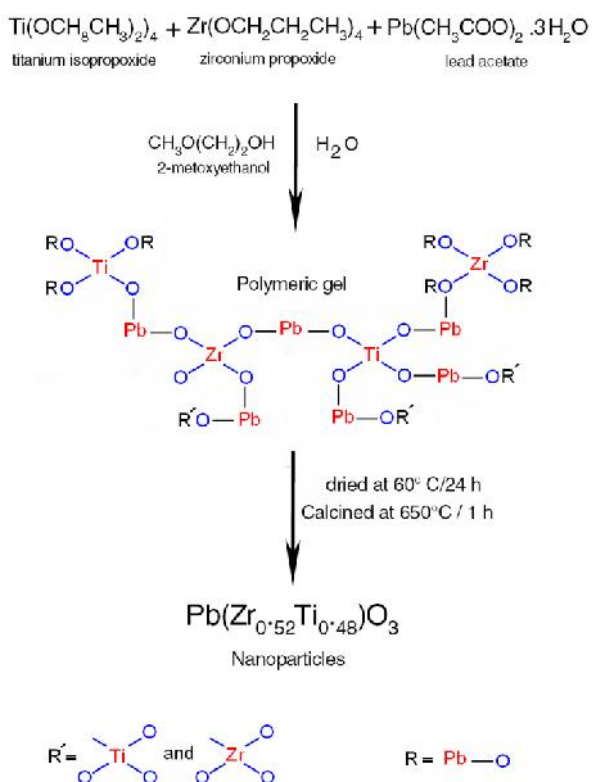


Figure 3.10: The structure of the formed gel.

The white gel was dried at 60 °C for 2 days. Finally, the white dried gel was milled and calcinated at 600 °C, 650 °C and 700 °C with a heating rate of 5 °C/min for 1 h to completely burn out the organic compounds and obtain yellow PZT-NPs. Thermogravimetric analysis (TGA) and Differential thermal analysis (DTA) were used to analyze the thermal behavior and reaction mechanisms of the gel powders. The molecular structures of the solid phase were investigated by Fourier transform infrared (FTIR). The structure evolution of the PZT-NPs was studied by X-ray powder diffraction analysis (XRD). The flowchart of preparation of the PZT-NPs is shown in Figure 3.11.

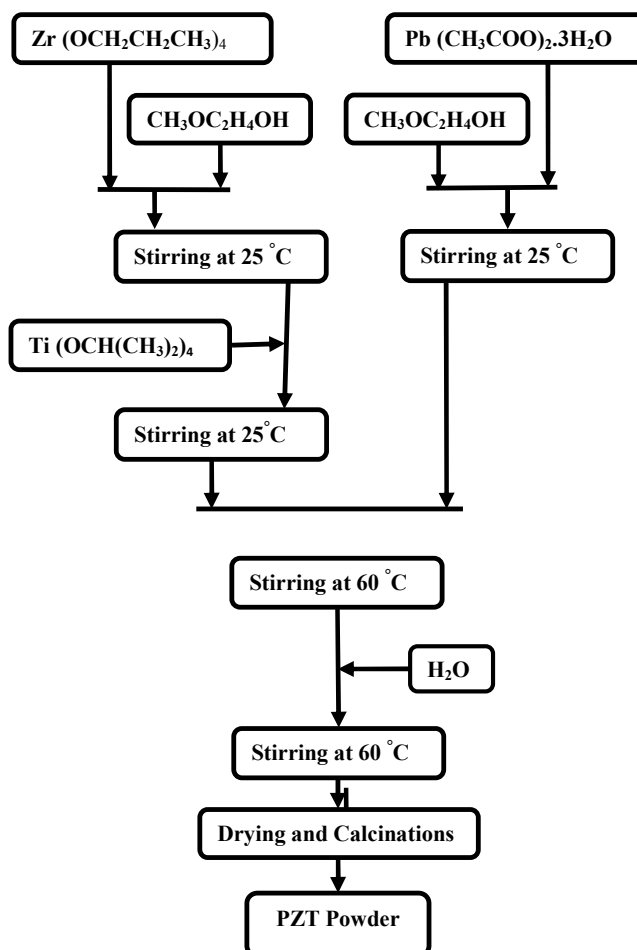


Figure 3.11: Synthesis flowchart of the PZT-NPs prepared by sol-gel method.

3.4. CHARACTERIZATION TECHNIQUES AND INSTRUMENTATION

In this section, the characterization methods and instruments that have been used in this project are described. The prepared nanostructures were characterized by powder X-ray diffraction (XRD), ultraviolet–visible (UV–vis) spectroscopy, Fourier-transform infrared Spectroscopy (FTIR), Field emission scanning electron microscopy (FESEM), thermogravimetry (TGA) and transmission electron microscopy (TEM).

3.4.1. X-ray diffraction (XRD) analysis

X-ray diffraction is one of the primary techniques used by mineralogists and solid state chemists to examine the physico-chemical make-up of unknown materials. Two important characteristics can be obtained using the XRD pattern produced by this technique. These include a fingerprint characterization of the crystallite materials and a determination of their structure. The fundamental of XRD analysis are based on Bragg's law ($n\lambda = 2d_{hkl} \sin \theta$). According to this law, scattered waves originating from each atom which are in the different planes, will be in phase with each other. Figure 3.12 shows the requirements for this condition.

In our study, the phase evolutions and structure of the ZnO and PZT nanoparticles were studied by Siemens D5000 XRD Diffractometer. The diffraction experiments were applied at a fixed wavelength (λ , $\text{CuK}_\alpha = 1.54056 \text{ \AA}$) and different angles (2θ). The ZnO (hexagonal), PZT (tetragonal and rhombohedral) lattice parameters, e.g., the values of d , the distances between adjacent crystal planes (hkl), were calculated from the Bragg equation, $\lambda=2d \sin\theta$; the lattice constants a , b and c ,

interplanar angles, the angles ϕ between the planes $(h_1k_1l_1)$ of spacing d_1 and the plane $(h_2k_2l_2)$ of spacing d_2 and the primary cell volumes, V , were calculated from the Lattice Geometry equation (Cullity, 1956).

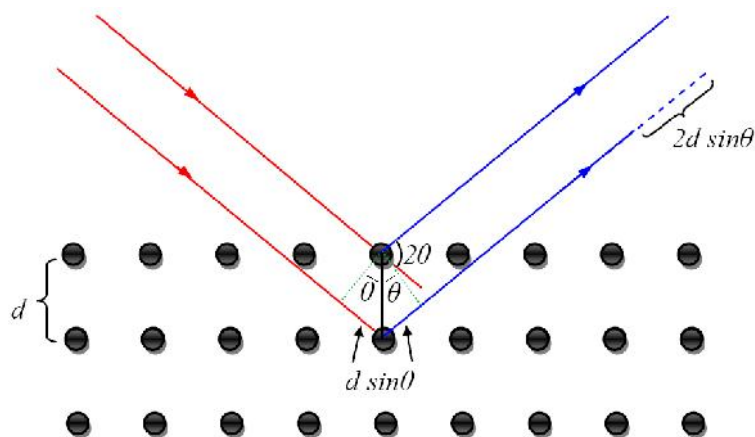


Figure 3.12: Schematic of the diffraction of an X-ray beam by parallel atomic planes in crystallite materials.

The crystallite sizes of nanopowders were determined by means of the X-ray line broadening method using the Scherrer equation: $D = k\lambda / \beta \cos \theta$, where D is the particle size in nanometers, λ is the wavelength of the radiation (1.54056 Å for $\text{CuK}\alpha$ radiation), k is a constant equal to 0.94, B is the corrected peak width at half-maximum intensity and θ is the peak position.

3.4.2. Fourier Transforms Infrared Spectroscopy (FTIR)

The most useful tool for identifying chemicals, organic or inorganic, is FTIR machine. This tool can be used to analyze materials in the liquids, solid, and gasses. The characteristic of the chemical bond can be detected from the wavelength of the absorbed light as can be seen in the spectrum. The chemical bonds of the molecule can be determined by studying the infrared absorption spectrum. Each pure compound has a

unique FTIR spectra that called fingerprint. Although the spectrum of an organic material is very rich and detailed, inorganic compounds have a simple absorption spectra. For example, ZnO has and absorption bond around 400 cm^{-1} and PZT has two absorption (generally 4 absorption bonds but we can detect 2 of them) bonds around 350 and 510 cm^{-1} . Therefore, the unknown materials can be identified by comparison of their spectrum to a library of known compound. The FTIR machine that used was Fourier transform-infrared (FT-IR) spectrometer (1650; Perkin Elmer, Waltham, MA). The absorption bonds between 280 to 4000 cm^{-1} can be detected by this machine which gives us this ability to detect two of the absorption bonds of PZT and one for ZnO in this region.

3.4.3. Transmission Electron Microscopy (TEM)

Transmission electron microscopy (TEM) is a microscopy technique whereby a beam of electrons is focused onto an ultra thin specimen and transmitted through it, interacting with the specimen as it passes through. As a result of this interaction, an image is formed. The image is magnified and focused onto an imaging device, such as layer of photographic film or fluorescent screen or is detected using a sensor (e.g., CCD camera). In this work a Hitachi H-7100 electron microscopy is used in TEM studies. To prepare sample to use for TEM, a little amount of powders were dispersed in ethanol. The concentration of the suspension should be controlled and depends on the type of the material. One or two drops of the solution are poured on top surface of copper grid. The copper grid is placed in an oven at $40\text{ }^{\circ}\text{C}$ for one day.

3.4.4. Field emission scanning electron microscopy (FESEM)

Scanning electron microscopy (SEM) is one of the most versatile and well known analytical techniques. Compared to a conventional optical microscope, an electron microscope offers advantages that include high magnification, large depth of focus, and high resolution, as well as easy sample preparation and observation. In this technique, electrons generated from an electron gun enter the surface of the sample and generate many low energy secondary electrons. The intensity of these electrons is governed by the surface topology of the sample. An image of the sample surface is therefore constructed by measuring secondary electron intensity as a function of the position of the scanning primary electron beam. In our microscopy lab, a state-of-the-art, high resolution FEI Quanta 200F field emission scanning electron microscopy (FESEM) from OXFORD is available. To prepare a sample from the powders, first, a little amount of the powders were dispersed in acetone and then poured on top surface of a silicon wafer, because silicon is conducting a clear picture can be obtained. Finally, the coated silicon was dried at 50 °C for 1h.

3.4.5. Ultraviolet-visible spectroscopy (UV-vis)

Ultraviolet and visible (UV-Vis) absorption spectroscopy can be described as the measurement of the attenuation of a light beam after reflection from a sample surface or after it passes through a sample. A single wavelength over an extended spectral range can be used for absorption measurements. Infrared spectroscopy looks at vibrational motions but ultraviolet-visible spectroscopy looks at transitions of electrons. Because, ultraviolet and visible light are energetic enough to excite outer electrons to go to higher

energy levels. Although UV-Vis spectra have broad features that are of limited use for sample identification, they are very helpful for quantitative measurements. UV-Vis spectroscopy is used to characterize the absorption, transmission, and reflectivity of several of technologically important materials, such as pigments, coatings, windows, and filters. Also, it is used to calculate the optical properties of materials. For example, the absorption spectrum can be used to calculate optical band gap. Several methods are used for this, such as Kubelka–Munk model and first derivative methods as mentioned in literature. For this work, the Thermo Scientific Evolution 300 UV-vis spectrophotometer was used to get the absorption spectra of the materials in liquid dispersed form in the range of 200 to 1000 nm, in powder form in the range of 300 to 750 nm.

3.4.6. Thermogravimetric Analysis (TGA)

Thermogravimetric analysis or thermal gravimetric analysis (TGA) is used to determine changes in weight of sample in relation to change in temperature. It contains of analysis relies on a high degree of precision in weight, temperature, and temperature change measurements. Many of the weight losses curves looks similar, therefore, the weight loss curve needs transformation before interpreting the results. For example, a derivative weight loss curve can identify the maximum weight loss point. TGA is commonly employed in research and testing to determine characteristics of materials such as polymers and to determine degradation temperatures. The gel of the nanoparticles was tested by TGA to investigate the decomposition of its organic groups to form nanoparticles and to obtain the suitable calcination temperature. In this work, the temperature range of 50 to 1000 °C was used.

3.5. SUMMARY

In this chapter, the experimental process including synthesis and characterization techniques were presented. In the synthesis part, the synthesis of the nanoparticles were explained according to method of synthesis. In the instrumentation part a brief explanation on the instrument used for the characterization of the prepared nanoparticles was provided.

CHAPTER 4:

RESULTS AND DISCUSSIONS 1:

CHARACTRIZATION OF ZNO AND PZT

NANOSTRUCTURES

4.1. INTRODUCTION

In this chapter, the optical and structural characterization results of the produced ZnO and PZT nanoparticles were presented. Explanation for the results and the growth mechanism of the nanostructures have been presented. In TGA results behavior of the gel, xerogel or dried gel during the heating treatment is discussed and now they were used to find the best calcination temperature is elaborated. The XRD and FTIR results have been used to prove that the produced materials have good crystallinity and high purity. Whereas, the UV-vis absorption results were used to calculate the band-gap of the materials.

4.2. ZNO NANOPARTICLES AND NANOSTRUCTURES

Zinc oxide is a flexible material that can be prepared in different morphologies by using different methods. But it is very important to study the quality of the final products. Depending on the preparation method the used to prepare ZnO nanostructure, there are some phases which may remain in the final products. For example, in the ZnO nanostructures that were prepared by hydrothermal, solvothermal or sonochemical methods the existence of zinc hydroxide will be detected in the final product if the processes have not been completed. So, in this section the characterization results of the

prepared ZnO nanostructures were analyzed in order to evaluate the quality of the products.

4.2.1. ZnO nanoparticles prepared using gelatin media

The thermogravimetric and derivative analyze (TGA/DTA) curves of the ZnO-NPs synthesized by the sol-gel method in a gelatin environment are presented in Figure 4.1. The TG curve descends until it becomes horizontal around 500 °C. The TG and DTA traces show three main regions. The first weight loss between 50 and 135 °C (20%) is an initial loss of water—bend Ed₁. The second weight loss from 135 to 220 °C (22%) is attributed to the decomposition of chemically bound groups, which corresponds to bend Ed₂. The third step from 220 to 350 °C (18%) is related to both the decomposition of the organic groups and the formation of the pyrochlore phases—bends Ed₃. The last weight-loss from 350 to 500 °C (19%) is attributed to the decomposition of the pyrochlore phases and the formation of ZnO pure phases—bends Ed₄. No weight loss between 500 and 900 °C was detected on the TG curve, which indicates the formation of nanocrystallite ZnO as the decomposition product.

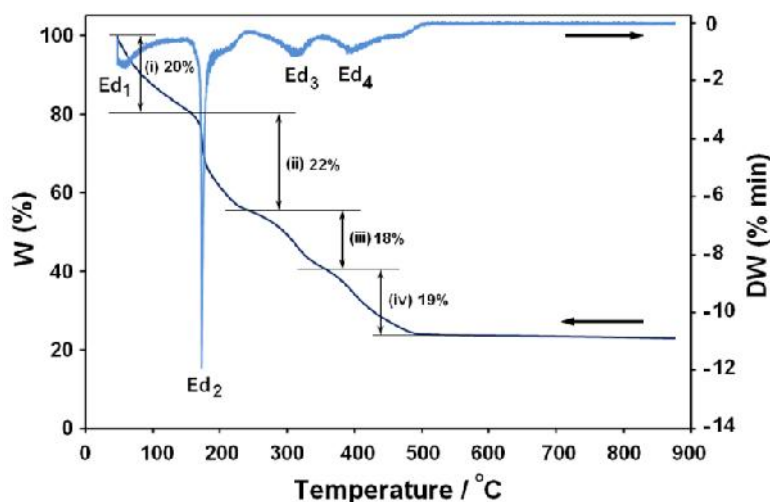


Figure 4.1: TGA and DTA curves of gels from 50 °C to 900 °C. The trace shows 71% loss weight in four steps to achieve ZnO-NPs.

Figure 4.2 shows the FTIR spectra of the ZnO samples calcined at different temperatures. For the FTIR spectra of the calcined samples at 400, 500, 600 and 700 °C, a series of absorption peaks from 1000 to 4000 cm^{-1} can be found which corresponds to the carboxylate and hydroxyl impurities in the materials. More specifically, the broad band at 3420 cm^{-1} was assigned to the O-H stretching mode of the hydroxyl group. The peaks observed at 1675, 1570, 1440, and 900 cm^{-1} are due to the asymmetrical and symmetrical stretching of the zinc carboxylate. As shown in the FTIR traces, the spectral signatures of carboxylate impurities disappear as the calcination temperature increases (500, 600 and 700 °C). This indicates the possibility of zinc carboxylate dissociation and conversion to ZnO during the calcination process.

For all of the samples in this study, a broad absorption band was observed at around 420 cm^{-1} . The band at 420 cm^{-1} corresponds to the E_1 vibration mode of hexagonal ZnO (Kaschner et al., 2002). There was also an absorption band at around 1150 cm^{-1} . This absorption band can be related to C-O and therefore can be neglected.

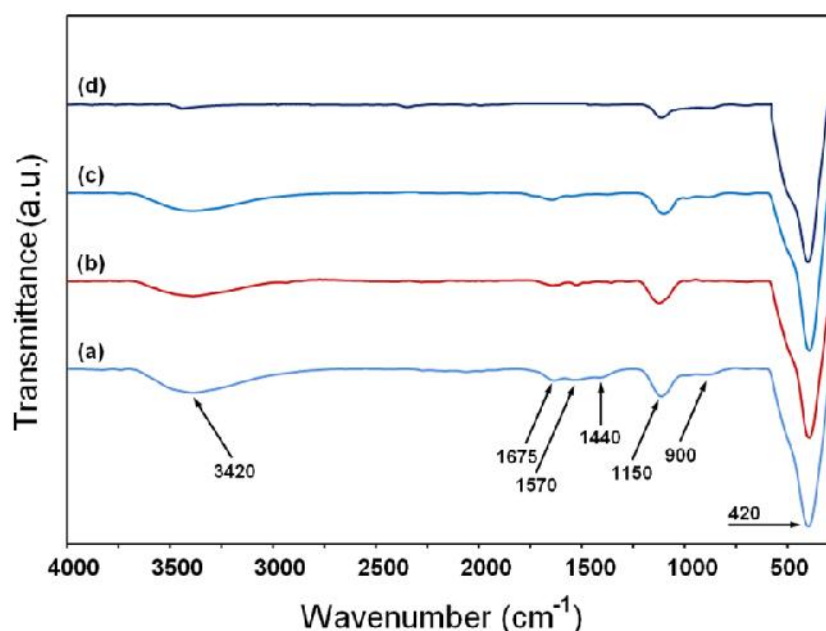


Figure 4.2: FTIR spectra of the ZnO-NPs prepared at different calcination temperatures: (a) 400, (b) 500, (c) 600 and (d) 700 °C. The absorption band related to Zn-O vibration mode was clearly observed at 420 cm^{-1} .

XRD patterns of the ZnO-NPs prepared in gelatin media were shown in Figure 4.3. All of the detectable peaks can be indexed to the ZnO wurtzite structure (PDF card no: 00-036-1451). The (112) and (201) planes were used to calculate the lattice parameters of the ZnO-NPs calcined at 700 °C, and the following values were obtained: $d_{(112)} = 0.1377$ nm, $d_{(201)} = 0.1358$ nm, $a=b = 0.3218$ nm, $c = 0.5330$ nm, $\varphi = 32^\circ$ and $V = 47.81$ nm³. The (102) plane was chosen to calculate the crystallite size (either plane can be used for this purpose). The crystallite size of the ZnO-NPs calcined at temperatures of 500, 600, and 700 °C were found to be 20 ± 2 , 23 ± 2 , and 26 ± 2 nm, respectively.

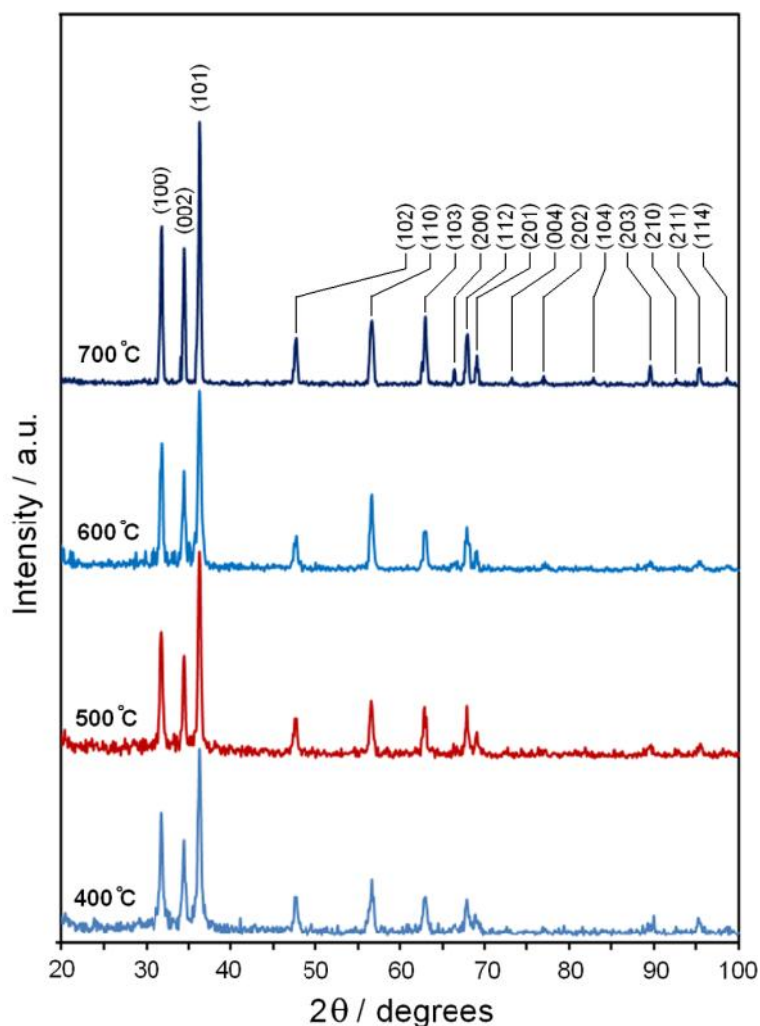


Figure 4.3: XRD patterns of ZnO-NPs prepared at different calcination temperatures of 400, 500, 600 and 700 °C.

The morphology and size distribution of the ZnO-NPs calcined at temperatures of 500, 600, and 700 °C are shown in Figure 4.4. It can be clearly observed that the nanoparticles grew as the calcination temperature increased. It was also observed that both hexagonal and circular shapes were exhibited by the nanoparticles that were calcined at 500 and 600 °C. However, the nanoparticles that were calcined at 700 °C were almost all hexagonal in shape. The number of hexagonally shaped nanoparticles increased as the calcination temperature increased, or in other word, the growing size increased the number of hexagonally shaped nanoparticles. This event can be related to quantum size effects. When the size of the particle is very small, the ratio of the atoms on the surface to all of the atoms in the particle increases. In this situation, the surface atoms can affect the morphology of the particle (Hosokawa et al., 2007). When the size of the particles grows, the ratio of the atoms on the surface to all of the atoms in the particle decreases. At a certain point, the effect of the surfaces atoms is negligible. The size histograms of the ZnO-NPs are shown next to the relative TEM images. The histograms show that the main particle size of the ZnO-NPs calcined at temperatures of 500, 600, and 700 °C were about 29 ± 5 , 40 ± 10 , and 58 ± 15 nm, respectively. The TEM and size distribution results confirm that a narrow size distribution can be obtained for ZnO-NPs prepared with gelatin media and calcined at temperatures of 500, 600, and 700 °C.

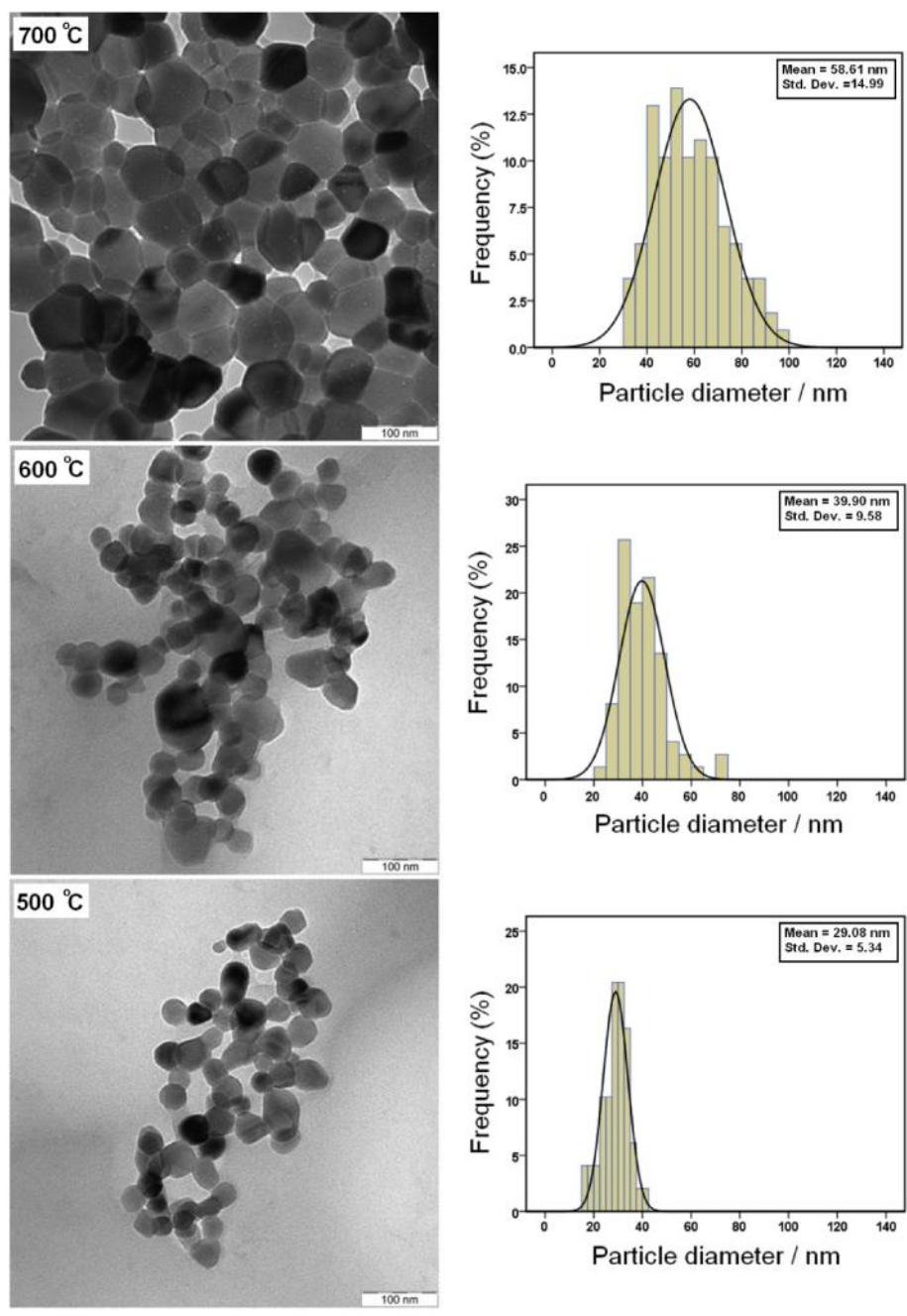


Figure 4.4: TEM images of ZnO-NPs prepared at different calcination temperatures.

4.2.2. ZnO nanoparticles prepared using starch media

The thermogravimetric and derivative analysis (TGA/DTA) curves of the ZnO-NPs synthesized by the sol-gel method in a starch environment are presented in Figure 4.5. The heating process was started at 50°C, and then increased up to 950°C with a temperature rate change of 10°C/min. The TG curve descends until it becomes horizontal around 400°C, and 52% weight loss was observed during the heating process. The TG and DTA traces show four main regions. The first weight loss between 50 and 90°C (2.5%) is an initial loss of water, bend Ed₁. The second weight loss from 90 to 180°C (12.1%) is attributed to the decomposition of chemical bound groups, which corresponds to bend Ed₂. The third step from 180 to 300°C (22.4%) is related to both the decomposition of the organic groups, and the formation of the pyrochlore phases, bend Ed₃. The last weight-loss step from 300 to 400°C (15%) is attributed to the decomposition of the pyrochlore phases and the formation of ZnO pure phases indicated by bend Ed₄. No weight loss between 400 and 900°C was detected on the TG curve, which indicates the formation of nanocrystallite ZnO as the decomposition product. Compare to the previous work in section 4.2.1., the pure phase is obtained at lower temperature.

Figure 4.6(a, b, c, d, and e) shows the FTIR spectra of the starch, dried gel, and ZnO samples calcined at different temperatures, respectively. Figure 4.6(a) shows the FTIR trace of starch. The peaks at 1050 and 1150 cm⁻¹ are related to the C–O bond stretching of C–O–C and C–O–H groups in starch, respectively. Also, there are two peaks between 2970 and 3370 cm⁻¹, which are attributed to C–H and O–H normal vibration modes.

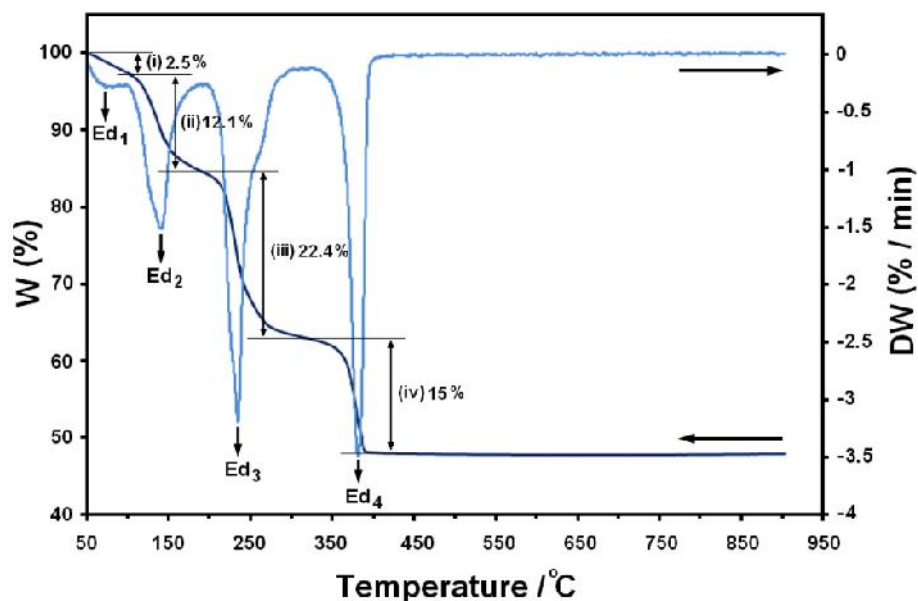


Figure 4.5: TGA and DTA curves of gels from 50 °C to 900 °C. The trace shows 52% loss weight in four steps to achieve ZnO-NPs.

The FTIR transmittance trace of the dried gel is shown in Figure 4.6(b). A new absorption peak is identified at 1654 cm^{-1} corresponds to the C=O normal stretching vibration mode. However, the peak which corresponds to C–O vibration modes disappeared from the FTIR trace of the dried gel. The characteristic peaks that appeared between 3300 and 3500 cm^{-1} can be attributed to C–H and O–H, $[\text{Zn}(\text{OH})_2]$ vibration modes. There were also two absorption peaks about 375 and 474 cm^{-1} that are related to Zn–O_δ vibration modes. The results of FTIR prove that the atomic bonds of starch are changed during the sol-gel process, as described in the reaction mechanism section. For all of the samples in this study which were calcined at 400, 500, and 600°C, broad absorption bands were observed at around 410 cm^{-1} .

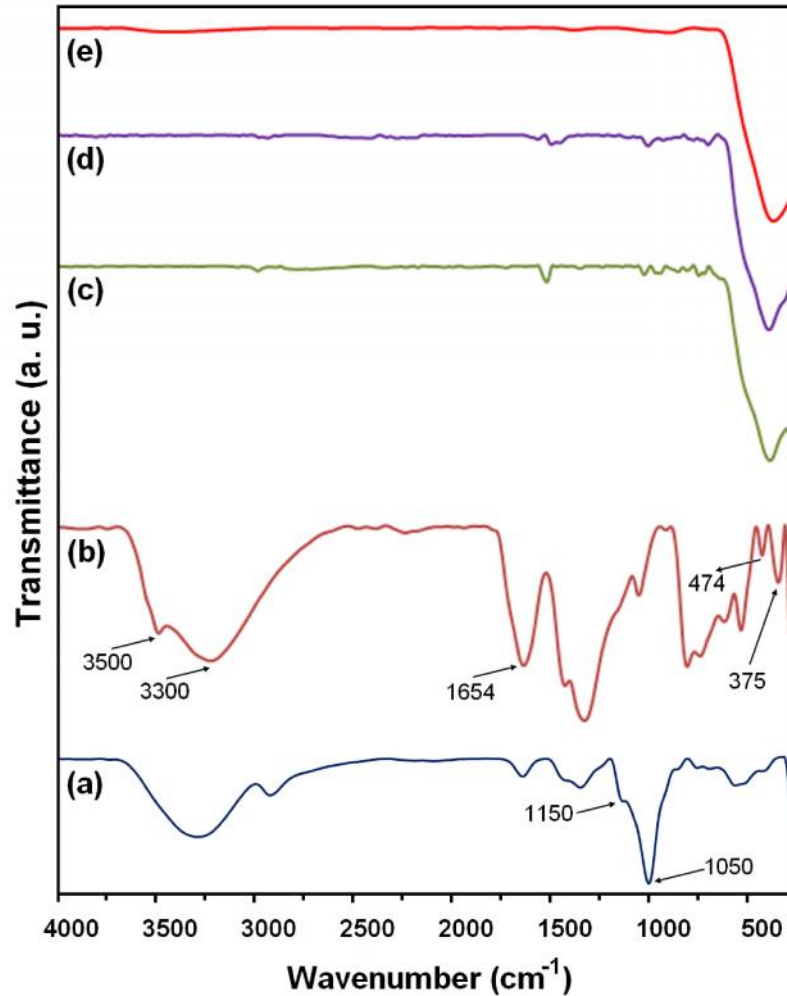


Figure 4.6: FTIR spectra of the (a) starch, (b) dried gel, and ZnO-NPs prepared at different calcination temperatures: (c) 400, (d) 500, and (e) 600 °C. The absorption band related to Zn-O vibration mode was clearly observed at 420 cm^{-1} .

The XRD patterns of the dried gel and ZnO-NPs calcined at different temperatures of 400, 500, and 600°C are shown in Figure 4.7 (a, b, c, and d), respectively. All of the detectable peaks can be indexed to the ZnO wurtzite structure (PDF card no: 00-036-1451). The (100) and (002) planes were used to calculate the lattice parameters of the ZnO-NPs calcined at different temperatures of 400, 500, and 600°C. Although the intensity of the (100) and (002) planes are increased as the temperature increases, the positions of the corresponding peaks are fixed at 31.9 and 34.5°, respectively. The increase in the intensity of the peaks can be related to the

different crystallite sizes of the ZnO-NPs calcined at different calcination temperatures.

The results were summarized in Table 4.1.

Table 4.1: Lattice parameters of ZnO-NPs prepared at different calcination temperatures; 400, 500, and 600 °C. (The measurements were done at room temperatures of 25 °C).

Temperature	2θ ± 0.1	hkl	d_{hkl} (nm) ± 0.0005	Structure	Lattice parameter (nm) ± 0.005 ± 0.01	V (nm ³) ± 0.2	$\text{Cos } \varphi$ ± 0.002
400 °C	66.6 68.0	(200) (112)	0.1403 0.1378	Hexagonal	$a=0.324$ $c/a=1.62$	48.1	0.848
500 °C	66.5 68.0	(200) (112)	0.1405 0.1378	Hexagonal	$a=0.325$ $c/a=1.61$	48.0	0.848
600 °C	66.4 68.0	(200) (112)	0.1407 0.1378	Hexagonal	$a=0.325$ $c/a=1.60$	47.7	0.847

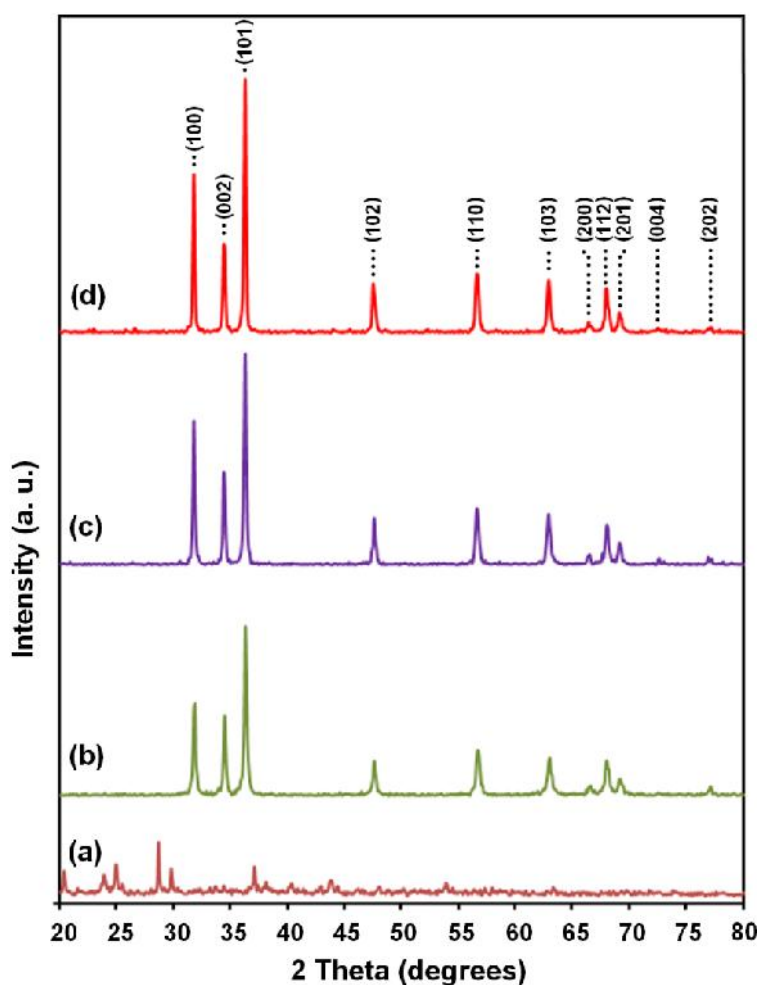


Figure 4.7: XRD pattern of (a) dried gel and ZnO-NPs prepared at different calcination temperatures of (b) 400, (c) 500, and (d) 600 °C.

The crystallite sizes of the ZnO-NPs were determined by means of an X-ray line-broadening method using the Scherrer equation. The (102) plane was chosen to calculate the crystallite size (either plane can be used for this purpose). The crystallite sizes of the ZnO-NPs calcined at temperatures of 400, 500, and 600°C were found to be 21 ± 2 , 33 ± 2 , and 42 ± 2 nm, respectively. According to these results, the crystallite size was increased as the calcination temperature increased. These results confirm the intensity growth of the XRD peak as described above.

Figure 4.8 shows the morphology and size distribution of the ZnO-NPs calcined at temperatures of 400, 500, and 600°C. It can be clearly observed that the nanoparticles grew as the calcination temperature increases. It is also observed that both hexagonal and circular shapes are exhibited by the nanoparticles that were calcined at 400, 500, and 600°C. The number of hexagonally shaped nanoparticles increased as the calcination temperature increased, or in other words, the growing size increased the number of hexagonally shaped nanoparticles. This event can be related to self-assembly effects. When the size of the particle is very small, the ratio of the atoms on the surface to all of the atoms in the particle increases. In this situation, the surface atoms can affect the morphology of the particle. When the size of the particles increases, the ratio of the atoms on the surface to all of the atoms in the particle decreases. At a certain point, the effect of the surface atoms is negligible.

The size histograms of the ZnO-NPs are shown next to the relative TEM images. The histograms indicate that the main particle sizes of the ZnO-NPs calcined at temperatures of 400, 500, and 600°C were about 28 ± 5 , 42 ± 8 , and 51 ± 12 nm, respectively. The TEM and size distribution results confirm that a narrow size distribution can be obtained for ZnO-NPs prepared with starch media and calcined at temperatures of 400, 500, and 600°C.

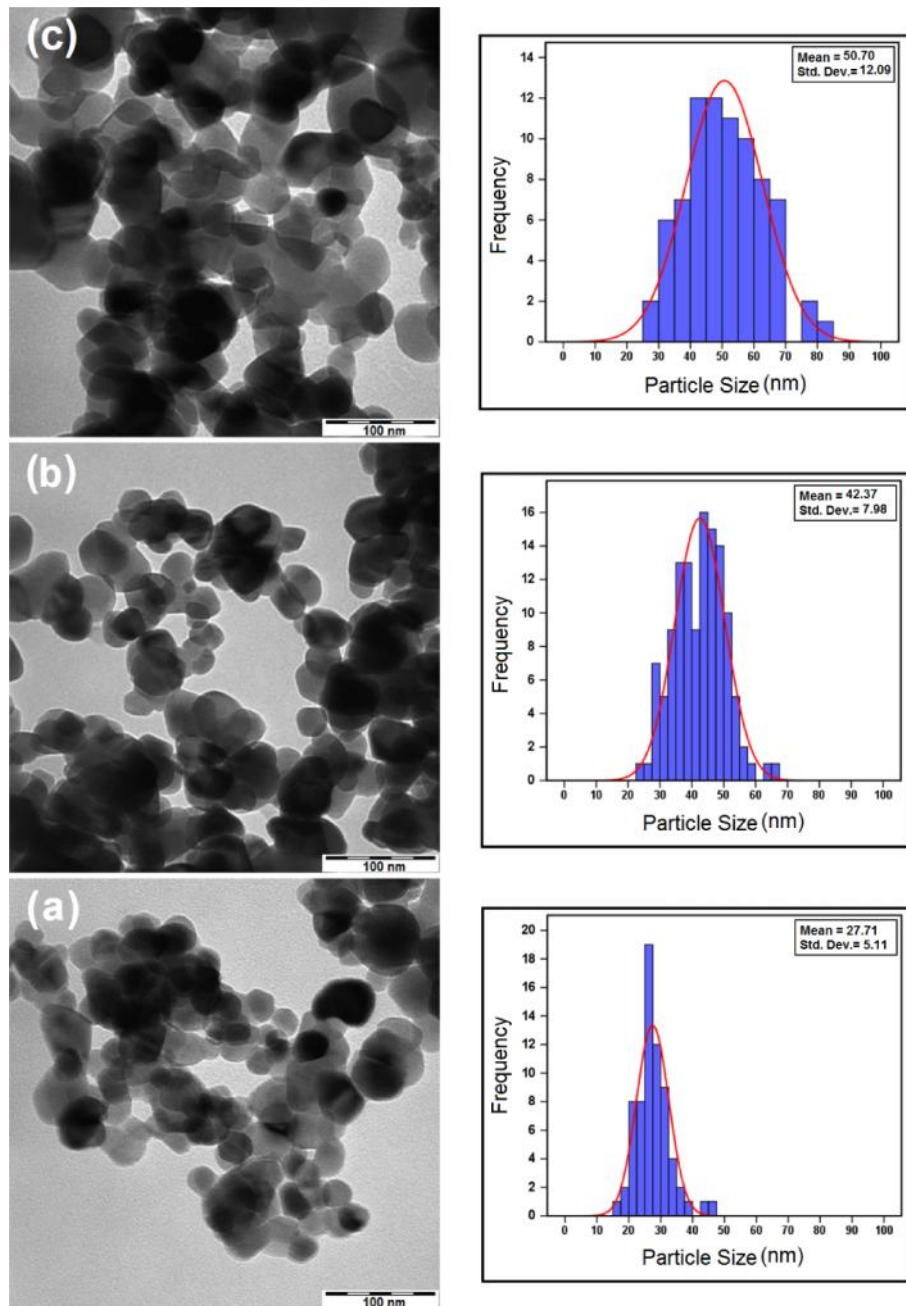


Figure 4.8: TEM images of ZnO-NPs prepared at different annealing temperatures: (a) 400, (b) 500, and (c) 600 °C. It is clearly observed that the particle sizes increases when the annealing temperature increases.

4.2.3. ZnO nanoparticles prepared by sol-combustion method

The TGA/DTA curves of ZnO-NPs synthesized by the sol-gel combustion method, as described in chapter 2, are presented in Figure 4.9. The TG traces show a minor weight loss (3 %) during the heating step from 50 °C to 190 °C. This minor weight loss was attributed to the removal of physically absorbed water. A major weight loss (22 %) was also observed in the step from 190°C to 750°C, which was related to the combustion of organic materials. No further weight loss was observed up to 900 °C. This indicates that the formation of nanocrystallite ZnO as the decomposition product was complete at 750°C.

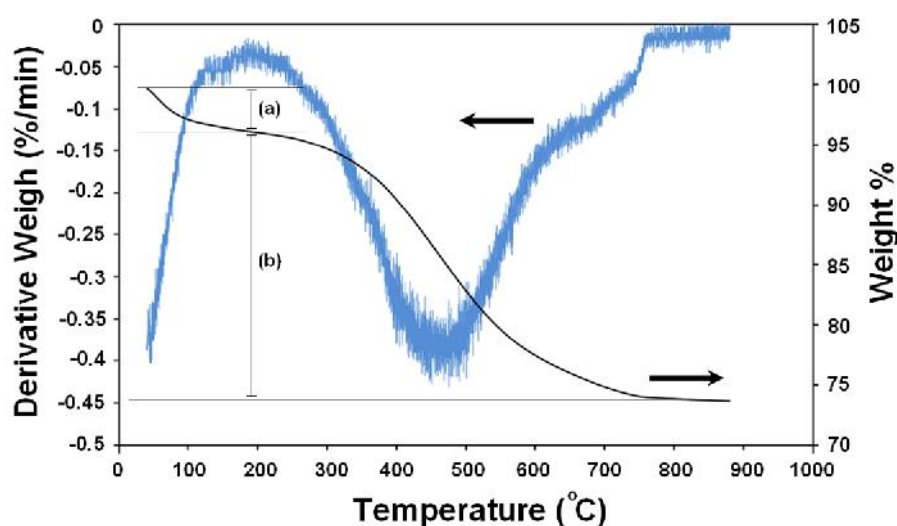


Figure 4.9: TGA and DTA curves of xerogels from 50 °C to 900 °C. The traces show two steps; (a) is related to the evaporation of water and (b) is related to the decomposition of organic materials.

Figure 4.10 shows the FTIR of the ZnO-NPs prepared by the sol-gel combustion method, in the range of 4000-280 cm^{-1} . A broad band is observed for each spectrum that is attributed to a Zn-O vibration mode. It is also observed that there is a negligible shift to a lower wavenumber due to increase in the annealing temperature. This shift can be

related to a change in the lattice parameters of the ZnO-NPs. There were several absorption bands at 1750, 1350 and 1250 cm^{-1} . These absorption bands were likely related to CO_2 absorbed from the atmosphere (air) and can therefore be neglected.

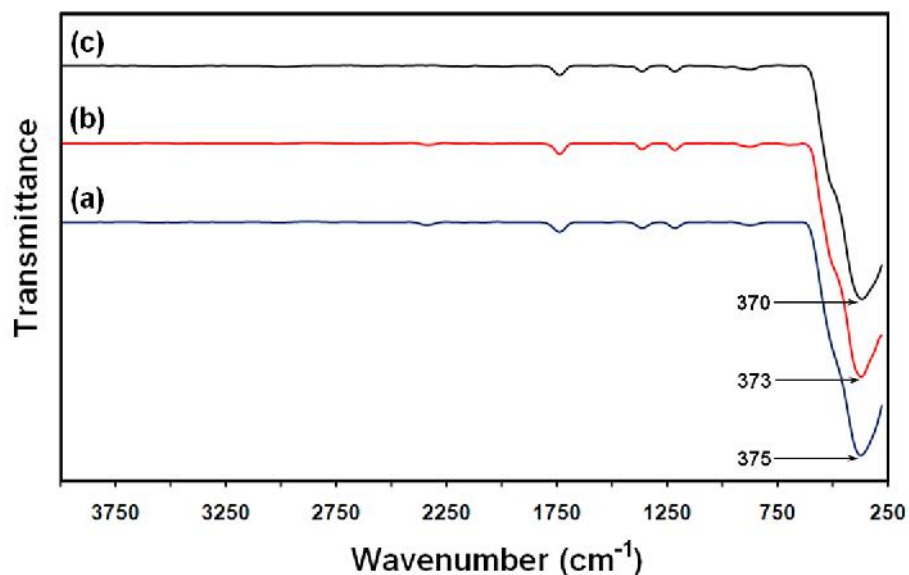


Figure 4.10: FTIR spectra of the ZnO-NPs prepared at different annealing temperatures: (a) 600 $^{\circ}\text{C}$, (b) 650 $^{\circ}\text{C}$ and (c) 750 $^{\circ}\text{C}$. The absorption band related to Zn-O vibration mode was clearly observed.

The XRD patterns of the prepared samples are shown in Figure 4.11. All the detectable peaks can be indexed to the ZnO wurtzite structure. The reflection peaks clearly became sharper with increasing thermal decomposition temperature, indicating an enhancement of crystallinity. It was observed that there was little change in the lattice parameters when the annealing temperature was increased. This change in lattice parameters can be attributed to the change of particle size and quantum size effects (Hosokawa et al., 2007). The lattice parameters of the ZnO-NPs calcined at different temperatures are summarized in Table 4.2.

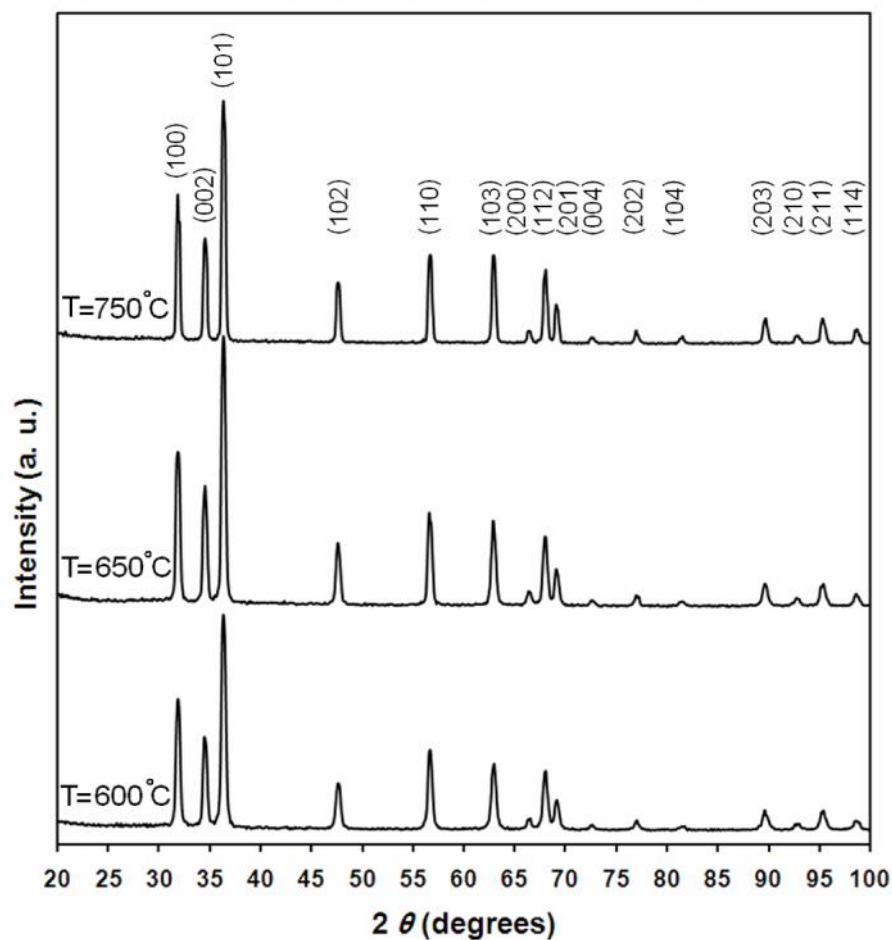


Figure 4.11: XRD pattern of ZnO-NPs prepared at different annealing temperatures. A slight change of intensity and position was observed for the (201) peak.

Table 4.2: lattice parameters of ZnO-NPs prepared at calcination temperatures of 600, 650 and 750 °C. (The measurements were done at room temperatures of 25 °C)

<i>Temperature</i>	2θ ± 0.1	<i>hkl</i>	d_{hkl} (nm) ± 0.006	<i>Structure</i>	<i>Lattice parameter</i> (a)(nm) ± 0.005 (c/a) ± 0.01	V (nm ³) ± 0.2	<i>Cos φ</i> ± 0.002
600 °C	67.9 69.1	(112) (201)	0.138 0.136	Hexagonal	a=0.322 c/a=1.67	48.1	0.848
650 °C	67.9 69.0	(112) (201)	0.138 0.136	Hexagonal	a=0.322 c/a=1.66	48.0	0.848
750 °C	68.0 69.0	(112) (201)	0.138 0.136	Hexagonal	a=0.322 c/a=1.65	47.7	0.847

Although TEM is the best way to determine the particle size of nanoparticles, XRD is also widely used. The Scherrer method for calculating crystal size gives an average value. However, with TEM, besides directly measuring particle size, the morphology of the particles can also be observed. The crystal sizes of the ZnO-NPs were determined by means of an X-ray line-broadening method using the Scherrer equation: $D = (k\lambda/\beta_{hkl}\cos\theta)$, where D is the crystal size in nanometers, λ is the wavelength of the radiation (1.54056 Å for CuK $_{\alpha}$ radiation), k is a constant equal to 0.94, β_{hkl} is the peak width at half-maximum intensity and θ is the peak position. The (102) and (110) planes were chosen to calculate the crystal size (either plane can be used for this application); the results are presented in Table 4.3.

Table 4.3: The crystal size of ZnO-NPs prepared at calcination temperatures of 600, 650 and 750 °C.

<i>Temperature</i>	<i>2θ ± 0.1</i>	<i>FWHM ± 0.01</i>	<i>Average crystal size (nm)</i>	
600 °C	47.5	0.53	17.1	18 \pm 2
	56.6	0.50	19.0	
650 °C	47.5	0.49	18.4	19 \pm 2
	56.6	0.50	19.0	
750 °C	47.5	0.44	20.8	21 \pm 2
	56.6	0.44	21.4	

The typical TEM result shows various hexagonal shapes with smooth surfaces. There was a ~25% variation between the TEM and XRD results for particle size. In very small particles, the atoms on the surface apply a strain on the particle due to the surface effect (Hosokawa et al., 2007). However, this effect is not considered in the XRD measurements. The TEM results are presented in Figure 4.12.

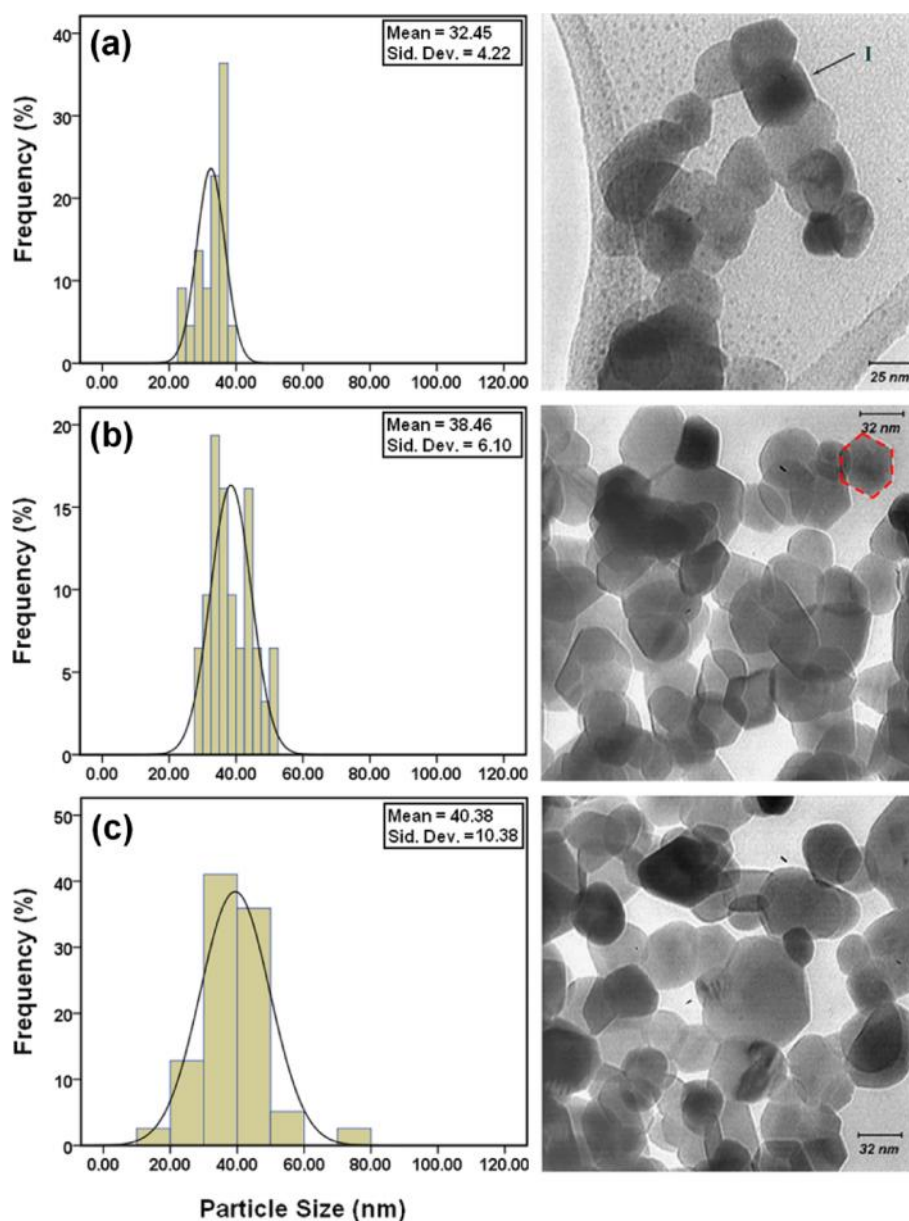


Figure 4.12: TEM images of ZnO-NPs prepared at different annealing temperatures: (a) 600, (b) 650 and (c) 750 °C. The nearly hexagonal plate shape of the ZnO-NPs is clearly shown (in I, for example).

The UV–vis absorption spectra of the ZnO-NPs prepared at annealing temperatures of (a) 600, (b) 650 and (c) 750 °C are shown in the inset of Figure 4.13. The relevant increase in the absorption at wavelengths less than 400 nm can be assigned to the intrinsic band-gap absorption of ZnO due to the electron transitions from the valence band to the conduction band ($O_{2p} \rightarrow Zn_{3d}$) (Yu et al., 2006). Interestingly, an obvious red-shift in the absorption edge was observed for the nanoparticles annealed at

different temperatures. This might be due to changes in their morphologies, particle size and surface microstructures. Moreover, the direct band-gap energies estimated from a plot of $(\alpha \times hv)^2$ versus the photo energy (hv) according to the Kubelka–Munk model (Yu et al., 2008a), shown in Figure 4.13, were 3.31 ± 0.05 , 3.26 ± 0.05 and 3.24 ± 0.05 eV for the ZnO-NPs obtained at the increasing annealing temperatures of (a) 600, (b) 650 and (c) 750 °C, respectively. Such an increase in the ZnO band-gap energy is in good agreement with the corresponding red-shift seen in the absorption edge mentioned above.

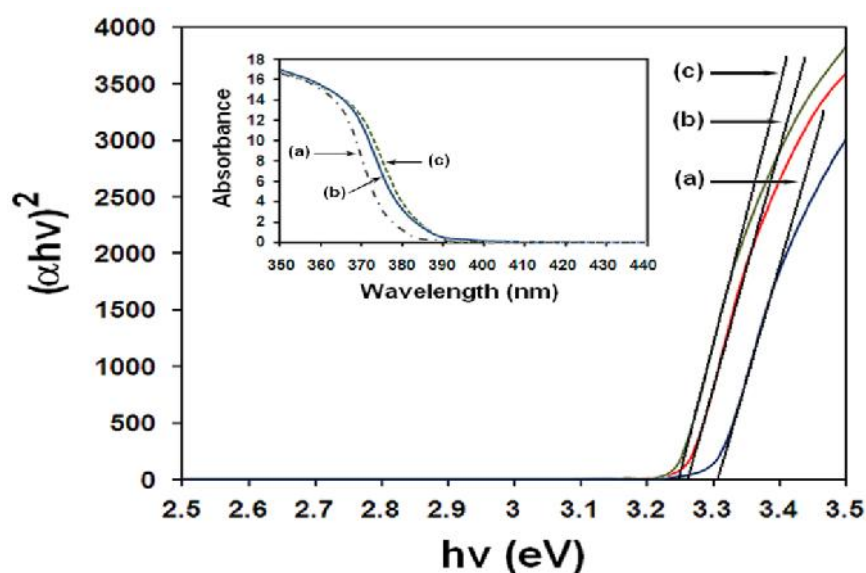


Figure 4.13: Absorption edge (inset) and band gap of the ZnO-NPs prepared at different annealing temperatures: (a) 600, (b) 650 and (c) 750 °C.

4.2.4. ZnO nanoparticles prepared by solvothermal method

Figure 4.14 shows the FTIR of the ZnO-NPs prepared by the solvothermal method, in the range of 4000-280 cm^{-1} . A broad absorption band was observed at around 375 cm^{-1} . The band at 375 cm^{-1} corresponds to the E_2 vibration mode of hexagonal ZnO. There were several small absorption bands at 930, 1050, and 3400 cm^{-1} . These absorption bands were likely related to CO_2 (C-O) and H_2O (O-H) absorbed from the atmosphere (air), and can therefore be neglected. The FTIR results show the high purity of the obtained ZnO-NPs.

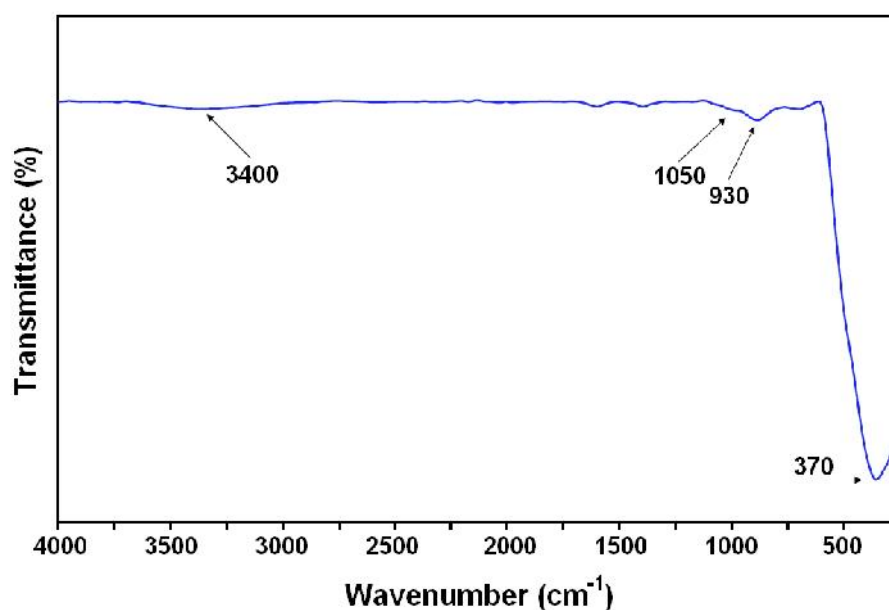


Figure 4.14: The FTIR patterns of the ZnO-NPs prepared by the solvothermal method at 150°C.

The XRD pattern of the ZnO-NPs prepared by the solvothermal process at 150°C for 18 h is shown in Figure 4.15. All detectable peaks can be indexed to ZnO wurtzite structure (PDF card no: 00-036-1451). The wurtzite lattice parameters were calculated from the *Lattice Geometry* equation. The (100) and (002) planes were used to

calculate the lattice parameters of the prepared ZnO-NPs, and the following values were obtained: $d_{(100)} = 0.2787 \pm 0.0002$ nm, $d_{(002)} = 0.2598 \pm 0.0002$ nm, $a=b= 0.3218 \pm 0.0005$ nm, $c= 0.5195 \pm 0.0005$ nm, $\varphi=90^\circ$, and $V= 46.58 \pm 0.02$ nm³.

The Scherrer equation: $D = (k\lambda/\beta_{hkl}\cos\theta)$, was used to determine The crystallite sizes of the ZnO-NPs where D is the crystallite size in nanometers (nm), λ is the wavelength of the radiation (1.54056 Å for CuK_α radiation), k is a constant equal to 0.94, β_{hkl} is the peak width at half-maximum intensity, and θ is the peak position. The (102) plane was chosen to calculate the crystallite size (either plane can be used for this purpose). The crystallite sizes of the ZnO-NPs prepared at 150°C for 18 h were observed to be 33 ± 2 nm.

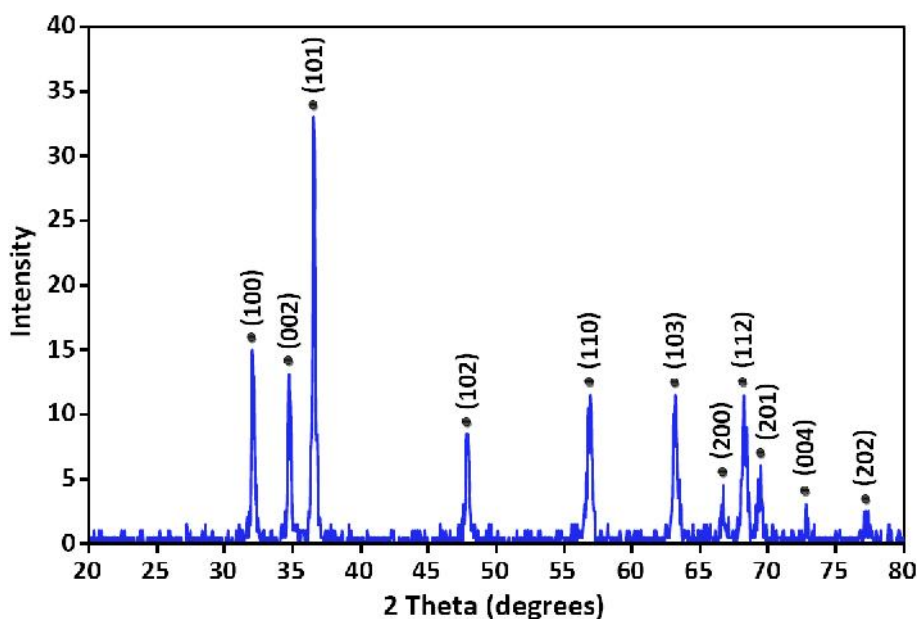


Figure 4.15: The XRD patterns of the ZnO-NPs prepared by the solvothermal method at 150°C.

The room temperature UV-Vis absorption spectra of ZnO-NPs are shown in Figure 4.16. The ZnO-NPs were dispersed in ethanol with concentration of 0.1% wt and then the solution was used to perform the UV-vis measurement. The spectrum reveals a characteristic absorption peak of ZnO at wavelength of 370 nm which can be assigned

to the intrinsic band-gap absorption of ZnO due to the electron transitions from the valence band to the conduction band ($O_{2p} \rightarrow Zn_{3d}$) (Yu et al., 2006). In addition, this sharp peak shows that the particles are in nano-size, and the particle size distribution is narrow. It is clearly shown that the maximum peak in the absorbance spectrum does not correspond to the true optical band gap of the ZnO-NPs. A common way to obtain the band gap from absorbance spectra is to get the first derivative of the absorbance with respect to photon energy and find the maximum in the derivative spectrum at the lower energy sides (Ebrahimizadeh Abrishami et al., 2010). The derivative of the absorbance of the ZnO-NPs is shown in the inset of Figure 4.16, and it indicates a band gap of 3.30 ± 0.01 eV for the ZnO-NPs. The good absorption of the ZnO-NPs in the UV region proves the applicability of this product in medical application such as sun-screen protectors or as antiseptic in ointments (Harding, 2006).

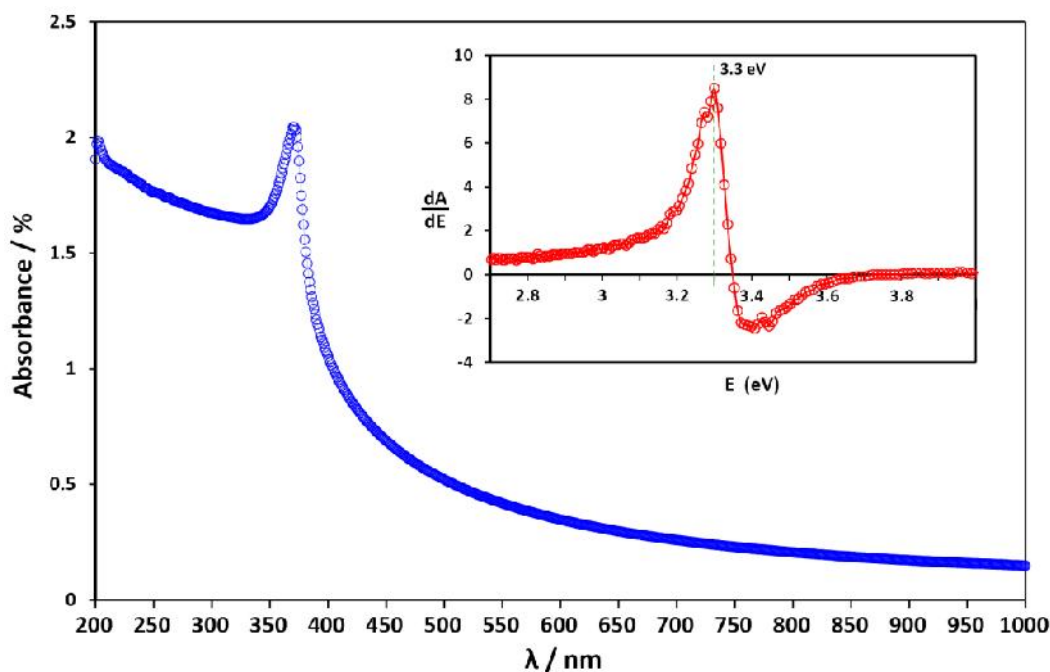


Figure 4.16: The UV-vis absorbance spectrum of ZnO-NPs from 200 nm to 1000 nm. Inset shows the derivative of the absorbance spectrum.

Figure 4.17 (a, b, and c) show the TEM, SEM, and size distribution of the ZnO-NPs prepared by the solvothermal method at 150°C for 18 h. The TEM, Figure 4.17(a),

exhibit that the ZnO-NPs have grown in a near-hexagonal shape, which demonstrates the good quality of the ZnO-NPs. Figure 4.17(b) shows the SEM micrograph of the ZnO-NPs at 150,000X magnification. The SEM figure indicates a homogeneous shape and size for ZnO-NPs. Also, it shows the ZnO-NPs are well dispersed in the powder form. The size histograms of the ZnO-NPs are shown in Figure 4.17(c). The histograms indicate that the main particle sizes of the ZnO-NPs made by the solvothermal method at temperature of 150°C for 6 h is about 48 ± 7 nm. The TEM, SEM, and size distribution results confirm that a narrow size distribution can be obtained for ZnO-NPs prepared by a solvothermal method using TEA as a polymerization agent, compared to some of the other results (Wang et al., 2010).

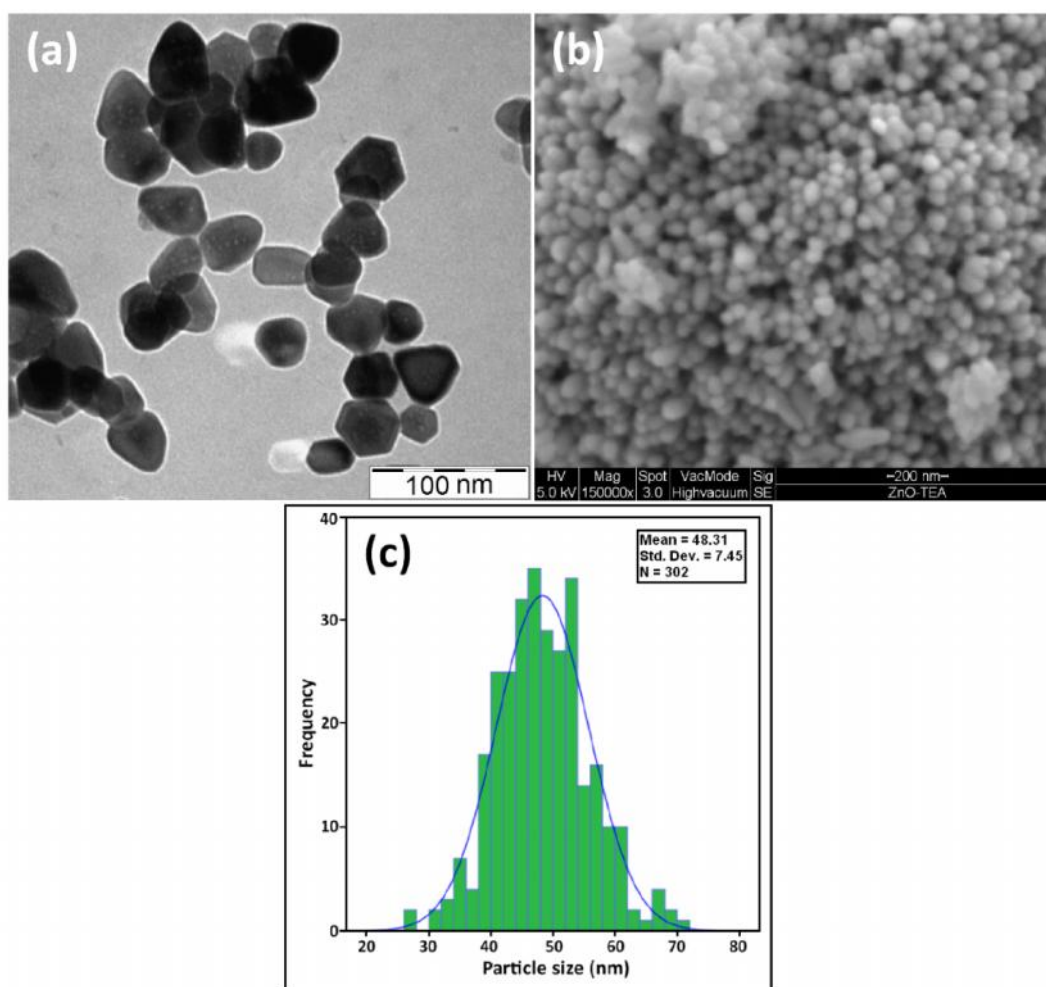


Figure 4.17: The TEM morphology image of ZnO-NPs (a), the SEM micrograph of the ZnO-NPs (b), and the particle size distribution of the ZnO-NPs (c).

In the solvothermal, alcohol plays a very important role in contributing the unoccupied oxygen to Zn^{+2} in order to form ZnO. The formed ZnO seeds are attracted to some of the TEA chains because of the ionic-dipolar interaction between the hydrogen atoms in the polymer and oxygen in the ZnO. The ZnO-NPs will grow with the association of the ZnO seeds. On the other hand, some of the TEA chains are attracted to each other by hydrogen-bonding forces. So, the growth of the particles will be eliminated, because the polymer chains do not permit the ZnO seeds to reach each other. The complete process is shown in Figure 4.18.

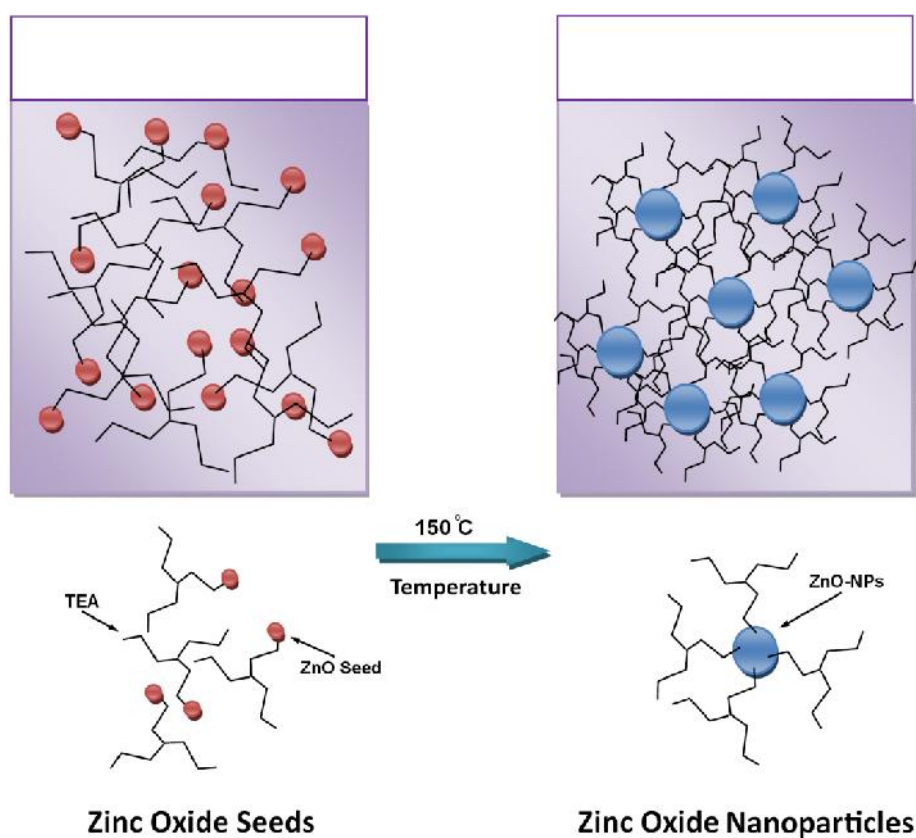


Figure 4.18: Schematic images of formation of the ZnO-NPs from the ZnO seed, and the role of TEA as a polymerization agent.

4.2.4.1. Effect of ethanolamine family on morphology of the ZnO nanostructures

Figure 4.19 (a, b, and c) Show the SEM and TEM micrograph of the ZnO nanostructures prepared by solvothermal method at 150 °C for 18 h using MEA, DEA, and TEA, respectively. The powders were dispersed in acetone by ultrasonic bath and then prepared for TEM. From Figure 4.19(a), both of the TEM and SEM images show freestanding ZnO nanoparticles for the sample that was prepared in MEA media. The SEM image in Figure 4.19(c) shows that the ZnO nanoparticles are sticking together but become easily separated after sonication, as shown in the TEM image of Figure 4.19(c). But the particles which were prepared in DEA media have retained their microsphere morphology, even after sonication as shown in the SEM and TEM images of Figure 4.19(b).

In formations of the ZnO-MNs, DEA chains acted as a bridge to form the ZnO-MNs and stopped the growth of the ZnO nanoparticles. This can even occur for the sample that was prepared in TEA media. The formed ZnO seeds are attracted to some of the TEA chains, due to the ionic-dipolar interaction between the hydrogen atoms in the polymer and the oxygen in the ZnO. The ZnO-NPs will grow with the association of the ZnO seeds. On the other hand, some of the TEA chains are attracted to each other by hydrogen-bonding forces. However, TEA has one O-H branch more than DEA. So, porous ZnO-MNs were formed by ZnO nanoparticles, because the polymer chains do not permit the ZnO nanoparticles to reach each other. That is why the nanoparticles are separated easily by sonication. In MEA media, the ZnO seeds became attached to the MEA from the OH end, but there is no bonding between the other ends of the MEA chains. Like before, The ZnO-NPs grow with the association of the ZnO seeds. When the number of reached ZnO seeds increases, the other seeds cannot reach the

nanoparticles. Therefore, the growth of nanoparticles will be eliminated. See Figure 4.20.

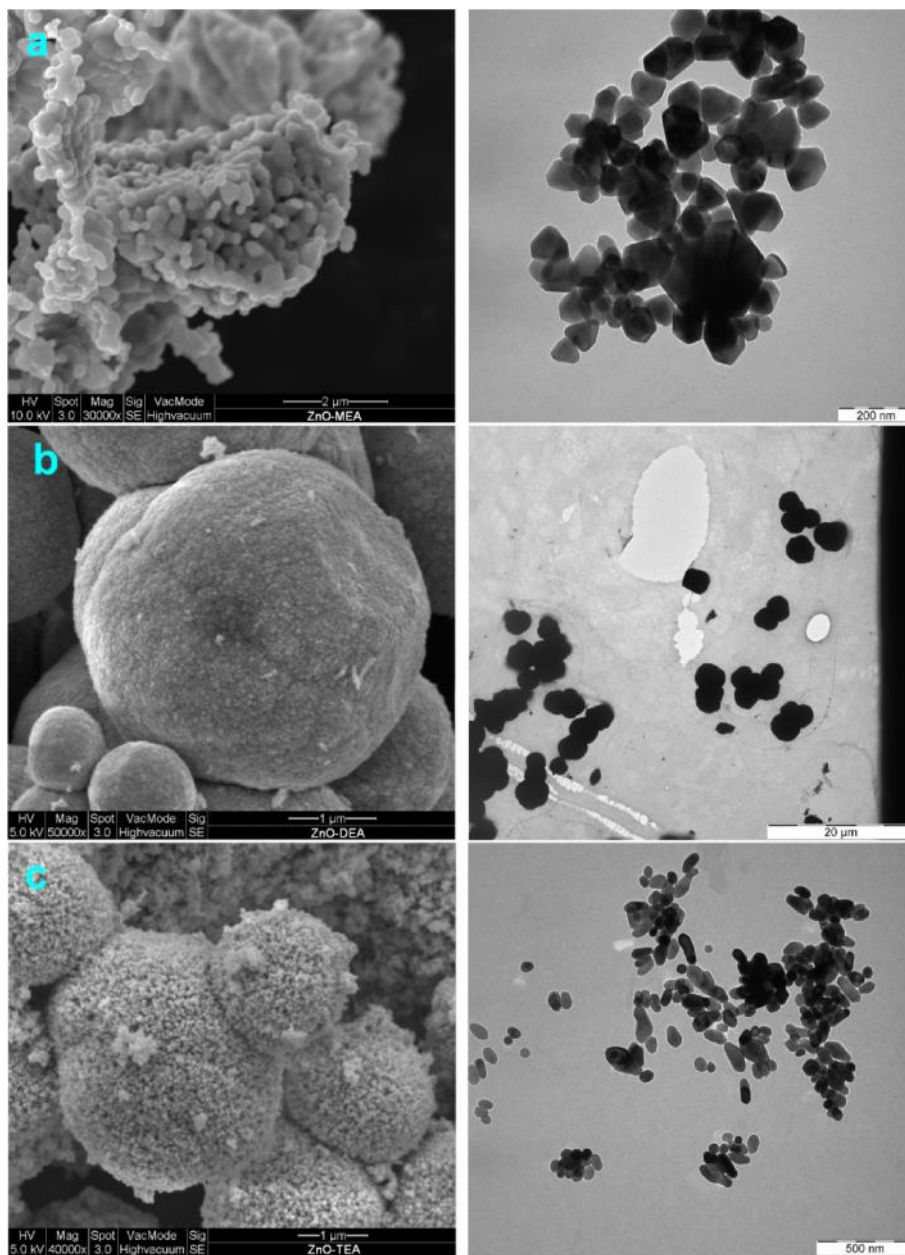


Figure 4.19: ZnO nanostructures prepared in different medias of (a) MEA, (b) DEA, (c) TEA.

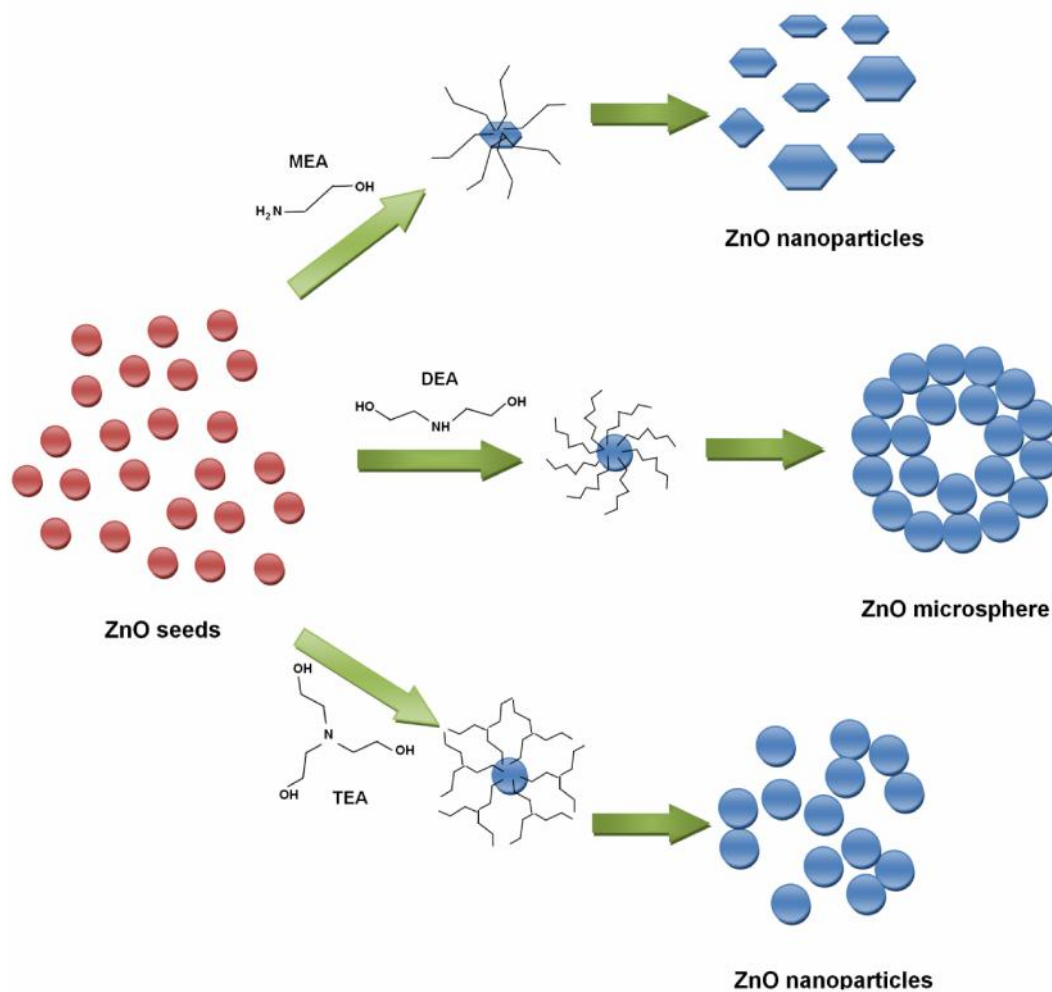


Figure 4.20: Schematic images to show the growth mechanism of the ZnO nanostructures in different medias of MEA, DEA, and TEA.

4.2.5. ZnO nanoparticles prepared by sonochemical method

The XRD patterns of the dried gel and ZnO-NS prepared at different times of 5, 15, 30, and 60 min are shown in Figure 4.21 (a, b, c, and d), respectively. Figure 4.21(a) shows XRD pattern for sample after 5 minutes ultrasonication which indicate both the Zn (OH)₂ and ZnO were presents. Whereas, all of the detectable peaks in Figure 4.21 (b, c, and d) can be indexed to the ZnO hexagonal structure (Ref. code: 00-036-1451) without any other peaks indicate that all the Zn (OH)₂ were converted to ZnO after 15 min ultrasonication. The hexagonal lattice parameters, for e.g. the values of d, the distances

between adjacent crystal planes (hkl) were calculated from the Bragg equation, $\lambda=2d \sin\theta$. The (100) and (002) planes were used to calculate the lattice parameters of the ZnO-NS prepared at different times of 15, 30, and 60 min. The changes in intensity of the peaks can be related to the different crystallite sizes and shape of the ZnO-NS produced at different ultrasonication times. The results of the XRD analysis were summarized in Table 4.4.

Table 4.4: The structure parameters of ZnO-NS prepared at different ultrasonication times of 15, 30, and 60 min.

<i>Compound</i>	<i>2θ</i> ±0.01	<i>hkl</i>	<i>d_{hkl}</i> (nm) ±0.0005	<i>Structure</i>	<i>Lattice parameter</i> (nm) ±0.0005	<i>V (nm³)</i> ±0.2	<i>Cos φ</i> ±0.002
ZnO nanorod (15 min)	31.92 34.57	(100) (002)	0.2801 0.2592	Hexagonal	a=0.3235 c=0.5185	46.98	0
ZnO flowers (30 min)	31.83 34.46	(100) (002)	0.2809 0.2600	Hexagonal	a=0.3244 c=0.5201	47.39	0
ZnO flowers (60 min)	31.97 34.63	(100) (002)	0.2797 0.2588	Hexagonal	a=0.3230 c=0.5176	46.76	0

The crystallite sizes of the ZnO-NS were determined by means of an X-ray line-broadening method using the Scherrer equation: $D = (k\lambda/\beta_{hkl}\cos\theta)$, where D is the crystallite size in nanometers, λ is the wavelength of the radiation (1.54056 Å for CuK α radiation), k is a constant equal to 0.94, β_{hkl} is the peak width at half-maximum intensity, and θ is the peak position. The (101) plane was chosen to calculate the crystallite size (either plane can be used for this purpose). The crystallite sizes of the ZnO-NS prepared at different times of 15, 30, and 60 min were found to be 30±2, 38±2, and 36±2 nm, respectively. According to these results, the crystallite size was increased as the ultrasonication time increased from 15 to 30 minutes but does not further increase after 30 minutes.

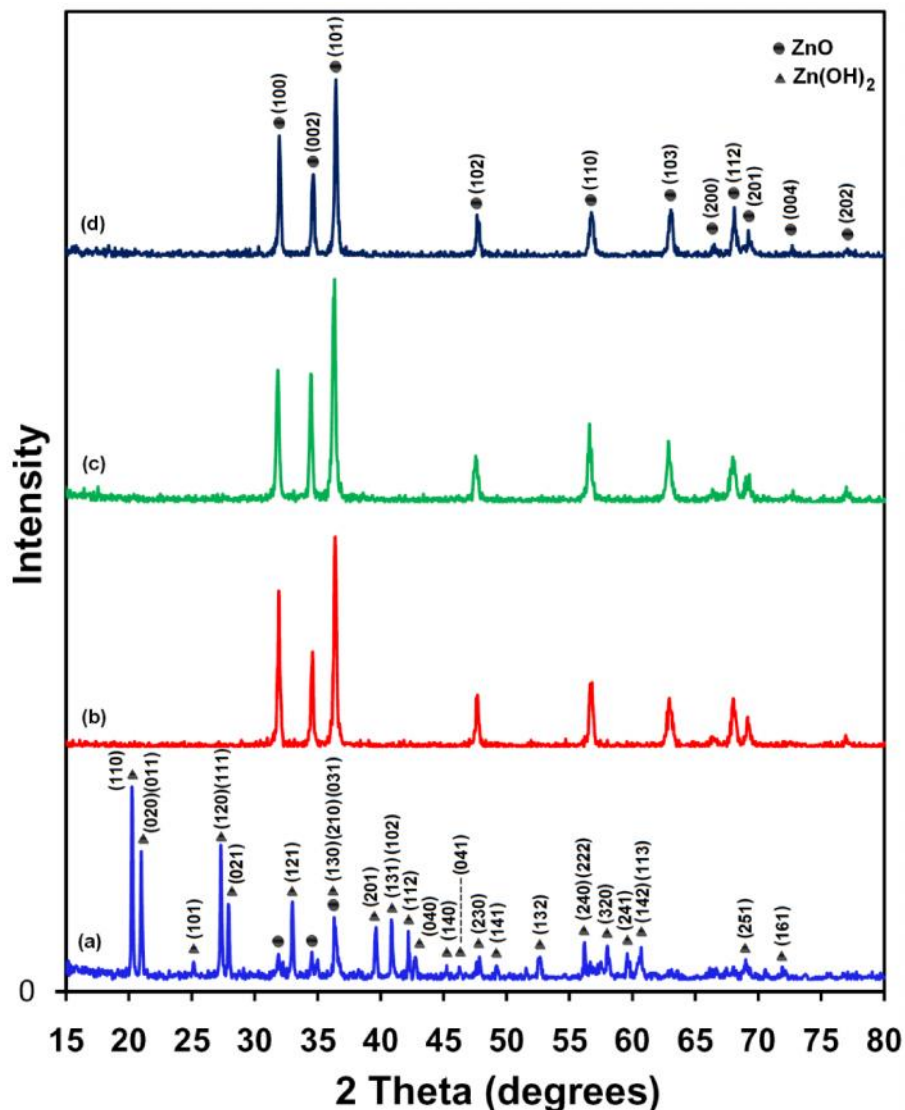


Figure 4.21: XRD patterns for samples prepared after various ultrasonication time (a) 5 minutes, (b) 15 minutes, (c) 30 minutes and (d) 60 minutes.

Figure 4.22a, b, c, and d shows the morphology of the Zn(OH)₂ and ZnO-NS prepared at different times of 5, 15, 30, and 60 min, respectively, while Figure 4.23a and b shows morphology of ZnO nanoflowers and nanorods from low to high magnifications. It was found that, the Zn(OH)₂ crystals were formed after 5 min ultrasonication whereas, ZnO nanorod with diameter around 50 nm and length of 5-8 μm were formed after 15 minutes of ultrasonication time. Both the TEM and SEM micrographs show ZnO nanorods with uniform size as shown in Figure 4.22b. Upon

increasing the ultrasonication time to 30 min, flower-like ZnO were formed (Figure 4.22c) but further increasing the ultrasonication time to 60 min does not change the morphology further but merely increase slightly the diameter of the nanoflower from 4 μm to 6 μm .

The nanorod and flower-like ZnO have been investigated more details under FESEM by varying the magnification as shown in Figure 4.23. It was found that for both nanorod and flower-like ZnO, the percentage of rod-like and flower-like shape in both samples is almost 100% as there are no other foreign shapes that can be found in these two images. This shows that the ZnO nanostructured material that we produce using this method is of very high quality. According to the FESEM images at high magnification in Figure 4.23 for the flower-like ZnO, it shows that it has hexagonal morphology, which indicates that the main growth direction of the ZnO is in [001] direction.

The formation of the ZnO flowers from ZnO nanorods can be described as below. When a ZnO nanorod was formed, the density of charges in each end of the rod will be increased which eventually contribute to the high aspect ratio of the ZnO nanorod as preferential growth is along the high density of charges. The longer the ZnO nanorod, the higher the charge density at each end of the nanorod until one point the nanorod fused together at one end of the rod to form flower shaped ZnO as shown in Figure 4.24.

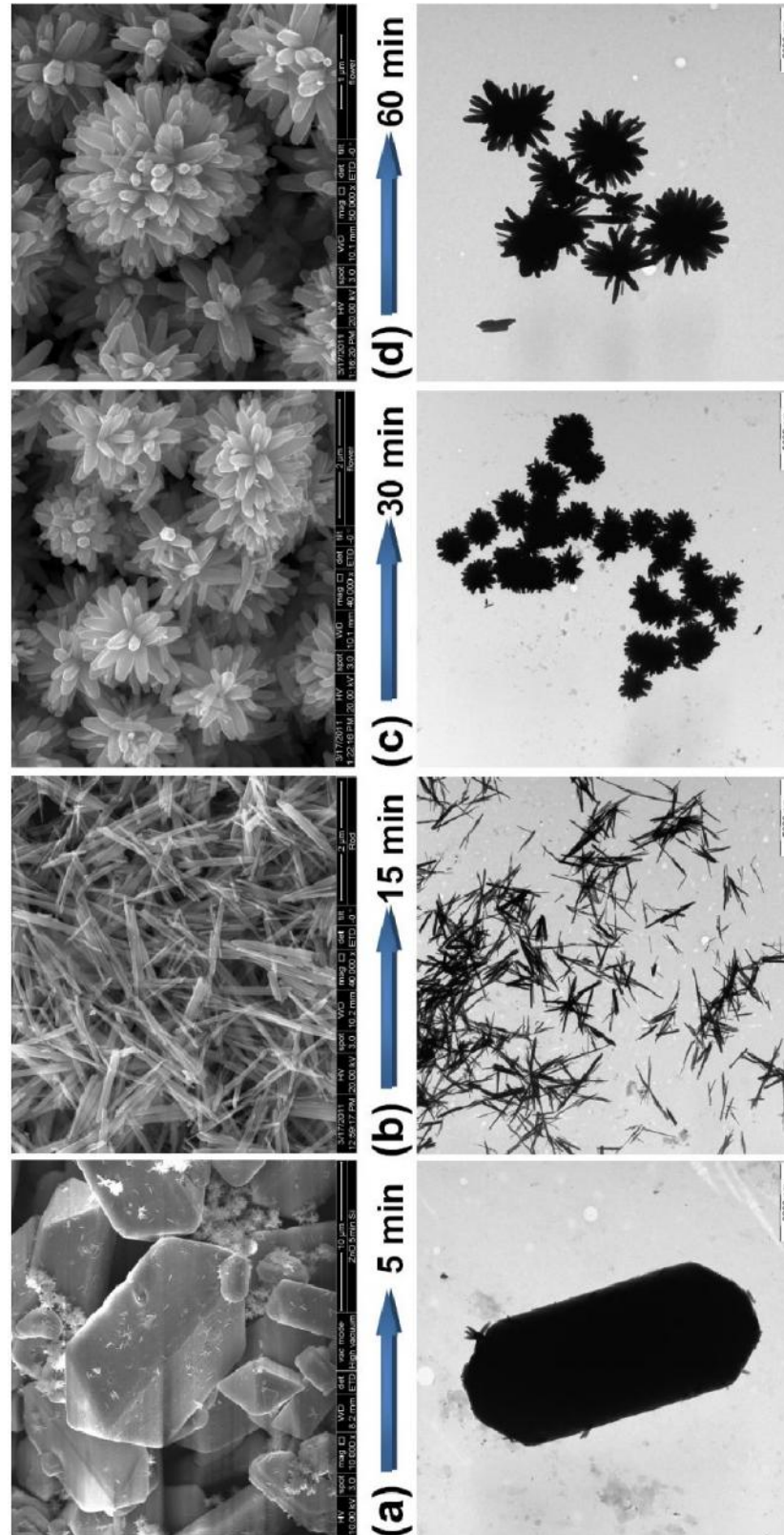


Figure 4.22: FESEM and TEM micrographs for (a) Zn(OH)₂ crystals, (b) ZnO nanorods, (c,d) ZnO flowers.

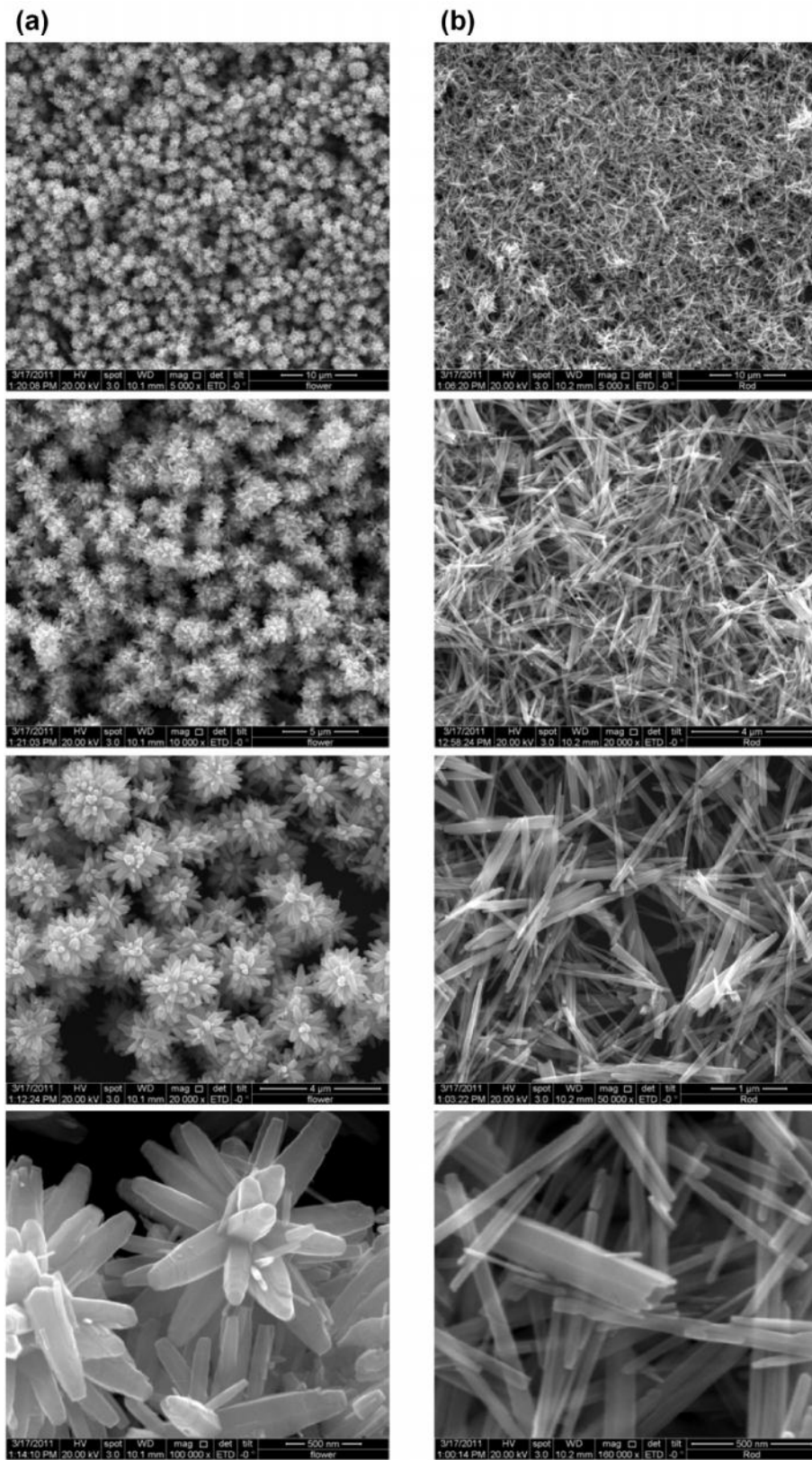


Figure 4.23: FESEM micrographs for ZnO nanorods (a) and nanoflowers (b) with varying magnification.

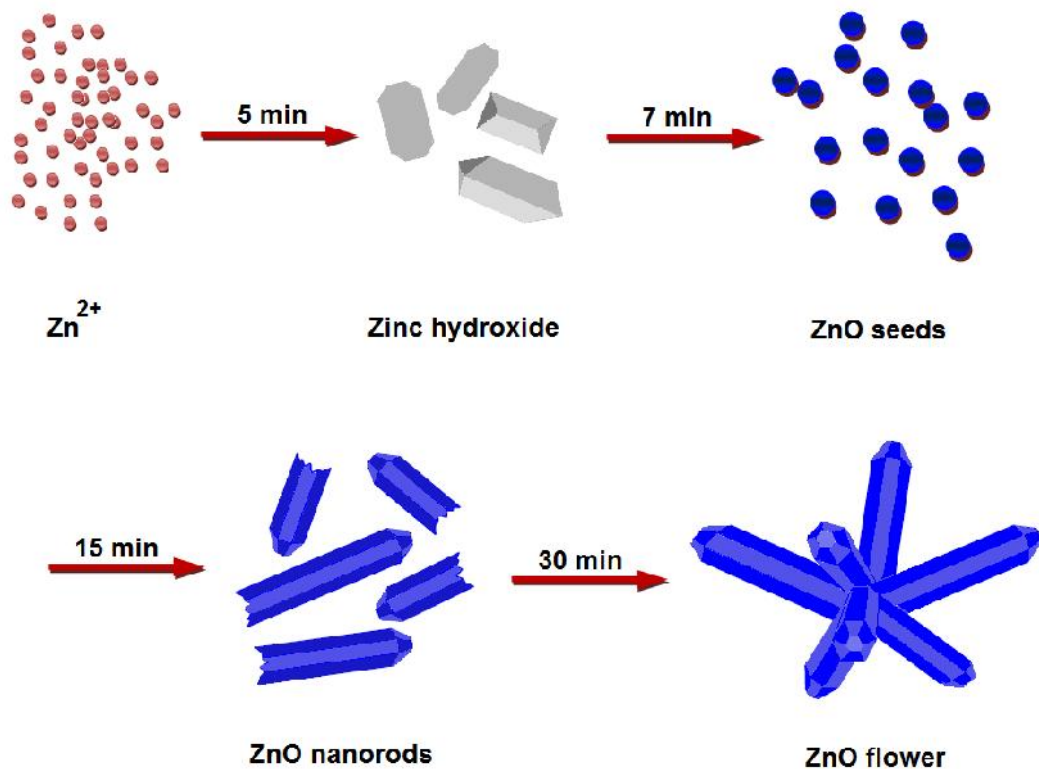


Figure 4.24: The $\text{Zn}(\text{OH})_2$ crystals are formed after 5 min ultrasonication. After about 7 min, ZnO nanoseeds are formed. The ZnO nanorods are formed by continuing the ultrasonication time to 15 min and by further ultrasonication times ZnO flowers are formed.

Figure 4.25 shows the morphology and crystal structure of the ZnO nano seeds that form the ZnO nanorods and flowers. The HRTEM image (see Figure 4.25c), FFT pattern (see Figure 4.25d), and SAED pattern (see Figures 4.26a and 4.26b) clearly show that the nodular structure is made of a lot of nanoscale particles which are around 2-4 nm in diameter. By the indexed SAED rings, the crystal structure of the nodular crystallite aggregates could be hexagonal ZnO phase with PDF No. 36-1451, which is consistent with the corresponding XRD result.

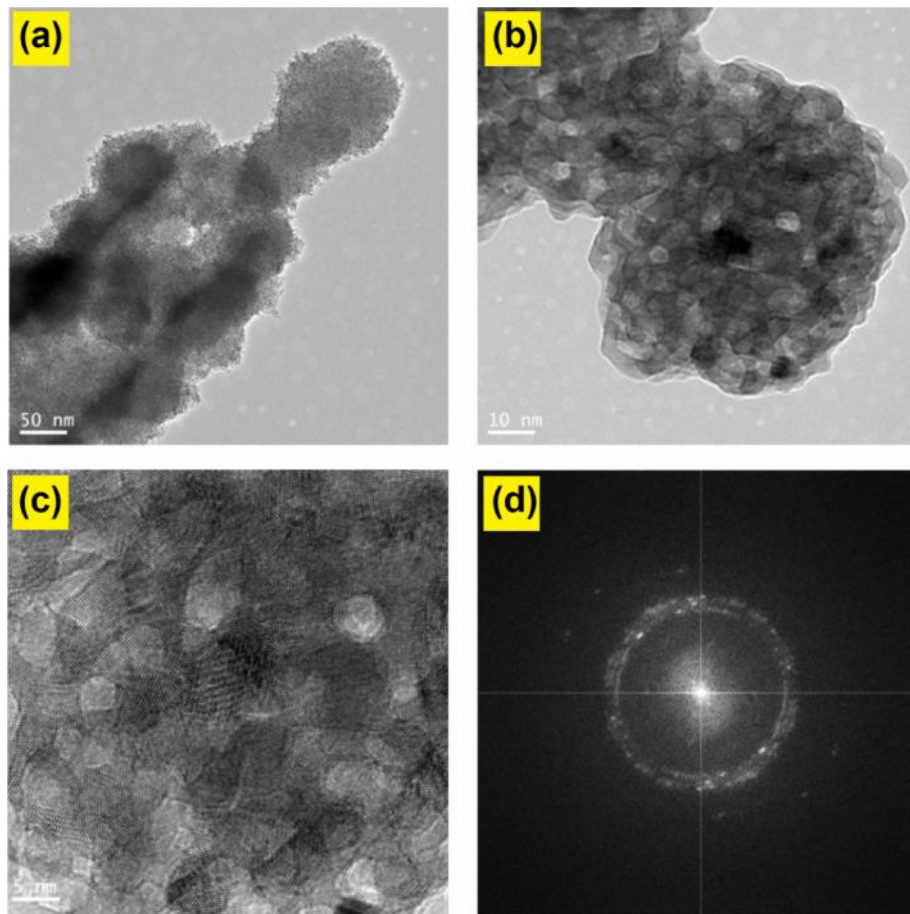


Figure 4.25: (a) End of a nodular structure, (b) Nanoscaled crystallites in the nodular, (c) Lattice image of the crystallites, (d) FFT pattern of (b) and (c).

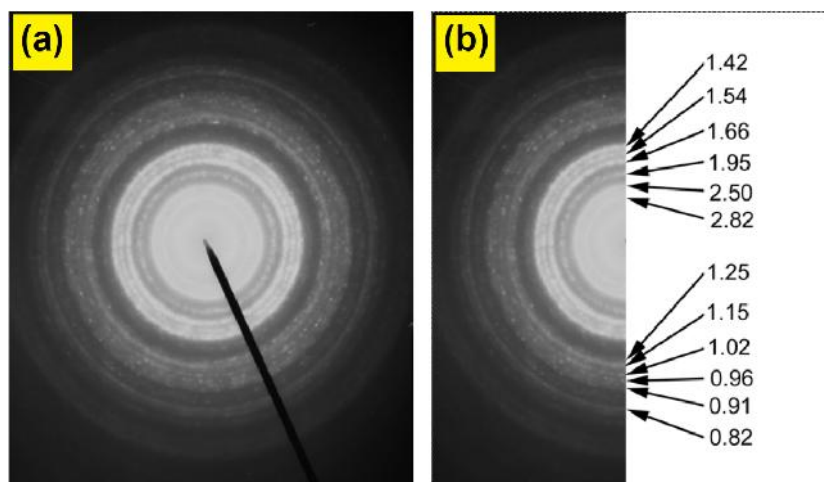


Figure 4.26: (a) SAED rings of Figure 4.25 (b) and (c), (b) Indexed SAED pattern of (a).

As shown in Figure 4.27a, these ZnO nanorods are mm-long and around 50 nm in diameter. Each nanorod has good crystal microstructure, supported by the crystal lattice images in Figures 4.27b, 4.27c, and 4.27d (4.27c, 4.27d came from the bottom left of the nanorod in 4.27b). The SAED (Figure 4.28a, 4.28c) and FFT (Figure 4.28b, 4.28d) patterns clearly show that the axial direction of the rod is along [0001] of wurtzite (hexagonal, $a = 0.325$ nm, $c = 0.52$ nm, which are in good agreement with XRD results) structure. This growth direction is consistent with previous report (see Fig. 3e in (Lao et al., 2003) and Fig. 2b in (Pan et al., 2001)). In these two references, the SAED patterns were indexed correctly, which are direct examples for the indexing of Figure 4.27d (inset) and Figures 4.28a and 4.28b.

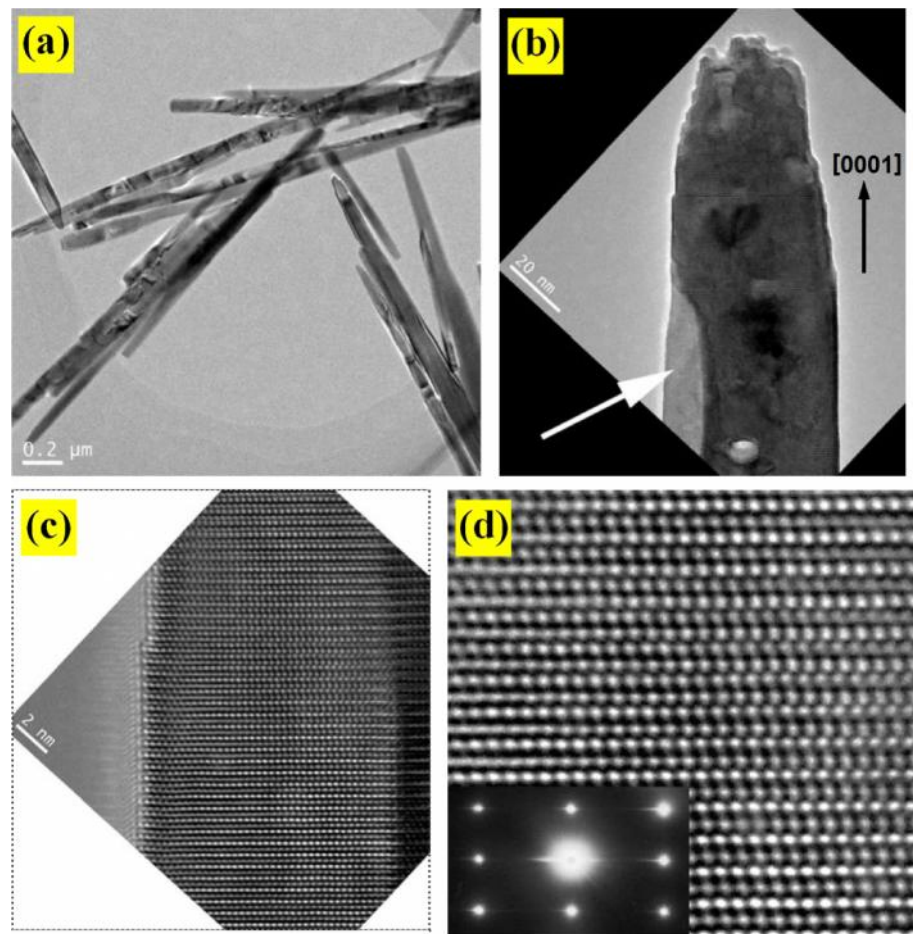


Figure 4.27: (a) TEM image of ZnO nanorod, (b) HRTEM image of ZnO nanorod, (c) Enlarged HRTEM image of (b), (d) Modified and enlarged lattice image of (c) and its SAED in inset.

Normally, one indexed SAED pattern is not enough to identify or confirm a kind of crystal structure (phase). Herein, Figure 4.28c and 4.28d were deliberately recorded by keeping the rod axis direction fixed and rotating the rod until a new SAED pattern was achieved. Accordingly, the “R2” directions in Figure 4.28b and 4.28d should be the same (along [0001]). By the way, the streaks (some horizontal lines) in Figure 4.28a were caused by the limited thickness of the nanorod (around 50 nm in diameter) – diffuse diffraction effect of thin crystals.

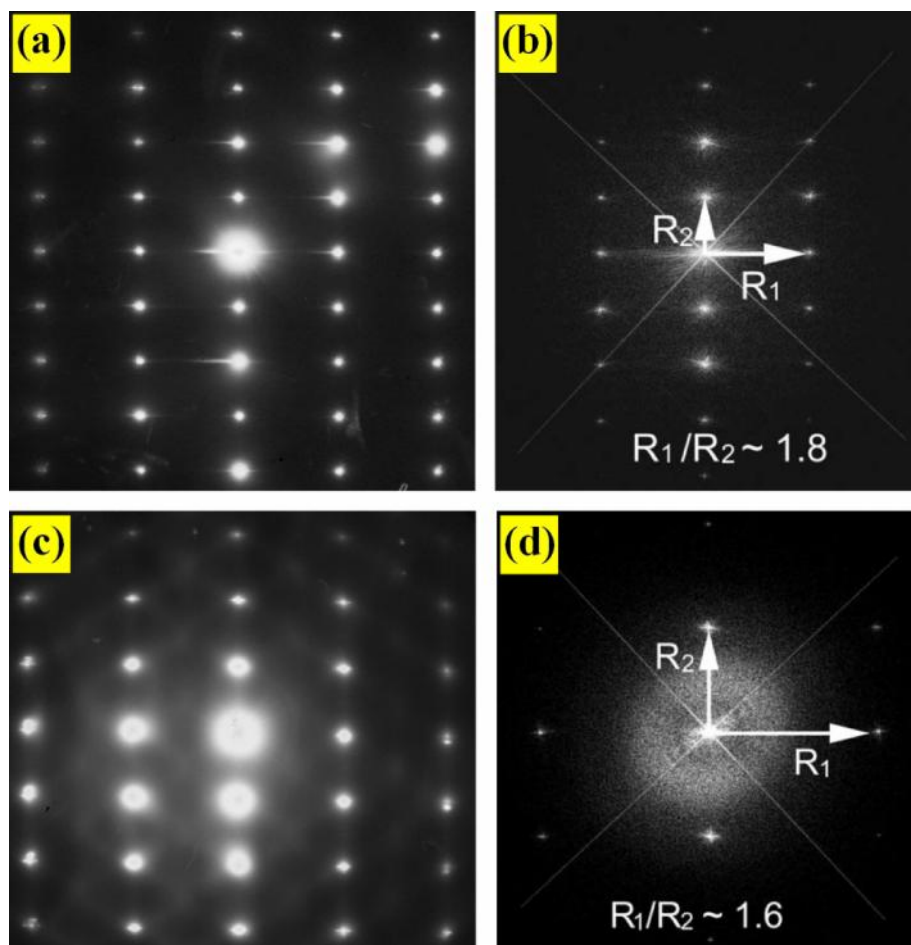


Figure 4.28: (a) [-2110] SAED pattern of Figure 4.27b, (b) FFT pattern of Figures 4.27b-4.27d, (c) Another SAED pattern of Figure 4.27b, (d) FFT pattern corresponding to (c).

The room temperature UV-Vis absorption spectra of ZnO-NS are shown in Figure 4.29. The ZnO-NS were dispersed in ethanol with concentration of 0.1% wt and then the solution was used to perform the UV-vis measurement. The spectrum reveals a characteristic absorption peak of ZnO at wavelength of 368, 378, and 380 nm for samples made in 15, 30, and 60 min respectively, which can be assigned to the intrinsic band-gap absorption of ZnO due to the electron transitions from the valence band to the conduction band ($O_{2p} \rightarrow Zn_{3d}$) (Yu et al., 2006).

It is clearly shown that the maximum peak in the absorbance spectrum does not correspond to the true optical band gap of the ZnO-NS. A common way to obtain the band gap from absorbance spectra is to get the first derivative of the absorbance with respect to photon energy and find the maximum in the derivative spectrum at the lower energy sides. The derivatives of the absorbance of the ZnO-NS are shown in the inset of Figure 4.29, and it indicates a band gap of 3.3, 3.22, and 3.2 eV for the ZnO-NS produced at 15, 30, and 60 min, respectively.

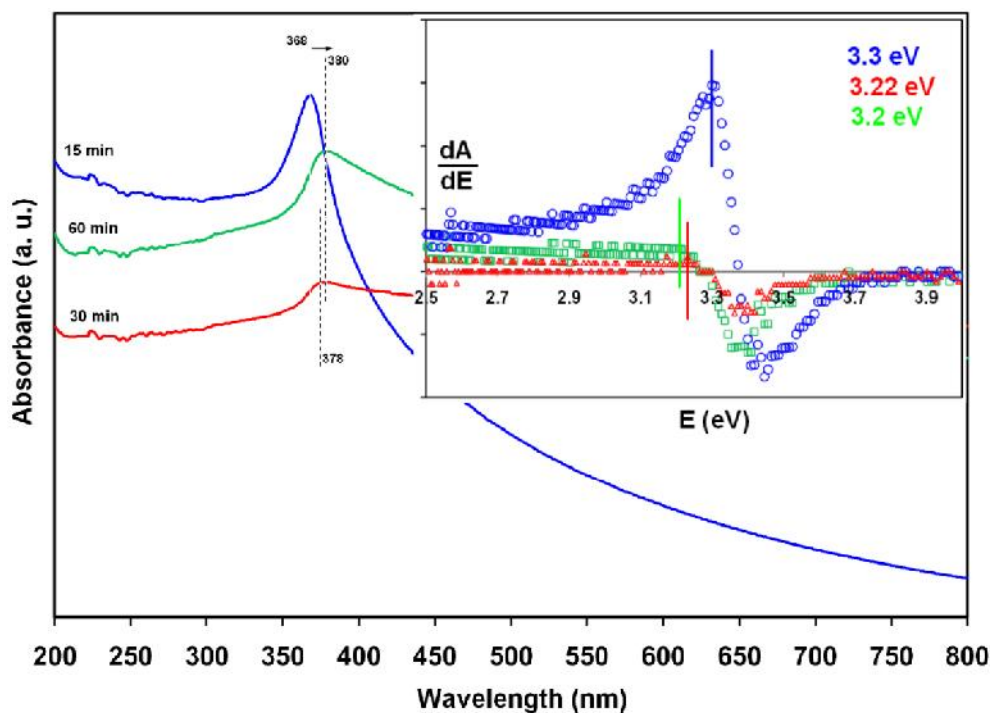


Figure 4.29: Uv-Visible absorption spectra for ZnO samples for 15 min, 30 min and 60 min.

4.3. PZT NANOPARTICLES

As mentioned in chapter 3, synthesis of the PZT nanoparticles are more complicated than ZnO nanoparticles and many defects may occur in the final product. The most important defect is lead vacancies in the lattice due to the evaporation of Lead during the calcination process. This problem extremely affects the properties of the PZT nanoparticles. In addition, it is very important to be sure about the purity of the final product. Therefore, it is more important to investigate the quality of the PZT nanoparticles after preparation process.

4.3.1. PZT nanoparticles prepared by sol-gel method using aqueous polyol solution

The thermal behavior of dried gel of PZT was characterized by using thermal analysis. The results of thermogravimetric analysis (TGA) and differential thermal analysis (DTA) are shown in Figure 4.30. The TGA-DTA curves had two major stages of weight loss in the range of 50- 900 °C, with weight loss about 61.4% of the total weight of the PZT gel. In addition, a small weight decrease of about 0.8% occurred in the range of 50- 130 °C, due to the elimination of residual water or volatile esters. Finally, when completing the decomposition reactions at 740 °C, no further weight loss or other chemical reactions were observed. In the DTA curve, two exothermal peaks were clearly observed at 380 and 440 °C. The first peak can be attributed to the decomposition of acetate, acetylacetonate (acac) groups and residues of PEG (Sriprang et al., 2000), and may be related to the formation of the pyrochlore phase. Perovskite

phase formation can also be observed from the next peak (Lenza and Vasconcelos, 2003, Sriprang et al., 2000).

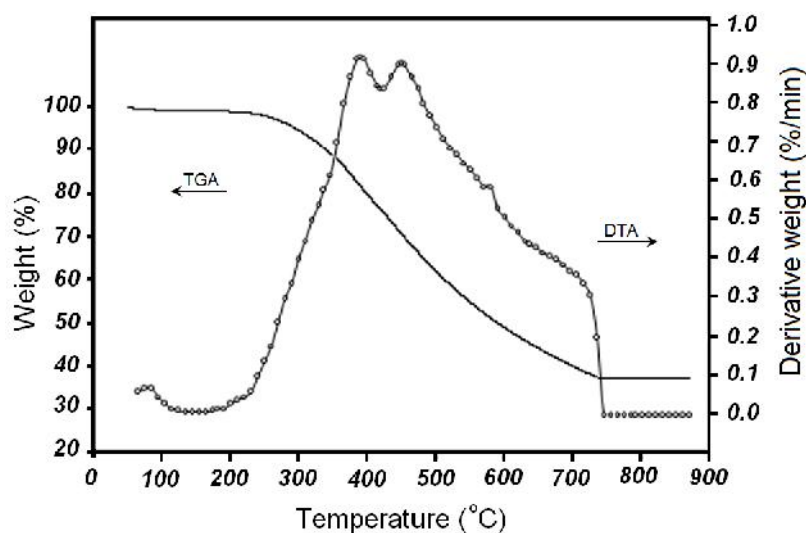


Figure 4.30: Thermal analyses (TGA-DTA) of xerogel of PZT.

The FTIR absorption spectra of PZT-NPs synthesized at different calcination temperatures were collected at room temperature from 4000 to 280 cm^{-1} , Figure 4.31. In these spectra, vibration peaks of metal-oxygen bands mainly appeared in the low frequency domain, about $280\text{--}700\text{ cm}^{-1}$. The band that appeared around 343 cm^{-1} is attributed to the vibrations of the M-O band, and the centered shoulder around 543 cm^{-1} is attributed to cyclic M-O-M structure (Zimmermann-Chopin and Auer, 1994). The vibration bands at 1053 and 1414 cm^{-1} are related to C-O bonds in the PEG structure (Wang et al., 2008). Moreover, the band at 1582 cm^{-1} represents the asymmetric stretching vibrations of carboxyl groups C=O, and the bands at 810 , 1414 and 3362 cm^{-1} are characteristic of the stretching bands of C-H. The mid band around 3362 cm^{-1} is attributed to the O-H groups in the matrix (Tu et al., 1996).

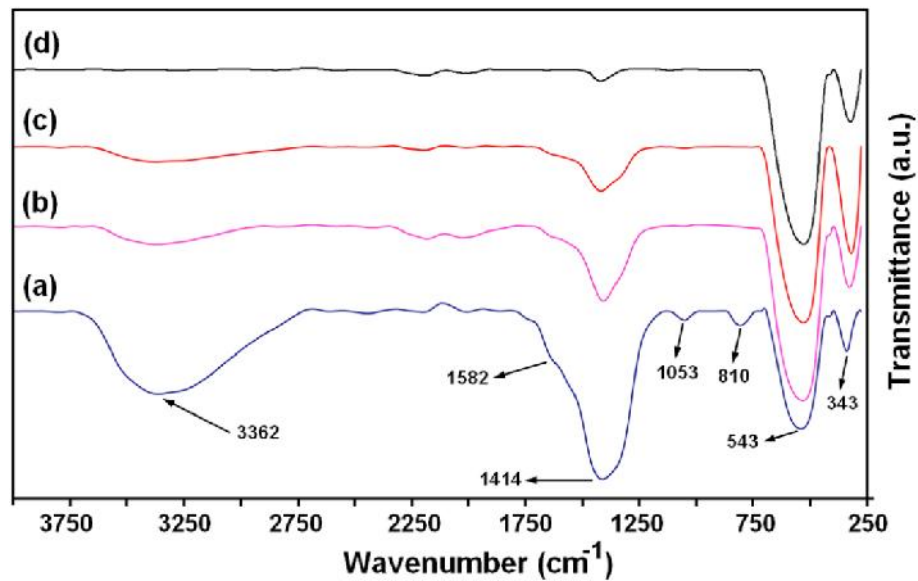


Figure 4.31: FTIR spectra of prepared PZT-NPs at different calcination temperatures for 2 h; 500 (a), 550 (b), 600 (c) and 650 °C (d).

The XRD patterns of calcinated PZT-NPs at different temperatures (500-650 °C) are shown in Figure 4.32. The preparation of the single PZT phase was started at calcination temperature of 550 °C with rhombohedral (R) crystal structure, and by increasing the calcination temperature to 600 °C, the rhombohedral phase was transformed to the tetragonal phase (T). The comparison of XRD results showed that the pyrochlore phase was completely removed at 650 °C and the pure perovskite phase of PZT-NPs is obtained at this temperature. This phase change can be related to surface effect (Gurin, 1998).

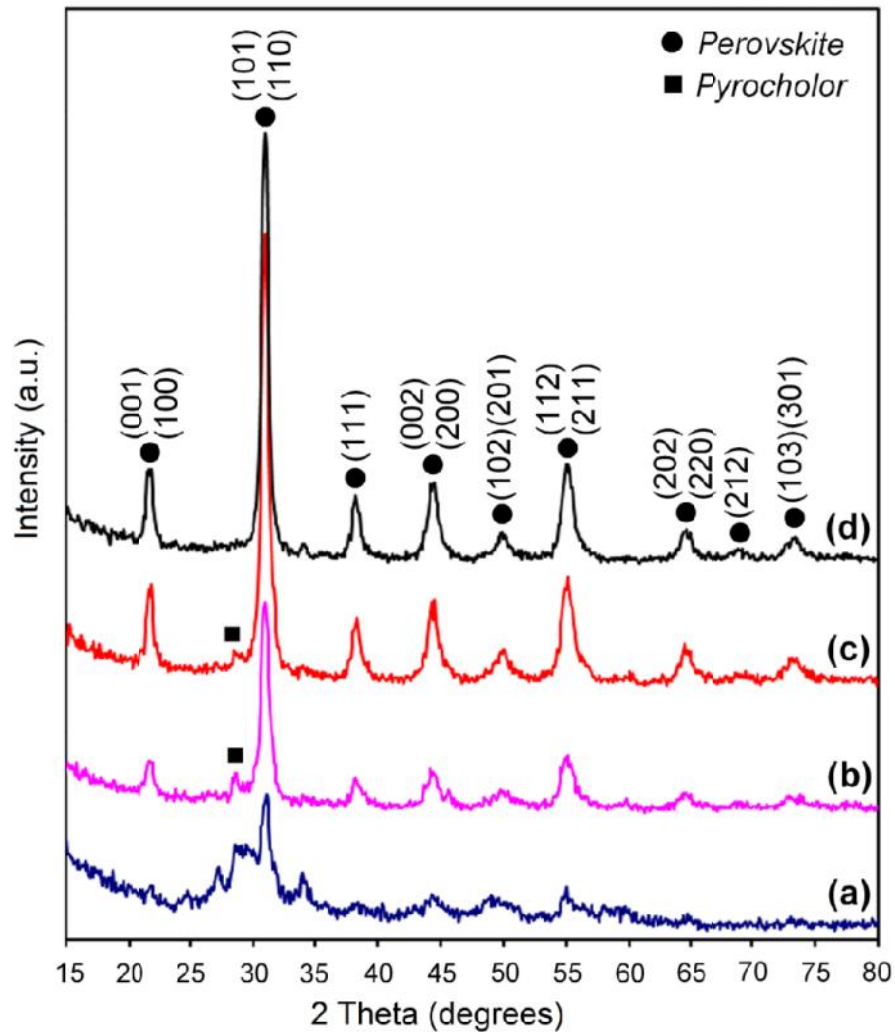


Figure 4.32: Typical XRD patterns of prepared PZT-NPs at different calcination temperatures for 2 h; 500 (a), 550 (b), 600 (c) and 650 °C (d).

The fraction of the atoms or the molecules located at the surface on the particles plays a great role, since they are more active than those inside the solid particles because of the free hand, which leads to easy bonding with the contacting materials and causes various changes in particle properties. The fraction of surface atoms of a 20 μ m cubic particle is only 0.006%, but it increases to 0.6% for a 200 nm particle and then it is estimated almost half of the atoms are situated at the surface of a 2 nm particle. On the other hand, as the micronization of solid particles, the specific surface area increases generally in reversal proportion to the particle size. In the above-mentioned case, when the particle of 1cm is micronized to 1 μ m and 10nm, the specific surface area becomes

ten thousand times and million times, respectively. As the increase in the specific surface area directly influences such properties like the solution and reaction rates of the particles, it is one of major reasons for the unique properties of the nanoparticles different from the bulk material together with the change in the surface properties of the particles itself. When the calcination temperature was increased the size of the PZT-NPs was increased and according to the above the structure of the particle was affected by atom of the surface (Gurin, 1998).

The lattice parameters of calcinated powders at different temperatures are summarized in Table 4.5. It can be observed that the average crystallite sizes increased with increasing calcination temperatures. The main crystallite size was found to be about 25 ± 2 nm for a sample that was calcinated in $650\text{ }^{\circ}\text{C}$ and free of the pyrochlore phase. A summary of the crystallite sizes of PZT-NPs calcinated at different temperatures is shown in Table 4.6.

Table 4.5: Lattice parameters of PZT-NPs prepared at different temperatures of (b) 550, (c) 600 and (d) 650 $^{\circ}\text{C}$ for 2 hrs.

<i>Temperature ($^{\circ}\text{C}$)</i>	<i>2θ ± 0.1</i>	<i>d_{hkl} (nm) ± 0.006</i>	<i>hkl</i>	<i>Structure</i>	<i>Lattice parameter (nm) ± 0.005</i>	<i>$V(\text{nm}^3)$ ± 0.2</i>	<i>Cos ϕ ± 0.002</i>
550	21.8 31	0.4074 0.2883	010 - 110	Rhombohedral	$a=b=c=0.4054$ $\alpha=90.08^{\circ}$	66.64	0.7154
600	21.7 21.9	0.4092 0.4055	001 100	Tetragonal	$a=b=0.4055$ $c=0.4092$ $c/a=1.009$	67.30	0.0
650	21.7 21.9	0.4092 0.4055	001 100	Tetragonal	$a=b=0.4055$ $c=0.4092$ $c/a=1.009$	67.30	0.0

Table 4.6: Average particle size of prepared PZT-NPs at different calcination temperatures for 2 h; 550 (a), 600 (b) and 650 °C (c).

Temperature (°C)	2θ (degrees)	FWHM (rad)	Size (nm)	Average crystallite size (nm)
550	31.0	7.87×10^{-3}	19.09	19 ± 2
	38.2	7.94×10^{-3}	19.30	
600	31.0	6.25×10^{-3}	24.05	24 ± 2
	38.3	6.16×10^{-3}	24.74	
650	31.0	5.71×10^{-3}	26.33	25 ± 2
	38.2	6.02×10^{-3}	25.45	
<i>Other Works:</i>				
450 (Liu et al., 2001)	31.1	-	-	35
350 (Jayasinghe et al., 2005)	27.8	-	-	50
650 (Lee and Jun, 2005)	15.01*	-	-	78
800 (Wang et al., 2008)	31.5	-	-	150
650 (Bruncková et al., 2004)	31.1	-	-	75
500 (Bel Hadj Tahar et al., 2007)	31	-	-	14.5

*The Molybdenum was used as a target in X-ray machine.

Figure 4.33 shows the SEM and TEM of PZT-NPs. After calcination, the powders have similar morphologies, and they consist of small agglomerates of fine particles that were easily broken after dispersal in ethanol by ultrasonic agitation. The TEM images show that the individual particles had size ~25 nm for PZT-NPs prepared at 650 °C.

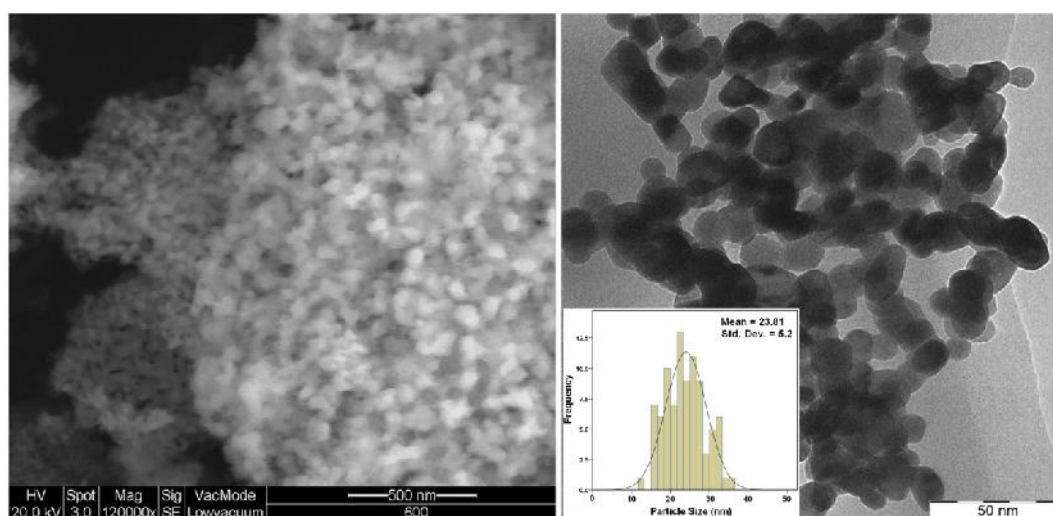


Figure 4.33: SEM and TEM micrographs of the prepared PZT-NPs calcinated at 650 °C (b) for 2 h.

4.3.1. PZT nanoparticles prepared by sol-gel method using 2-methoxyethanol

Figure 4.34 shows the results of thermogravimetric analysis, TGA, and differential thermal analysis, DTA. The TG curve descends until a horizontal is obtained around 620 °C. The horizontal curve obviously corresponds to the existence of PZT. The TG and DTA traces show three main regions. The first is an initial loss of water at around 60 °C, bend Ed₁, endothermic reaction, and corresponding 4.7 % weight loss. Then the decomposition of organic material occurs between 100 °C to 320 °C which corresponds to bend Ed₂, accompanied by a 17.439 % weight loss. Also, this important deflection at Ed₂, whose maximum is around 260 °C, is attributed to the formation of the pyrochlore phase and the initiation of crystallization of materials. Finally, the third deflection Ed₃ that occurs around 450 °C is related to the formation of the perovskite structure of PZT-NPs accompanied by 4.172 % weight loss (Bel Hadj Tahar et al., 2007). The horizontal curves of TG\DTA are achieved around 620°C, which indicates that the complete formation of the perovskite PZT-NPs is achieved at a furnace temperature of greater than 620 °C. The X-ray diffraction indicates that the perovskite structures are formed at around 650 °C, which agrees well with the TG\DTA results.

FTIR spectroscopy was used to study the transformation of basic material solutions during the thermal reactions, which leads to the perovskite PZT-NPs. The FTIR spectroscopy (in the range of 4000-280 cm^{-1}) of the PZT-NPs calcinated for 1 h at different temperatures of 600, 650 and 700 °C are presented in Figure 4.35. As in the case of other ABO_3 -type perovskite compounds, a broad band is observed for each spectrum from about 750 to 400 cm^{-1} , and another band from 400-300 cm^{-1} . These bands are related to B-O vibrations (BO_6 and B-O for ABO_3 structures). These results

confirm the formation of the pure perovskite structure of PZT-NPs at 700 °C (Last, 1957).

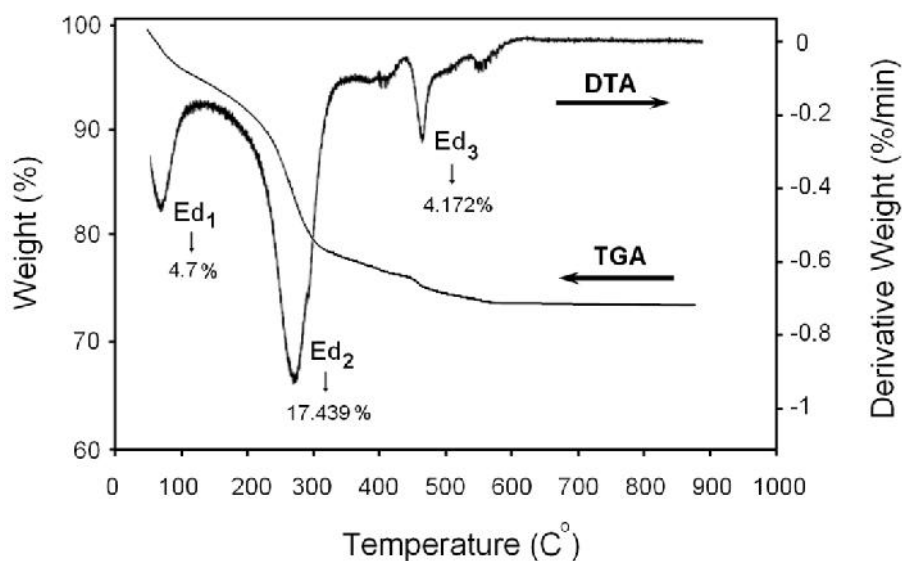


Figure 4.34: Thermal gravity and derivation analysis (TGA-DTA) of dried gel of PZT.

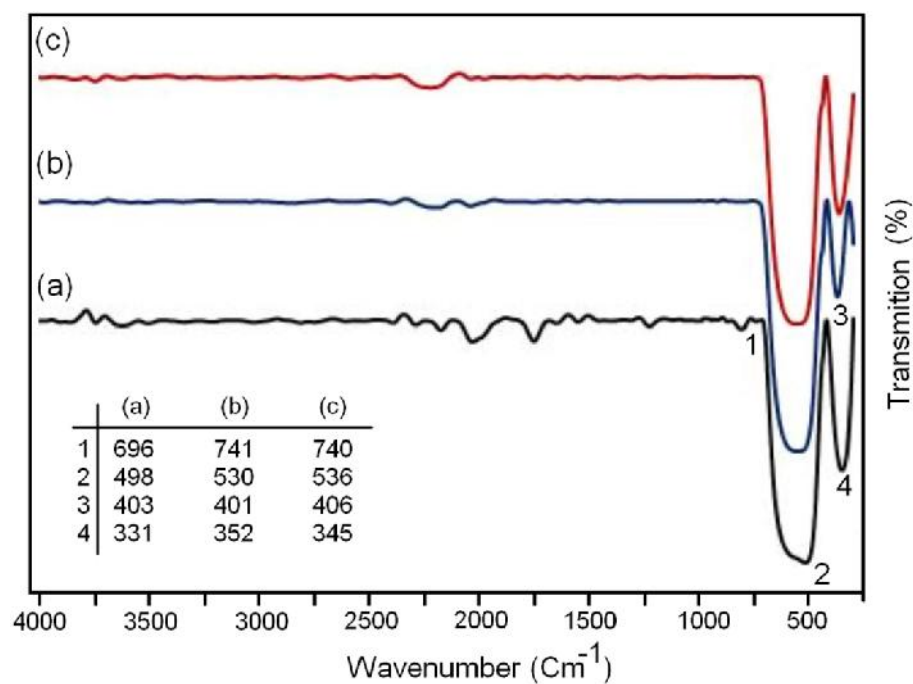


Figure 4.35: FTIR spectra of prepared PZT-NPs at different calcination temperatures for 1h; 600 (a), 650 (b) and 700 (c).

XRD patterns of PZT-NPs annealed for 1 h at different temperatures (600 °C, 650 °C and 700°C) are shown in Figure 4.36. At an annealing temperature of 600 °C, the PZT-NPs are predominantly in the rhombohedral phase, and there is also some pyrochlore phase. The rhombohedral phases are enhanced by increasing the annealing temperature to 650 °C, but at this stage a small amount of pyrochlore phase appears. At the annealing temperature of 700 °C, the pyrochlore phase disappears, while the pure rhombohedral phase is observed. The XRD results also reveal the existence of a perovskite-type phase for the PZT-NPs prepared by the sol-gel method for all temperatures. This result agrees well with the DTA measurement, which shows that the crystallization process is completed at about 650°C. The lattice parameters of powders calcinated at different temperature are summarized in Table 4.7.

Table 4.7: Lattice parameters of PZT-NPs prepared at different temperatures of 600, 650 and 700 °C for 1h.

<i>Temperature °C</i>	<i>2θ</i>	<i>d_{hkl} (nm)</i>	<i>hkl</i>	<i>Structure</i>	<i>Lattice parameter (nm)</i>	<i>V</i>	<i>Cos φ</i>
600	21.69 30.80	0.4094 0.2901	010 -110	Rhombohedral	$a=b=c= 0.4041$ $\alpha= 90.21766$	65.96	0.7303
650	21.70 30.87	0.4095 0.2894	010 -110	Rhombohedral	$a=b=c= 0.4092$ $\alpha= 90.0028$	68.51	0.7074
700	21.67 30.87	0.4098 0.2894	010 -110	Rhombohedral	$a=b=c= 0.4137$ $\alpha= 89.8455$	70.81	0.6911

The average crystallite size of PZT-NPs is determined by means of the X-ray line broadening method using the Scherrer equation. (110) peak is used for the rhombohedral specimen lines. It is observed that the average crystallite size increases as the calcination temperature increases. The average crystallite size is found about 14±2 nm, for a sample calcinated at 700 °C and free of pyrochlore phase. A summary of the average sizes of PZT-NPs calcinated at different temperatures is shown in Table 4.8.

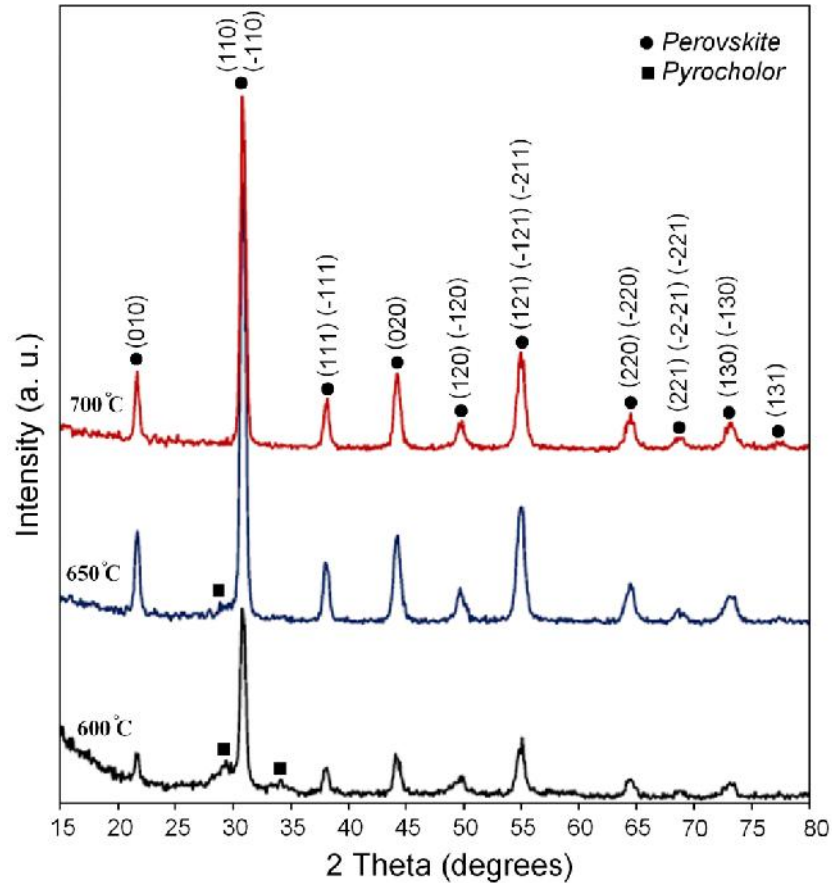


Figure 4.36: XRD patterns of PZT nanoparticles prepared at different calcination temperatures of 600, 650, and 700 °C.

Table 4.8: The diameter size of PZT-NPs obtained from different methods.

<i>Temperature (°C)</i>	<i>2θ (degrees)</i>	<i>FWHM (rad)</i>	<i>Size (nm)</i>	<i>Average size (nm)</i>
600	30.870	0.533	14.78	13.6±2
	44.176	0.721	12.42	
650	30.874	0.550	15.64	14.25±2
	44.229	0.697	12.85	
700	30.874	0.528	16.30	14.74±2
	44.242	0.680	13.17	

The typical TEM image of PZT-NPs calcinated at a temperature of 650 °C is shown in Figure 4.37. The figure shows that the PZT-NPs exhibit a narrow distribution and are almost spherical in shape. From TEM analysis, the primary particle size of PZT-NPs is found to be approximately 17 nm in diameter.

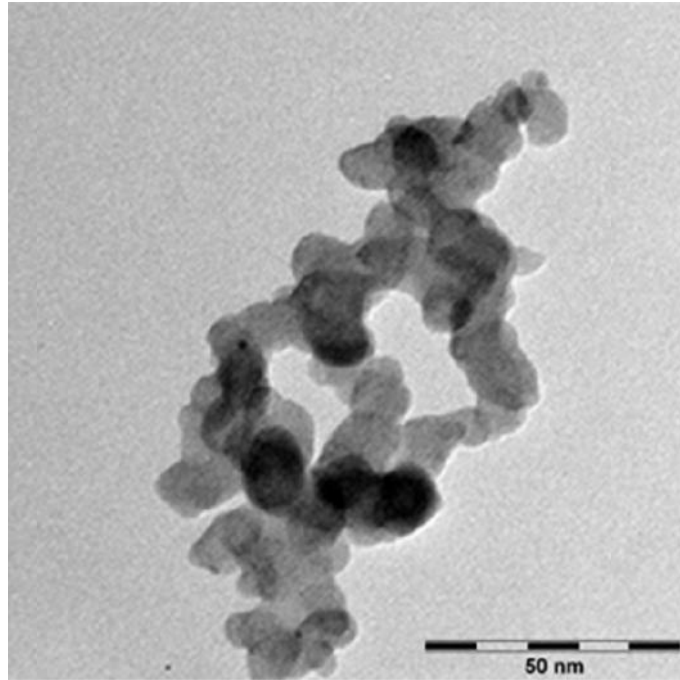


Figure 4.37: TEM micrograph of the prepared PZT-NPs at calcination temperatures of 650 °C for 1h.

4.4. SUMMARY

In this chapter the ZnO and PZT nanostructures that have been synthesized by different methods were investigated. The behavior of the gel and the quality of the achieved nanoparticles were studied by several techniques such as, Thermogravimetry, X-ray diffraction, Fourier transition infrared spectroscopy, ultraviolet-visible spectroscopy, transition electron microscopy and field emission scanning electron microscopy. According to the results, the nanostructures exhibited good quality and they can be used for further applications. The best results were related to ZnO nanoparticles which was prepared in gelatin media, ZnO nanostructures prepared by sonochemical method, and PZT prepared by sol-gel using 2-methoxyethanol. These nanostructures are homogenous and can be easily dispersed in liquids.

CHAPTER 5:

RESULTS AND DISCUSSIONS 2: THEORETICAL STUDIES AND APPLICATION PROPERTIES OF ZNO AND PZT NANOPARTICLES

5.1. INTRODUCTION

In this chapter, some theoretical methods such as Kramers-Kronig (K-K), Williamson-Hall (W-H), and Size Strain Plot (SSP) were used to study of the ZnO and PZT nanoparticles that prepared in this project. These studies give us a better understanding on the nanoparticles properties. In addition, some times it is complicated to calculate the some of the nanoparticles properties directly, thus, theoretical methods help to solve these problems. Here, Williamson-Hall, and Size Strain Plot have been used for investigating the mechanical properties of the nanoparticles. Whereas, Kramers-Kronig method has been used to calculate the optical properties of PZT nanoparticles.

5.2. X-RAY PEAK BROADENING ANALYSIS OF ZNO-NPS

This study was applied to the ZnO-NPs prepared by sol-combustion method at different temperatures of 650 °C and 750 °C for 2h (section 3.2.3). The powder X-ray diffraction was applied in the range of $2\theta = 20$ to 100° to obtain the structure properties of the ZnO-NPs and calculate their mechanical properties. The XRD patterns of the prepared samples are shown in Figure 5.1. All the detectable peaks could be indexed as the ZnO

wurtzite structure found in the standard reference data (PDF card no: 00-036-1451). It was clearly observed that the reflection peaks became sharper with the increases in the calcination temperature, indicating the enhancement of crystallinity. The wurtzite lattice parameters of the powders calcined at different temperatures are summarized in Table 5.1.

Table 5.1. The structure parameters of ZnO-NPs calcined at 650 °C and 750 °C.

<i>Temperature °C</i>	<i>2θ ±0.1</i>	<i>hkl</i>	<i>d_{hkl} (nm) ±0.006</i>	<i>Structure</i>	<i>Lattice parameter (nm) ±0.005</i>	<i>V (nm)³ ±0.2</i>	<i>Cos φ ±0.002</i>
650	67.9 69.0	(112) (201)	0.138 0.136	Hexagonal	a=0.322 c/a=1.656	47.99	0.8480
750	68.0 69.0	(112) (201)	0.138 0.139	Hexagonal	a=0.322 c/a=1.646	47.75	0.8479

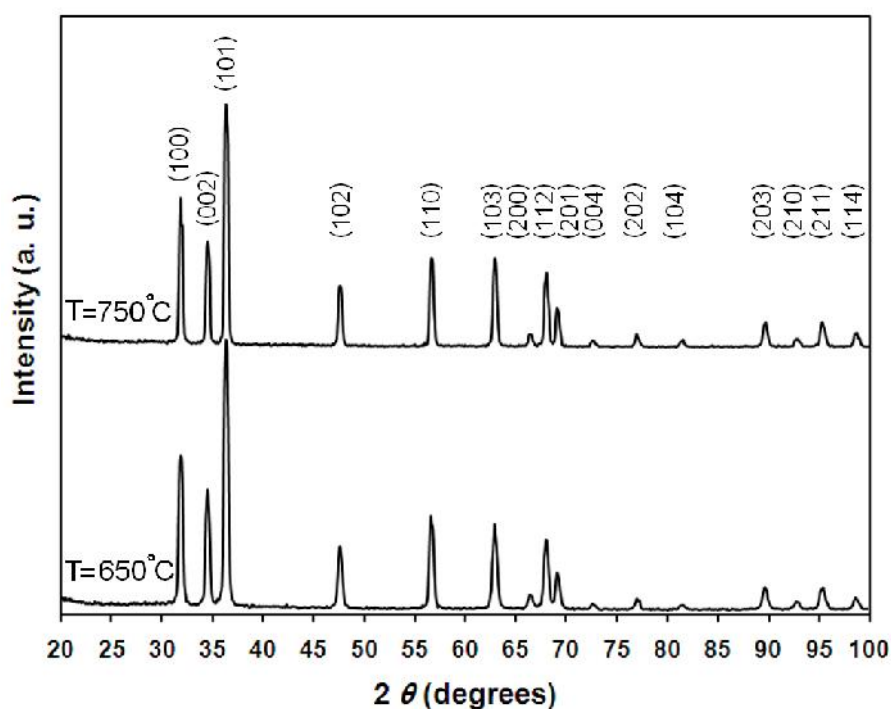


Figure 5.1: The XRD pattern of ZnO-NPs calcined at 650 °C and 750 °C. The XRD pattern shows that the sample product is crystallite with a hexagonal wurtzite phase and free from pyrochlore phases.

5.2.1. Average of Crystallite size calculation by Scherrer method

XRD can be utilized to evaluate peak broadening with crystallite size and lattice strain due to dislocation (Yogamalar et al., 2009). The crystallite size of the ZnO-NPs was determined by the X-ray line broadening method using the Scherrer equation: $D = (k\lambda/\beta_D \cos\theta)$, where D is the crystallite size in nanometers, λ is the wavelength of the radiation (1.54056 Å for CuK $_{\alpha}$ radiation), k is a constant equal to 0.94, β_D is the peak width at half-maximum intensity and θ is the peak position. The breadth of the Bragg peak is a combination of both instrument- and sample-dependent effects. To decouple these contributions, it is necessary to collect a diffraction pattern from the line broadening of a standard material such as silicon to determine the instrumental broadening. The instrument-corrected broadening (Rogers and Daniels, 2002) β_D corresponding to the diffraction peak of ZnO was estimated using the relation:

$$\beta_D^2 = [(\beta^2)_{measured} - \beta_{instrumental}^2] \Rightarrow \quad (5 - 1)$$

$$D = \frac{k\lambda}{\beta_D \cos\theta} \Rightarrow \cos\theta = \frac{k\lambda}{D} \left(\frac{1}{\beta_D} \right) \quad (5 - 2)$$

Plots were drawn with $1/\beta_D$ on the x -axis and $\cos\theta$ along the y -axis for the ZnO-NPs prepared at different temperatures such that the preferred orientation peaks of ZnO with the wurtzite hexagonal phase appeared between $2\theta=20^\circ$ and 100° . By fitting the data, the crystallite size D was extracted from the slope of the fit line; see Figure 5.2.

5.2.2. Mechanical properties calculations of ZnO-NPs by W-H methods

Strain-induced broadening arising from crystal imperfections and distortion are related by $\varepsilon \approx \beta_s / \tan \theta$. A remarkable property of Equation (5-2) is the dependency on the diffraction angle θ . The W-H method does not follow a $1/\cos \theta$ dependency as in the Scherrer equation but instead varies with $\tan \theta$. This fundamental difference allows for a separation of reflection broadening when both micro structural causes – small crystallite size and micro strain – occur together. The different approaches presented in the following assume that size and strain broadening are additive components of the total integral breadth of a Bragg peak (Birkholz, 2006). The distinct θ dependencies of both effects laid the basis for the separation of size and strain broadening in the analysis of Williamson and Hall. Addition of the Scherrer equation and $\varepsilon \approx \beta_s / \tan \theta$ results in following equations:

$$\beta_{hkl} = \beta_s + \beta_D \quad (5 - 3)$$

$$\beta_{hkl} = \left(\frac{k\lambda}{D \cos \theta} \right) + (4\varepsilon \tan \theta) \quad (5 - 4)$$

Rearranging Equation (7) gives:

$$\beta_{hkl} \cos \theta = \left(\frac{k\lambda}{D} \right) + (4\varepsilon \sin \theta) \quad (5 - 5)$$

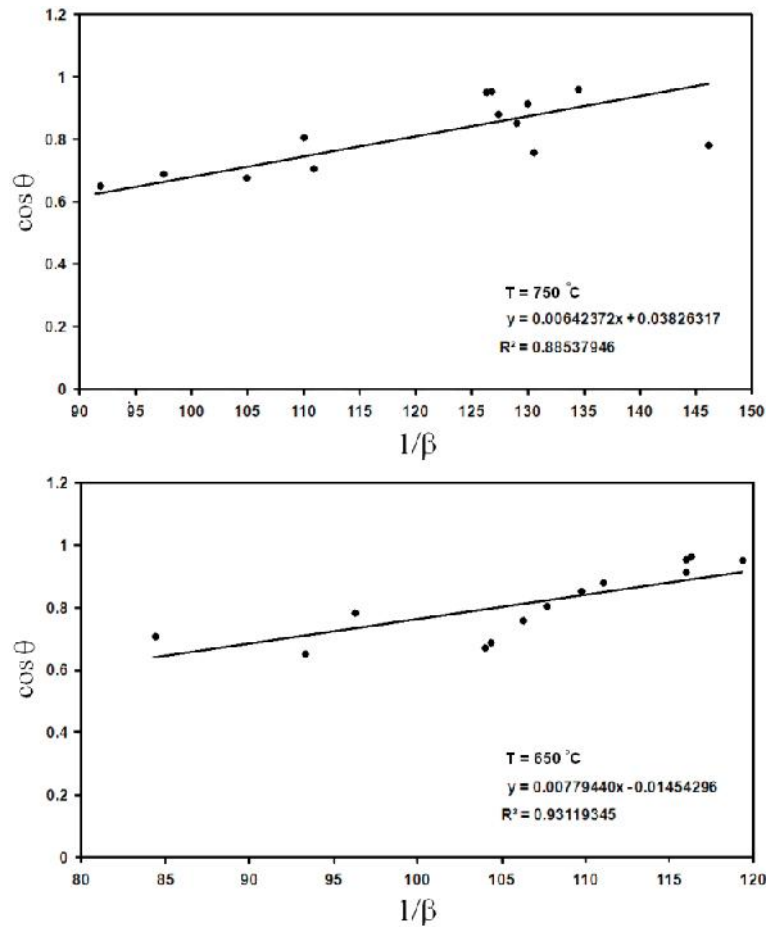


Figure 5.2: Sherrer plots of ZnO-NPs calcined at 650 °C and 750 °C. Fit to the data, the crystallite size D is extracted from the slope of the fit.

Equation (5-5) represents the uniform deformation model (UDM), where the strain was assumed uniform in all crystallographic directions, thus considering the isotropic nature of the crystal, where all the material properties are independent of the direction along which they are measured. The term $(\beta \cos \theta)$ was plotted with respect to $(4 \sin \theta)$ for the preferred orientation peaks of ZnO-NPs with the wurtzite hexagonal phase. Accordingly, the slope and y-intersect of the fitted line represent strain and crystallite size, respectively. The plots showed a negative strain for the ZnO-NPs. This strain may be due to the lattice shrinkage that was observed in the calculation of lattice parameters. The results of the UDM analysis for the ZnO-NPs are shown in Figure 5.3.

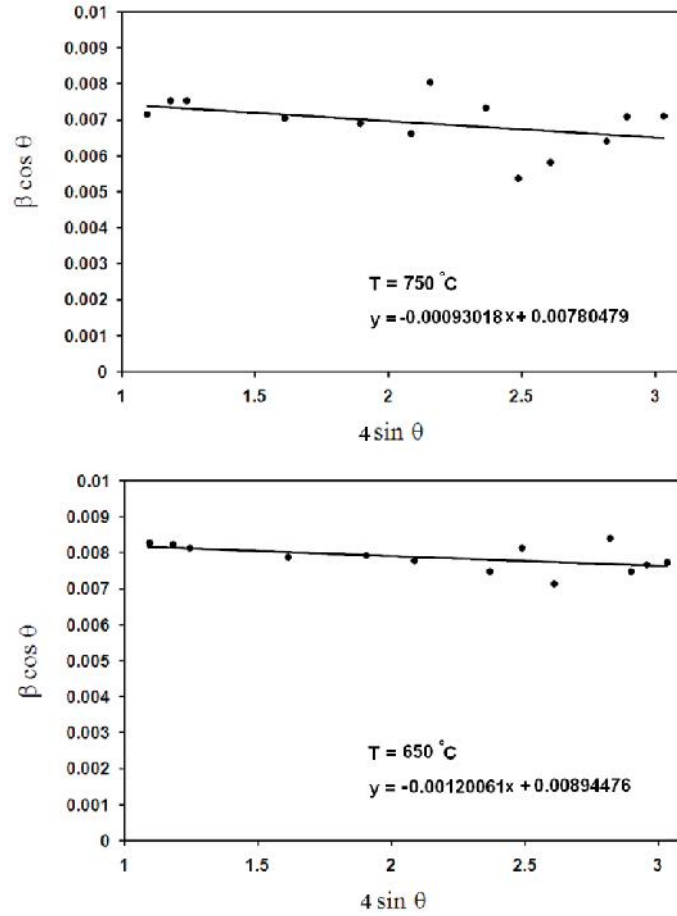


Figure 5.3: The W-H analysis of ZnO-NPs calcined at 650 °C and 750 °C assuming UDM. Fit to the data, the strain is extracted from the slope and the crystallite size is extracted from the y-intercept of the fit.

In the Uniform Stress Deformation Model, USDM, a generalized Hooke's law refers to the strain, keeping only the linear proportionality between the stress and strain as given by $\sigma = Y\varepsilon$, where σ is the stress of the crystal and Y is the modulus of elasticity or Young's modulus. This equation is merely an approximation that is valid for a significantly small strain. Assuming a small strain to be present in the ZnO-NPs, Hooke's law can be used here. With a further increase in strain, the particles deviate from this linear proportionality. Applying the Hooke's-law approximation to Equation (5-5) yields:

$$\beta_{hkl} \cos \theta = \left(\frac{k\lambda}{D} \right) + \left(\frac{4 \sigma \sin \theta}{Y_{hkl}} \right) \quad (5 - 6)$$

For a hexagonal crystal, the following relation, (Zhang et al., 2006a) gives Young's modulus:

$$Y_{hkl} = \frac{\left[h^2 + \frac{(h+2k)^2}{3} + \left(\frac{al}{c}\right)^2 \right]^2}{s_{11} \left(h^2 + \frac{(h+2k)^2}{3} \right)^2 + s_{33} \left(\frac{al}{c}\right)^4 + (2s_{13} + s_{44}) \left(h^2 + \frac{(h+2k)^2}{3} \right) \left(\frac{al}{c}\right)^2} \quad (5 - 7)$$

where s_{11} , s_{13} , s_{33} , s_{44} are the elastic compliances of ZnO with values of 7.858×10^{-12} , -2.206×10^{-12} , 6.940×10^{-12} , $23.57 \times 10^{-12} \text{ m}^2\text{N}^{-1}$, respectively (Nye, 1985). Young's modulus, Y , for hexagonal ZnO-NPs was calculated as $\sim 130 \text{ GPa}$. Plots were drawn with $(4 \sin \theta)/Y_{hkl}$ on the x -axis and $\beta_{hkl} \cos \theta$ on the y -axis for the ZnO-NPs calcined at different temperatures. The USDM plots for ZnO-NPs calcined at 650° C and 750° C are shown in Figure 5.4. The stress calculated from the slope of the fitted line is slightly greater for the ZnO-NPs calcined at 650° C than for those at 750° C .

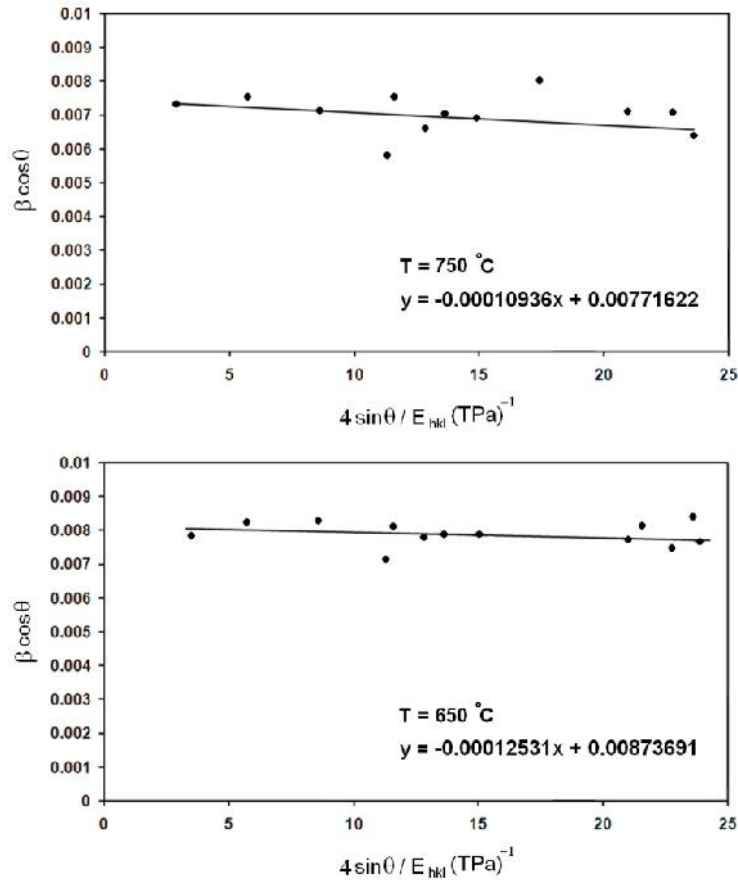


Figure 5.4: The modified form of W-H analysis assuming USDM for ZnO-NPs calcined at 650° C and 750° C .

There is another model that can be used to determine the energy density of a crystal called the Uniform Deformation Energy Density Model, UDEDM. In Equation (5-6), the crystals are assumed to have a homogeneous, isotropic nature. However, in many cases, the assumption of homogeneity and isotropy is not justified. Moreover, the constants of proportionality associated with the stress–strain relation are no longer independent when the strain energy density u is considered. For an elastic system that follows Hooke's law, the energy density u (energy per unit) can be calculated from $u = (\varepsilon^2 Y_{hkl})/2$. Then Equation (5-6) can be rewritten according the energy and strain relation.

$$\beta_{hkl} \cos \theta = \left(\frac{k\lambda}{D} \right) + \left(4 \sin \theta \left(\frac{2u}{Y_{hkl}} \right)^{1/2} \right) \quad (5 - 8)$$

Plots of $\beta_{hkl} \cos \theta$ versus $4 \sin \theta (2u/Y_{hkl})^{1/2}$ were constructed and the data fitted to lines. The anisotropic energy density u was estimated from the slope of these lines, and the crystallite size D from the y -intercept; see Figure 5.5. Previously, we had $\sigma = \varepsilon Y$ and $u = (\varepsilon^2 Y_{hkl})/2$, where the stress σ was calculated as $u = (\sigma^2/2Y_{hkl})$. The results of these plots show a slight change in energy density of the ZnO-NPs with increasing calcination temperature.

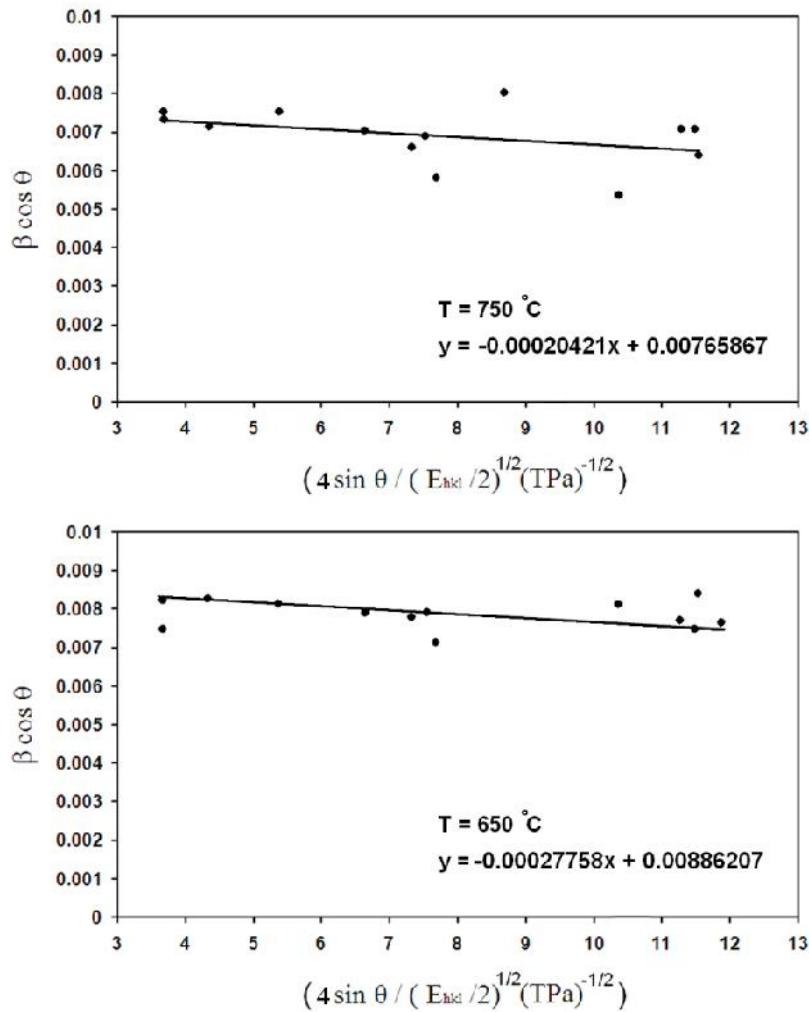


Figure 5.5: The modified form of W-H analysis assuming UDEDM for ZnO-NPs calcined at 650 °C and 750 °C. Fit to the data, the density of energy is extracted from the slope and the crystallite size is extracted from the y-intercept of the fit.

5.2.3. Mechanical properties calculations of ZnO-NPs by SSP method

The corresponding Williamson–Hall plot showed that line broadening was essentially isotropic. This indicates that the diffracting domains were isotropic and there was a micro strain contribution. However, in cases of isotropic line broadening, a better evaluation of the size-strain parameters can be obtained by considering an average “size-strain plot” (SSP), which has the advantage that less weight is given to data from reflections at high angles, where the precision is usually lower. In this approximation, it is assumed that the “crystallite size” profile is described by a Lorentzian function and

the “strain profile” by a Gaussian function, (Tagliente and Massaro, 2008).

Accordingly, we have:

$$(d_{hkl}\beta_{hkl} \cos \theta)^2 = \frac{K}{D} (d_{hkl}^2 \beta_{hkl} \cos \theta) + \left(\frac{\varepsilon}{2}\right)^2 \quad (5 - 9)$$

Where K is a constant that depends on the shape of the particles; for spherical particles it is given as $\frac{3}{4}$. In Figure 5.6, similarly to the W-H methods, the term $(d_{hkl}\beta_{hkl} \cos \theta)^2$ is plotted with respect to $(d_{hkl}^2 \beta_{hkl} \cos \theta)$ for the all orientation peaks of ZnO-NPs with the wurtzite hexagonal phase from $2\theta=15^\circ$ to $2\theta=100^\circ$. In this case, the crystallite size is determined from the slope of the linearly fitted data and the root of the y-intercept gives the strain.

5.2.4. TEM analysis of the ZnO-NPs

TEM micrographs are the best way to investigate nanoparticle size and shape. Figure 5.7 displays a TEM image of the ZnO-NPs. It was observed that the morphology of the ZnO-NPs was spherical and with a smooth surface. The typical micrographs consisted of an assembly of ZnO-NPs with an average diameter of 20 ± 2 nm. A nonuniform strain was also observed that for some of the particles, as shown in Figure 5.7. This is in close agreement with the results obtained from the powder XRD measurements.

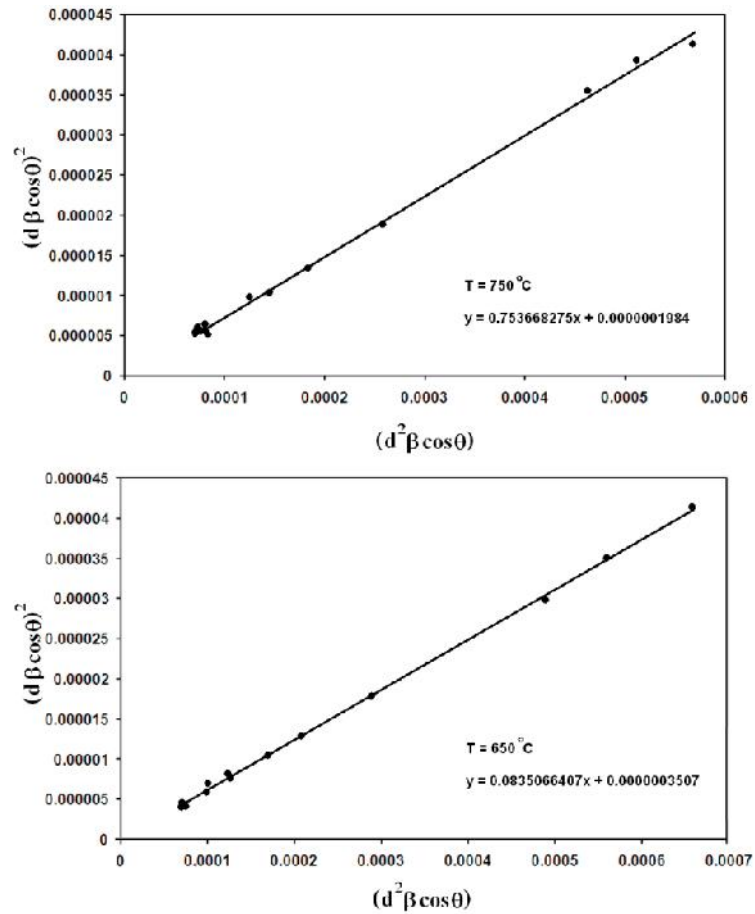


Figure 5.6: The SSP plots of ZnO-NPs calcined at 650 °C and 750 °C. The particle size is achieved from the slop of the liner fitted data and the root of y-intercept gives the strain.

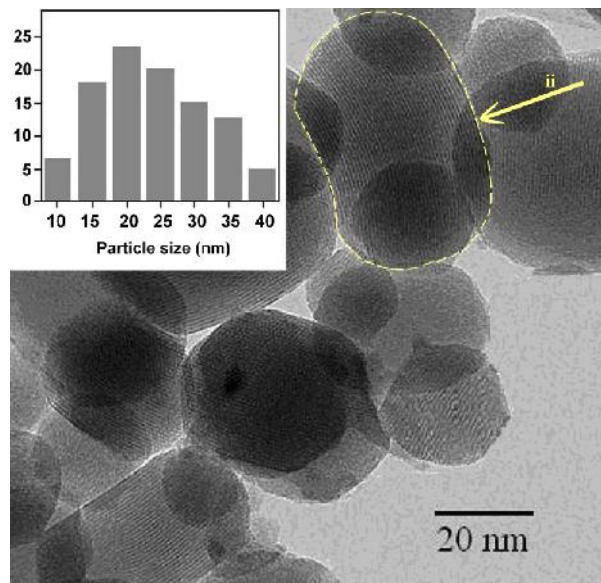


Figure 5.7: TEM micrographs of ZnO-NPs calcinated at 750 °C. This figure shows a nonuniform strain for some of the ZnO-NPs (ii as an example). The size distribution and abundance of the ZnO-NPs was shown in the inset.

The results obtained from the Scherrer method, UDM, USDM, UDEDM, SSP models and TEM are summarized in Table 5.2. The values of average crystallite size of the ZnO-NPs obtained from the different models are more or less similar, implying that the inclusion of strain in various forms has a very small effect on the average crystallite size of ZnO-NPs. However, the average crystallite size obtained from the Scherrer formula and the W–H analysis (see Table 5.2) shows a greater variation because of the difference in averaging the particle-size distribution. By inspection of the plots, it appears that the result of the SSP model was more accurate than the UDM, USDM and UDEDM methods, as the data were fitted more accurately in this method, with all data points touching the fitting line.

Table 5.2: Geometric parameters of ZnO-NPs calcined at 650 °C and 750 °C.

<i>Sample</i>	<i>Scherrer method</i>	<i>Williamson-Hall method</i>									<i>Size-Strain Plot method</i>				<i>TEM</i>
		<i>UDM</i>		<i>USDM</i>			<i>UDEM</i>				<i>D</i>	ε	σ	<i>u</i>	
		<i>D</i> (nm) ± 0.05	ε $\pm 0.0005 \times 10^{-3}$	<i>D</i> (nm) ± 0.05	ε $\pm 0.0005 \times 10^{-3}$	σ (MPa) ± 0.05	<i>D</i> (nm) ± 0.05	ε $\pm 0.0005 \times 10^{-3}$	σ (MPa) ± 0.05	<i>u</i> (KJm ⁻³) ± 0.005					
650 °C	18.58	16.19	1.2006	16.57	0.9867	125.31	16.34	1.1015	139.90	77.051	15.97	1.1843	150.41	89.681	-
750 °C	22.54	18.55	0.9302	18.77	0.8611	109.36	18.91	0.8104	102.92	41.702	17.69	0.8908	113.13	50.393	~20

5.3. X-RAY PEAK BROADENING ANALYSIS OF PZT-NPS BY W-H METHODS

PZT-NPs were calcined at different temperatures of 650 °C and 700 °C. For the entire experiment, the plot is drawn only for the preferred orientation peaks of PZT with the rhombohedral phase. The lattice planes corresponding to those preferred peaks are (010), (110), (111), (020), (120), (121), (220), (221) and (130). From the linear fit to the data, the crystallite size D was extracted from the y-intercept and the strain ϵ from the slope of the fit, Figure 5.8(a). Equation (5-5) represents the uniform deformation model, UDM, where the strain was assumed to be uniform in all crystallographic directions, considering the isotropic nature of the crystal, where all the material properties are independent of the direction along which they are measured. The UDM for PZT-NPs calcined at 650 °C and 700 °C are shown in Figure 5.8(b) and summarized in Table 4.9. From this plot, it is clear that the strain and particle size of PZT-NPs calcined at 650 °C are less than the strain and particle size of PZT-NPs calcined at 700 °C.

Table 5.3: the crystallite size and strain of the PZT-NPs prepared at different temperatures.

<i>Temperature</i> °C	<i>Particle size</i>			
	<i>Scherrer method</i>	<i>W-H method</i>		<i>TEM</i>
	<i>D (nm)</i> ±0.05	<i>D(nm)</i> ±0.05	<i>ε(no unit)</i> ±0.005	<i>D(nm)</i> ±2
600	13.02	-	-	-
650	13.64	18.23	0.002	-
700	14.11	21.66	0.003	18

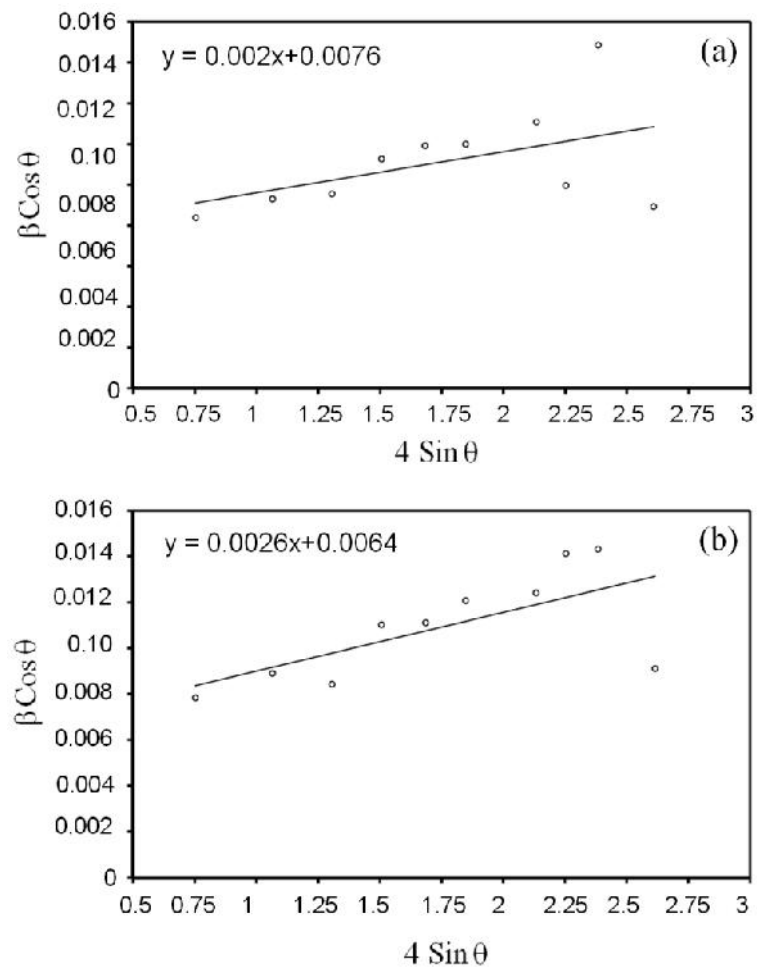


Figure 5.8: The W-H analysis of PZT-NPs; $T=650 \text{ }^\circ\text{C}$ (a) and $T=700 \text{ }^\circ\text{C}$ (b).

5.4. EFFECT OF SOLVENT ON OPTICAL PROPERTIES OF PZT-NPS IN INFRARED REGION

This study was carried out on PZT-NPs that prepared by sol-gel methods which mentioned in section (3.3.1) and (3.3.2). 2-methoxyethanol and poly ethylene glycol were used as two different solvents to prepare the precursor solutions for PZT-NP drawing. As mentioned before, the atomic ratio of the Pb:Zr:Ti of the solution was 1:0.52:0.48 and 10 % excess lead acetate was introduced. The polymeric precursor solutions were dried and calcinated at two different temperatures of 600 and 650 °C, to achieve pure perovskite PZT-NPs. X-ray diffraction analysis was used to study the formation of the perovskite phase in the range of 15°-80° by CuK α radiation. The FTIR results were used to calculate the absorption and reflectance parameters at range of 4000-280 cm⁻¹. The K-K method was used to analyze the reflection spectra to obtain the optical parameters of PZT-NPs.

5.4.1. X-ray diffraction and TEM results

The X-ray diffraction pattern of PZT-NPs prepared with two different solvents, 2-methoxyethanol, PZT-EGME and poly ethylene glycol, PZT-PGE, by the sol-gel method, are shown in Figure 5.9. For PZT-EGME, Figure 5.9(a), the rhombohedral phase was observed for both heating treatments and the perovskite phase is clearly formed at these temperatures. A perovskite structure is also for PZT-PGE, Figure 5.9(b), but a tetragonal phase was achieved by using poly ethylene glycol as the solvent for the sol-gel process. A small amount of pyrochlore phase was found at a calcination temperature of 600 °C for both methods. The pyrochlore phase disappeared and a pure

perovskite structure was obtained when the calcination temperature was increased to 650 °C.

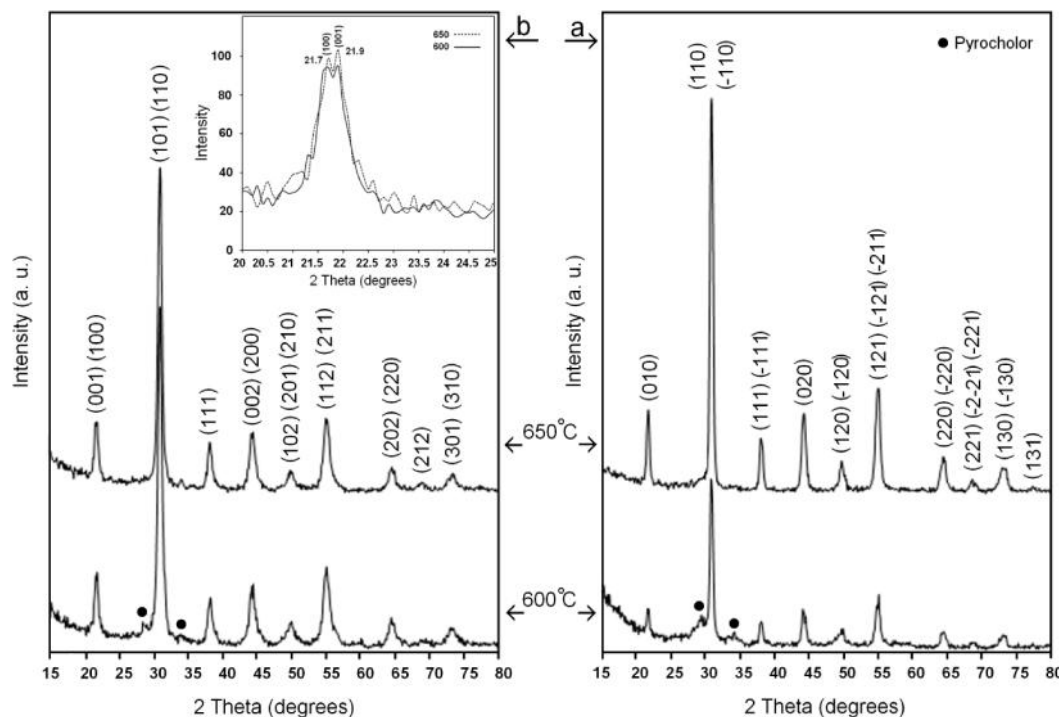


Figure 5.9: X-ray diffraction patterns of PZT-EGME (a) and PZT-PEG (b) calcined at 600 °C and 650 °C. Pure perovskite structure was obtained at 650 °C. Also the first XRD peak of PZT-PEG clearly shows a tetragonal phase.

The typical TEM image of the PZT-NPs prepared in different solvents are shown in Figure 5.10. From TEM analysis the primary particle size of the powders can be determined. The primary particles size of the PZT-NPs prepared in PEG and EGME were found to be approximately 25 and 17 nm, respectively.

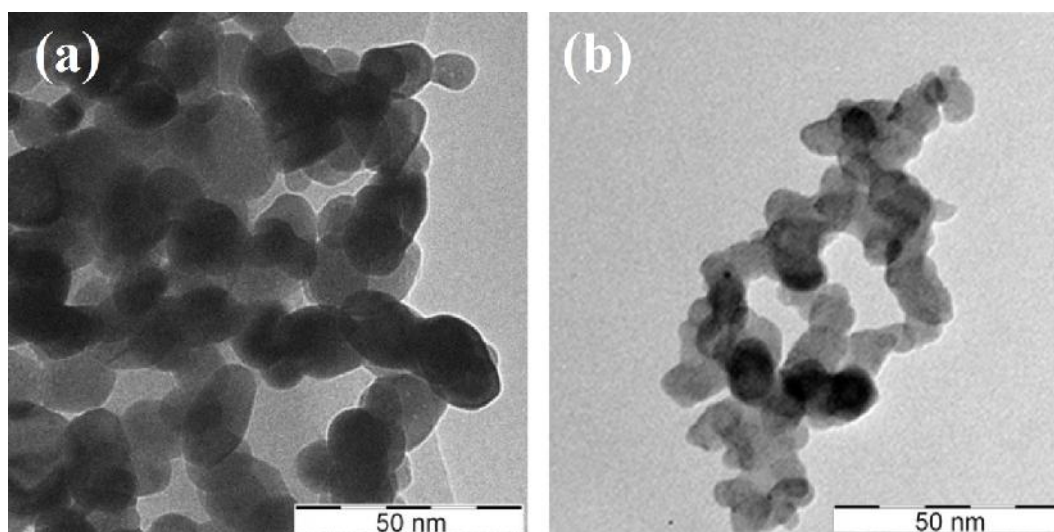


Figure 5.10: TEM morphology of the PZT-NPs prepared in different solvent media. (a) PZT-PEG and (b) PZT-EGME.

5.4.2. FTIR analysis

The room temperature transmittance of PZT-NPs has been investigated by Fourier Transform Infrared spectroscopy (FTIR) in the range of $280\text{-}4000\text{ cm}^{-1}$. The spectra are shown in Figure 5.11. A broad band was observed for each spectrum, with minimum transmittance at 530 cm^{-1} , and another band was observed with minimum transmittance at 350 cm^{-1} . From the previous studies, these two absorption bands were attributed to TiO_6 and ZrO_6 stretching and bending in the octahedral normal modes. There were few changes in the transmittance trace for the composites prepared by different solvents. Two small bands are also observed around 1500 and 3500 cm^{-1} in both of the PZT-PEG FTIR traces, which can be attributed to O-H and C-H bands from the remained burned organic materials. The FTIR results showed the formation of the perovskite structure of PZT-NPs, and they were in good agreement with the XRD results described previously (Last, 1957). There is another vibration mode (ν_3), which was described as a vibration of the cation- TiO_3ZrO_3 bond but this vibration mode is below the available

experimental frequency range (280-4000 Cm^{-1}) used in this research (Perry et al., 1964).

The results were presented in Table 5.3.

Table 5.3: Vibration bands and band widths for PZT-EGME and PZT-PEG calcined at 600 °C and 650 °C.

<i>Material</i>	<i>Temperature °C</i>	<i>ν_1 (Cm^{-1}) ± 1</i>	<i>Band wide $\nu_1(\text{Cm}^{-1}) \pm 1$</i>	<i>ν_2 (Cm^{-1}) ± 1</i>	<i>Band wide $\nu_2(\text{Cm}^{-1}) \pm 1$</i>
<i>PZT-EGME</i>	<i>600</i>	<i>498</i>	<i>293</i>	<i>331</i>	<i>142</i>
<i>PZT-PEG</i>	<i>600</i>	<i>532</i>	<i>289</i>	<i>323</i>	<i>196</i>
<i>PZT-EGME</i>	<i>650</i>	<i>530</i>	<i>340</i>	<i>352</i>	<i>98</i>
<i>PZT-PEG</i>	<i>650</i>	<i>532</i>	<i>336</i>	<i>326</i>	<i>148</i>

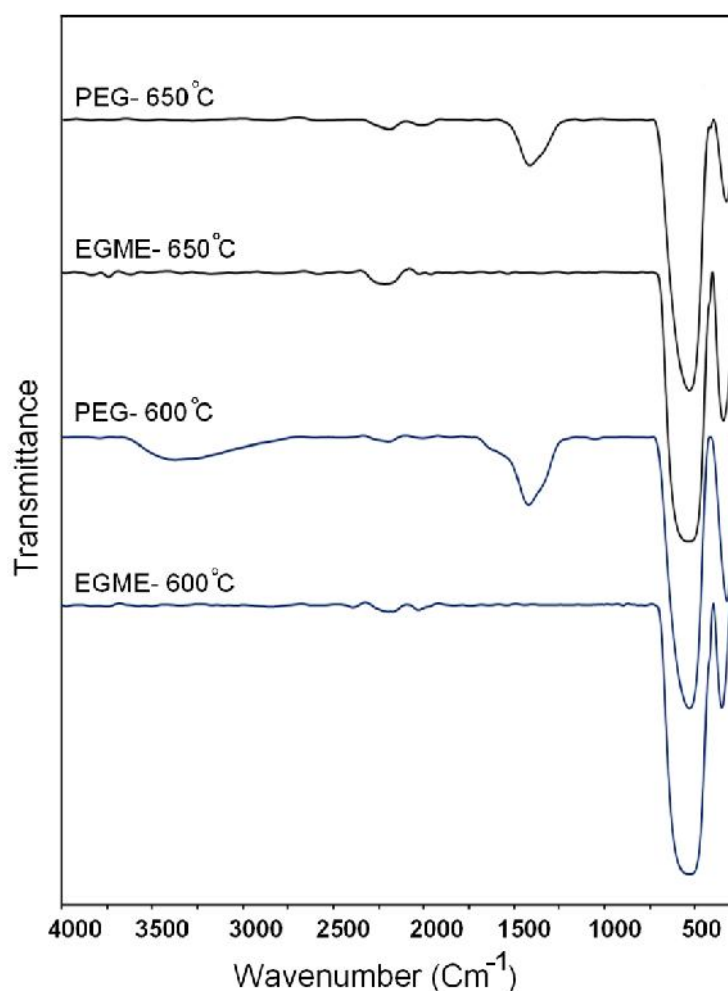


Figure 5.11: FTIR pattern of PZT-EGME and PZT-PEG calcined at 600 °C and 650 °C. The two important bands those are related to perovskite structure are seen in all FTIR traces.

5.4.3. Optical constants spectrum

As mentioned in section 2.4.2 chapter 2, the phase change of the emitted light can be calculated by using K-K method, Equation (2-34). After that, the real and imaginary parts of refractive index (n , k) can be extracted from Equation (2-31) and Equation (2-32) and finally the real and imaginary parts of permittivity from Equation (2-37).

The optical constants spectrum of the PZT-NPs prepared by the two different solvents at 600 °C and 650 °C are shown in Figure 5.12 and Figure 5.13. As shown in Figure 5.12(a) and Figure 5.13(a), the value of R and ϕ change as the two different solvents and temperatures are used. It is observed that a broader reflection peak exists for PZT-EGME at both calcination temperatures. It is also observed that the R peaks decreases as the temperature increases for both PZT-PEG and PZT-EGME.

The refractive index, n , and extinction coefficient, k , from 400 Cm^{-1} to 700 cm^{-1} are shown in Figure 5.12(b) and Figure 5.13(b). The n and k peaks are shifted to higher wavenumber for PZT-PEG to compare with PZT-EGME. The n peak value is decreased but k peak value is increased by temperature increased for both of compounds. The real and imaginary parts of the dielectric function of PZT-NPs are shown in Figure 5.12(c) and Figure 5.13(c). The main area of ϵ' and ϵ'' is from 400 Cm^{-1} to 600 Cm^{-1} . The ϵ' and ϵ'' peaks position of PZT-EGME shifted to lower wavenumbers with increased values compare to that the PZT-PEG. It seems that when the solvent is changed in the sol-gel process, the chemical reactions are changed and the lattice parameters and phases are affected by these changes. On the other hand, the resonance vibration frequencies of atom chains are related to the lattice parameters, so by changing the solvent, the optical parameters should also be changed.

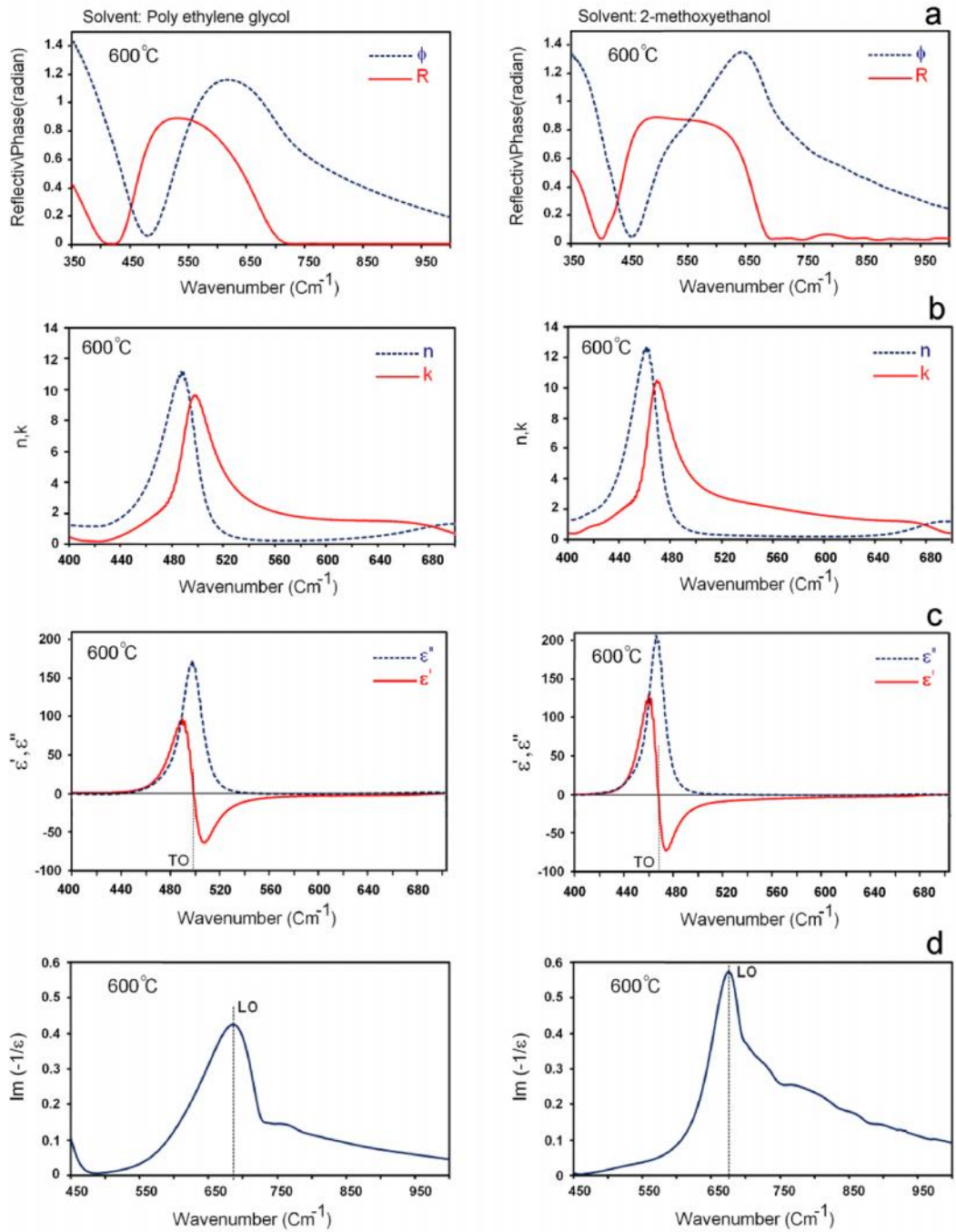


Figure 5.12: The reflectance and phase change spectrum, **a**, refractive index and extinction coefficient, **b**, real and imaginary parts of dielectric functions, **c**, and Electron-energy-loss function, **d**, of PZT-EGME and PZT-PEG calcined at 600 °C.

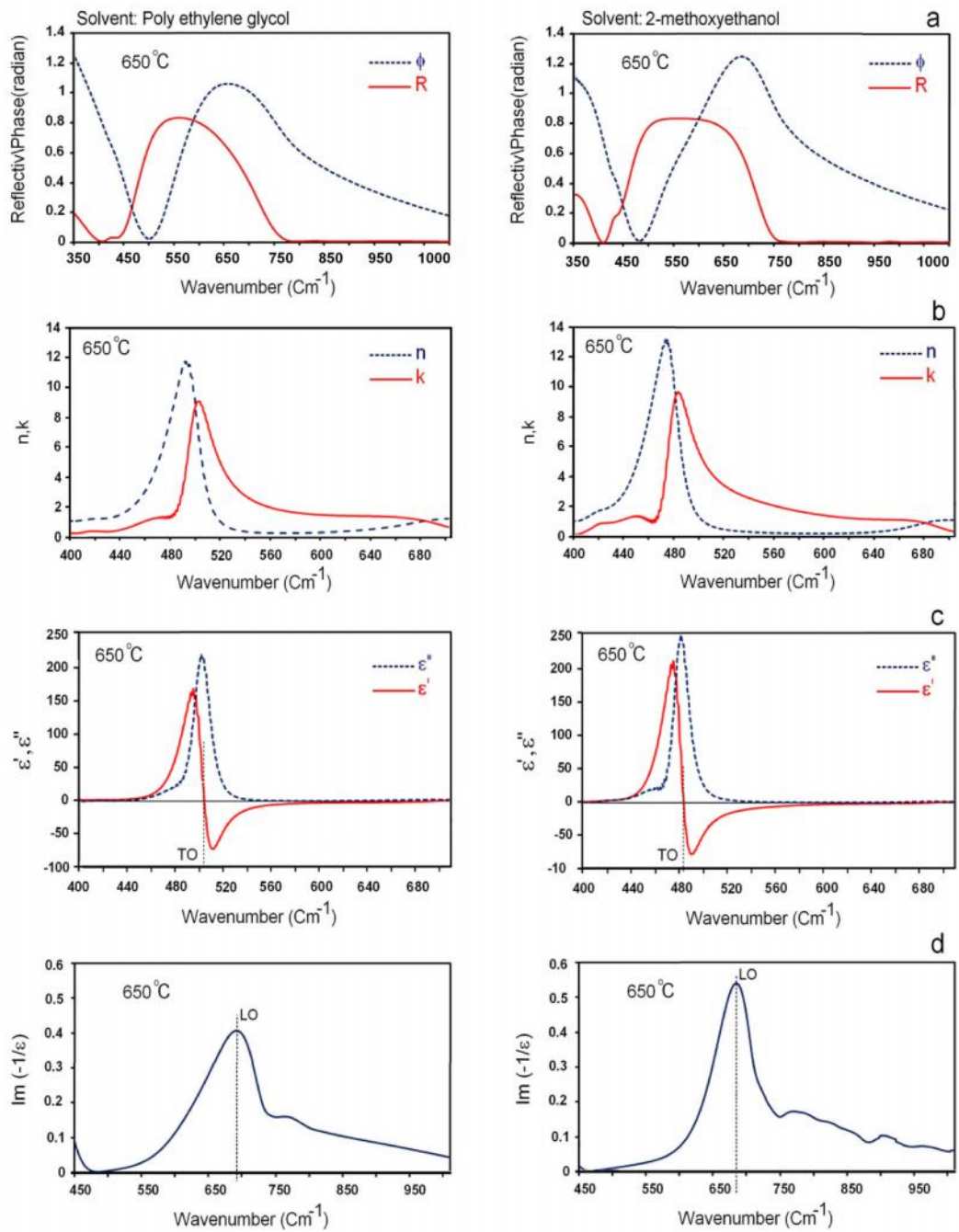


Figure 5.13 The reflectance and phase change spectrum, **a**, refractive index and extinction coefficient, **b**, real and imaginary parts of dielectric functions, **c**, and Electron-energy-loss function, **d**, of PZT-EGME and PZT-PEG calcined at 650 °C.

5.4.4. Optical phonon modes

The optical longitudinal, LO, and transverse optical, TO, phonons are useful to describe the optical interactions with the lattice. The TO mode frequencies correspond to the peak of the imaginary part of the dielectric function $\epsilon''(\omega)$ and the LO mode frequencies achieved from the imaginary part of $1/\epsilon$, Figure 5.12d and Figure 5.13d. Also, the TO and LO optical modes can be obtained from reflection and extinction trace. There are two intersect points for the n and k graphs. As a result of Figure 5.12b and Figure 5.13b, the first point is related to TO and second point is related to LO mode (Ng et al., 2006). The transverse and longitudinal optical phonons of PZT-PNs are presented in Table 5.4.

Table 5.4: Optical phonon for PZT-EGME and PZT-PEG calcined at 600 °C and 650 °C.

	<i>Material</i>	<i>Temperature (°C)</i>	
		<i>600</i>	<i>650</i>
<i>Transverse optical phonon (TO) Cm⁻¹</i>	<i>PZT-EGME</i>	464	478
	<i>PZT-PEG</i>	492	496
<i>Longitudinal optical phonon (LO) Cm⁻¹</i>	<i>PZT-EGME</i>	679	683
	<i>PZT-PEG</i>	685	693

5.5. EXPERIMENTAL AND THEORETICAL STUDIES OF PZT-NPS DIELECTRIC BEHAVIOR IN PVDF THIN FILMS MATRIX

In the present study, the polymeric material used to prepare the nanocomposite thin films was poly(vinylidene fluoride) (PVDF), and the ceramic material was lead zirconate titanate nanoparticles (PZT-NPs, with a diameter of ~ 20 nm). Both materials are dielectric but with quite different characteristics. PVDF has a low density ($\rho = 1,780$ kg/m³) compared to the PZT ($\rho = 7,500$ kg/m³); the PZT-NPs have a high dielectric constant ($\epsilon_r > 2,800$ at 100 kHz) compared to the PVDF ($\epsilon_r = 12$) (Lovinger, 1982). The frequency dependence of the electrical properties of the PVDF/PZT nanocomposite thin films was studied in the frequency range of 100 Hz to 40 MHz. In previous studies, for example Furukawa et al. (Furukawa et al., 1979) and Firmino et al. (Firmino Mendes et al., 2009), constant values of ceramic particles permittivity were examined over the entire frequency range to investigate the permittivity of the composites. In this work, the permittivity of the PZT-NPs was measured as a function of frequency, and the dielectric properties of the PVDF/PZT nanocomposites were investigated by experimental and theoretical approaches.

5.5.1. Sample preparation

The PZT-NPs powders were sonicated and dispersed in ethyl methyl ketone (EMK). Simultaneously, PVDF powder (Sigma-Aldrich) was dissolved in the EMK at 60 °C and stirred for 2 h. Next, the dispersed PZT-NPs were added to the PVDF solution and stirred for 2 h at 60 °C. The initial concentration of the solution was 0.2 g

PVDF per 15 milliliter of EMK and the PVDF/PZT-NP ratio was 85/15. The PVDF/PZT-NPs solution was coated onto a glass electrode substrate by a spin-coating method at 1,500 rpm for 30 s. The samples were then heated in an oven at 60 °C for 1 h to remove the solution and subsequently annealed on a hot plate at 110 °C for 1 h. Finally, the top electrode was coated onto the samples using a thermal evaporator.

5.5.2. Characterization results

The X-ray powder diffraction patterns obtained for the PZT-NPs calcined at temperatures of 700 °C is shown in Figure 5.14. PZT-NPs having a pure perovskite structure were obtained at this calcination temperature. The Scherrer method was used to calculate the crystallite size of the PZT-NPs, and it was found to be ~20 nm. The X-ray diffraction pattern of the PVDF and PVDF/PZT nanocomposite thin films are shown in Figure 5.15. It was estimated from these patterns that the PVDF, Figure 5.15 (a), existed in mixed α , β and γ phases. The peaks at 2θ corresponding to 17.5° (100), 18.0° (020), and 38.1° (200) were assigned to the α -PVDF, 22.2° (110) was assigned to the β -PVDF, whereas the peaks at $2\theta=26.4^\circ$ (022) could be indexed to the γ -PVDF (Ma et al., 2008, Thomas et al., 2010). The X-ray diffraction pattern obtained for the PVDF/PZT-NPs, Figure 5.15(b) clearly shows the PZT diffraction peaks.

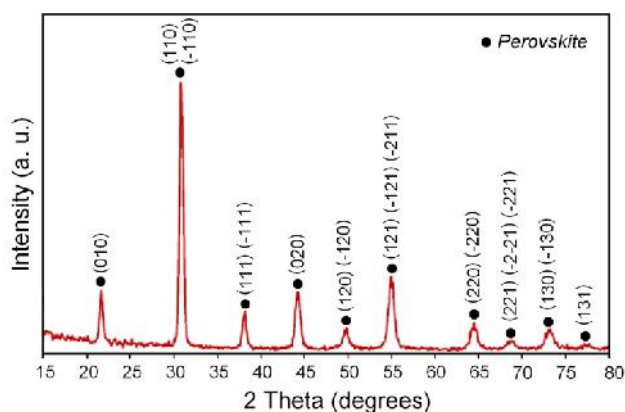


Figure 5.14: X-ray diffraction patterns for PZT-NPs calcined at different temperatures. The pure perovskite phase was achieved at 700 °C.

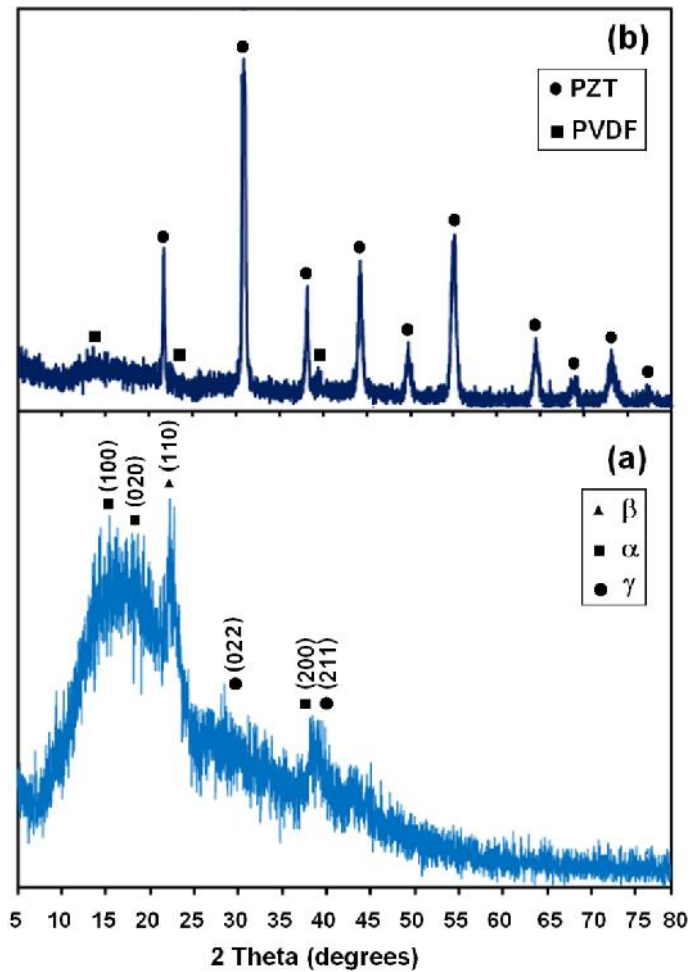


Figure 5.15: X-ray diffraction patterns for (a) pure PVDF, and (b) PVDF/PZT-NPs. The pattern of pure PVDF shows exists of α , β and γ phase in the compound.

In Figure 5.16, FTIR transmittance spectra of PVDF (a) and PVDF/PZT (b) are shown in the range of $285\text{-}1700\text{ cm}^{-1}$. The identified regions are rich in information on the conformational isomerism of the chain, providing information on α and β phase content. The absorption bands at 426 , 532 , and 1287 cm^{-1} are related to β -phase characteristic bands (Yu and Cebe, 2009). The band at 1287 and 532 cm^{-1} are assigned to CH_2 and CF_2 bending vibration bands, respectively. The mode at 426 cm^{-1} is parallel to a-axis of PVDF chain. The α -phases are observed at 492 , 615 , 765 , and 989 cm^{-1} (Yu and Cebe, 2009). The absorption band at 765 cm^{-1} can be related to a rocking vibration in the PVDF chain. The bending vibration of CF_2 is observed at 615 cm^{-1} also, bending and wagging vibration of CF_2 groups ascribed to the α -PVDF polymorph are detected at 492 cm^{-1} (Bharti et al., 1997). The absorption bonds at 310 and 362 cm^{-1} are attributed

to Ti,Zr-O normal vibration modes, also, there is C-H stretching vibration mode at 362 cm^{-1} (Zak and Majid, 2010). The γ -phase is estimated from the band occurred at 811 cm^{-1} (Yu and Cebe, 2009). The results which obtained from FTIR spectra were summarized in the Table 5.5.

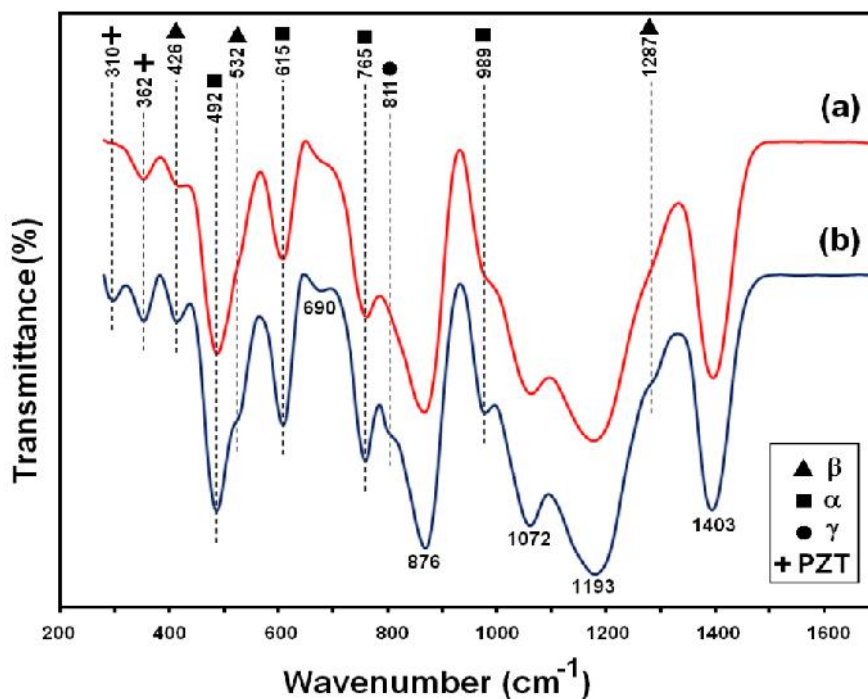


Figure 5.16: FTIR traces for (a) pure PVDF and (b) PVDF/PZT-NPs. The results show the existence of α , β and γ phase in the compound.

Table 5.5: Characteristic bands with specific vibrational modes and crystallite phases.

Wavenumber cm ⁻¹	Group	Vibration	Comments
310	(Zr, Ti)-O C-H	Stretching Stretching	
362	(Zr, Ti)-O	Bending	
426			β-Phase
492	CF ₂	Bending and wagging	α-Phase (in-phase combination)
532	CF ₂	Bending	β-Phase
615	CF ₂ and C-C-C	CF ₂ bending and C-C-C skeletal vibration	α-Phase
690			Presence of head to head and tail to tail configurations
765		In-plane bending Or rocking	α-Phase
811			γ-Phase
876	CH ₂ and CF ₂	CH ₂ rocking and CF ₂ stretching	β-Phase
989			α-Phase
1072	C-C-C	Bending	
1193	CH ₂	Wagging	β-Phase
1287	CH ₂	Rocking	β-Phase or γ-Phase
1403	CH ₂	In-plane bending Or scissoring	

Figure 5.17(a) shows a transmission electron micrograph of the PZT-NPs. The average initial size of the PZT-NPs was ~24 nm, as evidenced by the TEM micrographs. The surface morphology of the PVDF/PZT-NPs, dried PVDF, and annealed PVDF revealed by scanning electron microscopy (SEM) are shown in Figure 5.17 (b, c, and d) respectively. The SEM image of the composites, Figure 5.17(b) shows the excellent distribution of the PZT-NPs fillers within the PVDF matrix. The morphology of the dried PVDF Figure 5.17(c) and the annealed PVDF, Figure 5.17(d) indicate that the lamellas were formed during the annealing process. As it shown in Figure 5.18, the

lamellas start growing from a nucleus of a crystal. A slow diffusion leads to tree-like architecture of branches and twigs with built-in depletion zones (Cramer et al., 1998).

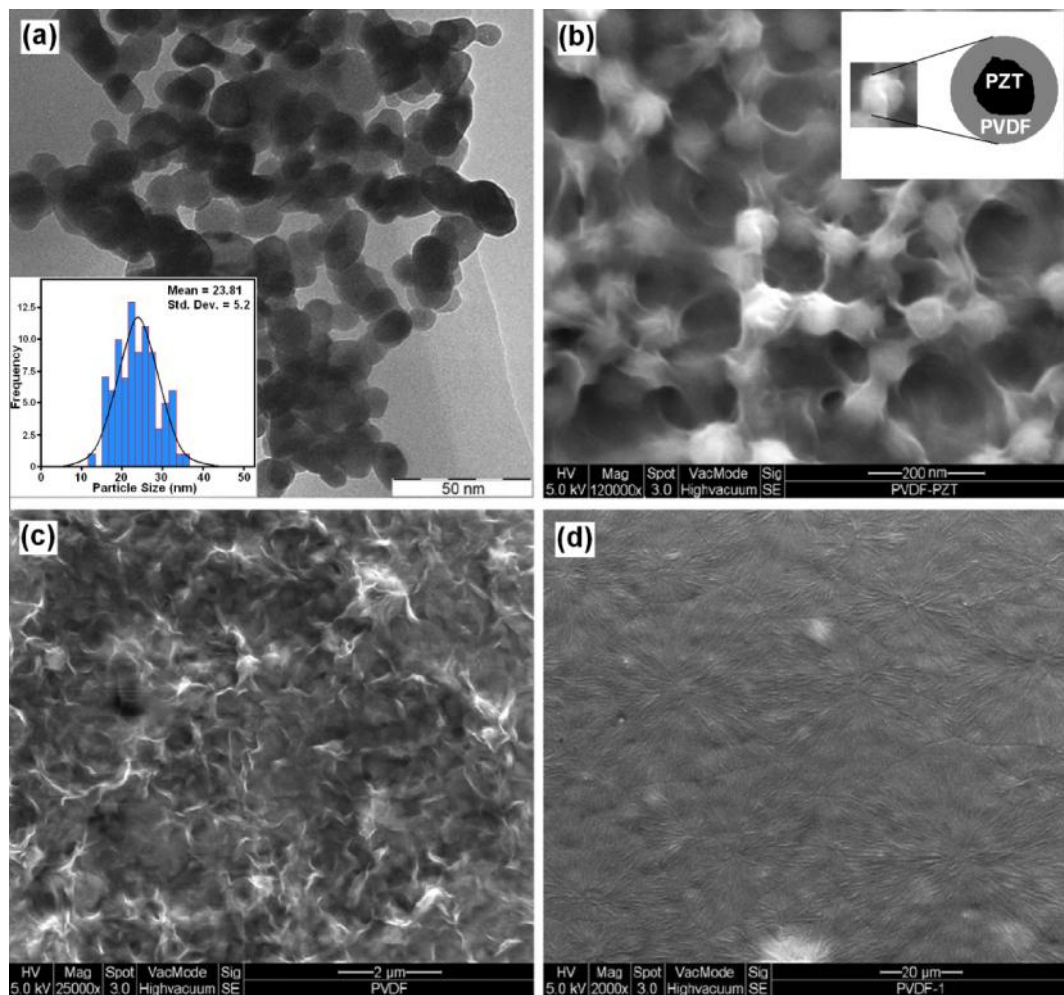


Figure 5.17: TEM morphology of the PZT-NPs (a), SEM micrographs of PVDF/PZT-NPs film (b), dried PVDF film (c), and PVDF film annealed at 110 °C. The inset image of figure 4b shows the coverage of the polymer surrounding the nanoparticles.

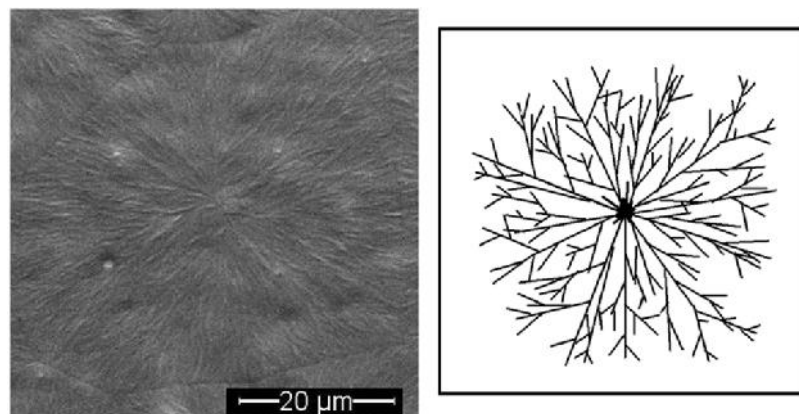


Figure 5.18: Crystallization starts from a nucleus of a crystal and grows in a blend melt with a tree-like architecture.

Figure 5.19 presents the variation of dielectric constant and loss with frequency for the PZT-NPs calcined at 700 °C for 1 h. The dielectric constant and the loss value start from 2,917 and 3.67, respectively, at 100 Hz, and then decrease to 330 and 0.08 as the frequency increases to 31 MHz. A resonance occurs at 38 MHz above this frequency, the value of the dielectric constant and the loss decreases again as frequency increases. The frequency dependence of the dielectric constant and loss of the nanocomposite thin films with 15% PZT-NPs and pure PVDF are shown in Figures 5.20 and 5.21, respectively. As expected, the effective dielectric constant (ϵ) was increased at all frequency as the PZT-NPs were added to the matrix under study. The effective dielectric constant obtained was higher than that of pure PVDF but much lower than that of the pure PZT-NPs. Based on the X-ray studies, it was confirmed that PVDF is present as mixed α and γ phases, which are both nonpolar. Due to the nonpolar nature of PVDF, and the constrained polymer chain hindering the formation of electrical polarization, the value of ϵ is lower than that of PZT-NPs (Thomas et al., 2010).

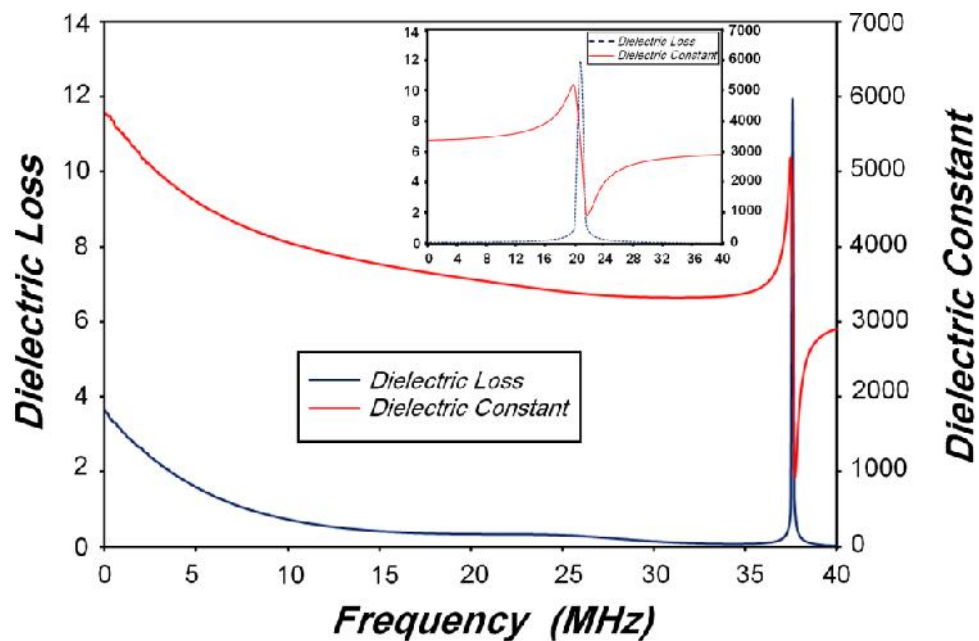


Figure 5.19: The experimental dielectric constant and loss of the PZT-NPs as a function of frequency at room temperature, from 100Hz to 40MHz. The inset shows the resonance area.

It was observed that the dielectric loss decreased as frequency increased for both pure PVDF and PVDF/PZT nanocomposite thin films from 100 Hz to 15 MHz, but increased as frequency increased further up to 39 MHz (Figure 5.21). The inset of Figure 5.21 shows that the frequency dependence of the dielectric loss of the pure PVDF and the PVDF/PZT nanocomposite were almost same in the frequency range of 100 Hz to 30 MHz. This suggests that the PVDF molecular chains play a more important role in this frequency range but that above 30 MHz the PZT-NPs play the main role in the dielectric loss behavior of the PVDF/PZT nanocomposite thin films.

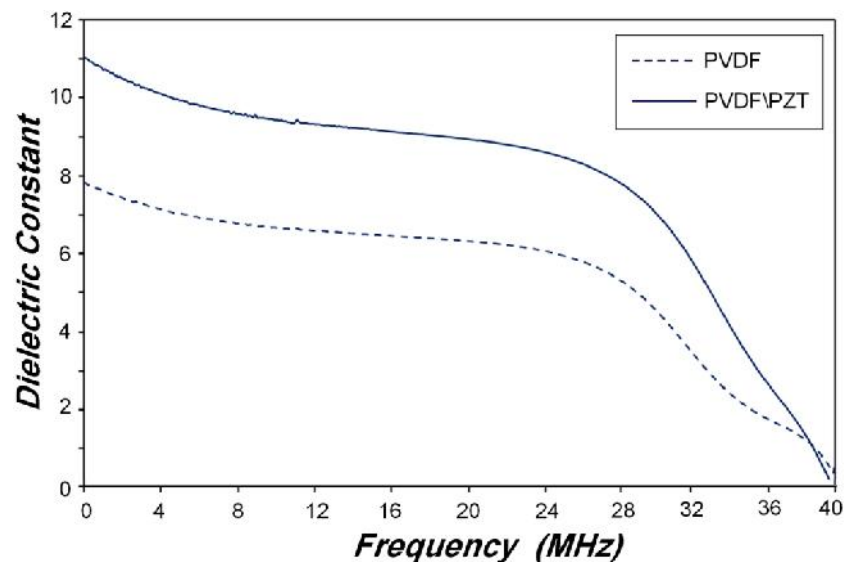


Figure 5.20: The experimental dielectric constant of the pure PVDF and PVDF/PZT-NPs as a function of frequency at room temperature, from 100Hz to 40MHz.

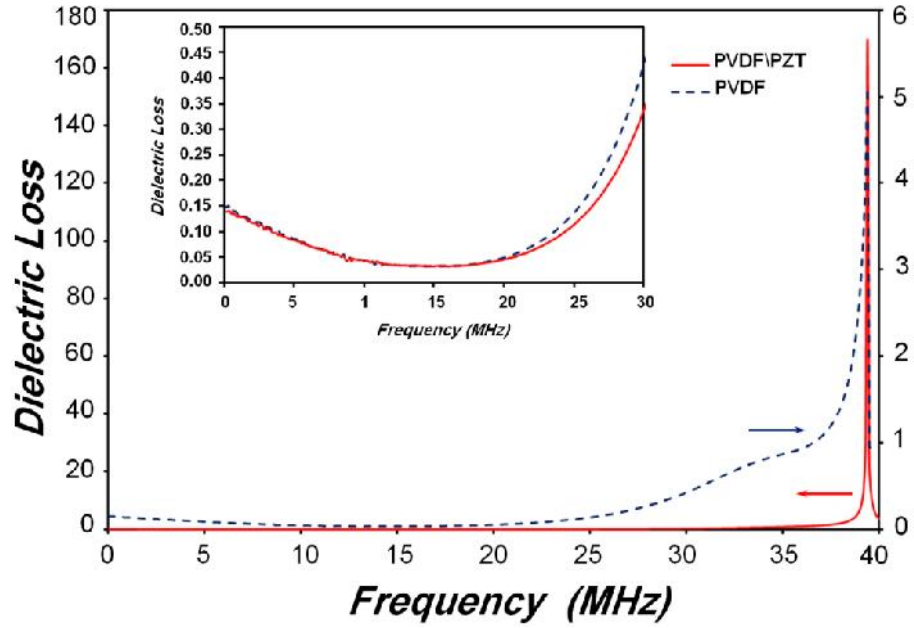


Figure 5.21: The experimental dielectric loss of the pure PVDF and PVDF/PZT-NPs as a function of frequency at room temperature, from 100Hz to 40MHz. The inset shows that the loss value of PVDF/PZT and PVDF are almost the same in frequency range of 100 Hz to 30 KHz.

5.5.3. Theoretical study of the dielectric behavior of PZT-NPs /PVDF nanocomposite thin films

To better understand the nature of the dielectric response of the composite material with increasing ceramic concentration, several theoretical models were employed. The first model developed to predict the dielectric behavior of the composites was proposed by Maxwell in 1904 (Maxwell, 1954); this model is still widely used. In this model, the dielectric response of the composite is given by:

$$\varepsilon = \frac{\alpha_1 \varepsilon_1 \left(\frac{2}{3} + \frac{\varepsilon_2}{3\varepsilon_1} \right) + \alpha_2 \varepsilon_2}{\alpha_1 \left(\frac{2}{3} + \frac{\varepsilon_2}{3\varepsilon_1} \right) + \alpha_2} \quad (5 - 10)$$

where ε_1 is the dielectric constant of the polymer, ε_2 is the dielectric constant of the filler, and α_1 , α_2 are the volume fractions of the polymer and filler, respectively.

In 1979, Furukawa, (Furukawa et al., 1979) derived an expression for biphasic composites with 0-3 connectivity. This model also assumes that the particles are spherical and uniformly dispersed throughout the polymer matrix. The entire system is dielectrically homogeneous and the response depends on the dielectric constant of the matrix. The dielectric behavior of the composite can be obtained from the following relation:

$$\varepsilon = \frac{1 + 2\alpha}{1 - \alpha} \varepsilon_1 \quad (5 - 11)$$

Where ε_1 is the dielectric constant of the matrix, ε is the effective dielectric constant and α is the volume fraction of the ceramic particles.

The Maxwell and Furukawa theories were used as the basis for a new theory that was presented by Rayleigh (Bhimasankaram et al., 1998). The Rayleigh equation correctly predicts the increase in permittivity when a small amount of inclusions are added to the matrix. In this model, the dielectric behavior of the composites is given by:

$$\varepsilon = \varepsilon_1 \left(\frac{2\varepsilon_1 + \varepsilon_2 + 2\alpha(\varepsilon_2 - \varepsilon_1)}{2\varepsilon_1 + \varepsilon_2 - \alpha(\varepsilon_2 - \varepsilon_1)} \right) \quad (5 - 12)$$

where ε_1 and ε_2 are the dielectric constants of the matrix and ceramic particles, respectively, ε is the effective dielectric constant and α is the volume fraction of the ceramic particles.

Figure 5.23 shows the typical experimental and theoretical permittivities of the PVDF/PZT nanocomposite thin films. It can be seen here that dielectric permittivity measured at lower frequencies (below 100 Hz) was always greater than that measured at higher frequency. The dielectric constant decreased slowly with increasing frequency up to 25 MHz, and with further frequency increases the dielectric constant decreases very rapidly up to 40 MHz, which is the upper limit of the frequency range in this study.

It was also observed that the results of the Furukawa theory were almost the same as the experimental results observed in the frequency range of 100 Hz to 25 MHz. There was an ~8% deviation between the results of the Rayleigh theory calculations and the experimental results, but the results of the Maxwell calculations were very different from the experimental results in this frequency range. These theories are based on a spherical morphology of the ceramic particles. Due to the nonspherical morphology of the PZT-NPs (see Figure 5.17(a)), the theoretical calculations of the dielectric constant were not completely in accord with the experimental results. Above 25 MHz, the Rayleigh theory seems to be more reliable for calculating the dielectric constant compared to the others. In this case, the results showed that the Maxwell and Garnett theory was not a suitable theory for calculating the dielectric constant of the PVDF/PZT nanocomposite thin films.

In the effective medium theory (EMT), (Yang et al., 2000) and (Yamada et al., 1982), theories, the morphology of the particles is considered in the calculation of the dielectric constant. By the EMT method, the dielectric constant of the composite can be estimated from the following equation:

$$\varepsilon = \varepsilon_1 \left(1 + \frac{\alpha(\varepsilon_2 - \varepsilon_1)}{\varepsilon_1 + n(1 - \alpha)(\varepsilon_2 - \varepsilon_1)} \right) \quad (5 - 13)$$

where ε_1 and ε_2 are the dielectric constants of the matrix and ceramic particles, ε is the effective dielectric constant, α is the volume fraction of the ceramic particles and n is the fitting factor.

The value of n depends on the morphology of the particles. When the morphology of the particles is almost spherical, then the value of n is very small. A high value of n indicates largely nonspherically shaped particles. The experimental values in

the frequency range of 100 Hz to 27 MHz were well fit by the EMT model with the shape parameter $n = 0.47$.

According to Yamada's model the dielectric constant is obtained from:

$$\varepsilon = \varepsilon_1 \left(1 + \frac{k\alpha(\varepsilon_2 - \varepsilon_1)}{k\varepsilon_1 + (1 - \alpha)(\varepsilon_2 - \varepsilon_1)} \right) \quad (5 - 14)$$

where k is the parameter related to the morphology of the particles.

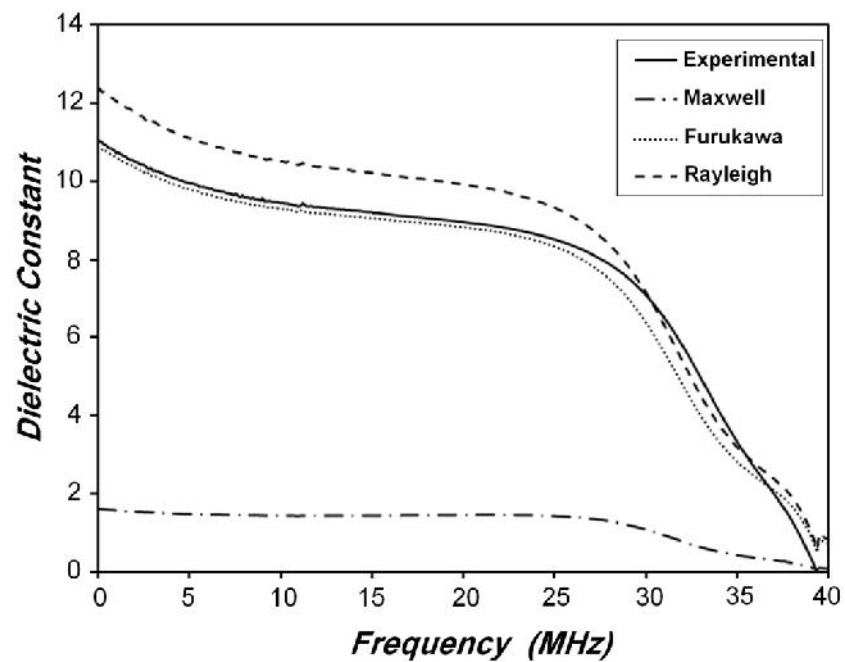


Figure 5.22: Dielectric constant of PVDF/PZT-NPs obtained from experimental test and theoretical calculation (Furukawa, Maxwell and Rayleigh theories) at room temperature, from 100 Hz to 40 MHz.

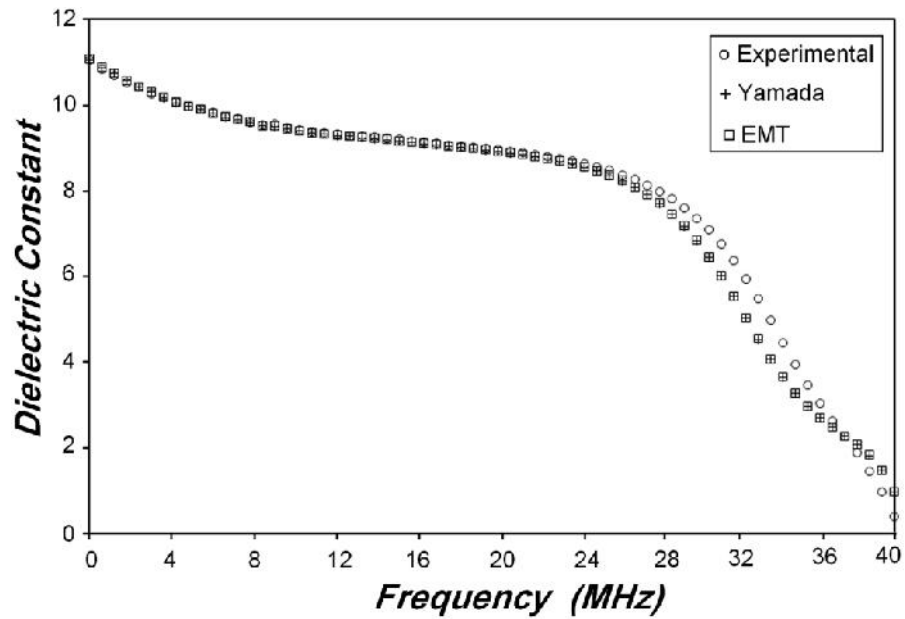


Figure 5.24: Dielectric constant of PVDF/PZT-NPs obtained from experimental test and theoretical calculation (Yamada and EMT theories) at room temperature, from 100 Hz to 40 MHz.

It is clear that for $k = 1/n$ Equation (5-13) and Equation (5-14) are equal. Thus, the results of this theory would be the same as obtained from the EMT when $k = 2.13$. The difference between the experimental data and the predicted values was close to zero in the frequency range of 100 Hz to 27 MHz, but the difference increased to 5% in the high-frequency range from 27 MHz to 40 MHz. The difference can be related to the resonance frequency of the nanoparticles (see Figure 5.20) because the resonance behavior of the PZT-NPs is affected by the polymer matrix. The results are shown in Figure 5.24.

5.6. SUMMARY

In this chapter, some theoretical investigations were carried out on the ZnO and PZT nanoparticles. The theoretical studies of the XRD patterns of ZnO and PZT nanoparticles show that the mechanical strain affects the peak broadening of the XRD pattern of the nanoparticles. Sometimes the error of the crystallite size is about 100 percent; therefore, it should be considered to calculate the crystallite size.

The optical properties of PZT-NPs were investigated in infrared region using the K-K relations. The results show that there is a resonance in dielectric function that related to TO vibration mode of the atoms in nanoparticles. Frequency of this vibration mode depends on the calcination temperature, structure and particles size. Because the number of atomic chains are related to the size of the particles.

In addition, the dielectric properties of PZT-NPs were experimentally and theoretically, with and without PVDF matrix, investigated. The results show that the PZT-NPs can improved the dielectric properties of the matrix as like as the PZT particle in micro size; therefore, can be used as suitable filler to improve dielectric properties of the polymeric matrix for microelectronic applications. Because it is possible to make ultrathin films by using nanoparticles in this range of size with improving the properties.

CHAPTER 6:

CONCLUSIONS

ZnO and PZT nanostructures were produced successfully by different chemical methods, and the nanostructures were characterized according to their physical and chemical properties. The PZT was prepared in the form of nanoparticles form, and different morphologies were achieved for ZnO by using different synthesis methods.

The main objective of this project was to find inexpensive and fast methods for preparing ZnO and PZT nanostructures. In addition, these methods should be suitable for producing nanopowders in large-scale facilities . In order to achieve these objectives, the least expensive starting materials were used. Another goal of the project was to prepare these nanostructures by simple methods that can be used in industry to prepare fine powders that have homogenous particle shapes. These objectives were successfully achieved, as indicated in the discussion below.

The ZnO NPs were prepared by the sol-gel method using gelatin (SG) and starch (SS) as two different natural materials for stabilizing the sols. The results showed that the particles were well dispersed and in the nano size range for both SG and SS, and the optical band-gap and crystallite size increased as the calcination temperature increased. However, the particles that were prepared by gelatin exhibited a narrower size distribution and were well-shaped compared to SS. This was because a lower temperature was required to produce pure nanoparticles when starch was used. It was found that the gelatin was expanding during the calcination process, causing it to behave as a terminator. The ZnO NPs also were synthesized using the sol-combustion method. According to the XRD and TEM results, good-quality (narrow size distributions and

uniform morphology) particles were produced, and they were well dispersed, just like the nanoparticles that were prepared using the sol-gel method. However, the sol-combustion method is more complicated than and not as safe as the sol-gel method. A minimum particle size of 29 nm and a crystallite size of 20 nm were achieved by the sol-gel method using gelatin. According to the results of the methods we investigated for preparing ZnO NPs, it was found that the best method for preparing a well-dispersed, homogeneous, and fine powder of ZnO NPs is the sol-gel method using gelatin as a stabilizer. This method can be used to produce commercial ZnO nanopowders. ZnO nanostructures, as well as nanoparticles, also were prepared by the solvothermal and sonochemical methods to control the morphology of the products. MEA, DEA, and TEA were used as polymerization agents in the solvothermal process. The characterization results showed that the morphology of the final products depended significantly on the type of polymerization agent used. The particles prepared in MEA and TEA media were in the nano size range, whereas the particles prepared in DEA were in the micro size range because of the structure of DEA. According to the TEM and SEM results, the nanoparticles that were prepared in TEA media were more homogeneous than those prepared in the MEA media. The results indicated that DEA and TEA were suitable polymers for use in preparing micro-sized and nano-sized, homogenous ZnO powders, respectively. In addition to the methods discussed above, ZnO nanostructures (rods and flowers) were prepared successfully in aqua solution by using sound as a source of energy. The XRD results showed that zinc hydroxide was formed after five minutes, after which the conversion to ZnO began. ZnO nanorods were formed completely after 10 minutes, and they changed to flower-shaped nanoparticles in 30 minutes. The TEM and SEM micrographs showed that the ZnO nanostructures were well-defined, which was confirmed by the XRD results. Band gaps of 3.3 eV and 3.2 eV were calculated for the ZnO nanorods and flowers, respectively. It

was found that the sonochemical method was the fastest method for preparing ZnO nanostructures.

The PZT NPs were synthesized by the sol-gel method using two different solvents, i.e., polyethylenglycol (PEG) and 2-methoxyethanol (EGME). The XRD results showed the formation of PZT NPs in the perovskite structure with rhombohedral and tetragonal phases. As shown by the FTIR results, the purity of the PZT NPs that were prepared in EGME was higher than that of the NPs prepared in PEG. The particle sizes of the PZT NPs that were prepared in PEG and EGME were about 25 nm and 17 nm, respectively, and they had the same morphology. The results showed that the sol-gel method using EGME as the solvent was a better method for the large-scale preparation of PZT NPs.

Finally, the structures of the ZnO and PZT nanoparticles were considered in the context of several theories, such as Williamson-Hall (W-H), the Size Strain Plot (SSP), and Kramers-Kronig. Investigation of the XRD results for the NPs by the W-H and SSP methods showed that strain affects the broadening of the diffraction peaks in the XRD patterns; therefore, this strain should be considered in the calculation of the crystallite size of the NPs. The optical properties of the PZT NPs were investigated using experimental data obtained by FTIR and using the K-K mathematical relationships. It was found that the optical properties of the NPs change as their particle sizes change. In addition, the dielectric properties of the PZT NPs were investigated in the absence and in the presence of the PVDF matrix. The results showed that the PZT NPs are suitable for use as a filler in microelectronic applications to improve the dielectric properties of the polymeric matrix.

Future work can be focused on the use of these nanoparticles for several applications, such as fillers, sensors, pigments, and electronic devices. They can be used

as fillers in polymeric matrices, such as PVDF and PVC to make electro-active composites. The methods that were mentioned to prepare the nanoparticles can be used to make other metal oxide composites, and they can be used to prepare doped metal oxides as well. For example, the ZnO NPs can be doped with Li, Na, and K to prepare p-type ZnO NPs. In addition, the anti-bacterial properties of the ZnO NPs can be improved by adding some Ag to the ZnO matrix, making them suitable for medical applications, especially in dentistry.

REFERENCES

- Ahn, M. W., Park, K. S., Heo, J. H., Kim, D. W., Choi, K. J. & Park, J. G. 2009. On-Chip Fabrication Of Zno-Nanowire Gas Sensor With High Gas Sensitivity. *Sensors And Actuators B: Chemical*, 138, 168-173.
- Amekura, H., Sakuma, Y., Kono, K., Takeda, Y., Kishimoto, N. & Buchal, C. 2006. Luminescence From Zno Nanoparticles/Sio₂ Fabricated By Ion Implantation And Thermal Oxidation. *Physica B: Condensed Matter*, 376-377, 760-763.
- Arguello, C. A., Rousseau, D. L. & Porto, S. P. S. 1969. First-Order Raman Effect In Wurtzite-Type Crystals. *Physical Review*, 181, 1351.
- Ashkenov, N., Mbenkum, B. N., Bundesmann, C., Riede, V., Lorenz, M., Spemann, D., Kaidashev, E. M., Kasic, A., Schubert, M., Grundmann, M., Wagner, G., Neumann, H., Darakchieva, V., Arwin, H. & Monemar, B. 2003. Infrared Dielectric Functions And Phonon Modes Of High-Quality Zno Films. *Journal Of Applied Physics*, 93, 126-133.
- Bai, Z., Xie, C., Zhang, S., Xu, W. & Xu, J. 2011. Microwave Sintering Of Zno Nanopowders And Characterization For Gas Sensing. *Materials Science And Engineering: B*, 176, 181-186.
- Bairamov, B. H., Heinrich, A., Irmer, G., Toporov, V. V. & Ziegler, E. 1983. Raman Study Of The Phonon Halfwidths And The Phonon—Plasmon Coupling In Zno. *Physica Status Solidi (B)*, 119, 227-234.
- Bel Hadj Tahar, R., Bel Hadj Tahar, N. & Ben Salah, A. 2007. Low-Temperature Processing And Characterization Of Single-Phase Pzt Powders By Sol-Gel Method. *Journal Of Materials Science*, 42, 9801-9806.
- Bezzi, F., Costa, A. L., Piazza, D., Ruffini, A., Albonetti, S. & Galassi, C. 2005. Pzt Prepared By Spray Drying: From Powder Synthesis To Electromechanical Properties. *Journal Of The European Ceramic Society*, 25, 3323-3334.
- Bharti, V., Kaura, T. & Nath, R. 1997. Ferroelectric Hysteresis In Simultaneously Stretched And Corona-Poled PvdF Films. *Dielectrics And Electrical Insulation, Ieee Transactions On*, 4, 738-741.
- Bhattacharyya, S. & Gedanken, A. 2008. A Template-Free, Sonochemical Route To Porous Zno Nano-Disks. *Microporous And Mesoporous Materials*, 110, 553-559.
- Bhimasankaram, T., Suryanarayana, S. V. & Prasad, G. 1998. Piezoelectric Polymer Composite Materials. *Current Science*, 74, 10.
- Birkholz, M. 2006. *Thin Film Analysis By X-Ray Scattering*, Weinheim, Wiley-Vch.
- Blom, F. R., Yntema, D. J., Van De Pol, F. C. M., Elwenspoek, M., Fluitman, J. H. J. & Popma, T. H. J. A. 1990. Thin-Film Zno As Micromechanical Actuator At Low Frequencies. *Sensors And Actuators A: Physical*, 21, 226-228.
- Bove, T., Wolny, W., Ringgaard, E. & Pedersen, A. 2001. New Piezoceramic Pzt-Pnn Material For Medical Diagnostics Applications. *Journal Of The European Ceramic Society*, 21, 1469-1472.
- Bruncková, H., Medvecký, L., Briancin, J. & Saksl, K. 2004. Influence Of Hydrolysis Conditions Of The Acetate Sol-Gel Process On The Stoichiometry Of Pzt Powders. *Ceramics International*, 30, 453-460.

- Calleja, J. M. & Cardona, M. 1977. Resonant Raman Scattering In Zno. *Physical Review B*, 16, 3753.
- Callender, R. H., Sussman, S. S., Selders, M. & Chang, R. K. 1973. Dispersion Of Raman Cross Section In Cds And Zno Over A Wide Energy Range. *Physical Review B*, 7, 3788.
- Cao, L., Zou, B., Li, C., Zhang, Z., Xie, S. & Yang, G. 2004. Laser Emission Of Low-Threshold Excitation From \Ensuremath Zno Nanowires. *Europhysics Letters*, 68.
- Capobianco, J. A., Vetrone, F., Boyer, J. C., Speghini, A. & Bettinelli, M. 2002. Visible Upconversion Of Er³⁺ Doped Nanocrystalline And Bulk Lu₂O₃. *Optical Materials*, 19, 259-268.
- Cardano, M. 1982. *Light Scattering In Solids Ii*, In *Springer Topics In Applied Physics*, Berlin, Springer.
- Cardin, J., Leduc, D., Schneider, T., Lupi, C., Averty, D. & Gundel, H. W. 2005. Optical Characterization Of Pzt Thin Films For Waveguide Applications. *Journal Of The European Ceramic Society*, 25, 2913-2916.
- Chakrabarti, N. & Maiti, H. S. 1997. Chemical Synthesis Of Pzt Powder By Auto-Combustion Of Citrate-Nitrate Gel. *Materials Letters*, 30, 169-173.
- Chandratreya, S. S., Fulrath, R. M. & Pask, J. A. 1981. Reaction Mechanisms In The Formation Of Pzt Solid Solutions. *Journal Of The American Ceramic Society*, 64, 422-425.
- Chang, C.-J., Hung, S.-T., Lin, C.-K., Chen, C.-Y. & Kuo, E.-H. 2010. Selective Growth Of Zno Nanorods For Gas Sensors Using Ink-Jet Printing And Hydrothermal Processes. *Thin Solid Films*, 519, 1693-1698.
- Chao, W., Zhang, X., Xiao, C., Liang, D. & Wang, Y. 2008. An Excellent Single-Layered Photoreceptor Composed Of Oxotitanium Phthalocyanine Nanoparticles And An Insulating Resin. *Journal Of Colloid And Interface Science*, 325, 198-202.
- Chen, J.-W., Perng, D.-C. & Fang, J.-F. 2011. Nano-Structured Cu₂O Solar Cells Fabricated On Sparse Zno Nanorods. *Solar Energy Materials And Solar Cells*, 95, 2471-2477.
- Chen, J., Lei, W., Chai, W., Zhang, Z., Li, C. & Zhang, X. 2008. High Field Emission Enhancement Of Zno-Nanorods Via Hydrothermal Synthesis. *Solid-State Electronics*, 52, 294-298.
- Chen, L. & Bi, X. 2008. Variations Of Microstructure, Conductivity And Transparency Of Al-Doped Zno Thin Films Prepared By Radio Frequency Magnetron Sputtering With Target-Substrate Distances. *Vacuum*, 82, 1216-1219.
- Chen, S. C., Cheng, C. H. & Lin, Y. C. 2007. Analysis And Experiment Of A Novel Actuating Design With A Shear Mode Pzt Actuator For Microfluidic Application. *Sensors And Actuators A: Physical*, 135, 1-9.
- Cho, S.-B., Oledzka, M. & Riman, R. E. 2001. Hydrothermal Synthesis Of Acicular Lead Zirconate Titanate (Pzt). *Journal Of Crystal Growth*, 226, 313-326.
- Choi, H., Veriansyah, B., Kim, J., Kim, J.-D. & Kang, J. W. 2010. Continuous Synthesis Of Metal Nanoparticles In Supercritical Methanol. *The Journal Of Supercritical Fluids*, 52, 285-291.
- Chou, C.-Y., Huang, J.-S., Wu, C.-H., Lee, C.-Y. & Lin, C.-F. 2009. Lengthening The Polymer Solidification Time To Improve The Performance Of Polymer/Zno Nanorod Hybrid Solar Cells. *Solar Energy Materials And Solar Cells*, 93, 1608-1612.

- Choy, J.-H., Han, Y.-S. & Kim, J.-T. 1995. Hydroxide Coprecipitation Route To The Piezoelectric Oxide $\text{Pb}(\text{Zr,Ti})\text{O}_3$ (Pzt). *Journal Of Materials Chemistry*, 5, 65-69.
- Choy, J.-H., Han, Y.-S. & Kim, S.-J. 1997. Oxalate Coprecipitation Route To The Piezoelectric $\text{Pb}(\text{Zr,Ti})\text{O}_3$ Oxide. *Journal Of Materials Chemistry*, 7, 1807-1813.
- Cimitan, S., Albonetti, S., Forni, L., Peri, F. & Lazzari, D. 2009. Solvothermal Synthesis And Properties Control Of Doped ZnO Nanoparticles. *Journal Of Colloid And Interface Science*, 329, 73-80.
- Cramer, K., Lima, M. F. S., Magonov, S. N., Hellmann, E. H., Jacobs, M. & Hellmann, G. P. 1998. Atomic Force Microscopy On Tree-Like Crystals In Polyvinylidene Fluoride Blends. *Journal Of Materials Science*, 33, 2305-2312.
- Cullity, B. D. 1956. *Elements Of X-Ray Diffraction*, California, Addison-Wesley Publishing Company Inc.
- Damen, T. C., Porto, S. P. S. & Tell, B. 1966. Raman Effect In Zinc Oxide. *Physical Review*, 142, 570.
- De-Qing, Z., Shao-Jun, W., Hong-Shan, S., Xiu-Li, W. & Mao-Sheng, C. 2007. Synthesis And Mechanism Research Of An Ethylene Glycol-Based Sol-Gel Method For Preparing Pzt Nanopowders. *Journal Of Sol-Gel Science And Technology*, 41, 157-161.
- De Sousa, V. C., Morelli, M. R. & Kiminami, R. H. G. 2000. Combustion Process In The Synthesis Of $\text{ZnO-Bi}_2\text{O}_3$. *Ceramics International*, 26, 561-564.
- Deng, Y., Liu, L., Cheng, Y., Nan, C.-W. & Zhao, S.-J. 2003. Hydrothermal Synthesis And Characterization Of Nanocrystalline Pzt Powders. *Materials Letters*, 57, 1675-1678.
- Djurisic, A. B., Ng, A. M. C. & Chen, X. Y. 2010. ZnO Nanostructures For Optoelectronics: Material Properties And Device Applications. *Progress In Quantum Electronics*, 34, 191-259.
- Dong, M. & Ye, Z. G. 2001. Microstructure And Electrical Properties Of Sol-Gel Derived $\text{Pb}(\text{Zr}_{0.53}\text{Ti}_{0.47})\text{O}_3/\text{MgO}$ Nanoparticles And Composite Ceramics. *Ferroelectrics*, 262, 1187-1192.
- Ebrahimzadeh Abrishami, M., Attaran Kakhki, E., Hosseini, S. M. & Kompany, A. 2010. Characterization Of Zinc Oxide Nanopowders Doped With MnO. *Modern Physics Letters B*, 24.
- Ekambaram, S. 2005. Combustion Synthesis And Characterization Of New Class Of ZnO-Based Ceramic Pigments. *Journal Of Alloys And Compounds*, 390, L4-L6.
- Elshall, M. S., Graiver, D., Pernisz, U. & Baraton, M. I. 1995. Synthesis And Characterization Of Nanoscale Zinc Oxide Particles .1. Laser Vaporization Condensation Technique. *Nanostructured Materials*, 6, 297-300.
- Erol, A., Okur, S., Comba, B., Mermer, Ö. & Arikan, M. Ç. 2010. Humidity Sensing Properties Of ZnO Nanoparticles Synthesized By Sol-Gel Process. *Sensors And Actuators B: Chemical*, 145, 174-180.
- Es-Souni, M. & Zhang, N. 2004. Erbium Doped Pzt And Multilayer Structures For Pyroelectric Applications. *Materials Science And Engineering B*, 106, 79-84.
- Feng, J.-J., Liao, Q.-C., Wang, A.-J. & Chen, J.-R. 2011. Mannite Supported Hydrothermal Synthesis Of Hollow Flower-Like ZnO Structures For Photocatalytic Applications. *Crystengcomm*, 13, 4202-4210.

- Firmino Mendes, S., Costa, C., Sencadas, V., Serrado Nunes, J., Costa, P., Gregorio, R. & Lanceros-Méndez, S. 2009. Effect Of The Ceramic Grain Size And Concentration On The Dynamical Mechanical And Dielectric Behavior Of Poly(Vinilidene Fluoride)/Pb(Zr_{0.53}Ti_{0.47})O₃ Composites. *Applied Physics A: Materials Science & Processing*, 96, 899-908.
- Furukawa, T., Ishida, K. & Fukada, E. 1979. Piezoelectric Properties In The Composite Systems Of Polymers And Pzt Ceramics *Journal Of Applied Physics*, 50, 9.
- Gajbhiye, N. S., Pandey, P. K. & Smitha, P. 2007. Low-Temperature Synthesis Of Nanostructured Pzt For Dielectric Studies. *Synthesis And Reactivity In Inorganic, Metal-Organic, And Nano-Metal Chemistry*, 37, 431 - 435.
- Gebhardt, S., Seffner, L., Schlenkrich, F. & Schönecker, A. 2007. Pzt Thick Films For Sensor And Actuator Applications. *Journal Of The European Ceramic Society*, 27, 4177-4180.
- Geng, J., Jia, X.-D. & Zhu, J.-J. 2011. Sonochemical Selective Synthesis Of ZnO/Cds Core/Shell Nanostructures And Their Optical Properties. *Crystengcomm*, 13, 193-198.
- Ghasemifard, M., Hosseini, S. M. & Khorrami, G. H. 2009a. Synthesis And Structure Of Pmn-Pt Ceramic Nanopowder Free From Pyrochlore Phase. *Ceramics International*, 35, 2899-2905.
- Ghasemifard, M., Hosseini, S. M., Khorsand Zak, A. & Khorrami, G. H. 2009b. Microstructural And Optical Characterization Of Pzt Nanopowder Prepared At Low Temperature. *Physica E: Low-Dimensional Systems And Nanostructures*, 41, 418-422.
- Ghasemifard, M., Hosseini, S. M., Zak, A. K. & Khorrami, G. H. 2009c. Microstructural And Optical Characterization Of Pzt Nanopowder Prepared At Low Temperature. *Physica E-Low-Dimensional Systems & Nanostructures*, 41, 418-422.
- Gong, L., Lu, J. & Ye, Z. 2010. Room-Temperature Growth And Optoelectronic Properties Of Gzo/Zno Bilayer Films On Polycarbonate Substrates By Magnetron Sputtering. *Solar Energy Materials And Solar Cells*, 94, 1282-1285.
- Gong, W., Li, J.-F., Chu, X. & Li, L. 2004. Effect Of Pyrolysis Temperature On Preferential Orientation And Electrical Properties Of Sol-Gel Derived Lead Zirconate Titanate Films. *Journal Of The European Ceramic Society*, 24, 2977-2982.
- Gopalakrishnan, N., Balakrishnan, L., Senthamizh Pavai, V., Elanchezhiyan, J. & Balasubramanian, T. 2011. Characterization Of (Zno)_{1-x}(Aln)_x/Zno Junction For Optoelectronic Applications. *Current Applied Physics*, 11, 834-837.
- Goya, G. F. 2004. Handling The Particle Size And Distribution Of Fe₃O₄ Nanoparticles Through Ball Milling. *Solid State Communications*, 130, 783-787.
- Gui, Y., Li, S., Xu, J. & Li, C. 2008. Study On Tio₂-Doped ZnO Thick Film Gas Sensors Enhanced By Uv Light At Room Temperature. *Microelectronics Journal*, 39, 1120-1125.
- Gupta, N., Singh, H. P. & Sharma, R. K. 2011. Metal Nanoparticles With High Catalytic Activity In Degradation Of Methyl Orange: An Electron Relay Effect. *Journal Of Molecular Catalysis A: Chemical*, 335, 248-252.
- Gurin, V. S. 1998. Nanoparticles Of Ternary Semiconductors In Colloids: Low-Temperature Formation And Quantum Size Effects. *Colloids And Surfaces A: Physicochemical And Engineering Aspects*, 142, 35-40.

- Haixiong, T. & Et Al. 2011. Nanocomposites With Increased Energy Density Through High Aspect Ratio Pzt Nanowires. *Nanotechnology*, 22, 015702.
- Hamdeh, H. H., Eltabey, M. M., Ho, J. C., Lee, P. C., Chen, K. & Chen, Y. Y. 2010. Magnetism In Nanoparticles Of Semiconducting Fesi₂. *Journal Of Magnetism And Magnetic Materials*, 322, 2227-2230.
- Han, N., Hu, P., Zuo, A., Zhang, D., Tian, Y. & Chen, Y. 2010. Photoluminescence Investigation On The Gas Sensing Property Of Zno Nanorods Prepared By Plasma-Enhanced Cvd Method. *Sensors And Actuators B: Chemical*, 145, 114-119.
- Harding, F. 2006. *Breast Cancer: Cause - Prevention - Cure*, Aylesbury, Tekline Publishing.
- Harris, D. C. & Bertolucci, M. D. 1978. *Symmetry, Spectroscopy And Introduction To Vibrational Electronic Spectroscopy*, New York, Dover.
- He, Y. 2004. Synthesis Of Zno Nanoparticles With Narrow Size Distribution Under Pulsed Microwave Heating. *China Particuology*, 2, 168-170.
- Hedayati, M., Salehi, M., Bagheri, R., Panjepour, M. & Maghzian, A. 2011. Ball Milling Preparation And Characterization Of Poly (Ether Ether Ketone)/Surface Modified Silica Nanocomposite. *Powder Technology*, 207, 296-303.
- Heszler, P. 2002. Emission Spectroscopy And Size Distribution Of Gas Phase Nanoparticles Generated By Laser-Based Methods. *Applied Surface Science*, 186, 538-545.
- Hingorani, S., Pillai, V., Kumar, P., Multani, M. S. & Shah, D. O. 1993. Microemulsion Mediated Synthesis Of Zinc-Oxide Nanoparticles For Varistor Studies. *Materials Research Bulletin*, 28, 1303-1310.
- Hongsith, N., Wongrat, E., Kerdcharoen, T. & Choopun, S. 2010. Sensor Response Formula For Sensor Based On Zno Nanostructures. *Sensors And Actuators B: Chemical*, 144, 67-72.
- Hosokawa, M., Nogi, K., Naito, M. & Yokoyama, T. 2007. *Nanoparticle Technology Handbook*, Amsterdam, Elsevier
- Hsiao, C. C., Hu, Y. C., Chang, R. C. & Chao, C. K. 2009. Residual Stresses And Mechanical Properties Of A Zno Pyroelectric Sensor. *Theoretical And Applied Fracture Mechanics*, 52, 1-6.
- Hsueh, T.-J., Chen, Y.-W., Chang, S.-J., Wang, S.-F., Hsu, C.-L., Lin, Y.-R., Lin, T.-S. & Chen, I. C. 2007. Zno Nanowire-Based Co Sensors Prepared On Patterned Zno:Ga/Sio₂/Si Templates. *Sensors And Actuators B: Chemical*, 125, 498-503.
- Huang, A. & Caro, J. 2010. Novel Zinc Oxide Twins With Perfect Mirror Symmetry By Solvothermal Synthesis Method. *Crystengcomm*, 12, 685-687.
- Hwang, C.-C. & Wu, T.-Y. 2004. Synthesis And Characterization Of Nanocrystalline Zno Powders By A Novel Combustion Synthesis Method. *Materials Science And Engineering B*, 111, 197-206.
- Ismail, A. A., El-Midany, A., Abdel-Aal, E. A. & El-Shall, H. 2005. Application Of Statistical Design To Optimize The Preparation Of Zno Nanoparticles Via Hydrothermal Technique. *Materials Letters*, 59, 1924-1928.
- Jayasinghe, S. N., Dorey, R. A., Edirisinghe, M. J. & Luklinska, Z. B. 2005. Preparation Of Lead Zirconate Titanate Nano-Powder By Electrohydrodynamic Atomization. *Applied Physics A: Materials Science & Processing*, 80, 723-725.
- Jeong, G.-H. 2009. Surface Functionalization Of Single-Walled Carbon Nanotubes Using Metal Nanoparticles. *Transactions Of Nonferrous Metals Society Of China*, 19, 1009-1012.

- Jia, Z., Chang, Q., Qin, J. & Sun, H. 2010. Preparation Of Nanoparticles With A Continuous Gas-Liquid Membrane Contactor: Absorption Process. *Journal Of Membrane Science*, 352, 50-54.
- Jimenez-Cadena, G., Comini, E., Ferroni, M., Vomiero, A. & Sberveglieri, G. 2010. Synthesis Of Different ZnO Nanostructures By Modified Pvd Process And Potential Use For Dye-Sensitized Solar Cells. *Materials Chemistry And Physics*, 124, 694-698.
- Jin, Z. C., Hamberg, I., Granqvist, C. G., Sernelius, B. E. & Berggren, K. F. 1988. Reactively Sputtered ZnO: Al Films For Energy-Efficient Windows. *Thin Solid Films*, 164, 381-386.
- Joni, I. M., Purwanto, A., Iskandar, F., Hazata, M. & Okuyama, K. 2009. Intense Uv-Light Absorption Of ZnO Nanoparticles Prepared Using A Pulse Combustion-Spray Pyrolysis Method. *Chemical Engineering Journal*, 155, 433-441.
- Kandjani, A. E., Tabriz, M. F. & Pourabbas, B. 2008. Sonochemical Synthesis Of ZnO Nanoparticles: The Effect Of Temperature And Sonication Power. *Materials Research Bulletin*, 43, 645-654.
- Kaschner, A., Haboek, U., Martin, S., Matthias, S., Kaczmarczyk, G., Hoffmann, A., Thomsen, C., Zeuner, A., Alves, H. R., Hofmann, D. M. & Meyer, B. K. 2002. Nitrogen-Related Local Vibrational Modes In ZnO:N. *Applied Physics Letters*, 80.
- Kassab, L. P. R., Ferreira Freitas, L., Ozga, K., Brik, M. G. & Wojciechowski, A. 2010. ZnO:TeO₂-Yb/Tm Glasses With Silver Nanoparticles As Laser Operated Quantum Electronic Devices. *Optics & Laser Technology*, 42, 1340-1343.
- Kim, S. H. & Zachariah, M. R. 2007. Gas-Phase Growth Of Diameter-Controlled Carbon Nanotubes. *Materials Letters*, 61, 2079-2083.
- Kittle, C. 1988. *Introduction To Solid State Physics*, Munich, Oldenbourg.
- Koyano, M., Quocbao, P., Thanhbinh, L. T., Hongha, L., Ngoclong, N. & Katayama, S. I. 2002. Photoluminescence And Raman Spectra Of ZnO Thin Films By Charged Liquid Cluster Beam Technique. *Physica Status Solidi (A)*, 193, 125-131.
- Kruis, F. E., Fissan, H. & Rellinghaus, B. 2000. Sintering And Evaporation Characteristics Of Gas-Phase Synthesis Of Size-Selected Pbs Nanoparticles. *Materials Science And Engineering B*, 69-70, 329-334.
- Kruis, F. E., Goossens, A. & Fissan, H. 1996. Synthesis Of Semiconducting Nanoparticles. *Journal Of Aerosol Science*, 27, S165-S166.
- Kubelka, P. & Munk, F. 1931. An Article On Optics Of Paint Layers. *Zeit. Für Tekn. Physik*, 12.
- Kumar, A., Singh, F., Khan, S. A., Agarwal, D. C., Tripathi, A., Avasthi, D. K. & Pivin, J. C. 2006. Precipitation Of Semiconducting Carbon Nanoparticles In Ion Irradiated Gels. *Nuclear Instruments And Methods In Physics Research Section B: Beam Interactions With Materials And Atoms*, 244, 23-26.
- Kundu, T. K. & Chakravorty, D. 1995. Nanocomposites Of Lead-Zirconate-Titanate Glass-Ceramics And Metallic Silver. *Applied Physics Letters*, 67, 2732-2734.
- Labuayai, S., Promarak, V. & Maensiri, S. 2009. Synthesis And Optical Properties Of Nanocrystalline ZnO Powders Prepared By A Direct Thermal Decomposition Route. *Applied Physics A: Materials Science & Processing*, 94, 755-761.

- Lähde, A., Raula, J. & Kauppinen, E. I. 2008. Simultaneous Synthesis And Coating Of Salbutamol Sulphate Nanoparticles With L-Leucine In The Gas Phase. *International Journal Of Pharmaceutics*, 358, 256-262.
- Lao, J. Y., Huang, J. Y., Wang, D. Z. & Ren, Z. F. 2003. Zno Nanobridges And Nanonails. *Nano Letters*, 3, 235-238.
- Last, J. T. 1957. Infrared-Absorption Studies On Barium Titanate And Related Materials. *Physical Review*, 105, 1740.
- Lathika Devi, S. K., Sudarsana Kumar, K. & Balakrishnan, A. 2011. Rapid Synthesis Of Pure And Narrowly Distributed Eu Doped Zno Nanoparticles By Solution Combustion Method. *Materials Letters*, 65, 35-37.
- Lavat, A. E., Wagner, C. C. & Tasca, J. E. 2008. Interaction Of Co-Zno Pigments With Ceramic Frits: A Combined Study By Xrd, Ftir And Uv-Visible. *Ceramics International*, 34, 2147-2153.
- Law, C. W., Tong, K. Y., Li, J. H. & Li, K. 1998. Effect Of Pyrolysis Temperature On The Characteristics Of Pzt Films Deposited By The Sol-Gel Method. *Thin Solid Films*, 335, 220-224.
- Lee, J., Easteal, A. J., Pal, U. & Bhattacharyya, D. 2009. Evolution Of Zno Nanostructures In Sol-Gel Synthesis. *Current Applied Physics*, 9, 792-796.
- Lee, J. S., Islam, M. S. & Kim, S. 2007. Photoresponses Of Zno Nanobridge Devices Fabricated Using A Single-Step Thermal Evaporation Method. *Sensors And Actuators B: Chemical*, 126, 73-77.
- Lee, S. & Jun, B. 2005. Preparation Of Ultrafine Pzt Powders By Ultrasonic Spray Combustion Synthesis (Uscs). *Ceramics International*, 31, 53-56.
- Lenza, R. F. S. & Vasconcelos, W. L. 2003. Study Of The Influence Of Some Dccas On The Structure Of Sol-Gel Silica Membranes. *Journal Of Non-Crystalline Solids*, 330, 216-225.
- Li, C., Liang, Z., Xiao, H., Wu, Y. & Liu, Y. 2010. Synthesis Of Zno/Zn₂SiO₄/SiO₂ Composite Pigments With Enhanced Reflectance And Radiation-Stability Under Low-Energy Proton Irradiation. *Materials Letters*, 64, 1972-1974.
- Li, X., Guan, Z., Agne, T., Wolf, H. & Wichert, T. 2004. Grain Size Effect On The Temperature Dependence Of The Electric Field Gradient In Nanocrystalline In. *Hyperfine Interactions*, 159, 63-69.
- Liao, K.-T., Shimpi, P. & Gao, P.-X. 2011. Thermal Oxidation Of Cu Nanofilm On Three-Dimensional Zno Nanorod Arrays. *Journal Of Materials Chemistry*.
- Linardos, S., Zhang, Q. & Alcock, J. R. 2006. Preparation Of Sub-Micron Pzt Particles With The Sol-Gel Technique. *Journal Of The European Ceramic Society*, 26, 117-123.
- Liu, C., Zou, B., Rondinone, A. J. & Zhang, Z. J. 2001. Sol-Gel Synthesis Of Free-Standing Ferroelectric Lead Zirconate Titanate Nanoparticle. *Journal Of American Chemical Society*, 123, 3.
- Liu, P. 2006. Facile Preparation Of Monodispersed Core/Shell Zinc Oxide@Polystyrene (Zno@Ps) Nanoparticles Via Soapless Seeded Microemulsion Polymerization. *Colloids And Surfaces A: Physicochemical And Engineering Aspects*, 291, 155-161.
- Liu, Y., Dong, J., Hesketh, P. J. & Liu, M. 2005. Synthesis And Gas Sensing Properties Of Zno Single Crystal Flakes. *Journal Of Materials Chemistry*, 15, 2316-2320.

- Lokhande, C. D., Gondkar, P. M., Mane, R. S., Shinde, V. R. & Han, S.-H. 2009. Cbd Grown ZnO-Based Gas Sensors And Dye-Sensitized Solar Cells. *Journal Of Alloys And Compounds*, 475, 304-311.
- Look, D. C. 2001. Recent Advances In ZnO Materials And Devices. *Materials Science And Engineering: B*, 80, 383-387.
- Lovinger, A. J. 1982. *In Developments In Crystalline Polymers*, London, Elsevier.
- Lucarini, V., Saarinen, J. J., Peiponen, K. E. & Vartiainen, E. M. 2004. *Kramers–Kronig Relations In Optical Materials Research*, New York, Springer Berlin Heidelberg.
- Luo, Q.-P., Lei, B.-X., Yu, X.-Y., Kuang, D.-B. & Su, C.-Y. 2011. Hierarchical ZnO Rod-In-Tube Nano-Architecture Arrays Produced Via A Two-Step Hydrothermal And Ultrasonication Process. *Journal Of Materials Chemistry*, 21, 8709-8714.
- Lupan, O., Chai, G. & Chow, L. 2008. Novel Hydrogen Gas Sensor Based On Single ZnO Nanorod. *Microelectronic Engineering*, 85, 2220-2225.
- Ma, S., Li, R., Lv, C., Xu, W. & Gou, X. 2011. Facile Synthesis Of ZnO Nanorod Arrays And Hierarchical Nanostructures For Photocatalysis And Gas Sensor Applications. *Journal Of Hazardous Materials*, 192, 730-740.
- Ma, W., Zhang, J., Chen, S. & Wang, X. 2008. [Beta]-Phase Of Poly(Vinylidene Fluoride) Formation In Poly(Vinylidene Fluoride)/Poly(Methyl Methacrylate) Blend From Solutions. *Applied Surface Science*, 254, 5635-5642.
- Mansur, H. S. 2010. Quantum Dots And Nanocomposites. *Wiley Interdisciplinary Reviews: Nanomedicine And Nanobiotechnology*, 2, 113-129.
- Mark, F. 2001. *Optical Properties Of Solids*, London, Oxford University Press.
- Maxwell, J. C. 1954. *A Treatise On Electricity And Magnetism*, New York, Dover Publ.Co.
- Mitra, S. S., Brafman, O., Daniels, W. B. & Crawford, R. K. 1969. Pressure-Induced Phonon Frequency Shifts Measured By Raman Scattering. *Physical Review*, 186, 942.
- Mitsui, A. & Sato, K. 2004. Thermal Stability Of Electrical Resistance Of (Zn:Ga,Y)/(Zn:Ga)/(Zn:Ga,Y) Multilayers For Electrically Heated Windows. *Vacuum*, 74, 747-751.
- Modeshia, D. R. & Walton, R. I. 2010. Solvothermal Synthesis Of Perovskites And Pyrochlores: Crystallisation Of Functional Oxides Under Mild Conditions. *Chemical Society Reviews*, 39, 4303-4325.
- Moleski, R., Leontidis, E. & Krumeich, F. 2006. Controlled Production Of ZnO Nanoparticles From Zinc Glycerolate In A Sol-Gel Silica Matrix. *Journal Of Colloid And Interface Science*, 302, 246-253.
- Moreno-Couranjou, M., Monthieux, M., Gonzalez-Aguilar, J. & Fulcheri, L. 2009. A Non-Thermal Plasma Process For The Gas Phase Synthesis Of Carbon Nanoparticles. *Carbon*, 47, 2310-2321.
- Mu, G., Yang, S., Li, J. & Gu, M. 2007. Synthesis Of Pzt Nanocrystalline Powder By A Modified Sol-Gel Process Using Water As Primary Solvent Source. *Journal Of Materials Processing Technology*, 182, 382-386.
- Muller, A., Lorenz, M., Brachwitz, K., Lenzner, J., Mittwoch, K., Skorupa, W., Grundmann, M. & Hoche, T. 2011. Fresnoite Thin Films Grown By Pulsed Laser Deposition: Photoluminescence And Laser Crystallization. *Crystengcomm*.

- Nakamura, R., Lee, J. G., Tokozakura, D., Mori, H. & Nakajima, H. 2007. Formation Of Hollow ZnO Through Low-Temperature Oxidation Of Zn Nanoparticles. *Materials Letters*, 61, 1060-1063.
- Naksata, M., Brydson, R. & Milne, S. J. 2003. Properties Of Lead Zirconate Titanate Thin Films Prepared Using A Sol-Gel Route. *Journal Of The American Ceramic Society*, 86, 1560-1566.
- Neppiras, E. A. 1972. Piezoelectric Ceramics 1971 : B. Jaffe, W. R. Cook Jr And H. Jaffe. London And New York: Academic Press. 317 Pp., £5.50. *Journal Of Sound And Vibration*, 20, 562-563.
- Nersisyan, H. H., Yang, B. S., Kim, B. B., Lee, J. H. & Won, C. W. 2005. Combustion Synthesis And Characterization Of Spherical Pzt Powder. *Materials Letters*, 59, 1066-1070.
- Ng, S. S., Hassan, Z. & Abu Hassan, H. 2006. Kramers-Kronig Analysis Of Infrared Reflectance Spectra With A Single Resonance. *Journal Of Teknologi*, 44, 10.
- Nualpralaksana, S., Phanichphant, S., Hengst, M. & Heimann, R. B. 2001. Hydrothermal Synthesis Of Lead Zirconate Titanate (Pzt) And Lead Lanthanum Zirconate Titanate (Plzt) Nanopowders. *Cfi-Ceramic Forum International*, 78, E34-E38.
- Nye, J. F. 1985. *Physical Properties Of Crystals: Their Representation By Tensors And Matrices*, New York, Oxford.
- Ohara, S., Sato, K., Tan, Z., Shimoda, H., Ueda, M. & Fukui, T. 2010. Novel Mechanochemical Synthesis Of Fine Fe₂O₃ Nanoparticles By A High-Speed Ball-Milling Process. *Journal Of Alloys And Compounds*, 504, L17-L19.
- Özgür, Ü., Alivov, Y. I., Liu, C., Teke, A., Reshchikov, M. A., Doğan, S., Avrutin, V., Cho, S.-J. & Morkoç, H. 2005. A Comprehensive Review Of ZnO Materials And Devices *Journal Of Applied Physics* 98.
- Padmanabhan, S. C., Ledwith, D., Pillai, S. C., McCormack, D. E. & Kelly, J. M. 2009. Microwave-Assisted Synthesis Of ZnO Micro-Javelins. *Journal Of Materials Chemistry*, 19, 9250-9259.
- Pan, Z. W., Dai, Z. R. & Wang, Z. L. 2001. Nanobelts Of Semiconducting Oxides. *Science*, 291, 1947-1949.
- Panigrahy, B., Aslam, M., Misra, D. S. & Bahadur, D. 2009. Polymer-Mediated Shape-Selective Synthesis Of ZnO Nanostructures Using A Single-Step Aqueous Approach. *Crystengcomm*, 11, 1920-1925.
- Park, I., Lim, Y., Noh, S., Lee, D., Meister, M., Amsden, J. J., Laquai, F., Lee, C. & Yoon, D. Y. 2011. Enhanced Photovoltaic Performance Of ZnO Nanoparticle/Poly(Phenylene Vinylene) Hybrid Photovoltaic Cells By Semiconducting Surfactant. *Organic Electronics*, 12, 424-428.
- Perry, C. H., Khanna, B. N. & Rupprecht, G. 1964. Infrared Studies Of Perovskite Titanates. *Physical Review*, 135, A408.
- Phan, T.-L., Yu, S. C., Vincent, R., Dan, N. H. & Shi, W. S. 2010. Photoluminescence Properties Of Various Cvd-Grown ZnO Nanostructures. *Journal Of Luminescence*, 130, 1142-1146.
- Phillips, J., Bowen, W., Cagin, E. & Wang, W. 2011. Electronic And Optoelectronic Devices Based On Semiconducting Zinc Oxide. In: Pallab, B., Roberto, F. & Hiroshi, K. (Eds.) *Comprehensive Semiconductor Science And Technology*. Amsterdam: Elsevier.

- Porto, S. P. S. & Krishnan, R. S. 1967. Raman Effect Of Corundum. *The Journal Of Chemical Physics*, 47, 1009-1012.
- Prakash, G. V., Pradeesh, K., Kumar, A., Kumar, R., Rao, S. V., Markham, M. L. & Baumberg, J. J. 2008. Fabrication And Optoelectronic Characterisation Of Zno Photonic Structures. *Materials Letters*, 62, 1183-1186.
- Qian, D., Jiang, J. Z. & Lenvig Hansen, P. 2003. Preparation Of Zno Nanocrystals Via Ultrasonic Irradiation. *Chemical Communications*, 1078-1079.
- Riddin, T., Gericke, M. & Whiteley, C. G. 2010. Biological Synthesis Of Platinum Nanoparticles: Effect Of Initial Metal Concentration. *Enzyme And Microbial Technology*, 46, 501-505.
- Rogers, K. D. & Daniels, P. 2002. An X-Ray Diffraction Study Of The Effects Of Heat Treatment On Bone Mineral Microstructure. *Biomaterials*, 23, 2577-2585.
- Roux, J. F., Cabaud, B., Treilleux, M., Hoareau, A. & Fuchs, G. 1995. Synthesis Of Size Controlled Nanoparticles In An Insulating Matrix. *Nanostructured Materials*, 6, 525-528.
- Rozenberg, E., Jung, G., Auslender, M., Gorodetsky, G., Felner, I., Sominski, E., Gedanken, A. & Mukovskii, Y. M. 2006. Magnetic Properties Of Crystalline La_{0.9}Ca_{0.1}MnO₃: Comparison Of Bulk And Nanometer-Sized Samples. *Journal Of Applied Physics*, 99, 08q305-3.
- Sahoo, T., Kim, M., Baek, J. H., Jeon, S.-R., Kim, J. S., Yu, Y.-T., Lee, C.-R. & Lee, I.-H. 2011. Synthesis And Characterization Of Porous Zno Nanoparticles By Hydrothermal Treatment Of As Pure Aqueous Precursor. *Materials Research Bulletin*, 46, 525-530.
- Seol, K. S., Tomita, S., Takeuchi, K., Miyagawa, T., Katagiri, T. & Ohki, Y. 2002. Gas-Phase Production Of Monodisperse Lead Zirconate Titanate Nanoparticles. *Applied Physics Letters*, 81, 1893-1895.
- Shao, D., Gao, D., Wei, Q., Zhu, H., Tao, L. & Ge, M. 2010. Structures And Properties Of The Polyacrylonitrile Fabric Coated With Zno-Ag Composites. *Applied Surface Science*, 257, 1306-1309.
- Shaw, D. T., Goronkin, H. & Roco, M. C. 1997. *Quantum Size Effect On The Absorbance Of Zno Nanoparticles* [Online]. Eindhoven: Philips Research Laboratories. [Accessed].
- Shibata, T., Unno, K., Makino, E., Ito, Y. & Shimada, S. 2002. Characterization Of Sputtered Zno Thin Film As Sensor And Actuator For Diamond Afm Probe. *Sensors And Actuators A: Physical*, 102, 106-113.
- Sik Kim, W., Ha, S.-M., Park, H.-H. & Eun Kim, C. 1999. The Effects Of Cation-Substitution On The Ferroelectric Properties Of Sol-Gel Derived Pzt Thin Film For Fram Application. *Thin Solid Films*, 355-356, 531-535.
- Song, Y.-W., Kim, K. & Lee, S. Y. 2009. Morphology Transition Of Ag-Doped Zno Nanostructures In Hot-Walled Pulsed Laser Deposition. *Thin Solid Films*, 518, 1318-1322.
- Spitzer, W. G., Miller, R. C., Kleinman, D. A. & Howarth, L. E. 1962. Far Infrared Dielectric Dispersion In BaTiO₃, SrTiO₃, And TiO₂. *Physical Review*, 126, 1710.
- Sriprang, N., Kaewchinda, D., Kennedy, J. D. & Milne, S. J. 2000. Processing And Sol Chemistry Of A Triol-Based Sol-Gel Route For Preparing Lead Zirconate Titanate Thin Films. *Journal Of The American Ceramic Society*, 83, 1914-1920.

- Stroschio, M. A. & Dutta, M. 2001. *Phonons In Nanostructures*, London, Cambridge University Press.
- Sulcova, P. & Trojan, M. 1999. New Green Pigments; ZnO-COO. *Dyes And Pigments*, 40, 83-86.
- Sun, Y., Hu, J., Wang, N., Zou, R., Wu, J., Song, Y., Chen, H., Chen, H. & Chen, Z. 2010. Controllable Hydrothermal Synthesis, Growth Mechanism, And Properties Of ZnO Three-Dimensional Structures. *New Journal Of Chemistry*, 34, 732-737.
- Suwanboon, S., Amornpitoksuk, P. & Bangrak, P. 2011. Synthesis, Characterization And Optical Properties Of ZnO Nanoparticles Prepared Via A High-Energy Ball Milling Technique. *Ceramics International*, 37, 333-340.
- Swihart, M. T. 2003. Vapor-Phase Synthesis Of Nanoparticles. *Current Opinion In Colloid & Interface Science*, 8, 127-133.
- Tagliente, M. A. & Massaro, M. 2008. Strain-Driven (0 0 2) Preferred Orientation Of ZnO Nanoparticles In Ion-Implanted Silica. *Nuclear Instruments And Methods In Physics Research Section B: Beam Interactions With Materials And Atoms*, 266, 1055-1061.
- Tanase, T., Nishikata, A., Iizuka, Y., Kobayashi, Y., Konno, M. & Miwa, T. 2002. Low-Temperature Synthesis Of Single-Phase Lead Zirconate Titanate Thin Film With A Nanoseeding Technique. *Journal Of The Ceramic Society Of Japan*, 110, 911-915.
- Tartaj, J., Moure, C. & Duran, P. 2001. Influence Of Seeding On The Crystallisation Kinetics Of PbTiO₃ From Gel-Derived Precursors. *Ceramics International*, 27, 741-747.
- Thomas, P., Varughese, K. T., Dwarakanath, K. & Varma, K. B. R. 2010. Dielectric Properties Of Poly(Vinylidene Fluoride)/CaCu₃Ti₄O₁₂ Composites. *Composites Science And Technology*, 70, 539-545.
- Thongtem, T., Phuruangrat, A. & Thongtem, S. 2010. Characterization Of Nanostructured ZnO Produced By Microwave Irradiation. *Ceramics International*, 36, 257-262.
- Tonto, P., Mekasuwandumrong, O., Phatanasri, S., Pavarajarn, V. & Prasertdam, P. 2008. Preparation Of ZnO Nanorod By Solvothermal Reaction Of Zinc Acetate In Various Alcohols. *Ceramics International*, 34, 57-62.
- Tsai, J. Z., Chen, C. J., Chen, W. Y., Liu, J. T., Liao, C. Y. & Hsin, Y. M. 2009. A New PZT Piezoelectric Sensor For Gravimetric Applications Using The Resonance-Frequency Detection. *Sensors And Actuators B: Chemical*, 139, 259-264.
- Tsuboi, M. & Wada, A. 1968. Optically Active Lattice Vibrations In Wurtzite-Type Crystals Of Zinc Oxide And Cadmium Sulfide. *The Journal Of Chemical Physics*, 48, 2615-2618.
- Tsuji, T. & Hirohashi, M. 2000. Influence Of Oxygen Partial Pressure On Transparency And Conductivity Of Rf Sputtered Al-Doped ZnO Thin Films. *Applied Surface Science*, 157, 47-51.
- Tsujino, J., Hidai, K., Hasegawa, A., Kanai, R., Matsuura, H., Matsushima, K. & Ueoka, T. 2002. Ultrasonic Butt Welding Of Aluminum, Aluminum Alloy And Stainless Steel Plate Specimens. *Ultrasonics*, 40, 371-374.
- Tu, Y.-L., Calzada, M. L., Phillips, N. J. & Milne, S. J. 1996. Synthesis And Electrical Characterization Of Thin Films Of Pt And PZT Made From A Diol-Based Sol-Gel Route. *Journal Of The American Ceramic Society*, 79, 441-448.
- Vafaei, M. & Ghamsari, M. S. 2007. Preparation And Characterization Of ZnO Nanoparticles By A Novel Sol-Gel Route. *Materials Letters*, 61, 3265-3268.

- Van Ommen, J. R., Yurteri, C. U., Ellis, N. & Kelder, E. M. 2010. Scalable Gas-Phase Processes To Create Nanostructured Particles. *Particuology*, 8, 572-577.
- Wang, C., Wang, E., Shen, E., Gao, L., Kang, Z., Tian, C., Zhang, C. & Lan, Y. 2006. Growth Of Zno Nanoparticles From Nanowhisker Precursor With A Simple Solvothermal Route. *Materials Research Bulletin*, 41, 2298-2302.
- Wang, D. G., Chen, C. Z., Ma, J. & Liu, T. H. 2008. Lead-Based Titanate Ferroelectric Thin Films Fabricated By A Sol-Gel Technique. *Applied Surface Science*, 255, 1637-1645.
- Wang, J., Li, Q. & Egerton, R. F. 2007. Probing The Electronic Structure Of Zno Nanowires By Valence Electron Energy Loss Spectroscopy. *Micron*, 38, 346-353.
- Wang, L.-L. & Jiang, J.-S. 2007. Preparation Of [Alpha]-Fe₂O₃ Nanoparticles By High-Energy Ball Milling. *Physica B: Condensed Matter*, 390, 23-27.
- Wang, Y., Zhang, C., Bi, S. & Luo, G. 2010. Preparation Of Zno Nanoparticles Using The Direct Precipitation Method In A Membrane Dispersion Micro-Structured Reactor. *Powder Technology*, 202, 130-136.
- Wegner, K. & Pratsinis, S. E. 2005. Gas-Phase Synthesis Of Nanoparticles: Scale-Up And Design Of Flame Reactors. *Powder Technology*, 150, 117-122.
- Wei, C. S., Lin, Y. Y., Hu, Y. C., Wu, C. W., Shih, C. K., Huang, C. T. & Chang, S. H. 2006. Partial-Electroded Zno Pyroelectric Sensors For Responsivity Improvement. *Sensors And Actuators A: Physical*, 128, 18-24.
- Wen, W. J., Tam, W. Y. & Sheng, P. 1998. Electrorheological Fluids Using Bidispersed Particles. *Journal Of Materials Research*, 13, 2783-2786.
- Wu, A., Vilarinho, P. M., Salvado, I. M. M. & Baptista, J. L. 2000. Sol-Gel Preparation Of Lead Zirconate Titanate Powders And Ceramics: Effect Of Alkoxide Stabilizers And Lead Precursors. *Journal Of The American Ceramic Society*, 83, 1379-1385.
- Xu, G., Weng, W., Yao, J., Du, P. & Han, G. 2003. Low Temperature Synthesis Of Lead Zirconate Titanate Powder By Hydroxide Co-Precipitation. *Microelectronic Engineering*, 66, 568-573.
- Xu, G., Zhao, G., Ren, Z., Shen, G. & Han, G. 2006a. Pva Assisted Synthesis Of Nanosized Perovskite Pzt Powder By A Two-Stage Precipitation Route. *Materials Letters*, 60, 685-688.
- Xu, H., Liu, X., Cui, D., Li, M. & Jiang, M. 2006b. A Novel Method For Improving The Performance Of Zno Gas Sensors. *Sensors And Actuators B: Chemical*, 114, 301-307.
- Yadav, R. S., Mishra, P. & Pandey, A. C. 2008. Growth Mechanism And Optical Property Of Zno Nanoparticles Synthesized By Sonochemical Method. *Ultrasonics Sonochemistry*, 15, 863-868.
- Yamada, T., Ueda, T. & Kitayama, T. 1982. Piezoelectricity Of A High-Content Lead Zirconate Titanate/Polymer Composite. *J. Appl. Phys*, 53, 5.
- Yang, R., Jianmin, Q., Marinis, T. & Wong, C. P. 2000. A Precise Numerical Prediction Of Effective Dielectric Constant For Polymer-Ceramic Composite Based On Effective-Medium Theory. *Components And Packaging Technologies, Ieee Transactions On*, 23, 680-683.
- Yasui, H., Kurosawa, M. K. & Higuchi, T. 2002. Hydrothermally Deposited Pzt Film And Its Application To Bending Vibration Devices. *Sensors And Actuators A: Physical*, 96, 28-33.

- Yebara, D. M., Kiil, S., Weinell, C. E. & Dam-Johansen, K. 2006. Dissolution Rate Measurements Of Sea Water Soluble Pigments For Antifouling Paints: ZnO. *Progress In Organic Coatings*, 56, 327-337.
- Yi, J., Lee, J. M. & Park, W. I. 2011. Vertically Aligned ZnO Nanorods And Graphene Hybrid Architectures For High-Sensitive Flexible Gas Sensors. *Sensors And Actuators B: Chemical*, 155, 264-269.
- Yogamalar, R., Srinivasan, R., Vinu, A., Ariga, K. & Bose, A. C. 2009. X-Ray Peak Broadening Analysis In ZnO Nanoparticles. *Solid State Communications*, 149, 1919-1923.
- Yousefi, R. & Kamaluddin, B. 2009. Effect Of S- And Sn-Doping To The Optical Properties Of ZnO Nanobelts. *Applied Surface Science*, 255, 9376-9380.
- Yousefi, R. & Zak, A. K. 2011. Growth And Characterization Of ZnO Nanowires Grown On The Si(1 1 1) And Si(1 0 0) Substrates: Optical Properties And Biaxial Stress Of Nanowires. *Materials Science In Semiconductor Processing*, 14, 170-174.
- Yu, H., Yu, J., Cheng, B. & Zhou, M. 2006. Effects Of Hydrothermal Post-Treatment On Microstructures And Morphology Of Titanate Nanoribbons. *Journal Of Solid State Chemistry*, 179, 349-354.
- Yu, J., Li, C. & Liu, S. 2008a. Effect Of Pss On Morphology And Optical Properties Of ZnO. *Journal Of Colloid And Interface Science*, 326, 433-438.
- Yu, L. & Cebe, P. 2009. Crystal Polymorphism In Electrospun Composite Nanofibers Of Poly(Vinylidene Fluoride) With Nanoclay. *Polymer*, 50, 2133-2141.
- Yu, X., Wang, J., Zhang, M., Yang, L., Li, J., Yang, P. & Cao, D. 2008b. Synthesis, Characterization And Anticorrosion Performance Of Molybdate Pillared Hydrotalcite/In Situ Created ZnO Composite As Pigment For Mg-Li Alloy Protection. *Surface And Coatings Technology*, 203, 250-255.
- Yue, Z., Li, L., Zhou, J., Zhang, H. & Gui, Z. 1999. Preparation And Characterization Of Ni_{0.5}Zn_{0.5}Ferrite Nanocrystalline Powders By Auto-Combustion Of Nitrate-Citrate Gels. *Materials Science And Engineering: B*, 64, 68-72.
- Zak, A. K. & Majid, W. H. A. 2010. Characterization And X-Ray Peak Broadening Analysis In Pzt Nanoparticles Prepared By Modified Sol-Gel Method. *Ceramics International*, 36, 1905-1910.
- Zeng, T., Dong, X. L., Chen, H. & Wang, Y. L. 2006. The Effects Of Sintering Behavior On Piezoelectric Properties Of Porous Pzt Ceramics For Hydrophone Application. *Materials Science And Engineering: B*, 131, 181-185.
- Zhang, J.-M., Zhang, Y., Xu, K.-W. & Ji, V. 2006a. General Compliance Transformation Relation And Applications For Anisotropic Hexagonal Metals. *Solid State Communications*, 139, 87-91.
- Zhang, J., Yang, Y., Jiang, F., Xu, B. & Li, J. 2005. Controlled Growth Of Semiconducting Oxides Hierarchical Nanostructures. *Journal Of Solid State Chemistry*, 178, 2804-2810.
- Zhang, M., Salvado, I. M. M. & Vilarinho, P. M. 2003. Synthesis And Characterization Of Lead Zirconate Titanate Fibers Prepared By The Sol-Gel Method: The Role Of The Acid. *Journal Of The American Ceramic Society*, 86, 775-781.
- Zhang, Q. Q., Djuth, F. T., Zhou, Q. F., Hu, C. H., Cha, J. H. & Shung, K. K. 2006b. High Frequency Broadband Pzt Thick Film Ultrasonic Transducers For Medical Imaging Applications. *Ultrasonics*, 44, E711-E715.

- Zhang, W.-H. & Zhang, W.-D. 2008. Fabrication Of Sno₂-Zno Nanocomposite Sensor For Selective Sensing Of Trimethylamine And The Freshness Of Fishes. *Sensors And Actuators B: Chemical*, 134, 403-408.
- Zhu, H., Hüpkes, J., Bunte, E., Owen, J. & Huang, S. M. 2011. Novel Etching Method On High Rate Zno:Al Thin Films Reactively Sputtered From Dual Tube Metallic Targets For Silicon-Based Solar Cells. *Solar Energy Materials And Solar Cells*, 95, 964-968.
- Zimmermann-Chopin, R. & Auer, S. 1994. Spray Drying Of Sol-Gel Precursors For The Manufacturing Of Pzt Powders. *Journal Of Sol-Gel Science And Technology*, 3, 101-107.
- Zinck, C., Pinceau, D., Defaÿ, E., Delevoye, E. & Barbier, D. 2004. Development And Characterization Of Membranes Actuated By A Pzt Thin Film For Mems Applications. *Sensors And Actuators A: Physical*, 115, 483-489.

LIST OF SELECTED ISI PUBLICATIONS

1. **Zak, A. K.** and Majid, W. H. A. (2010), 'Characterization and X-ray peak broadening analysis in PZT nanoparticles prepared by modified sol-gel method', *Ceramics International*, 36 (6), 1905-10.
2. **Zak, A. K.** and Abd Majid, W. H. (2011), 'Effect of solvent on structure and optical properties of PZT nanoparticles prepared by sol-gel method, in infrared region', *Ceramics International*, 37 (3), 753-58.
3. **Zak, A. K.**, Abd Majid, W. H., Darroudi M., (2010), 'Synthesis and characterization of sot-gel derived single-phase PZT nanoparticles in aqueous polyol solution', *Journal of Optoelectronics and Advanced Materials*, 12 (8), 1714-19.
4. **Zak, A. K.**, Chen, G. Majid, W.H. Abd., Darroudi, M. Velayutham, T.S., (2011), 'Experimental and theoretical dielectric studies of PVDF/PZT nanocomposite thin films', *Ceramics Internatuonal*, 37, 1653-1660.
5. **Zak, A. K.**, Razali, R., Majid, W. H., Darroudi M., (2011), 'Synthesis and characterization of a narrow size distribution of zinc oxide nanoparticles', *International Journal of Nanomedicine*, 6, 1399-403.
6. **Zak, A. K.**, Abd Majid, W. H., Darroudi, M., Yousefi, R., (2011), 'Synthesis and characterization of ZnO nanoparticles prepared in gelatin media', *Materials Letters*, 65 (1), 70-73.
7. **Zak, A. K.**, Abd Majid, W. H., Abrishami, M.E., Yousefi, R., (2011), 'X-ray analysis of ZnO nanoparticles by Williamson-Hall and size-strain plot methods', *Solid State Sciences*, 13 (1), 251-56.
8. **Zak, A. K.**, Abrishami, R., Abd Majid, W. H., M.E., Yousefi, Hosseini, S.M., (2011), 'Effects of annealing temperature on some structural and optical properties of ZnO nanoparticles prepared by a modified sol-gel combustion method', *Ceramics International*, 37 (1), 393-98.
9. **Zak, A. K.**, Chen, G. W., et al (2011), 'Dielectric Properties of PVDF/PZT', *AIP Conference Proceedings*, 1328, 238-40
10. **Zak, A. K.**, Abd Majid, W. H., W. H., Abrishami, (2011), 'Experimental and theoretical dielectric studies of PVDF/PZT nanocomposite thin films', *Ceramics International*, 37 (5), 1653-60.
11. Razali, R., **Zak, A. K.**, Majid, W. H., Darroudi M., (2011), 'Solvothermal synthesis of microsphere ZnO nanostructures in DEA media', *Ceramics International*, 37 (8) 3657-63.
12. **Zak A. K.**, Abd. Majid W. H., Huang, N. M., Wang, H. Z., Ren, Z. F., (2011) 'Sonochemical Synthesis of Hierarchical Nanostructured ZnO' Sonochemical Sonochemistry, Revised

INTERNATIONAL CONFERENCES ATTENDED

1. **A.K. Zak**, W.H. Abd. Majid, Synthesis and optical properties of PZT nanoparticles prepared by sol-gel method, International Inform Connect 2010, 13-15 January, 2010, Kuala Lumpur Malaysia. (Poster presentation)
2. **A.K. Zak**, M. Ebrahimizadeh Abrishami, W.H. Abd. Majid, Synthesis of ZnO nanoparticles by a modified sol-gel combustion method, International Conference on Functional Material & Devises, 14-17 Jun 2010, Terengganu, Malaysia. (Poster presentation)
3. **A.K. Zak**, Ramin Yousefi, W. H. Abd. Majid , M. R. Muhamad, Synthesis and characterization of $Zn_xK_{1-2x}O$ nanoparticles prepared in gelatin media, 2nd ASEAN–APCTP Workshop on Advanced Materials Science and Nanotechnology (Amsn 2010) 21–23 December 2010, Penang Malaysia. (Oral presentation)